Study of charmless $B_{(s)}$ meson decays involving η' and ϕ intermediate states at the LHCb experiment

Jessica PRISCIANDARO

ÉCOLE POLYTECHNIQUE
FÉDÉRALE DE LAUSANNE

Suisse
2015

Abstract

LHCb is one of the four main experiments located at the Large Hadron Collider (LHC) at CERN, and has collected about $3\,\mathrm{fb}^{-1}$ of proton-proton collisions at $\sqrt{s} = 7\,\mathrm{TeV}$ and 8 TeV between December 2009 and December 2012. Designed for the study of B-meson decays and for precision CP-violation measurements, the LHCb detector requires a high resolution vertex reconstruction, a precise measurement of the charged particle's momentum and an excellent particle identification. In this thesis, a study of the LHCb magnetic field map and two physics analyses are presented.

Based on the magnetic field measurements collected during a dedicated campaign in February 2011, the magnetic field map is corrected for mis-alignments, considering global translations and rotations. A more reliable mapping of the field is provided, and is used for the LHCb event reconstruction since June 2011. As a consequence of this study, the mass resolution is improved, and a better agreement between the software alignment and the survey measurements of the tracking stations is obtained.

The physics analyses presented in this thesis are focused on the study of charmless B decays, and exploit the $1\,\mathrm{fb}^{-1}$ of data at $\sqrt{s} = 7\,\mathrm{TeV}$ and the $2\,\mathrm{fb}^{-1}$ of data at $\sqrt{s} = 8\,\mathrm{TeV}$ collected in 2011 and 2012, respectively. Because of the tiny $b \to u$ tree and $b \to s(d)$ penguin transitions, and the large number of unexplored channels, charmless B decays constitute a very promising sector for new physics discovery, both in branching fraction measurements of penguin dominated decays, and in CP violation measurements.

The first analysis, performed with the 7 TeV data, is dedicated to the search of the rare $B^{\pm} \to \phi\pi^{\pm}$ decay and to the measurement of the $B^{\pm} \to \phi K^{\pm}$ CP asymmetry. In both cases, a deviation from the Standard Model predictions would be an indication of new physics.

The best upper limit on the $B^{\pm} \to \phi\pi^{\pm}$ and the most precise $B^{\pm} \to \phi K^{\pm}$ CP asymmetry are obtained:

$$\mathcal{B}(B^{\pm} \to \phi\pi^{\pm}) < 1.55(1.80) \times 10^{-7} \text{at } 90\% \text{ (95\%) CL}, \tag{1}$$

and

$$\mathcal{A}^{CP}(B^{\pm} \to \phi K^{\pm}) = (2.2 \pm 2.1(\text{stat}) \pm 0.7(\text{syst}) \pm 0.6(J/\psi K^{\pm})) \times 10^{-2}, \qquad (2)$$

where the last uncertainty accounts for the uncertainty on the knowledge of the $B^{\pm} \to J/\psi K^{\pm}$ charge asymmetry, used as reference.

Both measurements are compatible with the theoretical predictions, which are in the range $(0.5 - 6.0) \times 10^{-8}$ for the $B^{\pm} \to \phi \pi^{\pm}$ branching fraction and of $1 - 2\%$ with uncertainty of few percent for the $B^{\pm} \to \phi K^{\pm}$ CP asymmetry.

An update of the $B^{\pm} \to \phi K^{\pm}$ CP asymmetry is performed including the 2012 data leading to a further improvement in precision:

$$\mathcal{A}^{CP}(B^{\pm} \to \phi K^{\pm}) = (1.7 \pm 1.1(\text{stat}) \pm 0.2(\text{syst}) \pm 0.6(J/\psi K^{\pm})) \times 10^{-2}. \qquad (3)$$

A second analysis is described in this thesis, which aims at the study of $B^{\pm}$ and B_s^0 decays with η' resonances in the final state, exploiting the full 2011 and 2012 statistics. Two modes are investigated: the $B_s^0 \to \eta'\eta'$ mode, not observed yet, which branching fraction is predicted in the range $(14 - 50) \times 10^{-6}$, and the $B^{\pm} \to \eta' K^{\pm}$ mode, used as reference channel for the $B_s^0 \to \eta'\eta'$ search, and for which the CP asymmetry is also measured. All the η' resonances are reconstructed in the $\pi^+\pi^-\gamma$ final state, which introduces the additional challenge of identifying and reconstructing photons in the LHCb hadronic environment.

As a result, the $B_s^0 \to \eta'\eta'$ decay is observed for the first time with a significance of 6.4, and its branching ratio is measured to be:

$$\mathcal{B}(B_s^0 \to \eta'\eta') = (3.31 \pm 0.64(\text{stat}) \pm 0.28(\text{syst}) \pm 0.12(B^{\pm} \to \eta' K^{\pm})) \times 10^{-5}. \qquad (4)$$

Finally, the most precise measurement of the $B^{\pm} \to \eta' K^{\pm}$ CP asymmetry is obtained:

$$\mathcal{A}^{CP}(B^{\pm} \to \eta' K^{\pm}) = (-0.2 \pm 1.2(\text{stat}) \pm 0.1(\text{syst}) \pm 0.6(J/\psi K^{\pm})) \times 10^{-2} \qquad (5)$$

compatible with the current PDG average, $\mathcal{A}^{CP}(B_s^0 \to \eta' K^{\pm}) = 0.013 \pm 0.017$.

Résumé

LHCb est une des quatre expériences principales situées au Large Hadron Collider (LHC) du CERN, et a collecté, entre décembre 2009 et décembre 2012, environ $3\,\text{fb}^{-1}$ de données de collisions proton-proton à des énergies de 7 et 8 TeV. L'objectif prioritaire de l'expérience LHCb est l'étude des désintégrations des mésons B et la mesure précise des paramètres de la violation de la symétrie CP. Pour ce faire, le détecteur LHCb dispose d'une excellente reconstruction des vertex, d'une mesure précise de la quantité de mouvement des particules et d'un système d'identification optimal. Dans cette thèse, une étude de la carte du champ magnétique et deux analyses de physique sont présentées.

La correction de la carte du champ magnétique se base sur la campagne de mesures du champ réalisée en février 2011. Ces mesures permettent de corriger les défauts d'alignement au moyen de translations et de rotations globales. Une carte améliorée du champ a ainsi été développée, et a permis d'obtenir un meilleur accord entre l'alignement par logiciel et les mesures sur site des positions des stations de trajectographie. La nouvelle carte du champ est utilisée pour la reconstruction des événements de LHCb depuis juin 2011.

Les analyses de physique présentées dans cette thèse concernent l'étude de la désintégration sans charme des mésons B en exploitant $1\,\text{fb}^{-1}$ de données à 7 TeV et $2\,\text{fb}^{-1}$ à 8 TeV, correspondant aux données collectées en 2011 et 2012 respectivement. Du fait de la rareté des transitions $b \rightarrow u$ et $b \rightarrow s(d)$, les désintégrations sans charme des mésons B constituent un secteur très prometteur pour la recherche de nouvelle physique, tant par les mesures des probabilités de désintégration que par les mesures de violation CP.

La première analyse, faites sur les données à 7 TeV, est dédiée à la recherche de la désintégration rare $B^{\pm} \rightarrow \phi\pi^{\pm}$ et à la mesure de l'asymétrie CP dans les désintégrations $B^{\pm} \rightarrow \phi K^{\pm}$. Dans les deux cas, l'observation d'une déviation par rapport aux prédictions du modèle standard constituerait un signe de nouvelle physique.

Cette analyse a permis d'obtenir la limite supérieure la plus contraignante et la mesure

d'asymétrie *CP* la plus précise à ce jour:

$$\mathcal{B}(B^{\pm} \to \phi\pi^{\pm}) < 1.55(1.80) \times 10^{-7} \text{at } 90\% \ (95\%) \text{ CL} \,, \qquad (6)$$

et

$$\mathcal{A}^{CP}(B^{\pm} \to \phi K^{\pm}) = (2.2 \pm 2.1(\text{stat}) \pm 0.7(\text{syst}) \pm 0.6(J/\psi K^{\pm})) \times 10^{-2} \,, \qquad (7)$$

où la dernière erreur citée rend compte de l'incertitude sur l'asymétrie de charge dans la désintégration $B^{\pm} \to J/\psi K^{\pm}$, utilisée comme référence.

Ces mesures sont compatibles avec les prédictions théoriques qui sont dans les intervalles $(0.5 - 0.6) \times 10^{-8}$ pour le taux de branchement de la désintégration $B^{\pm} \to \phi\pi^{\pm}$ et $1 - 2\%$ pour l'asymétrie *CP* dans la désintégration $B^{\pm} \to \phi K^{\pm}$.

L'analyse a été réitérée en incluant les données de 2012, produisant la mesure plus précise suivante:

$$\mathcal{A}^{CP}(B^{\pm} \to \phi K^{\pm}) = (1.7 \pm 1.1(\text{stat}) \pm 0.2(\text{syst}) \pm 0.6(J/\psi K^{\pm})) \times 10^{-2} \,. \qquad (8)$$

Cette thèse décrit une seconde analyse, utilisant l'intégralité des données de 2011 et 2012, et dont le but est l'étude des désintégrations des mésons $B^{\pm}$ et B_s^0 produisant des résonances de type η' dans l'état final. Deux modes de désintégration sont investigués: le mode $B_s^0 \to \eta'\eta'$, encore inobservé et pour lequel un grand rapport de branchement par rapport aux autres désintégrations des B_s^0 est prédit, dans l'intervalle $(14 - 50) \times 10^{-6}$, et le mode $B^{\pm} \to \eta' K^{\pm}$, utilisé comme canal de référence pour la recherche de $B_s^0 \to \eta'\eta'$, et pour lequel l'asymétrie *CP* est mesurée. Les mésons η' sont reconstruits dans leur mode de désintégration $\eta' \to \pi^+\pi^-\gamma$, pour lequel la détection du photon est compliquée par l'environnement hadronique à LHCb.

Cette analyse a mené à la première observation de la désintégration $B_s^0 \to \eta'\eta'$ avec une significance de 6.4 déviations standards. La mesure de son rapport de branchement fournit la valeur suivante:

$$\mathcal{B}(B_s^0 \to \eta'\eta') = (3.31 \pm 0.64(\text{stat}) \pm 0.28(\text{syst}) \pm 0.12(B^{\pm} \to \eta' K^{\pm})) \times 10^{-5} \,. \qquad (9)$$

Finalement, la mesure suivante de l'asymétrie *CP* dans la désintégration $B^{\pm} \to \eta' K^{\pm}$ est obtenue:

$$\mathcal{A}^{CP}(B^{\pm} \to \eta' K^{\pm}) = (-0.2 \pm 1.2(\text{stat}) \pm 0.1(\text{syst}) \pm 0.6(J/\psi K^{\pm})) \times 10^{-2} \,. \qquad (10)$$

Cette mesure est la plus précise à ce jour, et est compatible avec la moyenne mondiale, $\mathcal{A}^{CP}(B_s^0 \to \eta' K^{\pm}) = 0.013 \pm 0.017$.

Sommario

LHCb è uno dei quattro principali esperimenti collocati al Large Hadron Collider (LHC) al CERN, ed ha raccolto circa $3\,\text{fb}^{-1}$ di collisioni protone-protone a $\sqrt{s} = 7\,\text{TeV}$ e $8\,\text{TeV}$ nel periodo tra Dicembre 2009 e Dicembre 2012. Progettato per studiare il decadimento dei mesoni B e per effettuare precise misure di violazione di CP, l'esperimento è dotato di un eccellente risoluzione nella ricostruzione dei vertici di decadimento, nella misura dell'impulso delle particelle e di un' ottima discriminazione del tipo di particelle. Questa tesi riporta gli studi condotti per mappare il campo magnetico di LHCb e due analisi di processi fisici.

La mappa del campo magnetico di LHCb è stata prodotta basandosi sui dati raccolti nella campagna di misura condotta nel Febbraio 2011 e sulla mappa precedentemente in uso. La nuova e più affidabile mappa, entrata in vigore a partire da Giugno 2011 è tuttora in uso nella la ricostruzione degli eventi, corregge i difetti della precedente tenendo in considerazione traslazioni e rotazioni globali del sistema. Come diretta conseguenza di questo lavoro, si sono ottenute una migliore risoluzione della massa ricostruita ed un migliore accordo tra le posizioni delle camere di tracciamento valutate tramite gli algoritmi di allineamento e le misure sperimentali.

I processi fisici oggetto di questa tesi vertono intorno ai decadimenti *charmless* (senza la presenza di quarks *c*) dei mesoni B e sfruttano i dati raccolti nel 2011 e 2012 ammontanti rispettivamente a $1\,\text{fb}^{-1}$ a $\sqrt{s} = 7\,\text{TeV}$ e $2\,\text{fb}^{-1}$ a $\sqrt{s} = 8\,\text{TeV}$. Data la scarsa probabilità delle transizioni $b \rightarrow u$ e $b \rightarrow s(d)$, i decadimenti charmless dei mesoni B, in gran parte ancora inesplorati, sono un campo molto promettente per osservare la presenza di nuovi fenomeni fisici, sia attraverso misure di probabilità di decadimento in stati finali dominati da diagrammi a pinguino, sia attraverso misure di violazione di CP.

La prima analisi presentata, basata sul campione di dati a 7 TeV, si concentra sulla ricerca del decadimento raro $B^{\pm} \rightarrow \phi\pi^{\pm}$ e sulla misura di asimmetria di CP nel decadimento $B^{\pm} \rightarrow \phi K^{\pm}$. In entrambi i casi, deviazioni dalle predizioni del Modello Standard indicherebbero la presenza di nuova fisica.

Il limite superiore alla probabilità di decadimento,

$$\mathcal{B}(B^\pm \to \phi\pi^\pm) < 1.55(1.80) \times 10^{-7} \text{at } 90\% \ (95\%) \ \text{CL} \,, \tag{11}$$

e il valore dell'asimmetria di *CP*,

$$\mathcal{A}^{CP}(B^\pm \to \phi K^\pm) = (2.2 \pm 2.1(\text{stat}) \pm 0.7(\text{syst}) \pm 0.6(J/\psi K^\pm)) \times 10^{-2} \,, \tag{12}$$

risultano essere le migliori misure mai ottenute a riguardo. L'ultima sorgente di errore quotata per l'asimmetria di *CP* è legata all'incertezza sull'asimmetria di carica nel decadimento $B^\pm \to J/\psi K^\pm$, usato come riferimento.

Entrambe le misure sono compatibile con le predizioni teoriche del Modello Standard, le quali prevedono una probabilitá per il decadimento $B^\pm \to \phi\pi^\pm$ nell'intervallo $(0.5 - 6.0) \times 10^{-8}$, e un'asimmetria di carica dell $1 - 2\%$ per il decadimento $B^\pm \to \phi K^\pm$.

Il valore dell'asimmetria di *CP* è stato aggiornato aggiungendo i dati raccolti nel 2012 ottenendo un risultato ancora più preciso:

$$\mathcal{A}^{CP}(B^\pm \to \phi K^\pm) = (1.7 \pm 1.1(\text{stat}) \pm 0.2(\text{syst}) \pm 0.6(J/\psi K^\pm)) \times 10^{-2} \,. \tag{13}$$

La seconda analisi presentata in questa tesi sfrutta tutti i dati raccolti nel 2011 e 2012 e studia due decadimenti dei mesoni $B^\pm$ e B^0_s i cui stati intermedi sono caratterizzati dalla presenza di risonanze η'. I due decadimenti sotto esame sono $B^0_s \to \eta'\eta'$, mai osservato, e la cui probabilitá di decadimento è predetta essere nell'intervallo $(14 - 50) \times 10^{-6}$, e il decadimento $B^\pm \to \eta' K^\pm$, utilizzato come canale di riferimento per la ricerca del decadimento precedente, e per il quale è stata effettuata una misura dell' asimmetria di *CP*. I decadimenti del mesone η' sono ricostruiti nello stato finale $\pi^+\pi^-\gamma$, aggiungendo all'analisi le difficoltà dovute all'identificazione e alla ricostruzione dei fotoni in ambiente adronico.

Dall'analisi dei dati risulta la prima osservazione del decadimento $B^0_s \to \eta'\eta'$ con una significatività di 6.4 deviazioni standard e con una probabilità di decadimento

$$\mathcal{B}(B^0_s \to \eta'\eta') = (3.31 \pm 0.64(\text{stat}) \pm 0.28(\text{syst}) \pm 0.12(B^\pm \to \eta' K^\pm)) \times 10^{-5} \,. \tag{14}$$

Infine, la misura dell'asimmetria di *CP* nel decadimento $B^\pm \to \eta' K^\pm$ ottenuta,

$$\mathcal{A}^{CP}(B^\pm \to \eta' K^\pm) = (-0.2 \pm 1.2(\text{stat}) \pm 0.1(\text{syst}) \pm 0.6(J/\psi K^\pm)) \times 10^{-2} \,, \tag{15}$$

risulta essere la più precisa disponibile, ed è compatibile con l'attuale media del PDG, $\mathcal{A}^{CP}(B^0_s \to \eta' K^\pm) = 0.013 \pm 0.017$.

Aknowledgments

Firstly, I would like to thank my supervisor, Olivier Schneider, who gave me the opportunity to start the most building experience of my life. Your guide, your teaching, and the passion for particle physics you passed on, made me love this field even more.

A particularly heartfelt thanks to Fred Blanc, my co-supervisor. Thank you for everything you taught me during these four years, for all the illuminating discussions we had, and for the billions of emails to which you have always answered promptly. And, most of all, thank you for always trusting my abilities, even when I didn't, and for having helped me to integrate when first I arrived at EPFL four years ago. It was a great pleasure working with you.

Thanks to the entire EPFL group (and I hope not to forget anyone!). Thanks to Tatsuya Nakada, who guided me in my first task as a PhD student, and to Aurelio Bay, for his always useful advises. Thanks to Erika and Esther, the best secretaries ever. It is only thanks to you that I did not miss every single deadline of the past four years! Thanks to my former colleagues at the CERN office, Yasmine and Greig, for your help and your friendship. And thanks to all the people still in the group. To Giovanni, who firstly took a bit of Italy at EPFL, making me feeling a bit more at home, to Albert (and all the coffees we had!), to Mirco and our cool Pittsburg/New York trip. Thanks to Mark, Rita and all the other colleagues, who contributed to make these years memorable. I will miss you!

Last but not least, grazie alla mia famiglia. A mia mamma e mio papà, per tutti i sacrifici che avete fatto perchè oggi possa essere qui. A mia sorella, per tutto quello che abbiamo condiviso dal giorno in cui sei nata e per essere diventata un'amica su cui poter sempre contare. Alle mie nonne, per il vostro amore incondizionato. Grazie a tutti voi per avermi sempre consigliato ed incoraggiato ad andare avanti, anche quando andare avanti significava partire. Grazie per accogliermi a braccia aperte ogni volta che torno, e per nascondere la tristezza quando devo ripartire. È a voi che dedico questo successo.

E infine, grazie alla persona che, tenendomi per mano, mi ha accompagnato lungo questo percorso. Che con il suo amore, pazienza, complicità e fiducia mi ha dato il

coraggio per affrontare ogni sfida, condividendone le difficoltà e i traguardi. Non sarei qui senza di te. Grazie Mauro.

Contents

1

Introduction

The Standard Model (SM) of particle physics holds all our knowledge on the fundamental particles and their interactions up to the highest energy scale experimentally accessible so far. SM theoretical predictions have been extensively validated by experiments at accelerators and colliders, like KEKB, LEP, PEP-II and Tevatron. Despite the good agreement between experimental results and theory, it is however well-known that the SM is an incomplete theory, which does not explain many observed phenomena.

After the recent discovery of the Higgs boson at the Large Hadron Collider (LHC) [1,2], the main goal of the particle physics community is to explore higher-energy frontiers and search for hints of New Physics (NP) that could incorporate the SM in a larger and more complete theory. Measurements of CP-violating observables and of loop-dominated transitions in the flavour sector, described in the SM by the Cabibbo-Kobayashi-Maskawa (CKM) mechanism [3,4], are a valuable probe for NP searches. The b-hadron decays are particularly interesting for this purpose since large deviations from the SM are predicted in many beyond-the-SM theories. The two experiments BaBar and Belle, located at asymmetric e^+e^- colliders and operating at centre-of-mass energies between 10 and 11 GeV, have been dedicated to the study of B-meson decays. They collected large samples of $B\bar{B}$ pairs at the energy of the $Y(4S)$ resonance, observing for the first time CP violation in the b sector [5,6] and establishing the validity of the CKM mechanism. With the LHCb experiment operating at the LHC, new insights can be gained. The larger $b\bar{b}$ production cross-section at high-energy hadronic machines, and hence the resulting larger statistics, allows for more precise measurements, while the higher energies open the way to the investigation of all species of b-hadrons.

The main subject of this thesis is the study of $B^{\pm}$ and B_s^0 meson decays into charmless final states. Charmless B decays constitute a very promising sector of b physics for NP searches. Because of the suppression of $b \to u$ tree transitions, each charmless decay described by both a tree and a loop amplitude is a potential candidate for NP discovery.

This document is organised in the following way. Chapter 2 gives an overview of the theoretical aspects underlying the analyses presented here. After an introduction on the Standard Model, the chapter is focused on flavour physics and charmless B decays,

and aims at giving a theoretical justification of the analyses that are performed. The LHC accelerator and the LHCb detector are presented in Chapters 3 and 4, respectively. Each part of the detector is described, and the detector performances are summarised. Chapter 5 is dedicated to the description of the magnetic field campaign performed in February 2011, resulting in a new mapping of the field used in the LHCb reconstruction since June 2011. The following three chapters of the thesis contain a detailed description of four charmless B decay analyses. Chapter 6 aims at giving an overview of the analysis structure, emphasizing the aspects that are common to these studies. The search for the rare $B^{\pm} \to \phi\pi^{\pm}$ decay as well as the measurement of the $B^{\pm} \to \phi K^{\pm}$ CP asymmetry are presented in Chapter 7, while Chapter 8 describes the analysis that led to the first observation of the $B_s^0 \to \eta'\eta'$ decay and the measurement of the $B^{\pm} \to \eta'K^{\pm}$ CP asymmetry. Finally, a discussion on the results and on future prospects is given in Chapter 9.

2

Charmless decays of B mesons in the Standard Model

This chapter explains the theoretical motivations of the physics analyses described in this thesis. After an introduction, which gives a general overview of the Standard Model and points out both its strength and incompleteness, we focus on the *flavour sector*, from which hints of New Physics can arise. Subsequently, a review of charmless B decays and of the different approaches to study them is given. Finally we concentrate on the four decay modes that are the subject of the physics analyses described in the following chapters.

2.1 The Standard Model

The Standard Model (SM) of particle physics gives the most complete and experimentally validated picture of what we see in nature, describing the universe in terms of matter and forces [7–10]. It is a *relativistic quantum field theory*, symmetric under local gauge transformations of the group

$$\mathrm{SU}(3)_C \times \mathrm{SU}(2)_L \times \mathrm{U}(1)_Y, \tag{2.1}$$

where C is the generator of the *colour charge*, Y is the generator of the *weak hypercharge*, and L denotes left-handed leptons. It covers three of the four fundamental interactions, the electromagnetic and weak interactions, unified in the electroweak force based on the $\mathrm{SU}(2)_L \times \mathrm{U}(1)_Y$ gauge group, and the strong interaction, with the symmetry group $\mathrm{SU}(3)_C$. The elementary constituents of matter, called *fermions*, are described by Dirac spinors, and are divided in leptons and quarks. All the fermions interact electromagnetically if charged, and weakly if left-handed. The leptons don't interact strongly, while the quarks are colour triplets under transformations of the $\mathrm{SU}(3)_C$ group. Fermions are further classified in three *generations*. The correspondent fermions of different generations have the same quantum charges but are characterised by different *flavours*. The main properties of the fundamental fermions are summarised in Table 2.1.

Table 2.1 *List of the fermions in the Standard Model [11]. The generation, the electric charge (Q) in unit of |e|, the mass (m) and the interactions to which they are sensitive are indicated. W, EW and S indicate the weak, the electroweak and the strong interaction, respectively.*

Symbol	Generation	Q (e)	m (MeV/c^2)	Interaction
Leptons
e^-	1st	-1	$0.510998910 \pm 0.000000013$	EW
ν_e	1st	0	$< 2.2 \times 10^{-6}$	W
μ^-	2nd	-1	$105.6583668 \pm 0.0000038$	EW
ν_μ	2nd	0	< 0.19	W
τ^-	3rd	-1	1776.82 ± 0.16	EW
ν_τ	3rd	0	< 18.2	W
Quarks
u	1st	2/3	2.34 ± 0.19	EW, S
d	1st	$-1/3$	4.78 ± 0.11	EW, S
c	2nd	2/3	1294 ± 4	EW, S
s	2nd	$-1/3$	100.2 ± 2.4	EW, S
t	3rd	2/3	$(172.9 \pm 0.6 \pm 0.9) \times 10^3$	EW, S
b	3rd	$-1/3$	$\left(4.670^{+0.018}_{-0.060}\right) \times 10^3$	EW, S

As a consequence of the local gauge invariance of the SM Lagrangian, the interactions among fermions proceed through the exchange of spin-1 particles, named *bosons*. The strong interaction is mediated by eight gluons, the mediators of the weak interaction are two charged and a neutral boson, $W^\pm$ and Z^0 respectively, while the electromagnetic interaction acts through photon exchange.

In the scenario described so far, it is not possible to give mass to the particles without violating the gauge symmetry. To have massive particles in the SM, a spin-0 boson, the Higgs field, has to be included. The Higgs field is a doublet of the $SU(2)_L$ group, and through a mechanism called *spontaneous symmetry breaking* gives mass to itself and to the $W^\pm$ and Z bosons. Finally, from the interaction of the Higgs field with fermions, the so called *Yukawa coupling*, all the fermions acquire mass.

In summary, the Standard Model Lagrangian can be written as the sum of four terms,

$$\mathcal{L} = \mathcal{L}_{\text{EW}} + \mathcal{L}_{\text{QCD}} + \mathcal{L}_{\text{Higgs}} + \mathcal{L}_{\text{Yukawa}} , \tag{2.2}$$

where $\mathcal{L}_{\text{EW}}$ describes the electroweak interaction, $\mathcal{L}_{\text{QCD}}$ is the term responsible of the strong interaction and the two terms $\mathcal{L}_{\text{Higgs}}$ and $\mathcal{L}_{\text{Yukawa}}$ give mass to the bosons and to the fermions, respectively. Moreover, flavour arises from the Yukawa term: the interaction of quarks with the Higgs field is in fact responsible of the mixing of the three quarks families under the weak interaction.

The SM describes with incredible precision all the interaction processes observed so far, in the full energy scale accessible experimentally. Its validation culminates with

the recent discovery, by the ATLAS [1] and CMS [2] experiments at the Large Hadron Collider (LHC) [12], of a resonance of mass $\sim 125\,\text{GeV}/c^2$ compatible with the Higgs boson [13, 14].

However the SM is not a complete theory. It does not include gravity, dark matter and dark energy, and does not explain the fundamental physics phenomena behind neutrino oscillations [15, 16] nor the matter-antimatter asymmetry of the Universe [17]. Moreover, the presence of a large number of free parameters and the hierarchy problem [18], may be an indication that the SM is a low-energy effective theory, that is part of a more fundamental theory.

Two complementary approaches for New Physics (NP) searches are investigated. *Direct* searches aim at observing NP in the products of high-energy collisions and require the highest possible energy in the centre of mass. *Indirect* searches look instead at physics observables in which NP can cause a deviation from the SM prediction. Indirect searches are therefore limited by the precision of measurements and predictions. Flavour physics constitutes one of the best areas for NP indirect searches.

2.2 The CKM matrix

We focus now on the Yukawa interactions in order to understand how NP can stem from the flavour sector.

In absence of the Higgs field, the weak interaction arises from the coupling of an u_L and a d_L quark with a $W^\pm$ boson, where L indicates left-handed quarks. This coupling is diagonal, *i.e.* the u_L and the d_L quark belong to the same multiplet.

With the introduction of the Higgs field, the Yukawa term appears in the Lagrangian to give mass to the quarks:

$$\mathcal{L}_{\text{Yukawa}} = -Y_{ij}^d \overline{Q_{Li}^I} \phi \, d_{Rj}^I - Y_{ij}^u \overline{Q_{Li}^I} \epsilon \, \phi^* \, u_{Rj}^I + \text{h.c.}, \tag{2.3}$$

where Y^u and Y^d are 3×3 complex matrices, ϕ is the Higgs field, Q_L^I is the left-handed doublet, d_R^I and u_R^I are the two right-handed singlets, i and j indicate the generation, I indicates the quark family, and ϵ is the antisymmetric tensor.

The mass states are obtained from the diagonalization of the two matrices Y_{ij}^d and Y_{ij}^u.

In this new basis the interaction among quarks and the $W^\pm$ boson is not diagonal, and assumes the form

$$-\frac{g}{\sqrt{2}} \overline{u'}_L^i \gamma^\mu W_\mu^+ V_{ij} d'^j_L + \text{h.c.}, \tag{2.4}$$

where V_{ij} are the elements of the Cabibbo-Kobayashi-Maskawa (CKM) quark mixing matrix V_{CKM} [3, 4],

$$V_{CKM} = \begin{pmatrix} V_{ud} & V_{us} & V_{ub} \\ V_{cd} & V_{cs} & V_{cb} \\ V_{td} & V_{ts} & V_{tb} \end{pmatrix} . \tag{2.5}$$

The CKM matrix is a complex unitary matrix and its off-diagonal terms allow for couplings between mass eigenstates of different generations. It contains all the flavour-changing couplings of the SM and does not affect the coupling of quarks to the Z boson.

Flavour-changing charged currents (FCCC), in which a quark changes flavour and charge, can therefore occur only through the exchange of a $W^{\pm}$ boson, at *tree level*. On the other hand, flavour-changing neutral currents (FCNC), in which the quark changes flavour but not charge, are suppressed and can occur only at the *loop level*, in which an intermediate exchange of at least a quark and a $W^{\pm}$ boson is required. Moreover, they are further suppressed by the GIM mechanism [19], which states that the smaller the mass splitting among the generations, the larger the suppression. Because of the high suppression, FCNC are good probes for NP. If non-SM particles exist, they can enter in the loop, affect the amplitude and phase of the process, and therefore induce a modification of the observables.

As a consequence of the unitarity of the CKM matrix, and since all the phases except one can be absorbed into the quark fields, only four independent parameters are needed to describe V_{CKM}. The standard parametrisation [11] uses three *mixing* angles θ_{ij}, and one complex phase δ responsible of *CP* violation:

$$V_{CKM} = \begin{pmatrix} c_{12}c_{23} & s_{12}c_{13} & s_{13}e^{-i\delta} \\ -s_{12}c_{23} - c_{12}s_{23}s_{13}e^{i\delta} & c_{12}c_{23} - s_{12}s_{23}s_{13}e^{i\delta} & s_{23}c_{13} \\ s_{12}s_{23} - c_{12}c_{23}s_{13}e^{i\delta} & -c_{12}s_{23} - s_{12}c_{23}s_{13}e^{i\delta} & c_{23}c_{13} \end{pmatrix}, \tag{2.6}$$

where $s_{ij} = \sin\theta_{ij}$ and $c_{ij} = \cos\theta_{ij}$.

This is the only source of *CP* violation in the SM. Many extensions of the SM imply additional sources of *CP* violation. *CP* violation is fundamental to explain baryogenesis [17], but the amount of *CP* asymmetry in the SM is too small. Measurements of *CP* violating observables are therefore fundamental to probe NP and test the SM.

A particularly useful parametrisation is the Wolfenstein parametrisation [20], based on the experimentally observed hierarchy $s_{13} \ll s_{23} \ll s_{12} \ll 1$. The Wolfenstein parametrisation expands the matrix in powers of $\lambda = s_{12} \approx 0.22$:

$$V_{CKM} = \begin{pmatrix} 1 - \frac{\lambda^2}{2} - \frac{\lambda^4}{8} & \lambda & A\lambda^3(\rho - i\eta) \\ -\lambda + A^2\frac{\lambda^5}{2}[1 - 2(\rho + i\eta)] & 1 - \frac{\lambda^2}{2} - \frac{\lambda^4}{8}(1 + 4A^2) & A\lambda^2 \\ A\lambda^3[1 - (1 - \frac{\lambda^2}{2})(\rho + i\eta)] & -A\lambda^2 + \frac{1}{2}A\lambda^4[1 - 2(\rho + i\eta)] & 1 - A^2\frac{\lambda^4}{2} \end{pmatrix} + \mathcal{O}(\lambda^6), \tag{2.7}$$

where A, ρ and η are defined as

$$s_{23} = A\lambda^2, \qquad s_{13}e^{i\delta} = A\lambda^3(\rho + i\eta). \tag{2.8}$$

The experimental values of A, ρ, λ and η are [11]:

$$\lambda = 0.2253 \pm 0.0007, \quad A = 0.808^{+0.022}_{-0.015}, \quad \rho = 0.132^{+0.022}_{-0.014}, \quad \eta = 0.341 \pm 0.013. \tag{2.9}$$

The unitarity of the CKM matrix imposes nine orthonormality conditions. Three constraints imply the *weak universality*, which states that the sum of the couplings of any of the up-type quarks to all the down-type quarks is the same for all the generations.

The six constraints expressing the orthogonality of rows and columns of the CKM matrix define unitarity triangles in the complex plane of $\bar{\rho} = \rho(1 - \frac{\lambda^2}{2})$ and $\bar{\eta} = \eta(1 - \frac{\lambda^2}{2})$, with area $J^{CP}/2$, where J^{CP} is the Jarlskog parameter. If the *CP* symmetry is violated $J^{CP} \neq 0$, as confirmed from the experimentally measured value $J^{CP} = (2.884^{+0.253}_{-0.053}) \times 10^{-5}$ [21]. The shapes of the six triangles are phase-convention independent and are therefore physical observables. The six triangles are:

$$\underbrace{V_{ud}V_{us}^*}_{\mathcal{O}(\lambda)} + \underbrace{V_{cd}V_{cs}^*}_{\mathcal{O}(\lambda)} + \underbrace{V_{td}V_{ts}^*}_{\mathcal{O}(\lambda^5)} = 0 \quad (ds \text{ triangle})$$

$$\underbrace{V_{ud}V_{ub}^*}_{(\rho+i\eta)A\lambda^3} + \underbrace{V_{cd}V_{cb}^*}_{-A\lambda^3} + \underbrace{V_{td}V_{tb}^*}_{(1-\rho-i\eta)A\lambda^3} = 0 \quad (db \text{ triangle})$$

$$\underbrace{V_{us}V_{ub}^*}_{\mathcal{O}(\lambda^4)} + \underbrace{V_{cs}V_{cb}^*}_{\mathcal{O}(\lambda^2)} + \underbrace{V_{ts}V_{tb}^*}_{\mathcal{O}(\lambda^2)} = 0 \quad (sb \text{ triangle})$$

$$\underbrace{V_{ud}V_{cd}^*}_{\mathcal{O}(\lambda)} + \underbrace{V_{us}V_{cs}^*}_{\mathcal{O}(\lambda)} + \underbrace{V_{ub}V_{cb}^*}_{\mathcal{O}(\lambda^5)} = 0 \quad (cu \text{ triangle})$$

$$\underbrace{V_{cd}V_{td}^*}_{\mathcal{O}(\lambda^4)} + \underbrace{V_{cs}V_{ts}^*}_{\mathcal{O}(\lambda^2)} + \underbrace{V_{cb}V_{tb}^*}_{\mathcal{O}(\lambda^2)} = 0 \quad (tc \text{ triangle})$$

$$\underbrace{V_{ud}V_{td}^*}_{(1-\rho-i\eta)A\lambda^3} + \underbrace{V_{us}V_{ts}^*}_{-A\lambda^3} + \underbrace{V_{ub}V_{tb}^*}_{(\rho+i\eta)A\lambda^3} = 0 \quad (tu \text{ triangle})$$

Among the six triangles the *db* triangle, also called unitarity triangle (UT), and the *tu* triangle are particularly interesting for studying *CP* violation. Their angles are $\mathcal{O}(1)$ and can be measured experimentally. The three angles of the UT triangle are

$$\alpha = \arg\left(-\frac{V_{td}^*V_{tb}}{V_{cd}^*V_{cb}}\right), \quad \beta = \arg\left(-\frac{V_{cd}^*V_{cb}}{V_{td}^*V_{tb}}\right), \quad \gamma = \arg\left(-\frac{V_{ud}^*V_{ub}}{V_{cd}^*V_{cb}}\right). \tag{2.10}$$

Another fundamental triangle is the *sb* triangle. Its angle

$$\beta_s = \arg\left(-\frac{V_{tb}^* V_{ts}}{V_{cb}^* V_{cs}}\right) \tag{2.11}$$

provides a measurement of the amount of *CP* violation in the B_s^0 sector. The current knowledge on the UT triangle is shown in Fig. 2.1 [21].
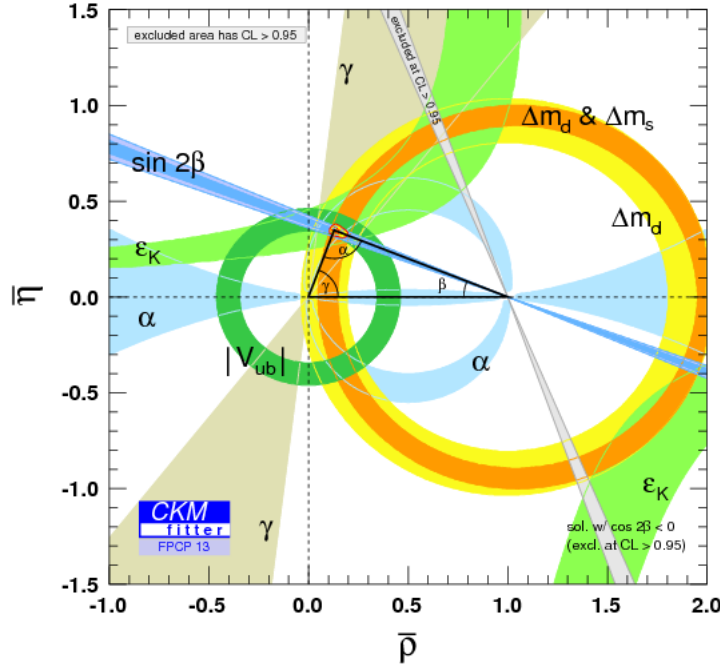
Figure 2.1   *Experimental constraints in the $(\overline{\rho}, \overline{\eta})$ plane [21]. The red hashed region of the global combination corresponds to 68% CL.*

2.3   *CP* violation in the Standard Model

As mentioned before, an approach to search for NP is to study *CP* violation. Let's consider the amplitude of a decay $B \to f$. In this decay we can have two different types of phases. The *weak* phase is the phase which appears in the coupling with the $W^{\pm}$ boson. It is *CP*-odd, *i.e.* it appears with opposite sign in the decay amplitude, A_f, and in its *CP* conjugate, $\overline{A}_{\overline{f}}$. The other type of phase is the *strong* phase. It can appear when the Lagrangian is real and is *CP*-even, *i.e.* it has the same sign in A_f and $\overline{A}_{\overline{f}}$. It arises from possible contributions of intermediate on-shell states or from rescattering due to the strong interaction. If we consider a decay amplitude with two contributions,

$A_f = a_1 + a_2$, we can write it as,

$$A_f = |a_1| \, e^{i(\delta_1 + \phi_1)} + |a_2| \, e^{i(\delta_2 + \phi_2)} \,, \tag{2.12}$$

and its *CP* conjugate as

$$\overline{A}_{\bar{f}} = |a_1| \, e^{i(\delta_1 - \phi_1)} + |a_2| \, e^{i(\delta_2 - \phi_2)} \,, \tag{2.13}$$

where ϕ_1 and ϕ_2 are the weak phases, and δ_1 and δ_2 are the strong phases. A *CP* asymmetry can arise only from the interference of amplitudes with different *weak* and *strong* phases.

In meson decays there are three possible ways for observing *CP* violation, depending on which phases contribute:

- *CP violation in decay*, or direct *CP* violation. It arises from the interference of two amplitudes, and the strong phase is due to rescattering.

- *CP violation in mixing*, or indirect *CP* violation. It is due to phenomena of *mixing* and it manifests if the mass eigenstate of neutral mesons are not *CP* eigenstate. It is purely an effect of the mixing, independent of the decay mode. The *strong* phase is due to the time evolution of the oscillation.

- *CP violation in interference*. It arises from the interference of the direct and mixed decay amplitudes. Again, the *strong* phase is due to the time evolution of the oscillation.

In charged meson decays, direct *CP* violation is the only source of *CP* asymmetry. The *CP* asymmetry is defined as

$$\mathcal{A}^{CP} \equiv \frac{\Gamma(B^- \to f^-) - \Gamma(B^+ \to f^+)}{\Gamma(B^- \to f^-) + \Gamma(B^+ \to f^+)} = \frac{\left|\overline{A}_{\bar{f}}\right|^2 - \left|A_f\right|^2}{\left|\overline{A}_{\bar{f}}\right|^2 + \left|A_f\right|^2} \,, \tag{2.14}$$

and, using Eq. 2.12, becomes

$$\mathcal{A}^{CP} = - \frac{2 \, |a_1 a_2| \, \sin(\delta_2 - \delta_1) \, \sin(\phi_2 - \phi_1)}{|a_1|^2 + |a_2|^2 + 2 \, |a_1 a_2| \, \cos(\delta_2 - \delta_1) \, \cos(\phi_2 - \phi_1)} \,. \tag{2.15}$$

2.4   Charmless *B* decays

A convenient way to study flavour-changing transitions is using a *low energy effective Hamiltonian*. *B* meson decays involve both short-distance effects and long-distance effects. The first determine quark-level flavour-changing transitions at the electroweak scale ($\sim M_W$), while long-distance effects are due to non-perturbative strong interactions at the scale Λ^{QCD} related to hadron formation. The computation of the decay amplitude is complicated by the presence of these two different energy scales. A solution consists in using the *factorization theorem* which separates the short and long-distance contributions. In the effective Hamiltonian approach, the decay amplitude of a hadronic decay, $B \to M_1 M_2$, becomes:

$$A(B \to M_1 M_2) = \langle M_1 M_2 | \mathcal{H}_{\text{eff}} | B \rangle = \frac{G_F}{\sqrt{2}} \sum_i \lambda_i c_i(\mu) \langle M_1 M_2 | O_i(\mu) | B \rangle, \qquad (2.16)$$

where λ_i are products of CKM matrix elements, $c_i(\mu)$ are *Wilson coefficients* which include all the perturbative short-distance effects above the scale μ, which for *B* decays is usually chosen as m_b, and $\langle M_1 M_2 | O_i(\mu) | B \rangle$ is the matrix element describing long-distance strong-interaction effects. Since $c_i(\mu)$ holds all the contributions at high energy, the existence of massive NP particles can be visible in the Wilson coefficients.

In the SM, the effective Hamiltonian for $b \to s$ transitions, excluding semileptonic and radiative decays, can be written as [22, 23]:

$$\mathcal{H}_{\text{eff}} = \frac{G_F}{\sqrt{2}} \sum_{q=u,c} V_{qs}^* V_{qb} \left[c_1(\mu) O_1^{(q)}(\mu) + c_2(\mu) O_2^{(q)}(\mu) + \sum_{i=3}^{10} c_i(\mu) O_i(\mu) \right], \qquad (2.17)$$

where the operators, illustrated in Fig. 2.2, can be grouped in the following categories:

- Current-current operators:

$$
\begin{aligned}
O_1^{(q)} &= (\bar{q}_i b_i)_{V-A} (\bar{s}_j q_j)_{V-A} \\
O_2^{(q)} &= (\bar{s}_i b_i)_{V-A} (\bar{q}_j q_j)_{V-A}
\end{aligned}
\qquad (2.18)
$$

- QCD-penguin operators:

$$
\begin{aligned}
O_3 &= (\bar{s}_i b_i)_{V-A} \sum_q (\bar{q}_j q_j)_{V-A} \\
O_4 &= \sum_q (\bar{q}_i b_i)_{V-A} (\bar{s}_j q_j)_{V-A} \\
O_5 &= (\bar{s}_i b_i)_{V-A} \sum_q (\bar{q}_j q_j)_{V+A} \\
O_6 &= \sum_q (\bar{q}_i b_i)_{V+A} (\bar{s}_j q_j)_{V-A}
\end{aligned}
\qquad (2.19)
$$

- Electroweak-penguin operators:

$$O_7 = \frac{3}{2}(\bar{s}_i b_i)_{V-A} \sum_q e_q (\bar{q}_j q_j)_{V+A} \qquad (2.20)$$

$$O_8 = \frac{3}{2} \sum_q e_q (\bar{q}_i b_i)_{V+A} (\bar{s}_j q_j)_{V-A}$$

$$O_9 = \frac{3}{2}(\bar{s}_i b_i)_{V-A} \sum_q e_q (\bar{q}_j q_j)_{V-A}$$

$$O_{10} = \frac{3}{2} \sum_q (\bar{q}_i b_i)_{V-A} (\bar{s}_j q_j)_{V-A}$$

where $(\bar{q}q)_{V\pm A} = \bar{q}\gamma_\mu(1 \pm \gamma_5)q$, i and j are the colour indices, and $e_{q'}$ is the electrical charge of quark q.

The main issue of the effective Hamiltonian approach is the evaluation of the hadronic matrix elements in a reliable way. Many methods have been developed in the last years, such as the QCD factorisation (QCDF) approach [24], the perturbative QCD (pQCD) method [25] and the soft-collinear effective theory (SCET) [26].

An alternative way to compute the decay amplitude, avoiding the evaluation of the hadronic matrix element, is based on the diagrammatic approach [27]. All the two-body charmless B amplitudes can be expressed using eight diagrams:

- the colour-favoured and colour-suppressed tree amplitudes $T^{(\prime)}$ and $C^{(\prime)}$;

- the gluonic-penguin amplitudes $P^{(\prime)}$;

- the colour-favoured and colour-suppressed electroweak-penguin (EWP) amplitudes $P^{(\prime)}_{EW}$ and $P^{(\prime)C}_{EW}$;

- the annihilation amplitude $A^{(\prime)}$;

- the exchange amplitude $E^{(\prime)}$;

- the penguin-annihilation amplitude $P^{(\prime)}_A$;

where the unprimed and the primed symbols denote $\Delta S = 0$ and $\Delta S = 1$ transitions, respectively. Considering $\lambda \simeq 0.22$, the magnitude of the various amplitudes is expected to follow the hierarchy:

$$
\begin{aligned}
1 &: \; |T|, \, |P'|, \qquad\qquad\qquad\qquad\qquad\qquad (2.21)\\
\mathcal{O}(\lambda) &: \; |C|, \, |P|, \, |T'|, \, |P'_{EW}|, \\
\mathcal{O}(\lambda^2) &: \; |E|, \, |A|, \, |P_{EW}|, \, |C'|, \, |P'_A|, \, \left|P'^C_{EW}\right|, \\
\mathcal{O}(\lambda^3) &: \; |P_A|, \, \left|P^C_{EW}\right|, \, |E'|, \, |A'| .
\end{aligned}
$$

A similar approach can be adopted for three-body decays, even if this is complicated because of the large number of resonant contributions.
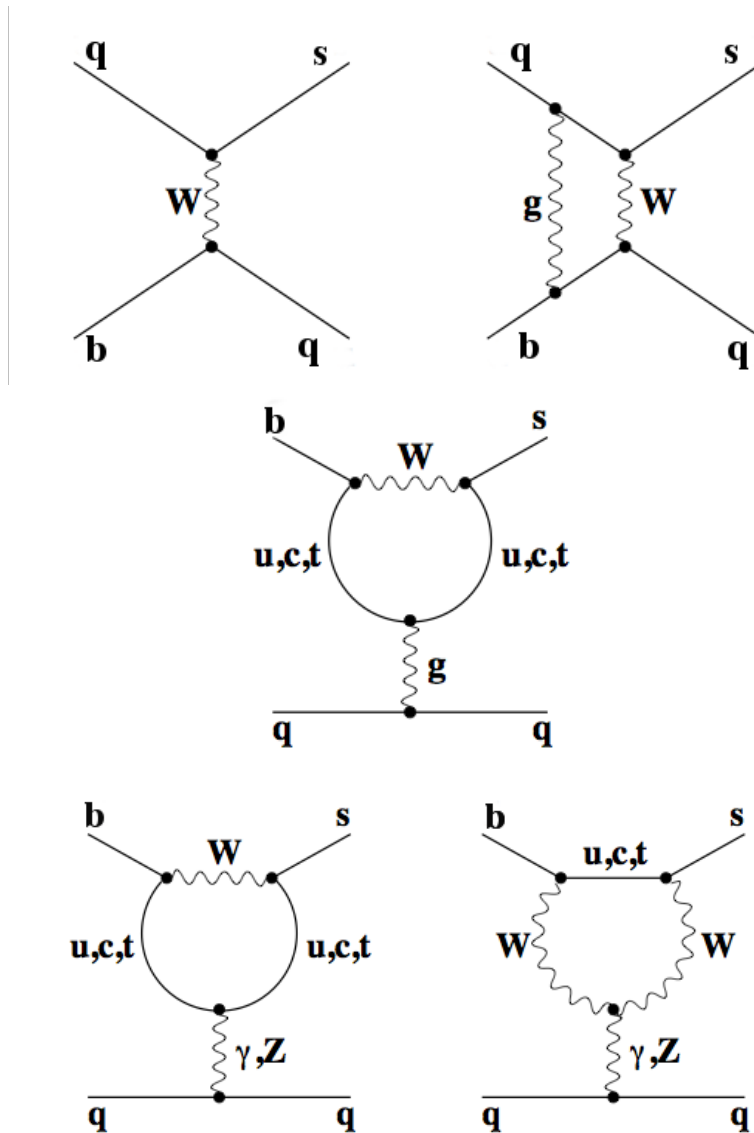
Figure 2.2   *Feynman diagrams for current-current (top), QCD-penguin (middle) and electroweak-penguin (bottom) operators [22].*

2.4.1 $B^\pm \to \phi\pi^\pm$ decay mode

The $B^\pm \to \phi\pi^\pm$ decay is considered to be a very sensitive probe to New Physics. Indeed, it is a flavour-changing neutral current process, driven by the $b \to ds\bar{s}$ quark-level transition (Fig. 2.3), highly suppressed because of the tiny product of the CKM matrix elements and because of the Okubo-Zweig-Iizuka (OZI) rule [1] [28–30] associated with the creation of the colourless $s\bar{s}$ pair forming the ϕ meson.

Theoretical predictions on the branching fraction are affected by large uncertainties [31].

---

[1] The OZI rule is an empiric rule which states that processes corresponding to disconnected quark diagrams are strongly suppressed.
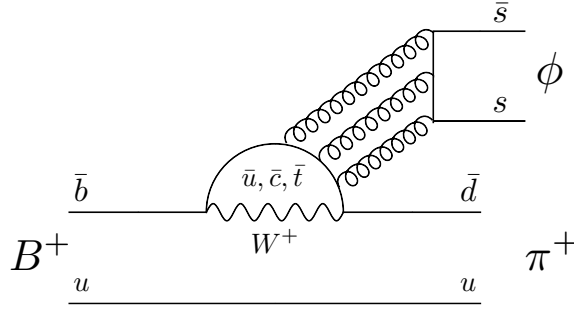
Figure 2.3 *Feynman diagram of the $B^\pm \to \phi\pi^\pm$ decay.*

A first large source of uncertainty is due to the approach adopted for the hadronic matrix element calculation. Moreover, for a given approach, different parameter scenarios and the choice of the factorisation scale introduce further uncertainties on the predicted value. The $B^\pm \to \phi\pi^\pm$ decay receives also non-perturbative corrections from long-distance contributions, such as $B \to K^* K^*$ rescattering. Finally, the largest source of uncertainty is due to $\omega - \phi$ mixing. The physical ω and ϕ meson states do not coincide exactly with the ideal $n\bar{n} = (|u\bar{u}\rangle + |d\bar{d}\rangle)/\sqrt{2}$ and $|s\bar{s}\rangle$ states, respectively.

They appear to be mixtures of these two states characterized by a small mixing angle δ_V. In the convention adopted in Ref. [32] it is possible to write,

$$\begin{pmatrix} \omega \\ \phi \end{pmatrix} = \begin{pmatrix} \cos\delta_V & -\sin\delta_V \\ \sin\delta_V & \cos\delta_V \end{pmatrix} \begin{pmatrix} n\bar{n} \\ s\bar{s} \end{pmatrix}. \tag{2.22}$$

The most recent prediction sets an energy-dependent mixing angle that varies from $\delta_V = 2.75°$ at the ω mass to $\delta_V = 3.84°$ at the ϕ mass [33]. In the QCD factorization approach, the $B^\pm \to \phi\pi^\pm$ branching fraction is predicted to be in the range $(5 - 10) \times 10^{-9}$ [34] if $\omega - \phi$ mixing is neglected, but can be enhanced up to 0.6×10^{-7} [31, 35] depending on the value of δ_V. However, the effect of $\omega - \phi$ mixing has not been observed in a recent search for $B^0 \to J/\psi\phi$ [36]. Values of the $B^\pm \to \phi\pi^\pm$ branching fraction in excess of 10^{-7} would be indicative of non-SM physics. The $B^\pm \to \phi\pi^\pm$ decay has not been observed yet. The best best upper limit prior to the analysis presented in this thesis, obtained by the BaBar collaboration [37], is:

$$\mathcal{B}(B^\pm \to \phi\pi^\pm) < 2.4 \times 10^{-7} \text{ at } 90\% \text{ CL}.$$

2.4.2 $B_s^0 \to \eta'\eta'$ decay mode

B_s^0 decays to ω, η, η' and ϕ resonances constitute an interesting and almost unexplored sector of charmless B decays. They have been studied by several authors in the framework of QCD factorisation [38,39], perturbative QCD [40], Soft Collinear Effective Theory (SCET) [41], and diagrammatic flavour SU(3) [42]. Among all the possible decays the $B_s^0 \to \eta'\eta'$ mode might have a large branching fraction compared to other B_s^0 decays. Indeed, it is related to the $B^+ \to \eta' K^+$ and $B^0 \to \eta' K^0$ decays by U-spin or SU(3) symmetry,

see Fig. 2.4. These B^+ and B^0 decays have the largest branching fractions among the known charmless B decay final states [11]:

$$\begin{aligned}
\mathcal{B}(B^+ \to \eta' K^+) &= (70.6 \pm 2.5) \times 10^{-6}, \\
\mathcal{B}(B^0 \to \eta' K^0) &= (66 \pm 4) \times 10^{-6}.
\end{aligned} \tag{2.23}$$

The predictions for the branching fraction for $B_s^0 \to \eta'\eta'$ range between 14×10^{-6} and 50×10^{-6}, with large uncertainties [38].

The $B_s^0 \to \eta'\eta'$ decay as well as all the $B_s^0 \to PP$ decays offer the possibility to test the Standard Model and search for New Physics also through *CP* violation measurements. A time-dependent analysis of such decays can in fact provide a measure of both mixing-induced *CP* violation and of direct *CP* violation. Because the $B_s^0 \to \eta'\eta'$ decay is penguin dominated and its tree amplitudes are colour suppressed, and since the ϕ_s $B_s^0 - \bar{B}_s^0$ mixing phase is small, both the direct and the mixing-induced *CP* asymmetries are expected to be small. The theories predict [38] a mixing-induced *CP* violation of $0.04^{+0.01+0.01}_{-0.01-0.01}$ (QCDF) and of $0.05^{+0.00}_{-0.01}$ in (pQCD) and a direct *CP* violation of $0.032^{+0.008+0.01}_{-0.006-0.012}$ (QCDF) and of $0.014^{+0.002}_{-0.002}$ in (pQCD). Larger uncertainties are instead present in the SCET predictions.

In this thesis the search and the first observation of the unseen $B_s^0 \to \eta'\eta'$ decay will be described.
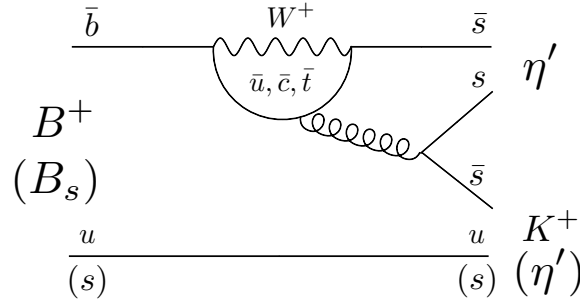
Figure 2.4   *Feynman diagram of the $B^\pm \to \eta' K^\pm$ and $B_s^0 \to \eta'\eta'$ decays.*

2.4.3   *CP* violation in the $B^\pm \to \phi K^\pm$ decay

The weak-interaction $B^\pm \to \phi K^\pm$ decay is governed by the $b \to ss\bar{s}$ transition and can therefore occur only through loop diagrams (see Fig. 2.5) leading to a branching fraction of the order of 10^{-5} [11].

Because the dominant amplitudes have similar weak phases, the *CP*-violating charge asymmetry is predicted to be small in the SM: $(1.6^{+3.1}_{-1.4})\%$ from pQCD predictions [43], and $(1^{+0}_{-1})\%$ from NLO pQCD [34]. A significantly larger value would signal interference with an amplitude not described in the SM. Large *CP* violation effects have been seen in some regions of the $B^\pm \to K^+ K^- K^\pm$ phase space, but not around the ϕ resonance [44].

One of the analyses described in this thesis intends to improve the measurement of the
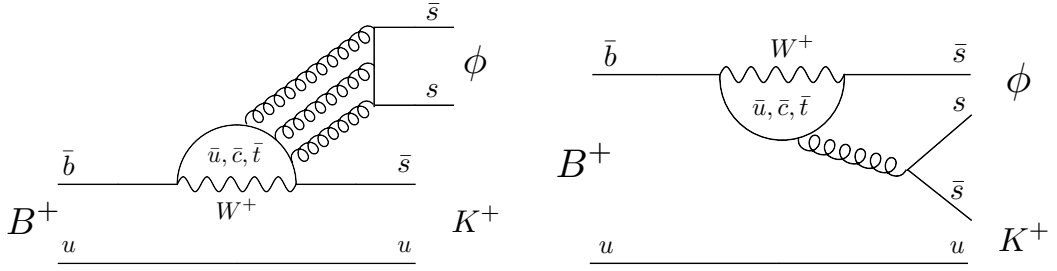
Figure 2.5 *Two main Feynman diagrams for the $B^+ \to \phi K^+$ decay.*

$B^\pm \to \phi K^\pm$ CP asymmetry. The PDG average prior to this study is [11]:

$$\mathcal{A}^{CP}(B^\pm \to \phi K^\pm) = \frac{\mathcal{B}(B^- \to \phi K^-) - \mathcal{B}(B^+ \to \phi K^+)}{\mathcal{B}(B^- \to \phi K^-) + \mathcal{B}(B^+ \to \phi K^+)} = 0.10 \pm 0.04.$$

2.4.4 *CP* violation in the $B^\pm \to \eta' K^\pm$ decay

The $B^\pm \to \eta' K^\pm$ decay is the charmless two-body charged B decay with the largest known branching fraction [11],

$$\mathcal{B}(B^\pm \to \eta' K^\pm) = (7.06 \pm 0.25) \times 10^{-5}. \tag{2.24}$$

This is partially explained by the $\eta - \eta'$ mixing. The η and the η' physical states are in fact a mixture of the $\eta_q = (u\bar{u} + d\bar{d})/\sqrt{2}$ and $\eta_s = s\bar{s}$ states according to the formula:

$$\eta = \eta_q \cos\phi - \eta_s \sin\phi, \quad \eta' = \eta_q \sin\phi + \eta_s \cos\phi, \tag{2.25}$$

where the mixing angle ϕ is measured to be $39.9° \pm 2.9°$ [45]. The interference of the B decay into the η_q and the η_s mesons is constructive for the $B^\pm \to \eta' K^\pm$ decay, which is therefore enhanced, while it is destructive for the $B^\pm \to \eta K^\pm$ decay, which is instead suppressed. The high $\mathcal{B}(B^\pm \to \eta' K^\pm)$ is however not completely explained by the $\eta - \eta'$ mixing and several other explanations are proposed [46].

The amplitude of the $B^\pm \to \eta' K^\pm$ decay can be expressed in terms of diagrams as:

$$A(B^\pm \to \eta' K^\pm) = \frac{1}{\sqrt{3}} \times (t + c + 2p + 4s), \tag{2.26}$$

where $t = T - P_{EW}^C$, $c = C + P_{EW}$, $p = P - P_{EW}^C/3 - P_A$, $s = S - P_{EW}/3$ and S is a flavour-singlet amplitude introduced to explain the large $B^\pm \to \eta' K^\pm$ rate. Because the $B^\pm \to \eta' K^\pm$ decay is dominated by penguin amplitudes, the direct CP asymmetry is expected to be small [47,48]. The current experimental CP asymmetry is [11]:

$$\mathcal{A}^{CP}(B^\pm \to \eta' K^\pm) = 0.013 \pm 0.017. \tag{2.27}$$

In this thesis the $B^\pm \to \eta' K^\pm$ decay mode is used as reference channel for the search of

the $B_s^0 \to \eta'\eta'$ decay. In addition, a measurement of the $B^\pm \to \eta' K^\pm$ CP asymmetry is performed.

3

The Large Hadron Collider at CERN

The Large Hadron Collider (LHC) [12] is the largest and most powerful particle accelerator in the world. It is a proton-proton circular collider installed in the 26.7 km tunnel previously used for the CERN LEP machine, between 45 and 170 m underneath the surface of the Geneva region. The aim of LHC is to test the Standard Model and look for new physics, through either direct or indirect searches. To achieve these goals it has been designed to reach centre-of-mass collision energies of up to 14 TeV. The first collisions were delivered on November 23rd 2009 with a beam energy of 450 GeV. After the winter shutdown, in March 2010, the first collisions at 7 TeV in the centre-of-mass were recorded. In 2012, after two years of data taking, a new record was achieved, with the first collisions at $\sqrt{s}$=8 TeV.

3.1   Accelerator chain

In order to accelerate the protons up to very high energies a chain composed of a series of particles accelerators is used (Fig. 3.1). The proton bunches, produced at 100 keV from ionised hydrogen atoms, are firstly injected into the linear accelerator Linac 2. Here they are accelerated up to 50 MeV and boosted in two synchrotrons: the first, called Booster, accelerates the beam up to 1 GeV, then the particles enter the Proton Synchrotron (PS) where they reach an energy of 26 GeV. Afterwards the beam is injected into the Super Proton Synchrotron (SPS), where it is accelerated up to 450 GeV. This beam, is split in two beams which are injected in LHC via the TI2 and TI8 tunnels. In LHC, the two beams are accelerated by superconducting radio frequency cavities (RF) and driven by superconducting dipole magnets. The magnets, cooled down to 1.9 K (–271.3 °C) using super-fluid Helium, produce a magnetic field of up to 8.34 T, corresponding to a maximum energy of 7 TeV per beam. The beams present a *bunch* structure, determined by the use of the radio frequency cavities. In the nominal running conditions, LHC is designed to contain 2808 bunches of 10^{11} protons each, with a bunch spacing of 25 ns and a bunch crossing rate of 40 MHz at the four interaction points.

CERN's accelerator complex
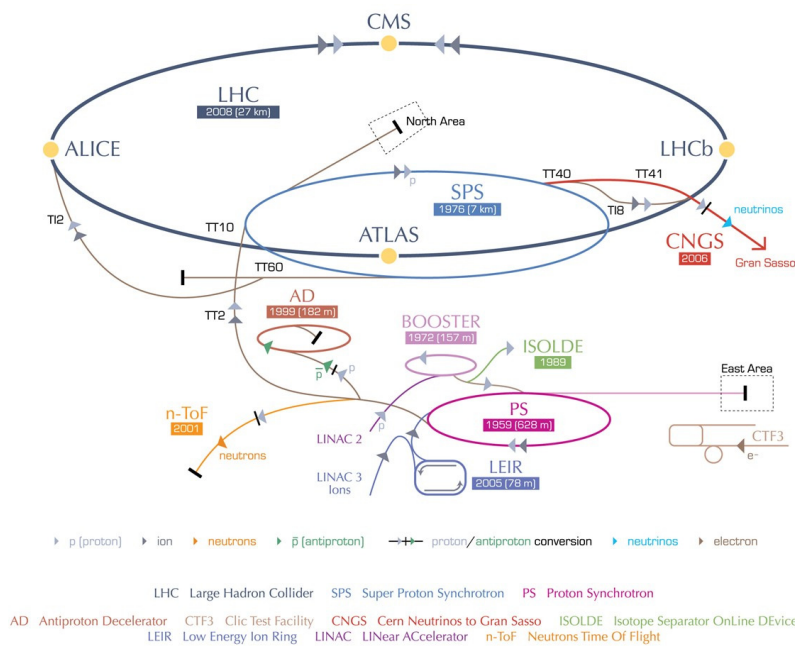
Figure 3.1   *CERN accelerator complex. The four interaction points along the LHC are indicated.*

The relevant LHC machine parameters are listed in Table 3.1. A similar acceleration

Table 3.1   *Relevant LHC machine parameters. The design values are compared to the ones reached at the end of the 2013 operations.*

Parameter	Design value	Best value achieved
Beam energy	7 TeV	4 TeV
Number of protons per bunch	1.15×10^{11}	1.5×10^{11}
Number of bunches	2808	1368
Crossing angle	300 μm	290 μm
Beam size	17 μm	20 μm
Normalized emittance	3.75 μm	2.4 μm
Peak luminosity	10^{34} cm^{-2}s^{-1}	7.5×10^{33} cm^{-2}s^{-1}

chain, starting from the Linac 3 accelerator, provides heavy-ion (Pb) beams during some LHC dedicated runs.

3.2   LHC experiments

Seven detectors have been placed along the LHC ring, located at the four interaction points. Six of them are described below, while the LHCb experiment is detailed in

Chapter 4.

ALICE (A Large Ion Collider Experiment) [49] is a detector dedicated to the physics of strongly interacting matter and quark-gluon plasma at extreme values of temperature and energy density in heavy-ion collisions. The 26 m-long, 16 m-high, and 16 m-wide detector, located at Point 2 in Saint-Genis-Pouilly, has been designed to cope with the very large multiplicity of particles produced in heavy nuclei (Pb-Pb) collisions.

ATLAS (A Toroidal LHC ApparatuS) [1] is one of the two general-purpose detectors at LHC. It is built to investigate a wide range of physics, including the search of the Higgs boson, extra dimensions and particles that could make up dark matter. It is located at Point 1 and is the biggest LHC detector, with 25 m of diameter, 44 m of length and approximately 7000 tons of weight (Fig. 3.2). The detector design is driven by the choice of the magnetic system: a central superconducting solenoid providing a field of 2 T and a toroid magnet system arranged with an eight-fold azimuthal symmetry.

CMS (Compact Muon Solenoid) [2] is the second general-purpose detector at LHC. Although it shares the same physics goals with the ATLAS experiment, the different magnet system and detector design make the two experiments complementary. CMS is placed at Point 5 and it is built around a huge superconducting solenoid which generates a 4 T magnetic field. The 21 m length and 15 m diameter make CMS the second biggest detector at LHC (Fig. 3.2), while it is the heaviest with its 12500 tons.

LHCf (Large Hadron Collider forward experiment) [50] is composed of two small detectors at 140 m on either side of the ATLAS collision point along the LHC beam line. Its goal is to study the same interactions as those of cosmic rays with nuclei in the upper atmosphere by detecting neutral particles produced in the very forward region of LHC. The physics goal is to verify hadronic models used in the study of Extremely High-Energy Cosmic-Rays.

TOTEM (Total elastic and diffractive cross-section measurement) [51] is a detector placed in the very forward region around CMS. It aims at precise measurements of the proton-proton interaction cross-section, as well as the study of the proton structure by looking at elastic scattering with a large range of momentum transfers.

MoEDAL (Monopole and Exotics Detector At the LHC) [52]. It is situated in the LHCb cavern. MoEDAL's primary goal is to search for magnetic monopoles. It also looks for highly ionising Stable Massive Particles, which are predicted by theories beyond the Standard Model.
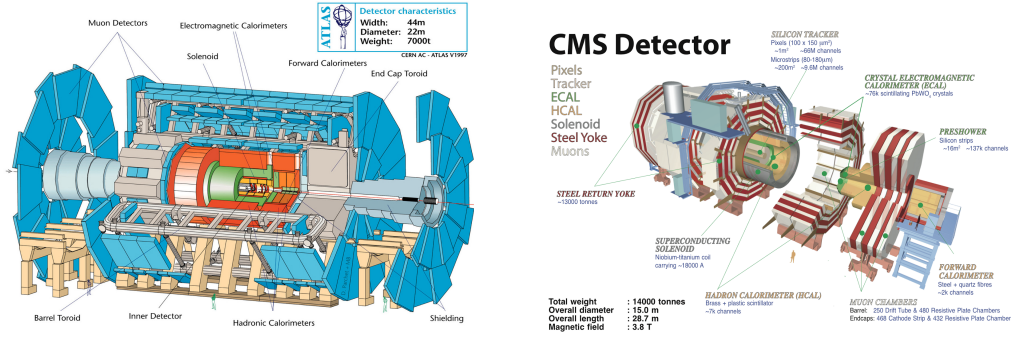
Figure 3.2 *Drawning of the ATLAS (left) and CMS (right) apparatus.*

3.3   Luminosity

The high luminosity designed for LHC is motivated by the physics program of the ATLAS and CMS experiments and depends on the cross-section for Higgs production, predicted to be of a few femtobarns. The number of events of a given type generated each second is indeed related to the instantaneous machine luminosity, $\mathcal{L}$, and to the cross-section of the process of interest, σ_{event}, by:

$$N_{\text{event}} = \mathcal{L}\sigma_{\text{event}}. \tag{3.1}$$

The machine luminosity, assuming a Gaussian beam distribution, can be written as:

$$\mathcal{L} = \frac{N_b^2 n_b f_{\text{rev}} \gamma_r}{4\pi\epsilon_n \beta^*} F, \tag{3.2}$$

where N_b is the number of particles per bunch, n_b the number of colliding bunches, f_{rev} the revolution frequency, γ_r the relativistic gamma factor, ϵ_n the normalized emittance, β^* the beta function at the collision point, describing the beam focalisation at the interaction points. F is the crossing angle factor, which depends on the crossing angle of the beams at the interaction point (IP), and can be expressed as:

$$F = \left[1 + \left(\frac{\theta_c \sigma_z}{2\sigma^*}\right)^2\right]^{-\frac{1}{2}}, \tag{3.3}$$

where θ_c is the full crossing angle at the IP, σ_z the RMS bunch length, and σ^* the transverse RMS bunch size at the IP.

From the formula above, it is then possible to see that the high luminosity needed by the ATLAS and CMS experiments can be achieved through higher beam intensities or higher beam collimations. The other LHC experiments aim at a lower luminosity: the luminosity foreseen for LHCb is $\mathcal{L} = 2 \times 10^{32}\,\text{cm}^{-2}\text{s}^{-1}$ [53], and TOTEM aims at a peak luminosity of $\mathcal{L} = 2 \times 10^{29}\,\text{cm}^{-2}\text{s}^{-1}$ with 156 colliding bunches.

<div style="text-align: right;">*4*</div>

The LHCb experiment

LHCb (Large Hadron Collider beauty experiment) [53] is one of the four main experiments hosted around the LHC ring. It is located at Interaction Point 8, in Ferney-Voltaire (France), where the DELPHI experiment was previously installed. The main goal of LHCb is to look for new physics through precise measurements of *CP* violating processes and measurements of rare decays of beauty and charm hadrons which are extensively produced at LHC because of the high luminosity and the high $b\bar{b}$ production cross-section. To reach its designated physics goals, the detector has to meet the following requirements:

- A high-performance trigger with an efficient event selection, able to select many different final states.

- An excellent vertex reconstruction. This is critical in the study of the oscillating $\bar{B}_s^0 - B_s^0$ system for which a good decay time resolution is required. In addition it helps in reducing the combinatorial background.

- An excellent identification of many different particles, such as kaons, pions, electrons, muons and photons in order to reconstruct cleanly the different final states and avoid mis-identifications which would introduce significant uncertainties in the measurement of *CP* asymmetries due to large background contamination.

In addition to the conditions listed above, a single *pp* interaction per bunch crossing would be desirable for a cleaner and easier reconstruction of the event. Because the probability for multiple interactions depends on the luminosity (Fig. 4.1), LHCb uses a lower luminosity than the ATLAS and CMS experiments. This has some further advantages: a lower occupancy in the detector, and a reduced radiation damage. The designed luminosity for LHCb is $2 \times 10^{32}\,\mathrm{cm}^{-2}\mathrm{s}^{-1}$ [54], corresponding to an average of $\mu = 0.4$ interaction per bunch crossing. Since the other nominal running conditions have not been reached, the LHCb luminosity has been increased to $\mathcal{L} = 3.7 \times 10^{32}\,\mathrm{cm}^{-2}\mathrm{s}^{-1}$ in 2011 and $\mathcal{L} = 4.0 \times 10^{32}\,\mathrm{cm}^{-2}\mathrm{s}^{-1}$ in 2012, corresponding to $\mu \sim 1.5$ and $\mu \sim 1.7$,
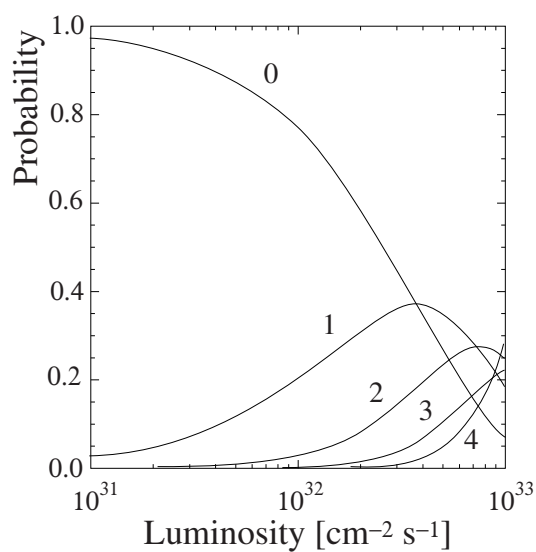
Figure 4.1   *Probability of having 0, 1, 2, 3 or 4* pp *interactions as a function of instantaneous luminosity.*

respectively. Under these conditions LHCb collected 1.1 fb^{-1} in 2011 at $\sqrt{s}$ = 7 TeV and 2.1 fb^{-1} in 2012 at $\sqrt{s}$ = 8 TeV, as shown in Fig. 4.2.
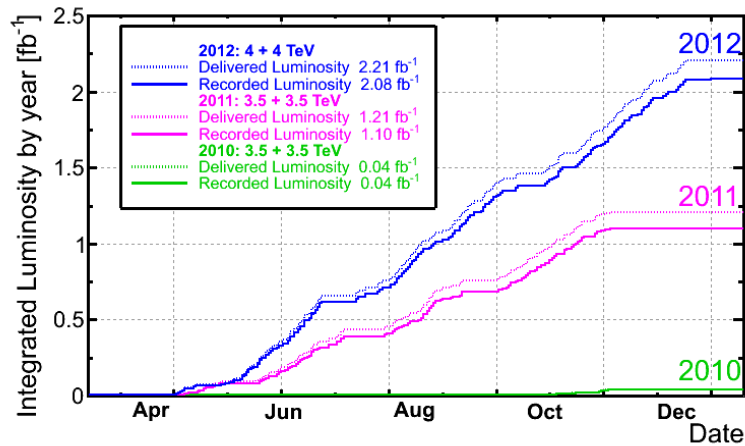
Figure 4.2 *Integrated luminosity delivered to and collected by the LHCb experiment.*

4.1 Detector layout

The design of the LHCb detector is strongly driven by the angular distribution of the produced $b\bar{b}$ pairs and is constrained by the available space in the cavern. In *pp* collisions the $b\bar{b}$ pairs are produced through the strong interaction. Two partons of the involved protons interact, exchanging a large fraction of momentum. The $b\bar{b}$ pair produced is boosted along the direction of the higher momentum parton, at very small angle with respect to the direction of the beam either in the forward or backward region (Fig. 4.3).

The LHCb detector, shown in Fig. 4.4, is therefore designed as a single-arm forward spectrometer, covering the forward region with an acceptance of $10 < \theta < 300$ mrad in the horizontal plane and $10 < \theta < 250$ mrad in the vertical plane, where θ is the polar angle with respect to the beam line. In order to exploit best the dimension of the cavern the interaction point has been displaced by 11.25 m from the centre. The spectrometer is 6 m wide, 5 m high and 20 m long and consists of:

- the magnet [55], described in Chapter 5;

- the tracking system, described in Sec. 4.2, composed of the VErtex LOcator (VELO) [56] and four tracking stations: the Tracking Turicensis (TT) [57] placed upstream of the magnet and three tracking stations (T1, T2 and T3) [58,59] downstream of the magnet;

- the particle identification system, described in Sec. 4.3, made of two Ring Imaging Cherenkov detectors (RICH1 and RICH2) [60], a calorimetric system (SPD, PS, ECAL and HCAL) [61] and five muon stations (M1–M5) [62] .
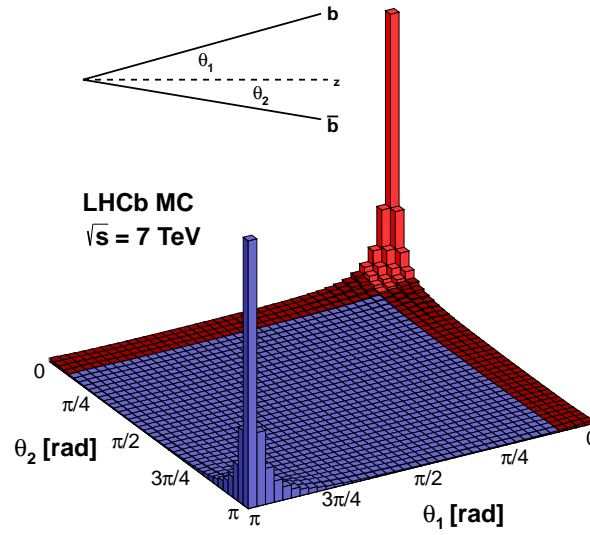
Figure 4.3   *Angular distribution of the $b\bar{b}$ pairs produced in* pp *collisions at $\sqrt{s} = 7$ TeV . The angles θ_1 and θ_2 of the b and $\bar{b}$ are defined with respect to one of the proton beam directions. The red part of the distribution shows the angular coverage of the LHCb detector.*
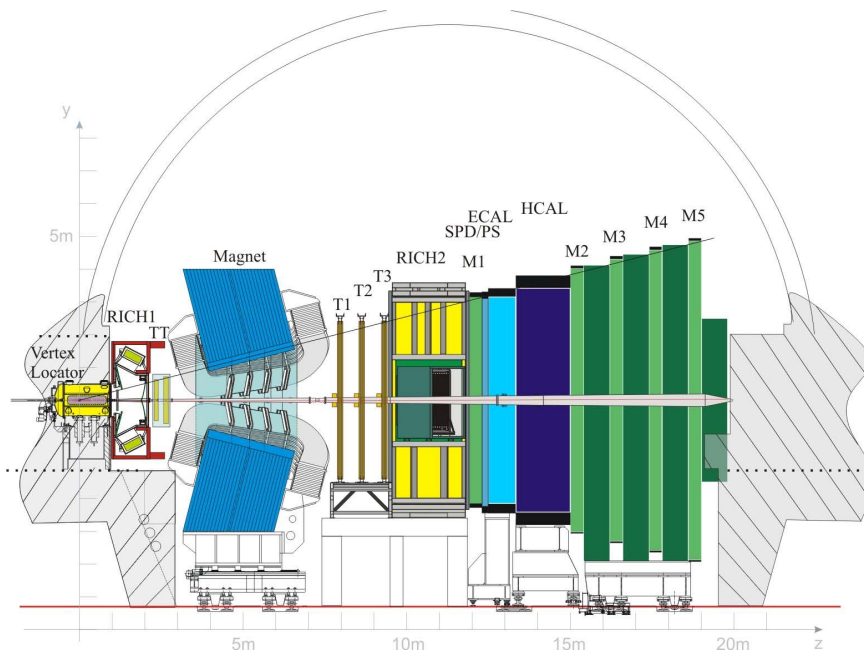
Figure 4.4   *Side view of the LHCb detector.*

4.2 Tracking system

In the LHCb experiment the ability to precisely reconstruct vertices and tracks is a fundamental requirement. In presence of a magnetic field, B, the tracking system provides a measurement of the radius of curvature, r, of a charged particle, and therefore of its momentum. In case of an homogeneous field we have:

$$p = 0.3 \left[\frac{\text{GeV}/c}{\text{T} \cdot \text{m}} \right] \cdot B \cdot r \tag{4.1}$$

An accurate measurement of the momentum is one of the key elements in *CP* violation measurements and rare decays searches, for which a precise knowledge of the particle lifetime and mass resolution is required. The lifetime is related to the momentum by the formula:

$$\tau = \frac{d_f m}{cp} , \tag{4.2}$$

where m is the mass of the particle. The distance of flight of the particle, d_f, which is the distance between the primary vertex where the B meson is produced and the secondary vertex where it decays, is also determined with the tracking system. The LHCb tracking system provides an extremely good momentum resolution, $\delta p / p \approx 0.4\%$, for momenta up to $200\,\text{GeV}/c$.

4.2.1 VErtex LOcator

The VELO detector, depicted in Fig. 4.5, is designed to reconstruct the tracks close to the interaction point going in the forward and backward directions, in order to identify and separate primary and secondary vertexes of *b*-hadron and *c*-hadron decays. It detects particles in the pseudorapidity ($\eta = -\ln(\tan(\theta/2))$) range $1.6 < \eta < 4.9$, coming from vertices in the range $|z| < 10.6$ cm, where z is defined along the beam axis pointing from the IP to the muon stations.

It consists of 21 silicon modules spread along the beam line direction, plus two upstream modules, called the pile-up veto detector, designed to contribute to the Level 0 trigger (Sec. 4.4). The modules are placed in a vessel that maintains the vacuum. Since the distance of the sensors from the beam pipe is smaller than the minimum required during the injection, each module is divided in two halves retractable by 3 cm. The first sensitive part of the detector is at 8.2 mm from the beam line, when in data taking position.

Two different types of sensors are placed back-to-back forming a module and providing a measurement of the r and ϕ coordinates, respectively. The choice of the cylindrical coordinates permits a fast 2D (rz) reconstruction of the tracks and the vertices used to trigger the event.

The geometry of the VELO sensors is shown in Fig. 4.6 . The r sensors measure the radial coordinate r by 512 circular strips centred on the beam axis. To reduce the occupancy each half disk is divided in four regions of $45°$. The strip pitch increases linearly with
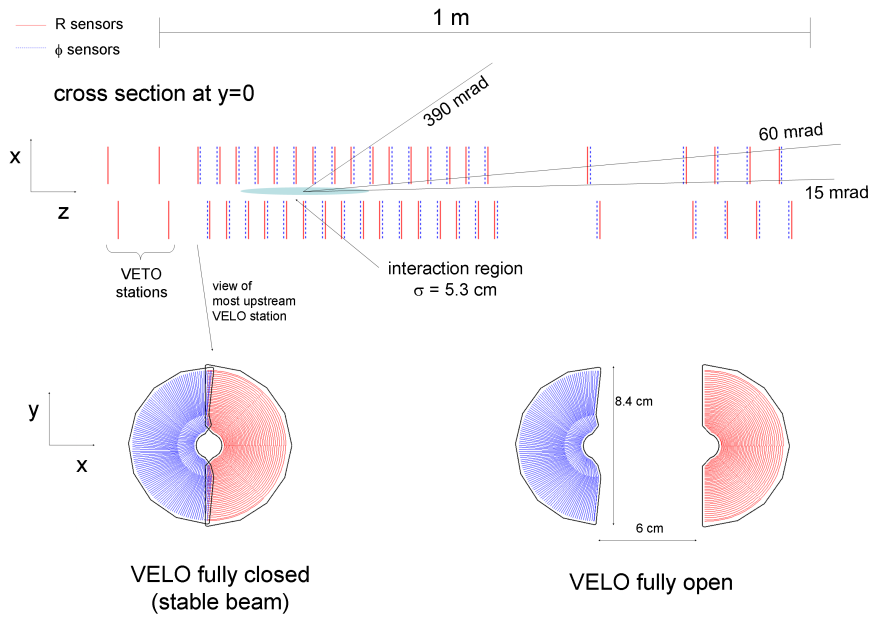
Figure 4.5 *Overview of the VELO detector: projection of the sensors on the x − z plane (top) and illustration of a sensor in the closed and open configuration (bottom).*

the radius from ∼ 32 μm to ∼ 101.6 μm. Depending on the radius and on the angle of the track, the hit resolution varies between 4 and 25 μm.

The φ sensor has instead radial strips and is divided in an inner and an outer region. The inner region is made of 683 strips skewed of 20° with respect to the radius, while the outer region contains 1365 strips with a skew of 10°. The pitch of the strips varies from 35.5 μm to 78.3 μm in the inner region and from 39.3 μm to 97 μm in the outer region. The modules are placed so that two consecutive φ modules have opposite skew.

4.2.2 Silicon Tracker

The Silicon Tracker (ST) consists of four stations: the Tracker Turicensis (TT), upstream of the magnet, and the Inner Tracker (IT), the central region of the three stations (T1–T3) located downstream of the magnet. Each station uses silicon microstrip sensors, and is composed of four layers: the first and the last have vertical strips measuring the x coordinate, while the two central layers, the u and v layers, have strips tilted by a stereo angle of −5° and +5°. The spatial resolution measured with 2011 data is ∼ 50 μm.

Tracker Turicensis

The TT sub-detector is placed between the RICH1 and the magnet, at $z \sim 2.5$ m. Its four layers are 150 cm wide and 130 cm high and cover the full LHCb acceptance. The
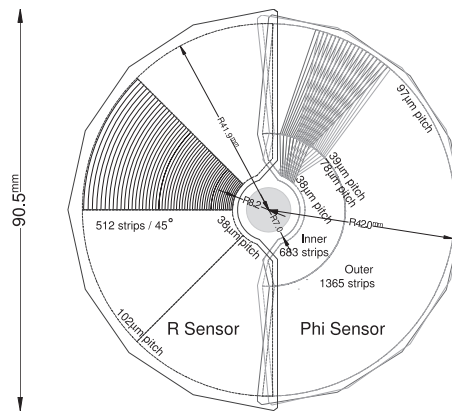
Figure 4.6 *Scheme of the rϕ geometry of a VELO sensor.*

first two layers (x, u) are placed at a distance of about 27 cm from the second two (v, z), in order to favour the tracking reconstruction algorithm. Each layer is composed of half-modules consisting of rows of seven (or eight in the two downstream layers) silicon sensors. Depending on the proximity to the beam pipe the sensors are organised in two or three readout sectors. Each sensor is 9.64 cm wide, 9.44 cm long and 500 μm thick and carries 512 readout strips. The layout of the TT sub-detector is illustrated in Fig. 4.7.

Inner Tracker

The IT covers the central region of the three stations downstream of the magnet, where the track density is higher. Each station is 120 cm wide and 40 cm high, with an active area of 4.0 m^2 and is composed of four independent detector boxes placed around the beam pipe, as illustrated in Fig. 4.8. The four boxes share a similar structure: each of them contains four layers made of seven detector modules. The modules of the boxes above and below the beam pipe consist in a single 320 μm thick sensor and a readout hybrid, while the modules of the left and the right boxes are made of two 410 μm thick sensors plus the readout hybrid. Each sensor is 7.6 cm wide and 11 cm long with 384 readout strips.

4.2.3 Outer Tracker

The OT, illustrated in Fig. 4.9, is located on the T1–T3 stations around the IT. It is the only non-silicon tracking detector and is used to reconstruct tracks in the region of the LHCb acceptance not covered by the IT. It uses straw tubes, with a diameter of 4.9 mm. They are filled with a mixture of Argon (70%) and CO_2 (30%) in order to satisfy the following requirements:

- the drift time has to be < 50 ns;

- the drift-coordinate resolution has to be ~ 200 μm.
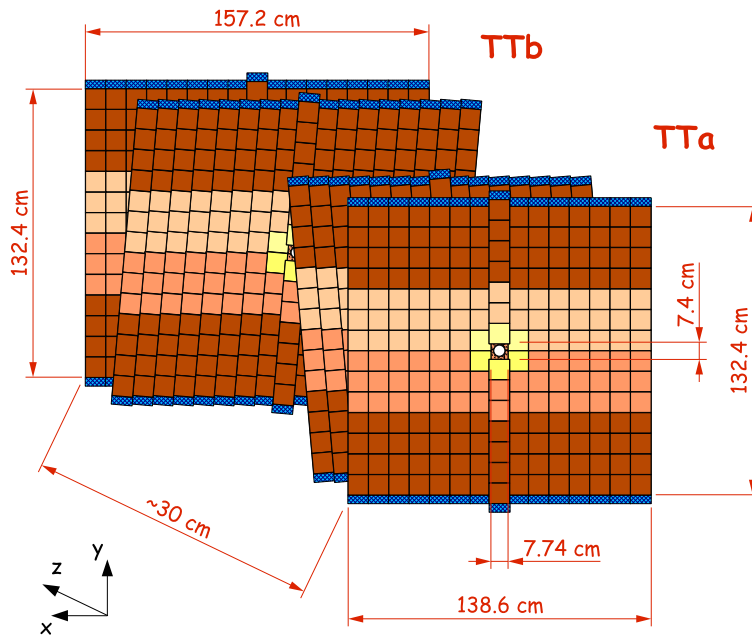
Figure 4.7   *Illustration of the four TT detector layers.*
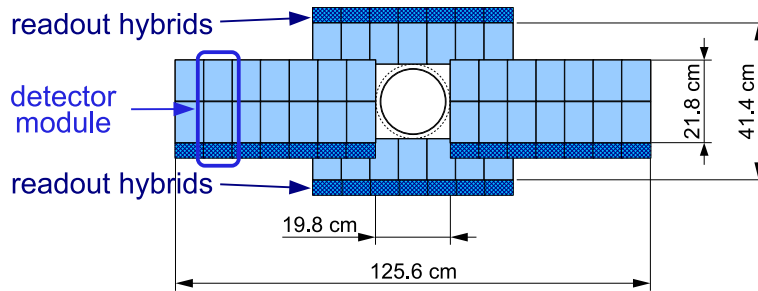
Figure 4.8   *Layout of one x-layer of the Inner Tracker sub-detector.*

The geometry adopted is similar to that of the IT, each station is composed of four layers in the x–u–v–x configuration. The OT covers an active area of 5971×4850 mm^2 where the inner boundaries are chosen in order to avoid an occupancy in excess of 10% at a luminosity of 2×10^{32}cm^{-2}s^{-1}.

4.2.4   Track reconstruction

Track reconstruction is performed with the dedicated software BRUNEL. Hits from the four tracking detectors, VELO, TT, IT and OT, are processed and tracks are reconstructed and grouped in five categories:

- **Long tracks**. They combine information from the VELO, T and TT stations, and have therefore the best momentum resolution. For this reason they are the most
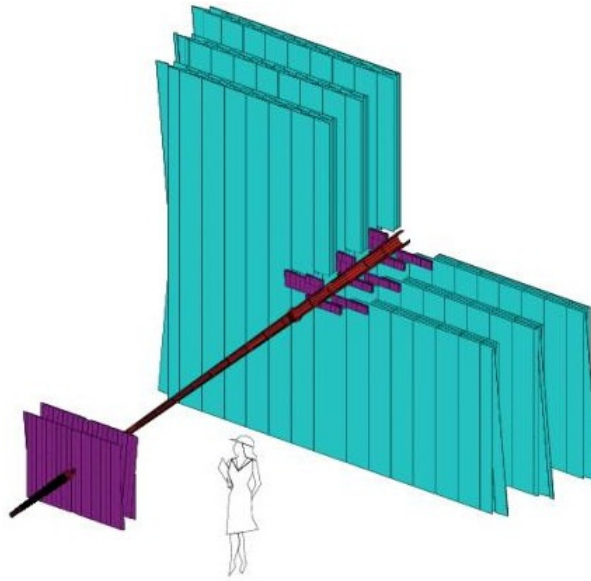
Figure 4.9 *Drawing of the tracking system, showing the OT stations (light-blue) and the TT and IT stations (purple).*

useful in physics analyses.

- **Upstream tracks**. They contain information only from the VELO and the TT. Usually they have very low momentum and are therefore bent out of the acceptance by the magnet.

- **Downstream tracks**. They have hits only in the TT and the T stations, and are usually produced from the decay of long-lived particles (such as K_s^0 or Λ) outside the VELO acceptance.

- **VELO tracks**. They traverse only the VELO, either in the forward or in the backward direction. They are extremely useful for the reconstruction of the primary interaction vertexes.

- **T tracks**. They traverse only the T stations, and are usually the product of secondary interactions.

The reconstruction of long tracks is made with two different algorithms. The first matches VELO tracks with hits in the T stations and finally looks for hits in the TT station. The second algorithm matches VELO tracks with T tracks. If a good candidate is found hits in the TT are added. Finally tracks are fitted with a Kalman fitter [63], that takes multiple scattering into account and corrects for energy losses. The efficiency for track reconstruction has been estimated to be above 96% for 2011 data, and slightly lower for 2012 because of the higher track multiplicity. The achieved momentum resolution goes from about 0.5% for particles with $p < 20\,\mathrm{GeV}/c$ to about 0.8% for particles with $p \sim 8\,\mathrm{GeV}/c$. This translates in a mass resolution $\sigma_m/m \sim 5\%$ up to the Υ mass.

4.3   Particle identification systems

The LHCb physics program requires a strong particle identification in the entire LHCb acceptance and in a wide momentum range, in order to cleanly reconstruct a deep variety of b-hadron decays. The detectors dedicated to particle identification can be divided in three groups:

- two Cherenkov detectors, RICH1 and RICH2, designed to optimise the π/K separation;

- the calorimeter system, composed of a Scintillator Pad Detector (SPD), a PreShower (PS), an electromagnetic calorimeter (ECAL) and an hadronic calorimeter (HCAL), to distinguish photons, electrons and hadrons;

- five muon chambers, dedicate to the muon identification.

4.3.1   RICH detectors

The spectrometer has two different RICH detectors, dedicated to identify kaons, pions and photons in different momentum ranges. The RICH1 is placed upstream of the magnet and it covers the entire LHCb acceptance. Its purpose is to identify charged particles in the low momentum range 1–60 GeV/c. In order to satisfy this requirement it uses aerogel ($n = 1.03$) and C_4F_{10} ($n = 1.0014$). The RICH2 is instead located after the tracking stations and is dedicated to identify particles with higher momentum, in the range 15–100 GeV/c. Since high momentum particles are produced at small angles with respect to the beam line, RICH2 covers a limited angular region, from $\sim$ 15 mrad to $\pm$120 mrad horizontally and from $\sim$ 15 mrad to $\pm$100 mrad vertically. It uses CF_4 as gas radiator ($n = 1.0005$). The separation power of the different radiators as a function of the particle momentum is depicted in Fig. 4.10.

In both RICH detectors, the Cherenkov light is deflected by spherical and flat mirrors and is detected by Hybrid Photon Detectors (HPDs) placed outside the spectrometer acceptance and shielded from the magnetic field with iron screens. The layout of the two RICH detectors is illustrated in Fig. 4.11.

4.3.2   Calorimeter system

The structure of the calorimeter system is strongly constrained by the wide spectrum of functionalities it has to fulfill:

- It has to distinguish among photons, hadrons and electrons, measuring their energies and positions.

- It contributes to the first trigger level (L0), selecting high-energy photons, hadrons and electrons. In particular, the electron trigger has to reject 99% of the inelastic
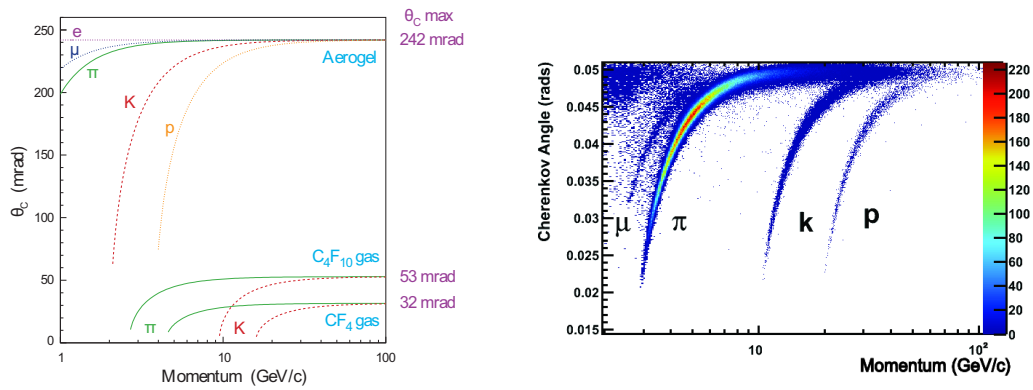
Figure 4.10 *Cherenkov angle of different radiators (left) and of* C_4F_{10} *(right) as a function of the particle momentum.*

pp collisions and provide an enrichment factor in *b*-decays larger than 15. This requirement imposes the strongest constraints on the overall structure. In order to satisfy this condition, the standard structure composed of an electromagnetic calorimeter (ECAL) and an hadronic calorimeter (HCAL) follows a scintillator pad detector (SPD) and a preshower detector (PS). The SPD has to select charged particles, rejecting the high-E_T π^0 background, while the PS removes the charged pion background.

- An optimal resolution and shower separation is required, in order to have a good efficiency for *b*-hadron decays and a good background subtraction. To fulfil this requirement the thickness of the ECAL is chosen to be 25 radiation lengths (X_0).

All the four calorimeters share the same technology: the scintillation light generated in the particle-detector interaction is collected by Wave-Length Shifting fibres (WLS) and is transmitted to PhotoMultipliers (PMTs). The lateral segmentation, shown in Fig. 4.12, varies depending on the hit density in acceptance regions and on the dimension of the particle shower (larger in the hadronic calorimeter).

The scintillating pad and the preshower detector

They consist of two high-granularity scintillating planes separated by a lead plane with a thickness of 25 X_0. The total active area of 7.6×6.2 m^2 is divided in cells of different dimensions. The cells are grouped in detector units of $\sim 48 \times 48$ cm^2, which are, in turn, organised into ~ 96 cm wide and ~ 7.7 m high supermodules.

The electromagnetic calorimeter

The ECAL is placed between the PS and the hadronic calorimeter at 12.5 m from the interaction point. It is composed of modules of 66 2 mm-thick lead slices alternated with 4 mm-thick scintillator layers. As for the SPD and the PS, cells of various dimensions are
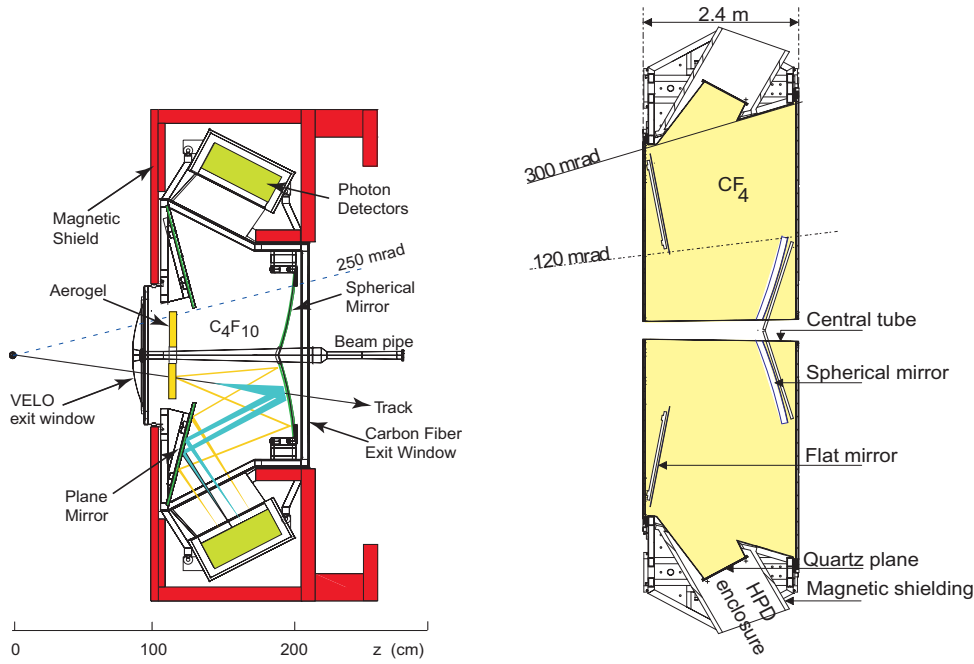
Figure 4.11   *Layout of the RICH1 (left) and RHICH2 (right) detectors.*
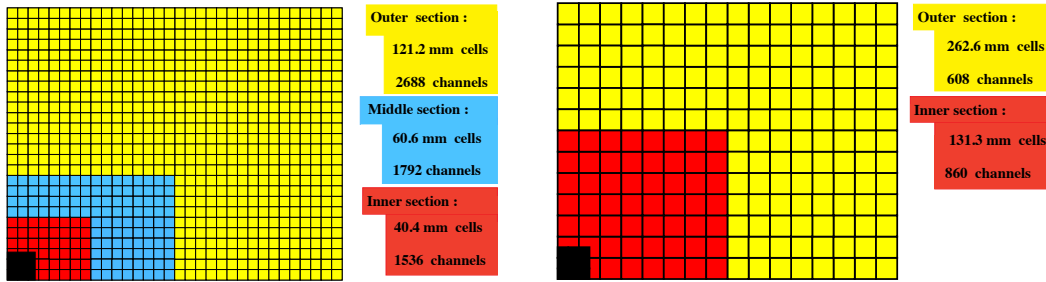
Figure 4.12   *Transverse segmentation of the SPD/PS and ECAL (left) and of the HCAL (right). Only one quarter of the system is shown. The black square on the bottom left corner is the beam pipe region.*

adopted at different distances from the beam pipe. The measured energy resolution is

$$\frac{\sigma_E}{E} = \frac{(9.0 \pm 0.5)\%}{\sqrt{E}} \oplus 0.8\%. \tag{4.3}$$

The hadronic calorimeter

In the hadronic calorimeter 6 mm-thick iron plates interlace with 4 mm-thick scintillating layers for a total thickness of 5.6 interaction lenghts. The limited dimension is constrained by the available space in the cavern. A special feature of the HCAL is that the scintillating tiles are parallel to the beam axis, as illustrated in Fig. 4.13. The detector is divided transversely into squared cells with a side of 131.3 mm in the inner section
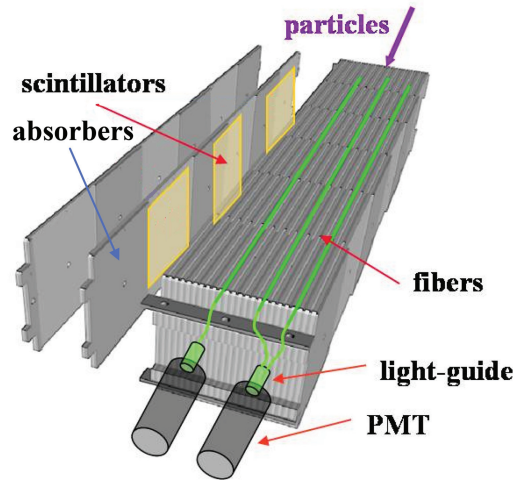
Figure 4.13   *Illustration of a piece of the hadronic calorimeter. The scintillating tiles run parallel to the beam axis.*

and of 262.6 mm in the outer section. The measured resolution of HCAL is

$$\frac{\sigma_E}{E} = \frac{(69 \pm 5)\%}{\sqrt{E}} \oplus (9 \pm 2)\%. \tag{4.4}$$

4.3.3   Muon chambers

The muon system is composed of five stations (M1–M5) and has two main functions:

- it has to provide information to the Level 0 trigger, selecting high-p_T muons;

- it is used in the high-level trigger and in the offline analysis for the muon reconstruction and identification.

Given the large number of rare and *CP*-sensitive *B* decays with muons in the final state, the muon system plays a fundamental role in pursuing the objectives of the LHCb physics program.

The full system is composed of 1380 chambers and covers an area of 435 m^2. One of the five stations, M1, is placed upstream of the calorimeter in order to improve the precision in the muon transverse momentum (p_T) measurement, while the other four stations are located downstream of the calorimeter. In order to select only the muons among the particles that outlasted the calorimeter, three layers of 80 cm-thick iron absorbers are interleaved between the stations M2 to M5. This imposes a minimum momentum of 6 GeV/c for the muons to be detected.

Two different technologies are involved: triple-GEM detectors are used in the inner region of the station M1, where a higher particle rate is expected, while multi-wire proportional chambers (MWPC) are used in the rest of the muon system.
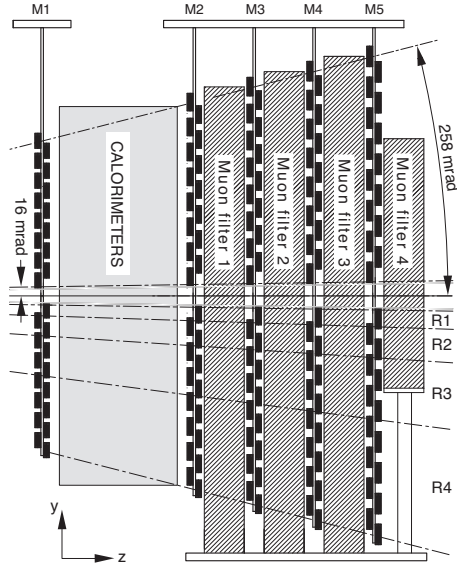
Figure 4.14   *Side view of the five muon chambers.*

A scheme of the muon system is shown in Fig. 4.14. Each station is divided in four regions, defined in a way that the flux of particles and the occupancy is approximately the same in each region of a given station. Each chamber is then divided in rectangular pads, with different dimensions, in order to have a better resolution close to the beam pipe and in the first three chambers (M1–M3). A p_T resolution of 20% is achieved in the first three chambers (M1–M3), dedicated to define the muon tracks and to measure their momentum, while a worse resolution is acceptable for the M4 and M5 stations, which aim at identifying penetrating particles.

4.3.4   Particle identification performance

Information obtained from the RICH detectors, the calorimeter system and the muon detectors are combined together in a set of variables dedicated to the identification of charged particles, while photons and neutral pions are identified with the electromagnetic calorimeter.

To identify the charged particles, the log-likelihood of each track is computed under both the mass-of-interest hypothesis and the pion mass hypothesis. The difference between the two is used as an estimator:

$$\text{DLL}_{X\pi} = \Delta \ln \mathcal{L}(X - \pi) = \ln \mathcal{L}_X - \ln \mathcal{L}_\pi , \tag{4.5}$$

where X can be the proton, kaon, electron or muon mass hypothesis.

A second method, known as ProbNN, has been recently developed to identify charged particles. It consists in using a multivariate method that takes as input information from all the sub-detectors and gives as output a probability value for each mass hypothesis.

RICH system particle identification   The algorithm for hadron identification with the RICH system matches the pattern observed in the RICH photodetectors to that expected for tracks reconstructed under different mass hypotheses. As output, the best hypothesis for each track in the event is given. The particle identification provided by the RICH is excellent in the full momentum range. For kaons with momenta between 2 and 100 GeV/c the average identification efficiency is $\varepsilon(K \to K) \sim 95\%$, with a pion misidentification efficiency of $\varepsilon(\pi \to K) \sim 5\%$.

Muon identification   In order to be identified as muons, particles with $p > 3\,\text{GeV}/c$ have to provide between 2 to 4 hits (depending on the momentum) in the muon stations. The hits are required within a certain field of interest, which depends on the extrapolated point of the track in the muon stations. The muon identification efficiency has been measured to be $\varepsilon(\mu \to \mu) \sim 94\%$ with a misidentification efficiency of $\varepsilon(\pi \to \mu) \sim 3\%$, using a sample of $B^0 \to J/\psi\,K^0_S$ events.

Electron identification   The electron identification is based on a combined log-likelihood probability, based on the information extracted from the calorimeter system (mainly the ECAL), the RICH and the muon chambers. The efficiency measured with a sample of $B^0 \to (J/\psi \to e^+e^-)K^0_S$ events is measured to be $\varepsilon(e \to e) \sim 95\%$, with a misidentification efficiency of $\varepsilon(e \to e) \sim 0.7\%$.

Neutral particles identification   Photons are identified using the electromagnetic calorimeter. For each event, the reconstructed tracks are matched to the ECAL cluster and an estimator, χ^2_γ, is built. Clusters without associated track ($\chi^2_\gamma > 4$) are considered to be photon candidates.

Neutral pions, which decay in two photons, are divided in two categories according to their transverse energy. For $E_T < 2.5\,\text{GeV}$ the two photons are reconstructed as a pair of separated photons and are called *resolved* pions. Above this energy they appear as a unique cluster and are called *merged* pions.

4.4   Trigger system

The trigger is designed to reduce the event rate from 10 MHz to 3 kHz before recording the events for offline analysis. It is made of three different stages: the Level-0 (L0) trigger and two High Level Triggers (HLT1 and HLT2). It is optimized in order to keep the efficiency as high as possible for the events of interest. A scheme of the LHCb trigger system is illustrated in Fig. 4.15.

Level-0

The L0 is a hardware trigger that uses custom-made electronics, synchronised with the bunch crossing frequency. It collects information from the calorimeters, the muon system and the pile-up system in the VELO, reducing the event rate to 1 MHz. The calorimeter trigger looks for high E_T candidates, and selects the highest E_T cluster for each particle hypothesis (hadrons, electrons and photons). It also provides a measurement of the total E_T in the HCAL to reject crossings without interaction, and it measures the SPD multiplicity. The muon trigger selects the two muons with the highest p_T.

The pile-up system, instead, distinguishes between single and multiple interactions. Because of the higher luminosity of 2011 and 2012, it is used only to trigger beam-gas interactions. All the information collected by the three sub-triggers are then sent to the Level-0 Definition Unit, where the trigger decision is taken. Finally, the decision is sent to the Readout Supervisor, which decides whether or not to accept the event.

High Level Triggers

The HLT trigger consists of a software filter divided in two steps. It has access to the full event information and rejects uninteresting events, reducing the rate to ∼50 kHz in the HLT1 and to ∼3 kHz in the HLT2. The HLT1 trigger consists in a set of inclusive trigger lines grouped in various classes, such as physical, technical, and muon-dedicated trigger lines. Moreover it applies a cut on the SPD multiplicity, in order to reject events with too many tracks. The rate entering the HLT2 is small enough to permit a full reconstruction of the event. It is composed of many lines, inclusive and exclusive, each of them optimised for a specific analysis.
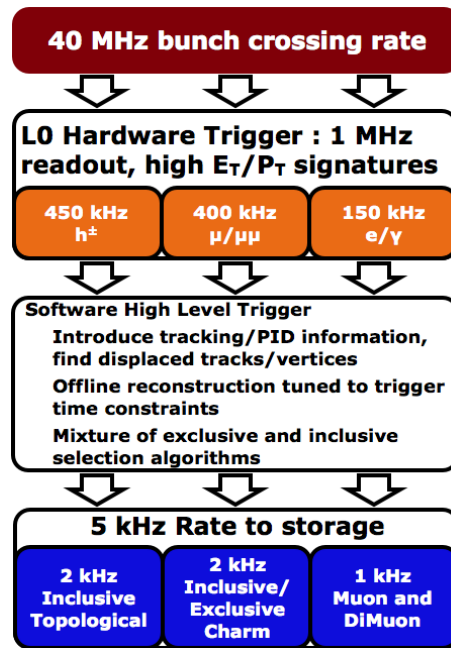
Figure 4.15 *Scheme of the LHCb trigger.*

4.5 LHCb software

The LHCb software is based on the software framework architecture GAUDI [64, 65], which supports all the online and offline applications. The main applications are:

- **GAUSS**. The GAUSS application [64] is responsible of the first steps in the simulation, taking care of all the physics aspects of the collision. It involves different softwares with specific tasks: *pp* collisions are simulated using PYTHIA [66], the decays of hadronic particles is simulated either with EVTGEN [67] or PYTHIA, while PHOTOS [68] generates the final state radiation in the decay processes. Finally, GEANT4 [69] handles particle interactions with the material.

- **BOOLE**. The BOOLE [70] application digitizes the output of the simulated particle-detector interaction. It simulates the response of the detector and of the readout electronics, as well as of the L0 trigger hardware. The output of BOOLE has the same format as that of real LHCb data.

- **MOORE**. The MOORE software package [71] runs the HLT trigger both on real and simulated data. In case of real data it acts as a filter, selecting only the events that pass the trigger lines. Simulated events are instead flagged according to the trigger response.

- **BRUNEL**. The BRUNEL software [72] is the LHCb reconstruction application used for both real and MC data. Starting from the tracking hits it defines the trajectory and the momentum of the particles, and it calculates their energy. Moreover, it runs the particle identification algorithms in order to identify the particles.

- **DAVINCI**. The DAVINCI application [73] takes the BRUNEL output and recon-
  structs the event. The vertex filter is applied, the decay chain of interest is recon-
  structed and all the kinematic variables useful for offline analysis are calculated.

5

The LHCb magnetic field map

5.1 Introduction

The LHCb magnet is a warm magnet with saddle-shaped coils, covering a forward acceptance of ± 250 mrad vertically and ± 300 mrad horizontally. It plays an essential role in the tracking of charged particles. Indeed, in presence of a magnetic field, the trajectory of a charged particle bends, and the particle momentum can be determined.

The momentum resolution provided by the magnet is $\delta p/p \sim 0.4\%$ for momenta up to $200\,\mathrm{GeV}/c$. This precision is achieved thanks to an integrated field, $\int B \cdot dl$, of approximately 4 Tm for 10 m-long tracks.

The magnet polarity is regularly flipped, allowing for the study of systematic effects due to a possible left-right detector asymmetry. An upward or downward polarity of the magnet is defined with respect to the sign of the main component of the magnetic field, B_y, positive or negative respectively. Coordinates are given in the LHCb Physicist System, illustrated in blue in Fig. 5.1 and defined as follow:

- Origin: nominal interaction point of the pp collisions (IP);

- z: axis along the beam axis, pointing from the IP to the muon stations;

- x: axis perpendicular to the beam axis, horizontal, pointing away from the centre of the LHC ring;

- y: axis perpendicular to the $x - z$ plane, in the upward direction.

The three components of the magnetic field are shown in Fig. 5.2.

The magnet design is strongly driven by the following requirements:

- a magnetic field lower than 2 Tm is required inside the RICH detector;

- the highest possible field is needed in the region between the VELO and the Tracker Turicensis stations;
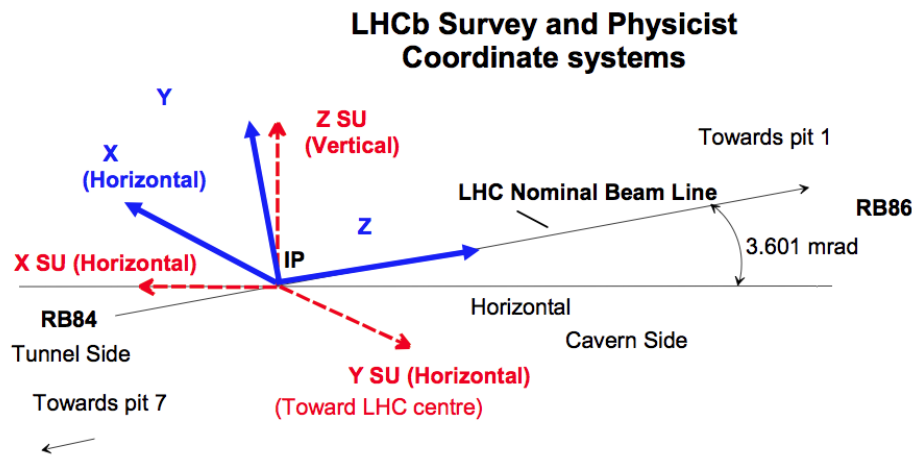
Figure 5.1 *LHCb coordinate systems. The survey (physicist) coordinate system is shown in red (blue).*

- constraints are imposed by the dimensions of the cavern.

In order to satisfy these requirements the following design choices are made: the yoke is composed of 100 mm-thick carbon steel plates, with pole pieces on the horizontal bottom and top parts to improve the quality of the lateral field, while two side parts placed mirror-symetrically to each other are used to close the flux return. Inside the yoke, two identical coils with conical saddle shape are placed. Each of them consists of fifteen pancakes arranged in triplets and made of pure Al-99.7 hollow conductor. A drawing is shown in Fig. 5.3.

In order to reach the required resolution on the particle momenta, a precision of approximately 10^{-3} T on the three magnetic field components is needed.

Between the end of 2004 and the end of 2005 several magnetic field measurement campaigns were performed. The main one took place in December 2005. Measurements of each of the three components of the magnetic field were collected for the two magnet polarities at more than 500k different points in space. Since the measurements did not cover the full acceptance, an extrapolation was needed to determine the field at all possible points inside the detector. Values of the magnetic field were calculated with TOSCA, an analysis and simulation package used to generate an initial estimate of the magnetic field map. In order to obtain the real magnetic field map, the residuals between the measured and simulated valued have been parametrized, separately for the three components of the magnetic field. The resulting magnetic field map was used in the simulation and reconstruction software from 2008 to June 2011.
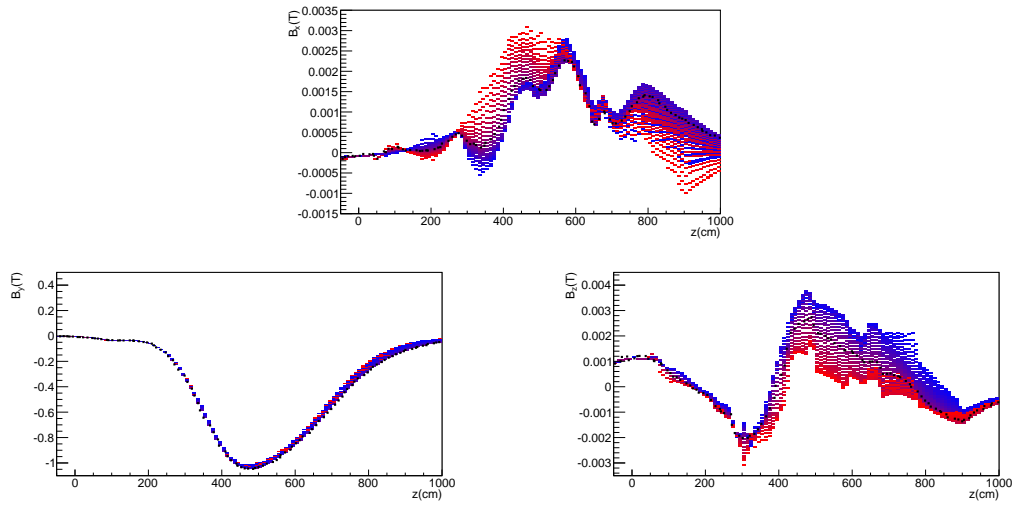
Figure 5.2 B_x, B_y, and B_z field components as a function of the z coordinate. The data are taken in a plane set at $y = 0$. The colour goes from red to blue, in the range given by the geometrical acceptance of the detector in the x direction. The black points are the field values at $x = 0$.
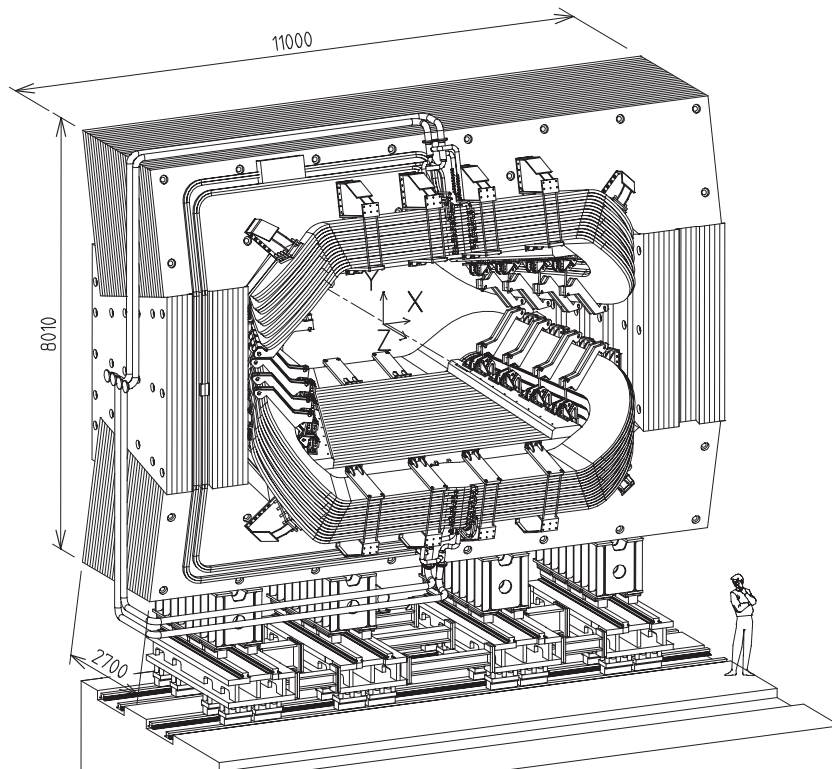
Figure 5.3 Drawing of the LHCb magnet.

5.2   2011 measurement campaign

A new campaign for the measurement of the magnetic field has been performed in February 2011. The motivation for this study originated in the alignment results and in the mass reconstruction results with the 2009–2010 data. Inconsistencies between magnet-on and magnet-off data were observed in alignment studies. A possible explanation was the displacement of the tracker in presence of the magnetic field, or an imperfect description of the magnetic field. Moreover, the mass measurements suggested a momentum scale correction at the level of 0.05%. Because of these reasons it was decided to re-measure the magnetic field in a restricted region to check the field map.

The measurements have been made with the detector closed and ready for data taking. Measurements were taken with both up and down magnet polarities, in a y–z plane at fixed x ($x = 22$ cm). The z coordinate was varied between 302 cm and 732 cm in steps of 5 cm. Along y, eight different positions were considered, in the range $-55.9 < y < 1.2$ cm.

5.2.1   Experimental setup

The experimental setup used for the magnetic field measurement campaign consists of a 7 m-long bench with a 90×90 mm^2 cross section, that supports a trolley holding six sensors. The trolley is moved by an external handle, and it is held with a pin into a series of holes. The holes are equally spaced by 5 cm in the z direction. The pin is released by compressed air in order to move the trolley along z. Due to a conflict with the beam-pipe support cables in the magnet, the trolley had to be dismounted to cover the full z range. Because of this, the z range is divided in three different regions as shown in Fig. 5.4: in the first region ($298 < z < 380$ cm) points in sixteen different z positions were measured, in the second ($389 < z < 410$ cm) only three z positions were considered, and the third region ($429 < z < 735$ cm) covered up to sixty z positions.

On the trolley six sensors are positioned at four different heights. The difference between the lowest and the highest positions is 17 cm. In view of systematic checks, three sensors are placed at the highest y position and are separated by 5 cm along z, scanning in this way the same points. The other three sensors are at different y but same z positions.

The y coordinate for each sensor and the relative z position with respect to the sensor at the bottom are shown in Table 5.1. The whole support can be fixed at two global y positions, separated by 5.7 cm. In this way sets of eight points with different y position can be measured for each z value.

The magnetic field is measured using Hall probes. Each sensor holds three probes, one for each component of the magnetic field, B_x, B_y and B_z. The probes are glued to a $4 \times 4 \times 2.3$ mm^3 glass cube. After calibration and temperature corrections, the precision reached is 0.2 mT. Figure 5.5 shows a picture of the magnetic field sensors as well as their positions on the trolley.

During the measurement campaign 14 sets of measurements were performed. They are

Table 5.1 *Absolute sensor y positions in the LHCb physicist frame. They are calculated consid-
ering the sensor support in hole number 6. Small corrections coming from the survey
measurements are added at each point. The relative z position is given with respect to
sensor 1 in hole number 6. The absolute z position of probe 1 is 328.535 cm. An offset in
y of +5.7 cm needs to be added when the trolley is in its upper position.*

Sensor	y [cm]	Δz [cm]
1	$-55.746\ (+5.700)$	0
2	$-38.646\ (+5.700)$	0
3	$-21.546\ (+5.700)$	-0.1
4	$-4.456\ (+5.700)$	$+0.1$
5	$-4.456\ (+5.700)$	-4.9
6	$-4.456\ (+5.700)$	-9.9

characterized by the polarity of the magnet, the vertical position of the trolley (0 for the
sets of measurements with lowest y position of the trolley and $+5.7$ cm if the trolley is
in its upper position), the z region covered by the measurements and the direction of
motion of the trolley. The conditions for the 14 sets are summarized in Table 5.2.

Table 5.2   *Sets of measurements taken during the magnetic field measurement campaign, classified according to the polarity of the magnetic field, the relative vertical position of the trolley Δy, the region covered on the z axis and the direction of measurements. The regions A, B and C cover the z ranges 298 < z < 380 cm, 389 < z < 410 cm and 429 < z < 735 cm respectively. The sets of measurements from the interaction point towards the T stations are indicated by $\leftarrow$, while the lines of measurements in the other direction are indicated by $\rightarrow$.*

Set	Polarity	Δy [cm]	Region	Direction
1	Down	0	C	$\leftarrow$
2	Down	+5.7	C	$\rightarrow$
3	Down	+5.7	C	$\leftarrow$
4	Down	+5.7	B	$\leftarrow$
5	Down	0	A	$\leftarrow$
6	Down	0	A	$\rightarrow$
7	Down	0	B	$\rightarrow$
8	Down	0	C	$\rightarrow$
9	Up	0	A	$\rightarrow$
10	Up	0	B	$\rightarrow$
11	Up	0	C	$\rightarrow$
12	Up	+5.7	C	$\leftarrow$
13	Up	+5.7	B	$\leftarrow$
14	Up	+5.7	A	$\leftarrow$
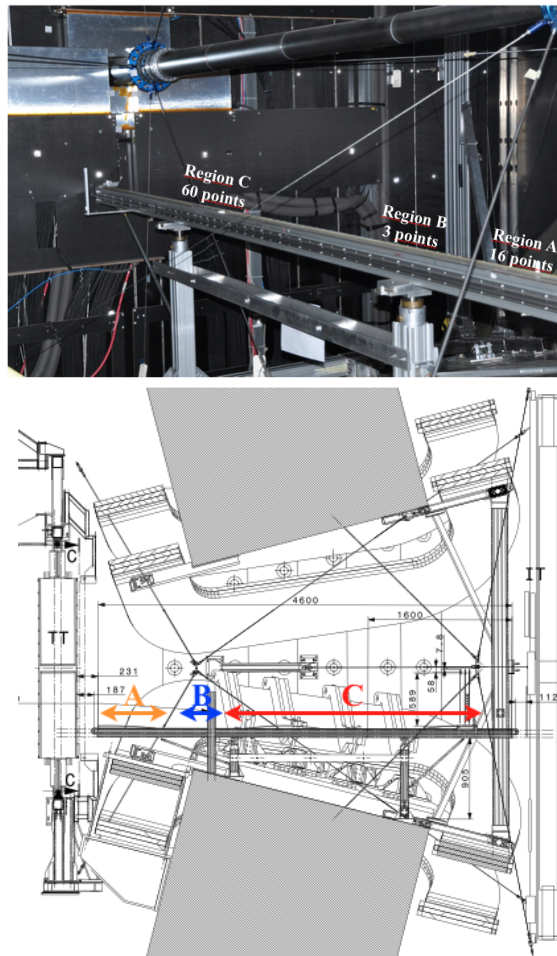
Figure 5.4 *Picture of the sensor support in data taking configuration (left) and side view of the magnet (right). The three z regions considered in the magnetic field measurements are indicated.*
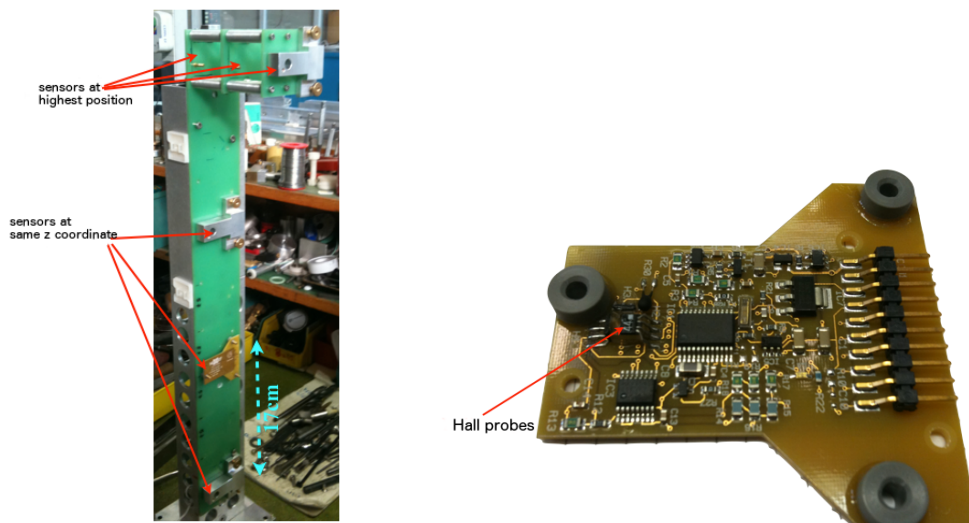
Figure 5.5 *Picture of the trolley with the position of the 6 sensors indicated (left) and picture of the magnetic field sensor (right).*

5.3   Data selection and sources of uncertainty

Systematic checks were performed to evaluate the accuracy of the measurements and to select the best data to be used in the analysis. From these studies two categories of uncertainties were defined: uncertainties correlated across the measurement points, called here systematic uncertainties, and uncorrelated uncertainties, assumed to be of statistical nature. The significant sources of uncertainty (summarised in Table 5.3) are:

- Chariot construction: mechanical accuracy in the bench, trolley and sensor support construction, estimated to be 0.1 mm.

- Rail construction: uncertainty due to the trolley movement along the rail. Variations of sensor position have been measured to be < 1 mm along the length of the bench (see Fig. 5.6). The uncertainty is estimated to be 0.5 mm at $1\,\sigma$.

- Field ON/OFF difference: survey measurements show evidence of a global shift of the bench moving from magnet ON to magnet OFF, from which a correlated uncertainty of 0.5 mm is deduced. In addition, an uncorrelated uncertainty of 0.2 mm is considered to take in account the precision of the measurement.

- Intrinsic probe sensitivity: uncertainty on the probe construction, equal to 0.2 mT.

- Probe calibration: difference between the measurements of probes 4, 5 and 6 (see Sec. 5.3.2).

- Mechanical reproducibility: difference between different measurements at the same point (see Sec. 5.3.3).

- Field Up vs Down: contribution coming from the magnetic field difference with upward polarity and downward polarity (see Sec. 5.3.4).

- Sensor orientation: uncertainty due to local rotations of the sensor. Variations of the sensor position can induce rotations of the sensor, which may affect the measure of the magnetic field components. Considering that 1 mrad rotation inside a 1 T vertical magnetic field corresponds to a 1 mT difference when measured along the x axis, a 1 mT correlated uncertainty is estimated.

5.3.1   Statistical fluctuation of the sensor measurements

To evaluate the statistical fluctuation, up to 100 measurements at the same coordinates were taken with the trolley in three different positions: $z = 4.07$, 4.32 and 7.32 m. From the values obtained, an uncorrelated error of 0.01 mT was assigned.
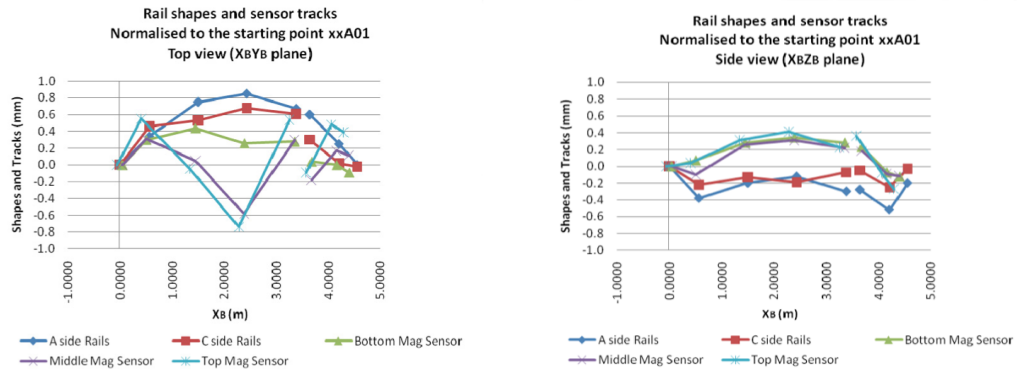
Figure 5.6 *Horizontal (left) and vertical (right) variations of the sensor and rail positions along the length of the bench. The coordinate system is local to the bench, with x_B parallel to the bench, z_B vertical, and y_B perpendicular to the other two axes.*

5.3.2 Comparison of sensor responses

Sensors 4, 5 and 6 are at the same height, and 5 cm apart in z. Since the trolley moves along z in steps of 5 cm, they measure the same points. Differences between measurements of the same point from different probes are used as systematic errors on the measured field. Figure 5.7 shows the difference of the three components, B_x, B_y and B_z, and the magnitude of the magnetic field, $\|\vec{B}\| = \sqrt{B_x^2 + B_y^2 + B_z^2}$, measured by any two probes as a function of z. A difference of magnetic field up to 3 mT is found. Since sensor 5 is always in best agreement between any two sensors, it is decided to use it as reference and assign a 1 mT systematic uncertainty on all the measurements due to the Hall probe calibration.

5.3.3 Comparison of two passes at the same points

Each set of measurements (at the same x and y coordinates but at different z coordinates) taken in the down-polarity configuration of the magnet has been performed twice, in the two directions along the z coordinate. No difference is expected if the experiment can be perfectly reproduced. However, the data show differences at the level of 1 mT.

We can distinguish two different cases:

- Two measurements of the same set are taken consecutively. Figure 5.8 shows the three components of the magnetic field and the magnitude of the magnetic field as a function of z for both measurements. Figure 5.9 shows the difference between the two measurements. In this case the difference is at the level of 0.1 mT. This value contributes to the uncorrelated uncertainties.

- The two measurements of the same set are not consecutive and separated by manipulation of the trolley: the trolley is moved to the upper y position to measure another set of points and then placed again at the initial coordinates. In this case

B_x

B_y

B_z

$\|\vec{B}\|$
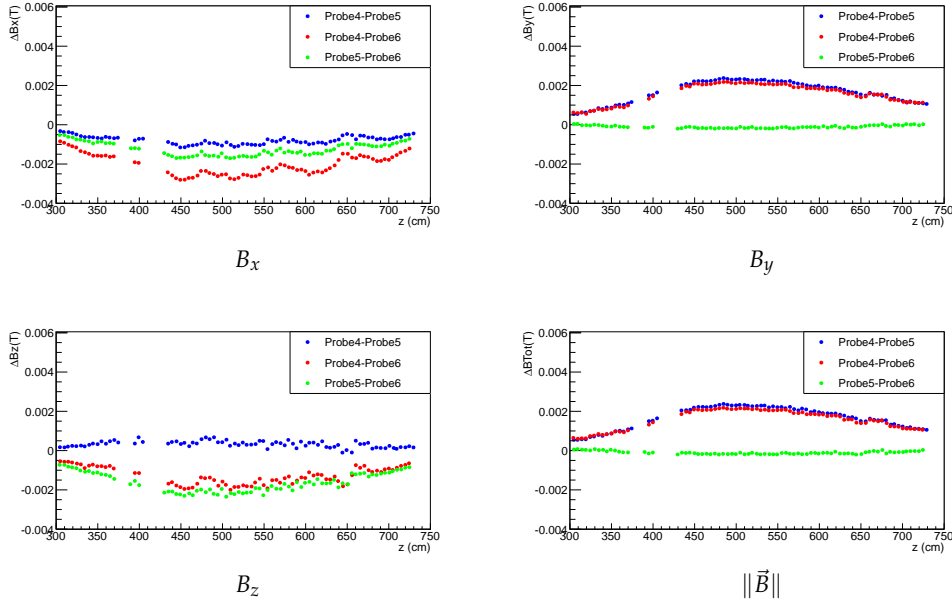
Figure 5.7   *Difference of magnetic field measurements by any two probes as a function of z. The blue points indicate the difference between probes 4 and 5, the red points between probes 4 and 6, and the green points between probes 5 and 6. The y coordinate is fixed at −4.5 cm.*

the difference between the first and second set of measurements is larger and it is estimated to be 1.0 mT. This contributes to the correlated uncertainty. Figures 5.10 and 5.11 show the absolute value and the difference of the three components and magnitude as a function of z, respectively.

5.3.4   Comparison between magnet up and magnet down measurements

The last systematic check concerns the comparison between measurements taken with opposite polarity of the magnetic field. The three components and the magnitude of the magnetic field for both polarities are shown in Fig. 5.12. The blue points represent the magnetic field with down polarity, whereas the red points the field with up polarity. The sign of the magnetic field component for magnet up is flipped to make the comparison with the polarity down measurements. The difference between magnet down and magnet up measurements (sum of the two components with the correct sign) is plotted in Fig. 5.13. We observe that all the components are in agreement within ± 1 mT. It is decided to use only the magnet up measurements and to assign a ± 1mT systematic uncertainty.

Table 5.3 *Sources of error with their contribution to correlated and uncorrelated uncertainties. For mm to mT conversions, we use the average dB/dz ≈ 0.6 mT/mm, considering the maximum variation of the magnetic field as a function of z. The total errors are the quadratic sums of the individual contributions.*

Source	Uncorrelated error	Correlated error
Chariot construction		± 0.1 mm
Rail construction	± 0.5 mm	
Field ON/OFF difference	± 0.2 mm	± 0.5 mm
Intrinsic probe accuracy	± 0.2 mT	
Mechanical reproducibility	± 0.1 mT	± 1.0 mT
Magnet up vs down		± 1.0 mT
Probe calibration		± 1.0 mT
Sensor orientation		± 1.0 mT
Total uncorrelated error	± 0.4 mT	
Total correlated error		± 1.75 mT

B_x

B_y

B_z

$\|\vec{B}\|$
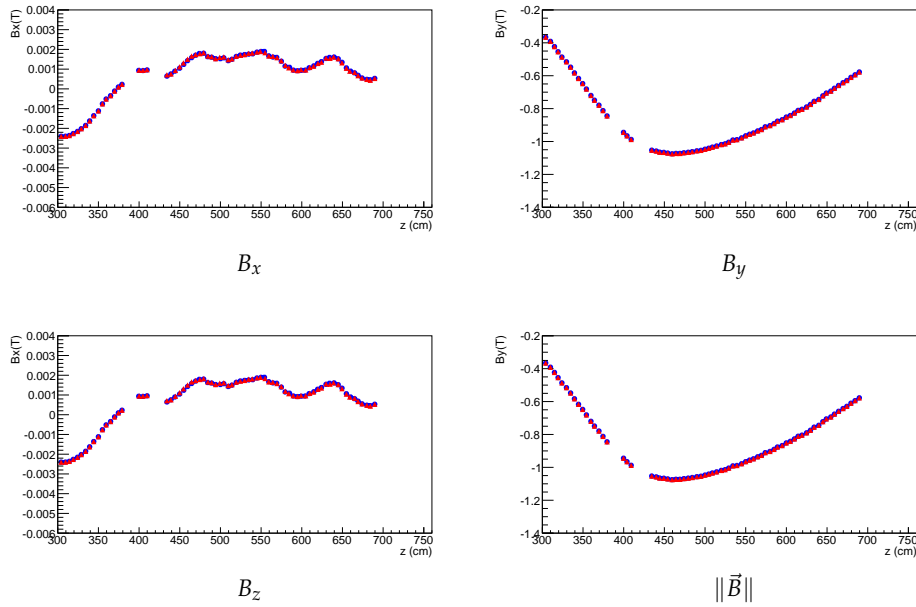
Figure 5.8 *Two sets of magnetic field measurements (in red and blue) at the same points along the z axis, taken in opposite direction without any manipulation of the trolley between the two sets. The data overlap almost perfectly. The y coordinate is fixed at -33.1 cm.*

B_x

B_y

B_z

$\|\vec{B}\|$
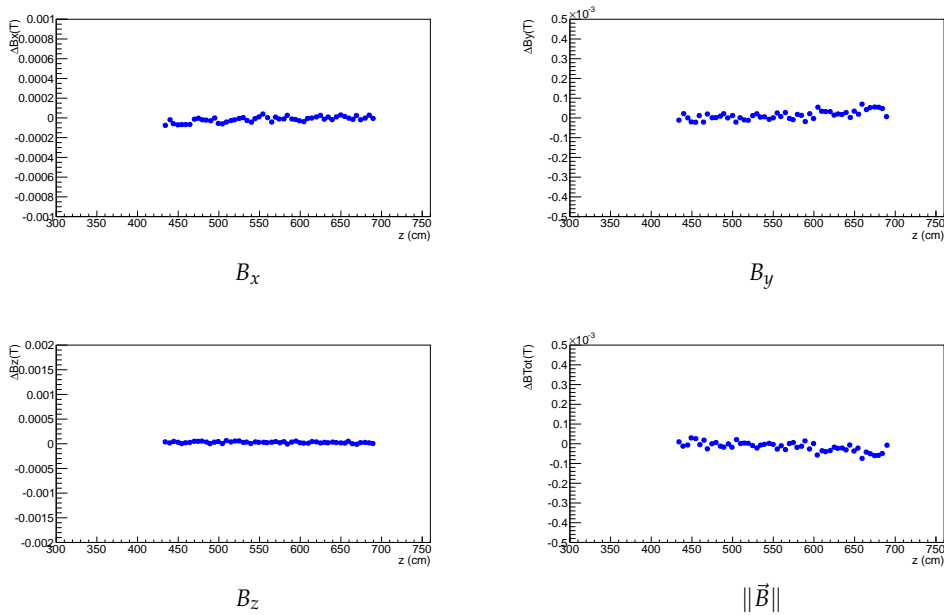
Figure 5.9 *Difference between the two sets of measurements shown in Fig. 5.8. The maximum difference is at level of 0.1 mT.*
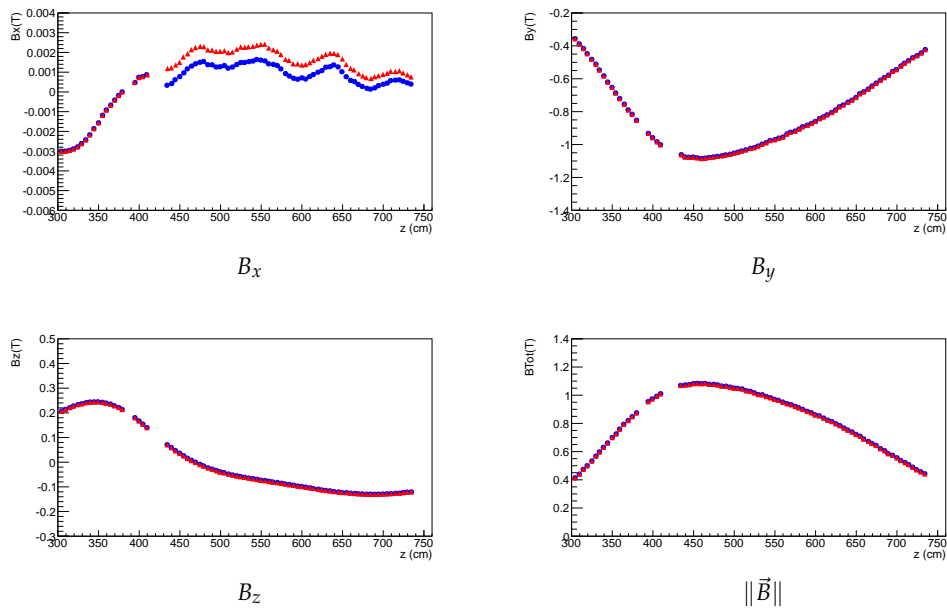
Figure 5.10   *Two sets of magnetic field measurements (in red and blue) of the same points along the*
z axis. Between the two sets of measurements, the trolley was manually manipulated.
A difference between the two measurements is visible for B_x, whereas they overlap for
B_y and B_z. The y coordinate is fixed at -38.8 cm.
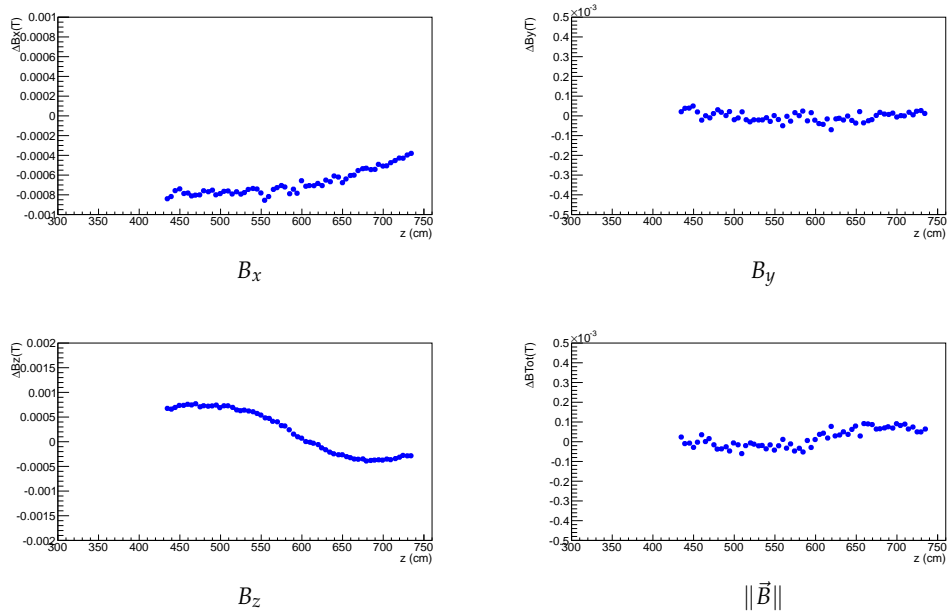
Figure 5.11   *Difference between the two sets of measurements shown in Fig. 5.10. The maximum*
difference observed is less than 1 mT.
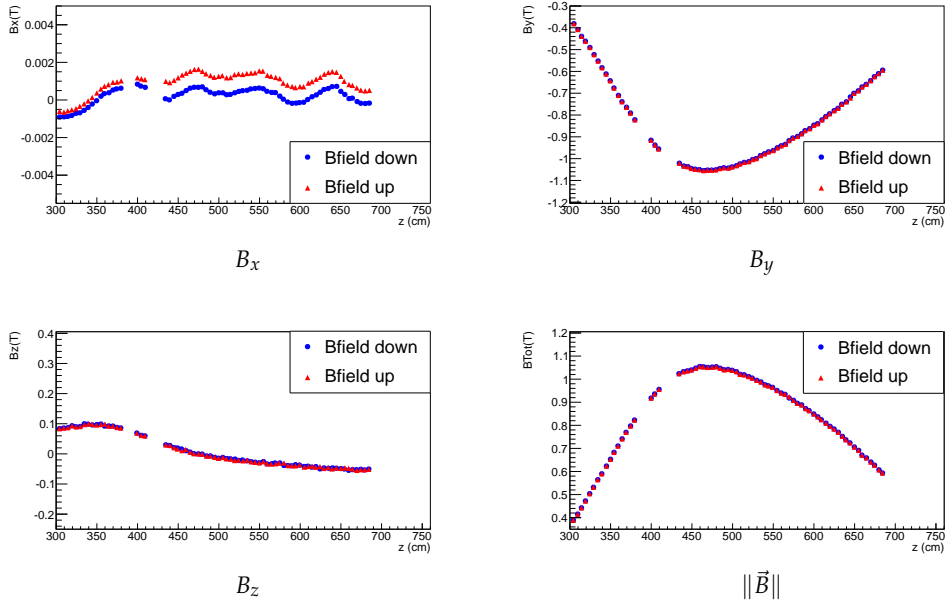
Figure 5.12 *Measurements with up (red points) and down (blue points) polarity configuration of the magnet as a function of z. The field components measured with magnet polarity up are multiplied by −1. The y coordinate is fixed at −15.9 cm.*
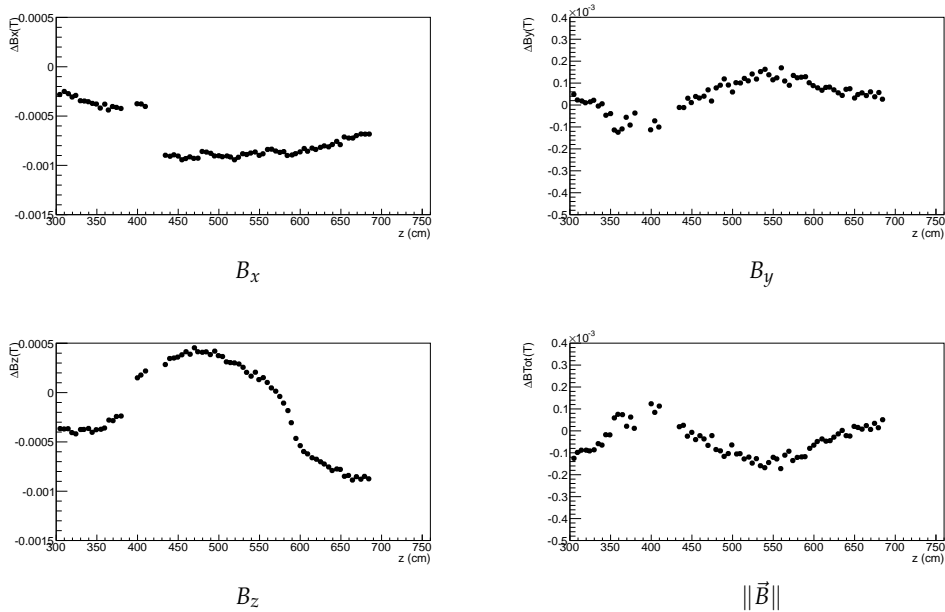
Figure 5.13 *Difference between the measurements shown in Fig. 5.12. Because the sign of the components is opposite in the two case, they are summed. The gap in the B_x plot is due to the manipulation of the trolley from region A to region B.*

5.4   Data analysis

After the data selection, the measurements are compared with the old magnetic field map. From a preliminary inspection a global z shift of the field map arises. Figure 5.14 shows the three components, B_x, B_y, B_z, and the magnitude, $\|\vec{B}\|$, of the magnetic field from the new measurements and for the values extrapolated from the old magnetic field map at the same coordinates as a function of z for a fixed value of y, while Fig. 5.15 shows the difference between the two. In the region $300 < z < 450$ cm, an increase of B_y as a function of z is observed with an estimated rate of 8 mT/cm. In the same region, the difference between new data and the old map is about 8 mT. From this, a shift of 10 mm along z can be deduced. A similar conclusion is reached using the region where B_y is decreasing ($z > 500$ cm).

A shift in the y direction can also be inferred. Figures 5.16 and 5.17 compare the new data and the map as a function of y for a fixed value of z. From the 6 mT/cm slope in the range $-60 < y < 10$ cm for B_z, and the 7 mT difference in the same y region, a shift of about 12 mm is expected, in the negative y direction.

To obtain a more precise estimate of the shifts and to investigate if rotations are involved, a fit of the old map to the new measurements is performed. Because of the limited region of the new measurements, the existing map is assumed to be correct up to global translations and rotations, and up to a global scale factor to account for a possible difference in the current in the coils. The six free parameters of the fit are:

- 2 global shifts T_y and T_z along y and z, respectively; as explained later, the effect of the x translation is found to be negligible and therefore T_x is fixed to 0;

- 3 global rotations of angles ϕ_x, ϕ_y and ϕ_z around the x, y and z axes, respectively;

- 1 global scale factor.

The pivot point (rotation point) is fixed to $(0, 0, 431.58)$ cm, at mid distance between the VELO and the T stations.

The χ^2 function to be minimized is defined as:

$$\chi^2 \;=\; \sum_i \sum_{j=1}^{3} \left(\frac{B_{ij}^{\mathrm{N}} - B_{ij}^{\mathrm{O}}(\vec{\alpha})}{\sigma} \right)^2 , \tag{5.1}$$

where the sums run over the spatial points i and the magnetic field components j, B_{ij}^{N} is the new measurement, and $B_{i,j}^{\mathrm{O}}$ the corresponding value obtained from the old magnetic field map after the global transformation (translations, rotations and scale factor). B^O depends on the free parameters of the fit $\vec{\alpha}$. Only the uncorrelated uncertainty, $\sigma = 0.4$ mT, is considered in the χ^2 minimization, while the correlated error will be added as systematic uncertainty on the fit results.

Table 5.4 *Result of the fit of the old LHCb map to the new measurements. The values that minimize the χ^2, the χ^2 value at the minimum and the number of degrees of freedom are given. The number of degrees of freedom is equal to the number of measurements (604 spatial points $\times$ 3 magnetic field components) minus the number of free parameters in the fit.*

T_y (mm)	T_z (mm)	ϕ_x (rad)	ϕ_y (rad)	ϕ_z (rad)	Scale factor	χ^2	ndf
-7.98 ± 0.04	-11.26 ± 0.06	0.00072 ± 0.00004	-0.0036 ± 0.0002	-0.00040 ± 0.00002	1.00056 ± 0.00002	7623	$1812-5$

Table 5.5 *Result of the fit of the old LHCb map to the new measurements using the MINUIT library. The values that minimize the χ^2, the χ^2 value at the minimum and the number of degrees of freedom are given.*

T_y (mm)	T_z (mm)	ϕ_x (rad)	ϕ_y (rad)	ϕ_z (rad)	Scale factor	χ^2	ndf
-8.00 ± 0.04	-11.26 ± 0.06	0.00073 ± 0.00003	-0.0036 ± 0.0001	-0.00040 ± 0.00004	1.00056 ± 0.00002	7623	$1812-5$

Table 5.6 *Correlation matrix obtained from the MINUIT fit.*

	T_y (mm)	T_z (mm)	ϕ_x (rad)	ϕ_y (rad)	ϕ_z (rad)	Scale factor
T_y (mm)	1.000					
T_z (mm)	$+0.000$	1.000				
ϕ_x (rad)	$+0.040$	-0.406	1.000			
ϕ_y (rad)	-0.006	-0.517	-0.009	1.000		
ϕ_z (rad)	$+0.086$	-0.012	-0.004	$+0.021$	1.000	
Scale factor	-0.277	-0.017	-0.050	$+0.016$	$+0.003$	1.000

In order to double-check the result, the minimization is performed using two different techniques:

- a manual scan of all the parameters to find the values that minimize the χ^2 function. The steps used are 0.02 mm for T_y and T_z, 0.02 mrad for ϕ_x and ϕ_z, 0.1 mrad for ϕ_y and 0.00002 for the scale factor.

- a minimization using the MINUIT [74] library.

The results obtained with both methods are compatible. Table 5.4 shows the results of the manual minimization, where the uncertainties are determined from the values of the parameters at which the χ^2 has increased by 1 relatively to the minimum. The results obtained from MINUIT are summarised in Tables 5.5 and 5.6. All the fitted parameters are significantly different from 0 and, as expected, large shifts along the z and y axes are observed.

In order to evaluate the effect of the corrections obtained from the fit, the residuals between the measurement and the old magnetic field map are plotted. They are defined as

$$\Delta B_{ij} = \frac{B_{ij}^{\mathrm{N}} - B_{ij}^{\mathrm{O}}(\vec{\alpha}_{\mathrm{fit}})}{\sigma}, \tag{5.2}$$

where i are the spatial points, j the magnetic field components or its magnitude and $\vec{\alpha}_{\mathrm{fit}}$ the parameters obtained from the fit.

Figures 5.18 and 5.19 show the residuals as a function of z and y, respectively. We conclude that the remaining differences are at the level of less than 1 mT for all the components.
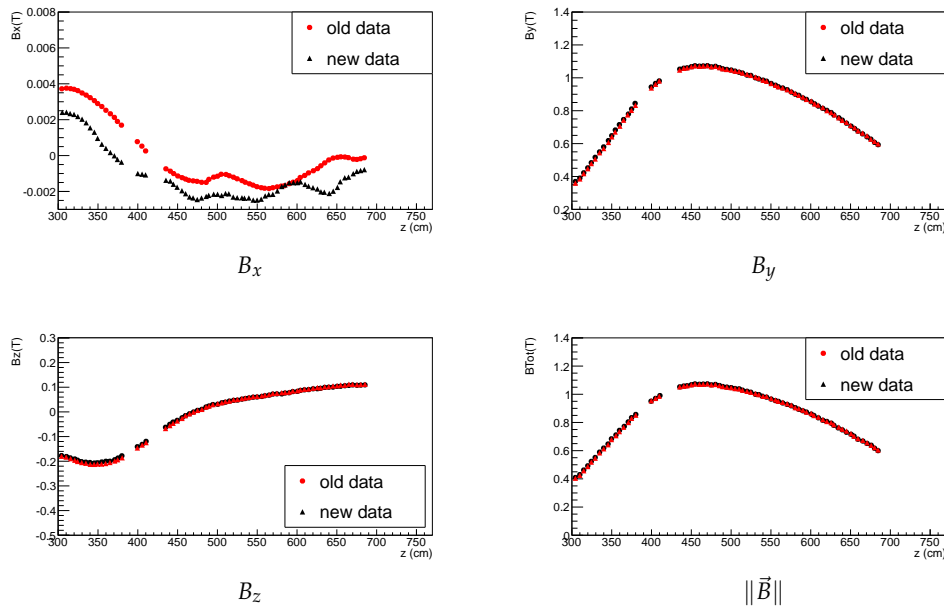
Figure 5.14 *Magnetic field obtained in the new measurement campaign (black points) compared to the values extracted from the old LHCb magnetic field map (red points) at the same coordinates. The magnetic field is plotted as a function of z. The y coordinate is fixed at −33.1 cm.*
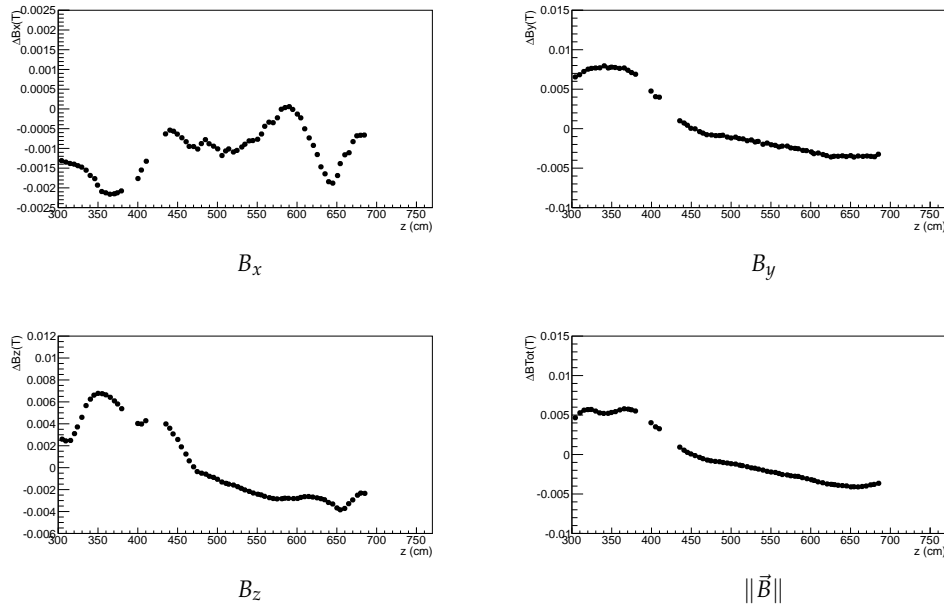
Figure 5.15 *Difference between the magnetic field measured in the new campaign and values extracted from the old LHCb magnetic field map at the same coordinates. The magnetic field is plotted as a function of z. The y coordinate is fixed at −33.1 cm.*
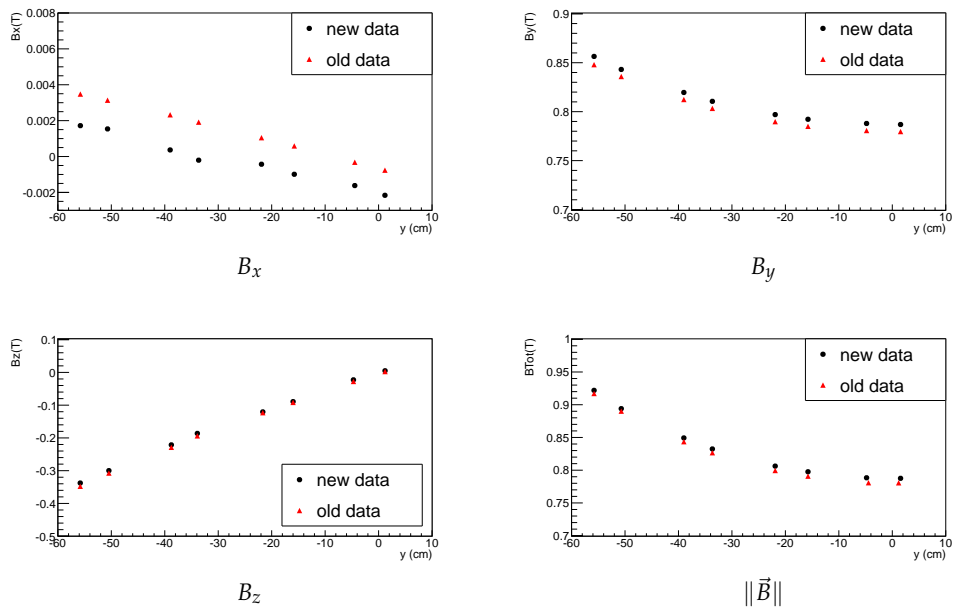
Figure 5.16 *Magnetic field obtained in the new measurement campaign (red points) compared to the values extracted from the old LHCb magnetic field map (black points) at the same coordinates. The magnetic field is plotted as a function of y, at z = 374.9 cm.*
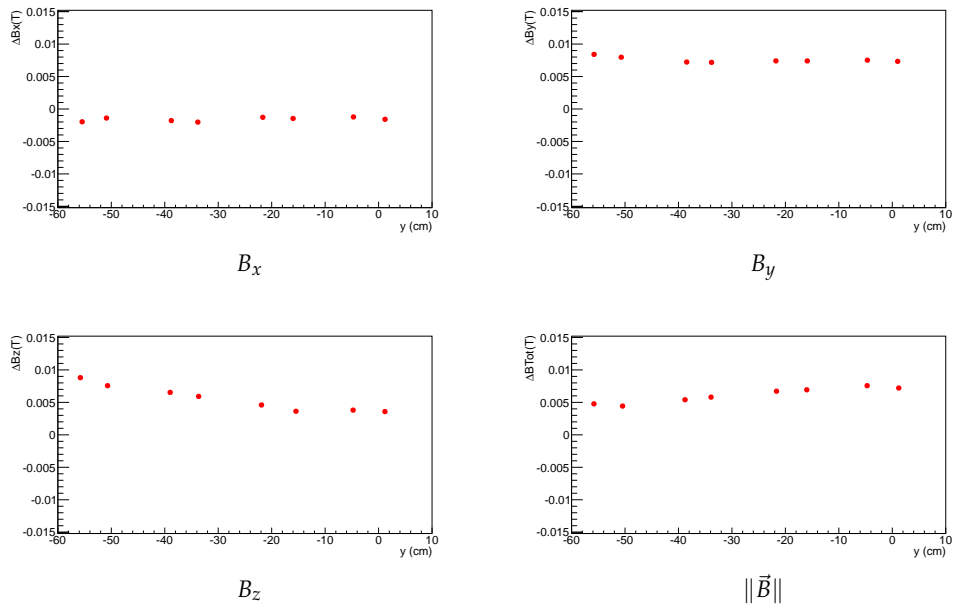
Figure 5.17 *Difference between the old magnetic field measured in the new measurement campaign and the values extracted from the old LHCb magnetic field map at the same coordinate. The magnetic field is plotted as a function of y, at z = 374.9 cm.*

B_x

B_y

B_z

$\|\vec{B}\|$
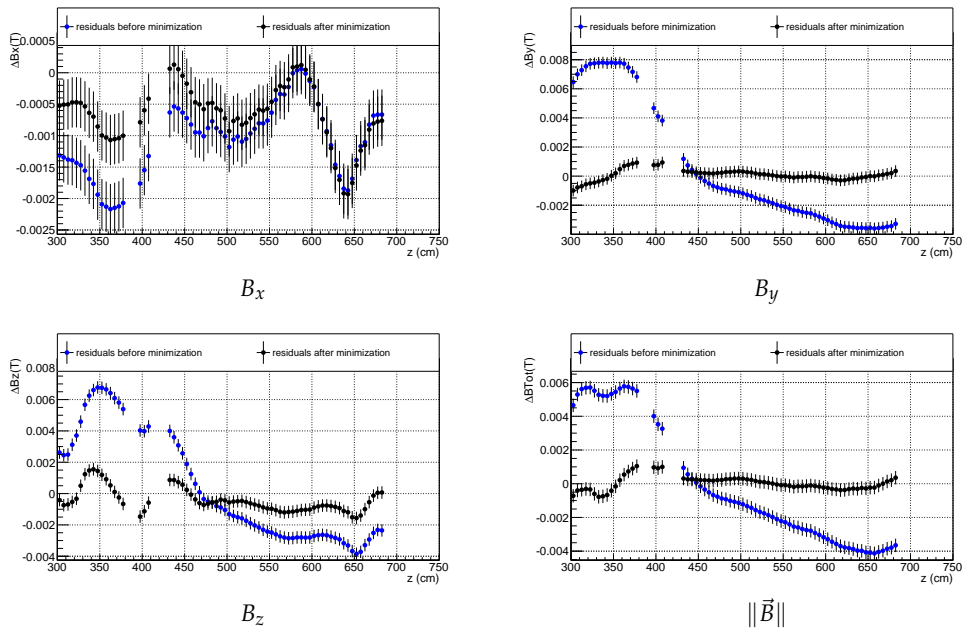
Figure 5.18   *Difference between the new measurements and the old map without (blue points) or with (black points) the corrections obtained from the global fit. The magnetic field is plotted as a function of z, at y = 33.1 cm.*

B_x

B_y

B_z

$\|\vec{B}\|$
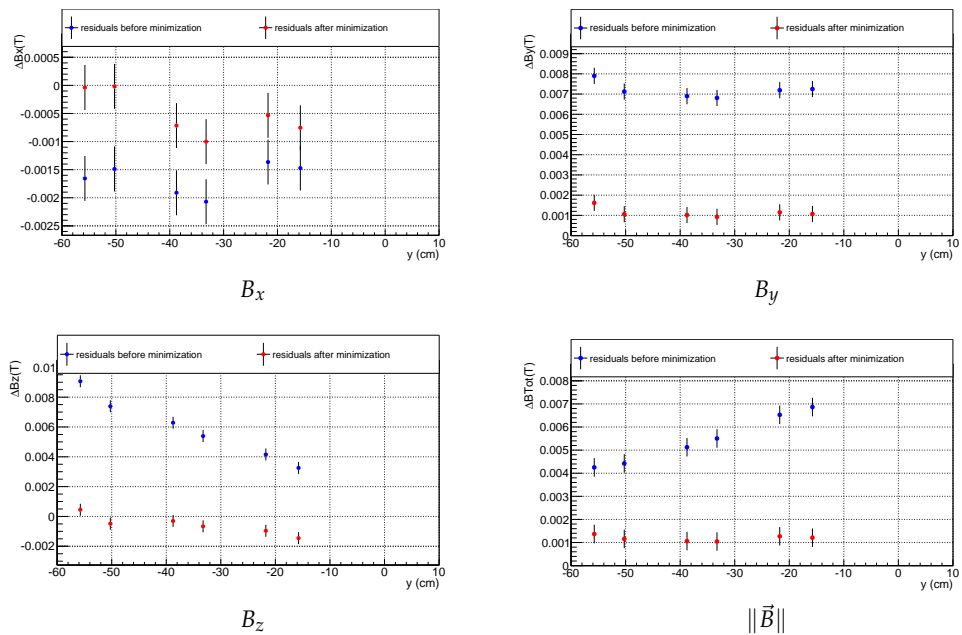
Figure 5.19   *Difference between the new measurements and the old map without (blue points) or with (red points) the corrections obtained from the global fit. The magnetic field is plotted in function of y, at z = 379.9 cm.*

5.5 Correlated uncertainties and discussions

5.5.1 Correlated uncertainties

In order to estimate the errors on the parameters due to the correlated errors in the measurements, systematic checks have been done. From Table 5.3 the correlated error on the magnetic field measurements is $\pm$ 1.75 mT. The χ^2 function was minimized by adding and subtracting 1.75 mT to the B_y component (that is the most relevant). The differences between the fitted parameters obtained from the minimization with and without the introduction of the correlated uncertainty are shown in Table 5.7.

The uncertainty on the parameters due to the correlated and uncorrelated errors and summarised in Table 5.8. The correlated errors are taken as the average of the two values in Table 5.7. Except for T_z and ϕ_x, the correlated uncertainty is dominant.

5.5.2 Crossckeck: fit in different *z* ranges

To verify the validity of the assumption of a global transformation of the field map, uniform on all the volume, the minimization is performed separately in four different *z* ranges:

- $300 < z < 400$ cm.

- $400 < z < 500$ cm.

- $500 < z < 600$ cm.

- $600 < z < 700$ cm.

Despite a global trend that supports the hypothesis of a global transformation, some systematic effects are seen, especially due to the manipulation of the trolley. The results are shown in Table 5.9. In the future, when a new magnetic field campaign will be performed a better understanding of the systematic uncertainty will be needed.

5.5.3 Pivot point

As mentioned before, the pivot point is chosen as (0, 0, 431.58) cm. The motion in three-dimensional space has six degree of freedom: three translations and three rotation angles. Therefore, the pivot point is not a real degree of freedom. Even if the parameter values that minimize the χ^2 depend on it, a transformation exists and connects two sets of parameters referred to different pivot points. This statement is not true anymore if we fix one parameter and scan the others in order to find the minimum.

To quantify the dependence and the sensitivity on the pivot point, a new fit was performed using another sensible pivot point, (0, 0, 460) cm, corresponding to the maximum magnetic field. The result is shown in Table 5.10. The values are compatible with those

Table 5.7   *Variation of the fit parameters obtained from the fit of the LHCb map to the new measurements. The measurements of the B_y component are globally shifted by ± 1.75 mT (correlated uncertainty).*

	ΔT_y (mm)	ΔT_z (mm)	$\Delta \phi_x$ (mrad)	$\Delta \phi_y$ (mrad)	$\Delta \phi_z$ (mrad)	Δ Scale factor
$B_y + 1.75$ mT	-0.590	-0.034	-0.005	$+1.120$	$+0.140$	$+0.00197$
$B_y - 1.75$ mT	$+0.550$	$+0.038$	$+0.015$	-1.360	-0.170	-0.00193

Table 5.8   *Correlated and uncorrelated error for each parameter.*

	T_y (mm)	T_z (mm)	ϕ_x (mrad)	ϕ_y (mrad)	ϕ_z (mrad)	Scale factor
Correlated error	∓ 0.57	∓ 0.04	∓ 0.01	± 1.2	± 0.16	± 0.00195
Uncorrelated error	± 0.04	± 0.06	± 0.03	± 0.1	± 0.04	± 0.00002

of Table 5.5 (considering both correlated and uncorrelated uncertainties), so we can conclude that the sensitivity to the pivot point is negligible at the level of the accuracy of our measurement.

5.5.4   Translation along x

In this study T_x is assumed to be 0. To validate this assumption, a global fit, including T_x, is done for two different pivot points. The results are collected in Tables 5.11 and 5.12.

To quantify the effect of the correlated error on T_x a further minimization was done, by globally shifting the B_y component by $+1.75$mT and -1.75mT. The final results for the x shift are:

- Pivot point $(0, 0, 431.58)$ cm: $T_x = 29.5 \pm 3.5$ (uncorr.) ± 34.7 (corr.) mm;

- Pivot point $(0, 0, 460)$ cm: $T_x = 30.2 \pm 3.4$ (uncorr.) ± 34.4 (corr.) mm.

The results are in agreement and T_x is compatible with zero within the total uncertainty. The large uncertainties due to the correlated errors demonstrate the lack of sensitivity in T_x. It is also important to point out that the range of measurements does not permit to say if a real shift in x exists or not. To confirm this, it would be necessary to measure points with different x coordinates, both positive and negative.

Table 5.9 *Fit of the LHCb map to the new data using the* MINUIT *library. The four sub-tables refer to different z ranges. The values that minimize the χ^2, the χ^2 value at the minimum and the number of degrees of freedom are given.*

T_y (mm)	T_z (mm)	ϕ_x (rad)	ϕ_y (rad)	ϕ_z (rad)	Scale factor	χ^2	ndf
$300 < z < 400$ cm							
−7.73 ±0.07	−10.04 ±0.18	0.00061 ±0.00009	−0.0021 ±0.0003	−0.00152 ±0.00008	1.00126 ±0.00015	1937	426−6
$400 < z < 500$ cm							
−8.14 ±0.19	−11.08 ±0.26	0.00045 ±0.00004	−0.0024 ±0.0007	−0.00005 ±0.00004	1.00080 ±0.00004	1182	384−6
$500 < z < 600$ cm							
−10.1 ±0.3	−4.6 ±0.6	0.00030 ±0.00009	−0.0028 ±0.0008	0.00006 ±0.00005	0.99925 ±0.00011	1173	480−6
$600 < z < 700$ cm							
−8.12 ±0.12	−6.6 ±0.4	0.00130 ±0.00010	−0.0003 ±0.0005	−0.00082 ±0.00007	0.99783 ±0.00017	1131	522−6

Table 5.10 *Result of the fit of LHCb map to the new measurements using the* MINUIT *library and the alternative pivot point (0, 0, 460) cm. The values that minimize the χ^2, the χ^2 value at the minimum and the number of degrees of freedom are given.*

T_y (mm)	T_z (mm)	ϕ_x (rad)	ϕ_y (rad)	ϕ_z (rad)	Scale factor	χ^2	ndf
−7.79 ±0.05	−11.27 ±0.06	0.00073 ±0.00003	−0.0037 ±0.0001	−0.00040 ±0.00002	1.00056 ±0.00002	7623	1812−5

Table 5.11 *Result of the fit of LHCb map to the new measurements using the* MINUIT *library and the default pivot point (0, 0, 431.58) cm. The T_x translation is also considered. The values that minimize the χ^2, the χ^2 value at the minimum and the number of degrees of freedom are given.*

T_x (mm)	T_y (mm)	T_z (mm)	ϕ_x (rad)	ϕ_y (rad)	ϕ_z (rad)	Scale factor	χ^2	ndf
29.51 ±3.47	−7.90 ±0.05	−11.32 ±0.06	0.00068 ±0.00003	−0.0024 ±0.0002	−0.00025 ±0.00003	1.00045 ±0.00002	7546	1812−6

Table 5.12 *Result of the fit of LHCb map to the new measurements using the* MINUIT *library and the pivot point (0, 0, 460) cm. The T_x translation is also considered. The values that minimize the χ^2, the χ^2 value at the minimum and the number of degrees of freedom are given.*

T_x (mm)	T_y (mm)	T_z (mm)	ϕ_x (rad)	ϕ_y (rad)	ϕ_z (rad)	Scale factor	χ^2	ndf
30.18 ±3.43	−7.71 ±0.05	−11.32 ±0.05	0.00068 ±0.00003	−0.0024 ±0.0002	−0.00025 ±0.00003	1.00045 ±0.00002	7546	1812−6

5.6 Summary

A campaign to measure the LHCb magnetic field was performed in February 2011. Measurements were taken both with down polarity and up polarity of the magnet in a plane at fixed x. After the data taking, some systematic checks were done, to select good measurements and to estimate the accuracy of the measurements. As a result, it was decided to use only the measurements taken with up polarity and to assign an uncorrelated and correlated error of ± 0.4 mT and ± 1.75 mT, respectively: the correlated errors is treated as a systematic uncertainty, while the uncorrelated error is treated as a statistical uncertainty. After the reduction of data, a comparison with the previous LHCb magnetic field map was done. Due to the difference between the new data and the field map, a fit of the LHCb map to the measurements has been performed, in order to have a more precise estimate of the shifts and rotations involved. Six parameters were applied to the map: two global shifts, a y translation and a z translation, three global rotations, and a global scale factor.

Systematic checks were done after the minimization to estimate the systematic errors. Other checks done include the study to quantify the dependence and the sensitivity on the pivot point and to confirm the insensitivity on the x translation of the measurements. The final corrections applied to the LHCb map to minimize the deviation from the measurements are:

$$
\begin{aligned}
T_y &= (-7.98 \pm 0.04 \mp 0.57) \text{ mm} \\
T_z &= (-11.26 \pm 0.06 \mp 0.04) \text{ mm} \\
\phi_x &= (0.72 \pm 0.02 \mp 0.01) \text{ mrad} \\
\phi_y &= (-3.6 \pm 0.1 \pm 1.2) \text{ mrad} \\
\phi_z &= (-0.40 \pm 0.04 \pm 0.16) \text{ mrad} \\
\text{Scale factor} &= 1.00056 \pm 0.00002 \pm 0.00195
\end{aligned}
\tag{5.3}
$$

where the first (second) quoted uncertainty results from the correlated (uncorrelated) errors.

Using these corrections, and assuming a global transformation of the field map, a new map was created and it is in use in the LHCb reconstruction starting from June 2011. The residual differences between measurements and the corrected map are at the level of 1 mT or less. With the new magnetic field map a better agreement between the software alignment and the survey measurements of the TT and OT tracking station positions is obtained, as shown in Fig. 5.20 for the z position. For the IT the deviation in z is up to 12 mm, which is qualitatively explained by the use of ferromagnetic connectors in the IT detector boxes.
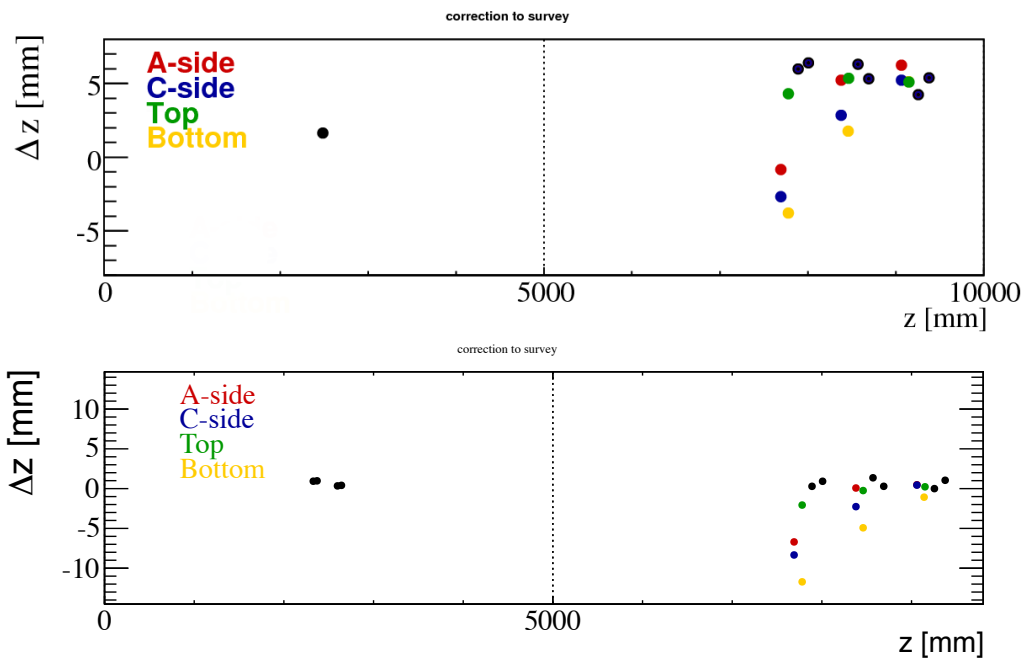
Figure 5.20 *Difference in z between the tracking station positions obtained with the software alignment and by the survey measurements, using the old (top) and the new (bottom) magnetic field map. The TT are represented by the points in the range $2 < z < 3m$. The red, blue, green and yellow points, show the position of the A-side, C-side, top and bottom IT detector boxes, respectively, while the remaining black points indicate the OT stations.*

Analysis strategy

The main goal of this thesis is the study of a few specific charmless B meson decays. Two analyses are performed: the first one, described in Chapter 7, has as objectives the search for the $B^{\pm} \to \phi\pi^{\pm}$ decay and the measurement of the direct CP asymmetry in $B^{\pm} \to \phi K^{\pm}$ decays. The second analysis, described in Chapter 8, presents the measurement of the $B^{\pm} \to \eta'K^{\pm}$ direct CP asymmetry and describes the results of the search for $B_s^0 \to \eta'\eta'$ decays.

This chapter describes the procedures adopted in the two analyses. Each measurement is performed with respect to a reference channel, in which the observable of interest is well known. In this approach, most systematic uncertainties cancel out. To avoid biases, the results are kept blind until the whole analysis procedure is finalised, *i.e.* the measurement is performed without looking at the final result.

6.1 Event selection and candidate reconstruction

The first demand to face in a data analysis is the enhancement of the sensitivity on the observables of interest. An optimised selection that reduces the number of background events has to be found. The chosen strategy is to define a selection that is as similar as possible for the signal channel and the reference channel, such that the cancellation of systematic uncertainties is maximised. The event selection proceeds through three different steps:

1. trigger selection,

2. offline pre-selection (stripping),

3. offline selection.

Trigger selection. In order to be stored and processed offline, the collected data are filtered at the L0 and the HLT trigger levels by specific trigger lines. Each event that passes

the selection can be classified as TOS (Trigger On Signal) or TIS (Trigger Independent of Signal). TOS events are triggered by a given line on the signal itself, independently from the rest of the event, while TIS events are triggered by a given line only due to the rest of the event. In both analyses, specific trigger lines for TOS or TIS events are required at each trigger level, in order to facilitate the understanding of the trigger efficiency. Using common trigger lines also allows the cancellation of most of the systematic uncertainty related to the trigger between the signal channel and the reference channel.

Offline pre-selection (stripping). Stored events are reconstructed by the BRUNEL application, which converts hits and calorimeter depositions into tracks and particles. The reconstructed events are then further filtered in a process called *stripping*, which uses the analysis tools contained in the DAVINCI application, such as particle identification algorithms and vertex fitting functions, to reduce the data sample. Different *stripping lines* are used, each of them optimised for a defined decay topology. Two stripping lines for the inclusive selection of charmless B candidates are used for the analyses of the four channels mentioned above: the `BetaSQ2B3piSelectionLine`, for decays with three charged particles in the final state, and the `BetaSQ2B4piSelectionLine`, used when the final state of interest contains four charged particles. In both cases the pion mass is assigned to all the particles that are combined into the final decay chain $B^{\pm} \rightarrow \rho^0 (\rightarrow \pi^+ \pi^-) \pi^{\pm}$ or $B^0 \rightarrow \rho^0 (\rightarrow \pi^+ \pi^-) \rho^0 (\rightarrow \pi^+ \pi^-)$. These lines are characterised by a large B mass window and by tight requirements on the B vertex separation from the primary vertex. A detailed list of the cuts defining the stripping lines are given in Chapters 7 and 8.

Offline selection. Once the events are stripped the decay chain is reconstructed, assigning the desired mass to the charged particles and adding possible neutral particles. A cut-based selection is applied to the reconstructed candidates, in order to further reduce the contamination from uninteresting events and improve the signal significance. The value of the applied cuts maximises a defined figure of merit. Different figures of merit are used, depending on the specific case. For already observed decay modes, such as the $B^{\pm} \rightarrow \phi K^{\pm}$ mode, the relative statistical uncertainty on the signal yield is minimised. For the search of predicted modes not yet observed, such as the $B_s^0 \rightarrow \eta' \eta'$ mode, a good choice is to maximise the figure of merit [75]

$$\frac{\varepsilon(t)}{a/2 + \sqrt{B(t)}} , \tag{6.1}$$

where $\varepsilon(t)$ is the signal Monte Carlo efficiency for a given set of cuts t, $B(t)$ is the number of background events in the signal region estimated from data in the B mass sidebands, and a is the significance for which the optimization is performed. A third method of optimization, adopted for a blind analysis, is based on Monte Carlo pseudo-experiments (toys). For each set of cuts, the expected number of signal and background events, extracted from signal MC and real data sidebands, is used to generate and fit toy samples. The ratio between the average signal yield ($\overline{N}_{sig}$) and its average uncertainty

($\overline{\sigma}_{N_{sig}}$) is used as figure of merit. This method, used as a crosscheck for the optimization of the $B_s^0 \rightarrow \eta'\eta'$ data selection, permits the study of the effect of multidimensional fit on the signal significance. However, it has to rely on theoretical predictions for the signal branching fraction, often dominated by large uncertainties.

Variables involved in the optimization are:

- Kinematic variables of the particles involved in the decay, such as momentum (p), transverse momentum (p_T), and energy (E).

- Particle IDentification (PID) variables, based on the information provided by RICH detectors, muon system, and calorimeters. To distinguish between pions and kaons the $DLL_{K\pi}$ variable is used, defined as the difference of logarithm of the likelihoods between the kaon and pion mass hypotheses:

$$DLL_{K\pi} = \ln \mathcal{L}_K - \ln \mathcal{L}_\pi. \tag{6.2}$$

The $DLL_{K\pi}$ variable has been recently replaced by a more performing PID variable, called ProbNN. It gives the bayesian posteriori probability of a particle to be a kaon (ProbNNk) or a pion (ProbNNπ).

Discrimination between photons and electrons is done by matching the ECAL cluster with the extrapolated reconstructed tracks. The $\Delta \ln \mathcal{L}$ between the photon and electron hypotheses is converted into a confidence-level variable CL_γ defined in the range $[0,1]$ as:

$$CL_\gamma = \frac{\tanh(\Delta \ln \mathcal{L}) + 1}{2} \tag{6.3}$$

- Vertex quality variables. Requirements are applied to the two-track or three-track combinations, accepting only candidates with a vertex fit χ^2 smaller than 9.

- Topological variables: events are accepted or rejected according to the value of `DIRA`, the angle between the B momentum vector and the vector joining the B production vertex to the B decay vertex, and `DOCA`, the distance between the B production vertex and the B momentum vector.

6.2 Efficiency

For each mode, the efficiency is defined as:

$$\varepsilon = \varepsilon^{geom} \times \varepsilon^{sel|geom} \times \varepsilon^{PID|sel\&geom} \times \varepsilon^{trig|PID\&sel\&geom}, \tag{6.4}$$

where

- ε^{geom} is the geometrical acceptance;

- $\varepsilon^{sel|geom}$ is the reconstruction and selection efficiency. It is calculated as the ratio between the number of Monte Carlo events passing the stripping and the offline

selection (except the PID cuts on pions and kaons), and the total number of generated events;

- $\varepsilon^{\text{PID}|\text{sel}\&\text{geom}}$ is the efficiency of the PID requirements on pions and kaons. It is calculated using the `PidCalib` tool [76] package. Calibration samples of kaons and pions from $D^{*\pm} \rightarrow D^0(K^+\pi^-)\pi^\pm$ are reweighed according to the p, η and track multiplicity distribution of Monte Carlo events selected by the stripping, the offline cuts and the trigger requirements;

- $\varepsilon^{\text{trig}|\text{PID}\&\text{sel}\&\text{geom}}$ is the efficiency of the trigger selection. For the analysis described in Chapter 7 it is computed on MC, on events passing the offline selection. The procedure to determine the trigger efficiencies for the analysis described in Chapter 8 is instead detailed in Sec. 6.2.1.

6.2.1   Trigger efficiency

For the study of the $B_s^0 \rightarrow \eta'\eta'$ and $B^\pm \rightarrow \eta' K^\pm$ decays, the trigger efficiency is factorized in three independent terms:

$$\varepsilon^{\text{trig}|\text{sel}\&\text{geom}} = \varepsilon^{\text{L0}|\text{sel}\&\text{geom}} \times \varepsilon^{\text{Hlt1}|\text{L0}\&\text{sel}\&\text{geom}} \times \varepsilon^{\text{Hlt2}|\text{Hlt1}\&\text{L0}\&\text{sel}\&\text{geom}} \tag{6.5}$$

where $\varepsilon^{\text{L0}|\text{sel}\&\text{geom}}$ is the efficiency of the L0 trigger selection and $\varepsilon^{\text{Hlt1}|\text{L0}\&\text{sel}\&\text{geom}}$, $\varepsilon^{\text{Hlt2}|\text{Hlt1}\&\text{L0}\&\text{sel}\&\text{geom}}$ are the efficiencies of the Hlt1 and Hlt2 trigger selections respectively.

Given the number of MC events selected by the stripping and the offline selection (including the PID selection), N_{sel}, we can define:

- $N_{\text{L0\_TIS}}$ as the subsample of N_{sel} that passes also the L0_TIS trigger lines;

- N_{L0} as the subsample of N_{sel} that passes also the L0 trigger lines;

- N_{Hlt1} as the subsample of N_{sel} that passes the L0 and Hlt1 trigger lines;

- N_{Hlt2} as the subsample of N_{sel} that passes the L0, Hlt1 and Hlt2 trigger lines;

and we define

$$\varepsilon^{\text{L0\_TIS}} = \frac{N_{L0\_TIS}}{N_{sel}}, \qquad \varepsilon^{\text{Hlt1}|\text{L0}\&\text{sel}\&\text{geom}} = \frac{N_{Hlt1}}{N_{L0}}, \qquad \varepsilon^{\text{Hlt2}|\text{Hlt1}\&\text{L0}\&\text{sel}\&\text{geom}} = \frac{N_{Hlt2}}{N_{Hlt1}}. \tag{6.6}$$

The L0 trigger efficiency has been computed from the efficiency of the L0_TIS and of the L0_TOS lines as:

$$\varepsilon^{\text{L0}|\text{sel}\&\text{geom}} = \varepsilon^{\text{L0\_TOS}} + \varepsilon^{\text{L0\_TIS}} - \varepsilon^{\text{L0\_TOS}} \times \varepsilon^{\text{L0\_TIS}} \tag{6.7}$$

where $\varepsilon^{\text{L0\_TOS}}$ is the efficiency of the L0Hadron_TOS line, which is calculated with dedicated efficiency tables from $D^0 \rightarrow K\pi$ calibration data [77]. The efficiency from the

tables, depending on the track type, the track p_T and the magnet polarisation, is used to reweight the Monte Carlo.

6.3 Maximum likelihood fit

The observables of interest in the analysis are extracted from simultaneous multi-dimensional unbinned extended maximum likelihood (ML) fit. The ML method provides an estimate of the parameters of a model describing the data, through the maximisation of the likelihood function. Considering a set of k variables, that in this specific case are the masses of the decaying particles of the decay chain, $\mathbf{m} = (m_1, ..., m_k)$, a set of N observations, and a vector of l model parameters, $\boldsymbol{\theta} = (\theta_1, ..., \theta_l)$, the likelihood function for each sample is written as:

$$\mathcal{L} = \exp(-\textstyle\sum_j N_j) \prod_{i=1}^{N} \left(\textstyle\sum_j N_j P_j^i(\mathbf{m}; \boldsymbol{\theta}) \right), \tag{6.8}$$

where N_j is the yield of fit component j, P_j^i is the probability of event i for component j, and the index i runs over the N events in the sample. Assuming that the mass variables are not correlated we have:

$$P_j^i(\mathbf{m}; \boldsymbol{\theta}) = P_j^1(m_1^i; \boldsymbol{\theta}) \times ... \times P_j^k(m_k^i; \boldsymbol{\theta}). \tag{6.9}$$

The maximum likelihood method provides the estimators, $\hat{\boldsymbol{\theta}}$ and $\hat{\mathbf{N}}$, as the values of $\boldsymbol{\theta}$ and $\mathbf{N}$ (where $\mathbf{N}$ indicates the vector of N_j yields) that maximise the likelihood:

$$\frac{\partial \mathcal{L}}{\partial \theta_i} = 0, \quad \frac{\partial \mathcal{L}}{\partial N_j} = 0. \tag{6.10}$$

6.4 Probability density function

Several probability density functions (PDFs) are employed to describe signal and background components in the selected data samples. Studies to determine the optimal PDF for each component are performed either on simulated MC samples or on real data. In this section, a list and a description of the PDFs used in the analyses detailed in Chapters 7 and 8 is given.

1. Double-sided Crystal Ball function. It consists of a Gaussian core with two power-law tails below and above a given threshold. The tails describe poorly reconstructed signal events and radiative corrections. This function is used to describe the mass distribution of long-lived particles, such as b-hadrons, for which the detector resolution dominates over the particle width. The analytical expression

of the double-sided Crystal Ball function with mass variable m is:

$$\mathrm{CB}(m; \mu, \sigma, \alpha_L, n_L, \alpha_R, n_R) = N_{\mathrm{CB}} \begin{cases} A_L \left(B_L - \frac{m-\mu}{\sigma} \right)^{-n_L} & \text{for } \frac{m-\mu}{\sigma} \leq -\alpha_L, \\ \exp\left(-\frac{(m-\mu)^2}{2\sigma^2} \right) & \text{for } -\alpha_L < \frac{m-\mu}{\sigma} < \alpha_R, \\ A_R \left(B_R + \frac{m-\mu}{\sigma} \right)^{-n_R} & \text{for } \frac{m-\mu}{\sigma} \geq \alpha_R, \end{cases}$$

(6.11)

with

$$A_i = \left(\frac{n_i}{\alpha_i} \right)^{n_i} \exp\left(-\frac{\alpha_i^2}{2} \right),$$

$$B_i = \frac{n_i}{\alpha_i} - \alpha_i.$$

(6.12)

The six parameters are the mass of the particle, μ, the mass resolution σ, and the tails parameters: $\alpha_L > 0$, $n_L > 0$ (low-mass tail) and $\alpha_R > 0$, $n_R > 0$ (high-mass tail). The normalization factor N_{CB} depends on σ and on the tail parameters.

2. Convolution of an ARGUS function f_{ARG} and a Gaussian resolution function G,

$$\mathrm{ARG}(m; m_0, p, c, \sigma) = \int_{-\infty}^{\infty} f_{\mathrm{ARG}}(m'; m_0, p, c) \, \mathrm{G}(m - m'; \sigma) \, dm',$$

$$f_{\mathrm{ARG}}(m; m_0, p, c) = N_{\mathrm{ARG}} \, m \left(1 - \left(\frac{m}{m_0} \right)^2 \right)^p \exp\left(c \left(1 - \left(\frac{m}{m_0} \right)^2 \right) \right),$$

$$\mathrm{G}(m - m'; \sigma) = \frac{1}{\sqrt{2\pi}\sigma} \exp\left(-\frac{1}{2} \left(\frac{m - m'}{\sigma} \right)^2 \right),$$

(6.13)

where N_{ARG} is a normalisation factor and m_0 defines the end-point of the distribution. It is used to describe partially-reconstructed background components.

3. Sum of a double-sided Crystal Ball function and a Gaussian function. Because of the correlation between momentum and resolution, a single PDF is not sufficient to describe properly the data if a large number of events is present. A solution is to use the sum of a double-sided Crystal Ball (CB) function and a Gaussian (G) function with a common mean value but with different widths,

$$f \times \mathrm{CB}(m; \mu, \sigma, \alpha_L, n_L, \alpha_R, n_R) + (1 - f) \times \mathrm{G}(m; \mu, \sigma_1)$$

(6.14)

where f is the fraction of events described by the CB.

4. Relativistic Breit-Wigner (BW) convoluted with a Gaussian resolution function (G) that takes in account the detector resolution. It is used to describe resonances, for which the decay width is not negligible compared to the detector resolution. In

the analyses described in the next chapters it is used to model the ϕ resonance.

$$(\text{BWG})(m_{KK}; m_\phi, \Gamma_\phi, \sigma_\phi) = \int_{-\infty}^{\infty} \text{BW}(m'_{KK}; m_\phi, \Gamma_\phi) \, \text{G}(m_{KK} - m'_{KK}; \sigma_\phi) \, dm'_{KK},$$

$$\text{BW}(m_{KK}; m_\phi, \Gamma_\phi) = N_{\text{BW}} \frac{m_{KK} \, m_\phi \, \Gamma(m_{KK}, m_\phi, \Gamma_\phi)}{(m_{KK}^2 - m_\phi^2)^2 + m_\phi^2 \, \Gamma(m_{KK}, m_\phi, \Gamma_\phi)^2},$$

$$\Gamma(m_{KK}, m_\phi, \Gamma_\phi) = \Gamma_\phi \left(\frac{q(m_{KK})}{q(m_\phi)} \right)^{2L+1} \left(\frac{m_\phi}{m_{KK}} \right),$$

$$q(m_{KK}) = \frac{\sqrt{(m_{KK}^2 - (m_{K^+} + m_{K^-})^2)(m_{KK}^2 - (m_{K^+} - m_{K^-})^2)}}{2m_{KK}}$$

$$= \sqrt{\frac{m_{KK}^2}{4} - m_K^2}, \tag{6.15}$$

where the three parameters are the mass resolution σ_ϕ, the ϕ mass m_ϕ, and the ϕ width Γ_ϕ. The normalization factor N_{BW} depends on m_ϕ and Γ_ϕ. The function $q(m_{KK})$ is the momentum of each kaon in the ϕ rest frame, $L = 1$ is the angular momentum between the two kaons, and m_K is the kaon mass. Since the parameters Γ_ϕ and σ_ϕ are very correlated, Γ_ϕ is always fixed to the known width of the ϕ meson, $\Gamma_\phi = 4.26 \, \text{MeV}/c^2$ [11].

5. First-order Chebychev polynomial. It is a linear function used to describe combinatorial components,

$$\text{LIN}(m; a) = \frac{1}{2}(1 + ax), \tag{6.16}$$

where

$$x = 2\frac{m - m_{\text{min}}}{m_{\text{max}} - m_{\text{min}}} - 1, \tag{6.17}$$

and a is a slope parameter.

6. Second-order Chebychev polynomial. It is a quadratic function used for the descriptions of combinatorial components,

$$\text{QUADR}(m; a, b) = \frac{3}{2(3 - b)} \left(1 + ax + b(2x^2 - 1) \right), \tag{6.18}$$

where the parameter x is defined as in Eq. 6.17.

6.5 Toy pseudo-experiments

To validate the fit procedure and check its stability Monte Carlo pseudo-experiments are used. Samples of similar contents as the real data samples, called toy samples, are generated and fitted with the fit model chosen to extract the parameters of interest. Two types of toy samples are used:

1. The "pure toy samples" consist of data generated from PDFs for all components. They allow tests of the fit stability and checks of the absence of fit bias.

2. The "embedded toy samples" contain signal and/or background events taken from the full Monte Carlo simulation and all other background events generated from the PDFs. These samples allow the evaluation of effects from the possible correlation between the fit variables.

Several toys samples are generated for each study. The distribution of the fitted parameters is expected to be Gaussian and centred on the generated value. In particular the pull, defined as

$$\text{Pull} = \frac{\theta_{\text{fit}} - \theta_{\text{gen}}}{E_{\theta_{\text{fit}}}} \tag{6.19}$$

is expected to have a distribution described by a Gaussian function centred in 0 and with $\sigma = 1$. In the equation, θ_{gen} is the generated value of the parameter of interest, while θ_{fit} and $E_{\theta_{\text{fit}}}$ are the value of the fitted parameter and its estimated error, respectively.

6.6   Search for new *B* decay modes

6.6.1   Expected signal yields

As mentioned in Sec. 6.3, the parameter of interest, either the yield of the decay mode under study or the ratio between the signal yield and the reference channel yield, is extracted from the maximum likelihood fit to the selected data. The number of signal events is related to the branching fraction according to:

$$N(B_q \to X) = \mathcal{B}(B_q \to X) \times \mathcal{L} \times \sigma(pp \to b\bar{b}) \times 2 \times f_q \times \varepsilon(B_q \to X), \tag{6.20}$$

where $\mathcal{L}$, $\sigma(pp \to b\bar{b})$ and f_q are the integrated luminosity, the $b\bar{b}$ production cross-section in pp collisions, and the fragmentation fraction, respectively, and ε is the total selection efficiency. The subscript q stands for the quarks u or s.

Equation 6.20 is used to estimate the expected number of events for the channel of interest, given a prediction of the branching fraction. The values of the parameters used in Eq. 6.20, as well as the estimated number of expected events for the $B^{\pm} \to \phi\pi^{\pm}$ and $B_s^0 \to \eta'\eta'$ decay modes, are summarised in Table 6.1.

6.6.2   Branching fraction measurement or limit extraction

In this thesis, the branching fractions of the channels of interest are measured with respect to well known control channels. This has two main advantages:

- many systematic effects entering in the selection efficiency cancel out if the selections are similar for the two channels;

Table 6.1 *Parameters used in the estimation of the signal yields in the 2011 ($\sqrt{s} = 7$ TeV) and the 2012 ($\sqrt{s} = 8$ TeV) data samples, expected in the LHCb experiment. The $B^\pm \to \phi\pi^\pm$ yield is estimated for 1 fb^{-1} of data, while the $B_s^0 \to \eta'\eta'$ yield is estimated taking in account the full 2011 and 2012 statistics (3 fb^{-1}). Efficiencies and possible corrections estimated from the control channels can be found in Chapters 7 and 8.*

	$\sqrt{s}=7$ TeV	$\sqrt{s}=8$ TeV
$\mathcal{L}$	1.017 ± 0.036 fb^{-1}	2.057 ± 0.072 fb^{-1}
$\sigma(pp \to b\bar{b})$	284 ± 53 μb [78]	298 ± 36 μb [79]
f_u	$(40.1 \pm 0.8)\%$ [11]	
f_s	$(10.5 \pm 0.6)\%$ [11]	
$\mathcal{B}(B_s^0 \to \eta'\eta')$	$(14$ to $50) \times 10^{-6}$ [38]	
$\mathcal{B}(\eta' \to \pi^+\pi^-\gamma)$	0.291 ± 0.005 [11]	
$\mathcal{B}(B^\pm \to \phi\pi^\pm)$	$(5$ to $60) \times 10^{-9}$ [31,34,35]	
$\mathcal{B}(\phi \to K^+K^-)$	0.489 ± 0.005 [11]	
$N(B_s^0 \to \eta'\eta')$	4 to 26	10 to 50
$N(B^\pm \to \phi\pi^\pm)$	2 to 25	

- additional sources of uncertainties, due to $\mathcal{L}$ and $\sigma(pp \to b\bar{b})$ in Eq. 6.20, do not need to be taken in account.

The branching fraction of the signal mode is obtained from:

$$\mathcal{B}(B_q \to X) = \mathcal{B}(B_{q'} \to Y) \times \frac{N(B_q \to X)}{N(B_{q'} \to Y)} \times \frac{\varepsilon(B_{q'} \to Y)}{\varepsilon(B_q \to X)} \times \frac{f_{q'}}{f_q} \qquad (6.21)$$

where $B_{q'} \to Y$ is the reference channel.

The statistical significance s_{stat} of the signal channel is computed as $s_{stat} = \sqrt{2(\ln \mathcal{L}_{max} - \ln \mathcal{L}_0)}$ where $\mathcal{L}_{max}$ is the likelihood value resulting from the fit when all the parameters are free, and $\mathcal{L}_0$ is the likelihood value obtained from the fit when the number of signal events is fixed to 0. If the systematic uncertainty, σ_{syst}, is significantly lower than the statistical uncertainty, σ_{stat}, the significance s including the systematic uncertainty can be computed as:

$$s = \frac{s_{stat}}{\sqrt{1 + (\sigma_{syst}/\sigma_{stat})^2}}. \qquad (6.22)$$

In case of a measured yield with significance smaller than $3\,\sigma$, an upper limit is computed following the Bayesian approach and assuming a flat prior in the region with positive yield. The profile likelihood is performed by maximising the likelihood for fixed values of the signal yield, while all other parameters are free.

The limit at 90% (95%) confidence level is defined as the value of the yield, N_U for which

$$\frac{\int_0^{N_U} \mathcal{L}(N) dN}{\int_0^\infty \mathcal{L}(N) dN} = 90\% \ (95\%) \,. \tag{6.23}$$

The same formula can be applied to the yield ratio between the signal and reference channel.

To correctly compute the limit on the branching fraction the effect of the systematic uncertainty on the likelihood curve has to be taken in account. We have to distinguish between additive systematic uncertainties, due to the systematic uncertainties on the signal yield, and multiplicative systematic uncertainties, due to the uncertainties on multiplicative correction factors such as the efficiency and the other parameters of Eq. 6.21.

Assuming Gaussian errors, the likelihood can be related to the χ^2 distribution,

$$\chi^2(N) = -2\ln \mathcal{L}(N) = \frac{(N - N_0)^2}{\sigma^2(N)} \,, \tag{6.24}$$

where N_0 is the global minimum for the fit variable N. The total uncertainty including statistical and Gaussian additive systematic errors becomes:

$$\sigma_{\text{add}}^2(N) = \sigma_{\text{stat}}^2(N) + \sigma_{\text{syst}}^2(N) \,, \tag{6.25}$$

and the resulting χ^2 distribution can be expressed as:

$$\chi_{\text{add}}^2(N) = \frac{\chi_{\text{stat}}^2(N)}{1 + \chi_{\text{stat}}^2(N) \frac{\sigma_{\text{syst}}^2}{(N - N_0)^2}} \,. \tag{6.26}$$

If we express the branching fraction as $\mathcal{B} = N \alpha$, where α contains all the multiplicative terms of Eq. 6.21, the χ^2 distribution of the branching fraction, including also the multiplicative systematic uncertainties σ_α is:

$$\chi^2(\mathcal{B}) = \chi_{\text{add}}^2 \left(\frac{\mathcal{B}}{\alpha}\right) \times \frac{1}{1 + \chi_{\text{add}}^2 \left(\frac{\mathcal{B}}{\alpha}\right) \frac{N_0^2 \sigma_\alpha^2}{(\mathcal{B} - \mathcal{B}_0)^2}} \,. \tag{6.27}$$

6.7 $\mathcal{A}^{CP}$ measurement

In $B^\pm$ decays a measurement of the direct CP asymmetry is provided by the charge asymmetry $\mathcal{A}^{CP}$. Experimentally, the raw asymmetry

$$\mathcal{A}_{\text{raw}}^{CP} = \frac{N^- - N^+}{N^- + N^+} \tag{6.28}$$

is measured in the fit, where N^+ and N^- are the number of positively and negatively charged B candidates. $\mathcal{A}^{CP}_{\text{raw}}$ is related to the physics asymmetry $\mathcal{A}^{CP}$ through the relation

$$\mathcal{A}^{CP}_{\text{raw}} = \mathcal{A}^{CP} + \mathcal{A}_{\text{D}} + \mathcal{A}_{\text{P}}, \tag{6.29}$$

which is valid for small asymmetries, and where, in the specific case of CP asymmetry in $B^\pm \to \phi K^\pm$ and $B^\pm \to \eta' K^\pm$ decays, $\mathcal{A}_{\text{D}}$ is the detection charge asymmetry for the bachelor $K^\pm$ and $\mathcal{A}_{\text{P}}$ is the production asymmetry of $B^\pm$ mesons.

6.7.1 Production and detection asymmetry

Because of the pp nature of the collisions at the LHC, the net number of u quarks exceeds the number of $\bar{u}$ quarks, making the B^+ production more probable than the B^- production. The asymmetry $\mathcal{A}_{\text{P}}$ is therefore expected to be non-zero. A non-zero $\mathcal{A}_{\text{D}}$ is instead due to the different probability of detecting and identifying a positively or a negatively charged kaon. Since the detector is made of matter a K^- meson is more likely to interact strongly with the detector than a K^+ meson. The production and detection asymmetries are determined from a control channel with well known CP asymmetry, $B^\pm \to J/\psi K^\pm$, $J/\psi \to \mu^+ \mu^-$:

$$\mathcal{A}_{\text{P}} + \mathcal{A}_{\text{D}} = \mathcal{A}^{CP}_{\text{raw}}(B^\pm \to J/\psi K^\pm) - \mathcal{A}^{CP}(B^\pm \to J/\psi K^\pm) \tag{6.30}$$

with $\mathcal{A}^{CP}(B^\pm \to J/\psi K^\pm) = 0.003 \pm 0.006$. This value takes into account the recent $B^\pm \to J/\psi K^\pm$ charge asymmetry measurement by the D0 collaboration [80] not yet included in the average of the PDG [11]. The previous measurement [81] is replaced with the new one [80] and the uncertainty is scaled by a factor 1.8 according to the PDG averaging rules.

Combining Eqs. 6.29 and 6.30, and assuming identical production and detection asymmetries for the signal and the reference channel we obtain:

$$\begin{aligned}
\Delta\mathcal{A}^{CP} &= \mathcal{A}^{CP} - \mathcal{A}^{CP}(B^\pm \to J/\psi K^\pm) \\
&= \mathcal{A}^{CP}_{\text{raw}} - \mathcal{A}^{CP}_{\text{raw}}(B^\pm \to J/\psi K^\pm),
\end{aligned} \tag{6.31}$$

where $\mathcal{A}^{CP}$ and $\mathcal{A}^{CP}_{\text{raw}}$ are the physics and the raw asymmetry of the signal channel.

The measurement of CP asymmetry is performed separately for two different categories of events. The first contains events selected at the Level 0 on the signal hadrons, by the so-called L0Hadron TOS trigger line, while the other contains events triggered on the rest of the event, but not on the signal, by the so-called L0 TIS (and not-TOS) trigger lines. This is needed because of the different detector response when different trigger criteria are applied. Therefore, if the fraction of events in the two categories is not the same for the signal and the reference channels, additional charge asymmetries due to the trigger would not completely cancel. Moreover, a systematic uncertainty due to the different number of hadrons in the signal and reference channel has to be applied to the fraction of event that are selected by the L0Hadron TOS trigger line. The difference

between the physics asymmetries of the signal and reference channels are computed separately for TIS and TOS and then combined as:

$$\Delta\mathcal{A}^{CP} = f\Delta A_{\mathrm{TOS}}^{CP} + (1-f)\Delta A_{\mathrm{TIS}}^{CP},$$

(6.32)

where f is the fraction of events selected by the L0Hadron TOS trigger line.

<div style="text-align: right; font-size: 3em;">7</div>

Search for $B^{\pm} \to \phi\pi^{\pm}$ decays and measurement of the charge asymmetry in $B^{\pm} \to \phi K^{\pm}$ decays

The objectives of this analysis are to measure the branching fraction of the $B^{\pm} \to \phi\pi^{\pm}$ decay and to extract the $B^{\pm} \to \phi K^{\pm}$ *CP* asymmetry.

The motivations as well as the theoretical principles underlying these studies are analysed in Chapter 2.

To extract the $B^{\pm} \to \phi\pi^{\pm}$ and the $B^{\pm} \to \phi K^{\pm}$ yields a two-dimensional maximum likelihood fit to the unbinned $B^{\pm}$ and ϕ mass distributions is performed. Two different samples are fitted simultaneously: the first one is used to extract the $B^{\pm} \to \phi\pi^{\pm}$ yield while the second is optimised for the measurement of the $B^{\pm} \to \phi K^{\pm}$ reference yield.

In order to suppress systematic effects and to improve the significance, the $B^{\pm} \to \phi\pi^{\pm}$ branching fraction is measured with respect to the $B^{\pm} \to \phi K^{\pm}$ mode, adopting the same event selection and data description when possible. In the measurement of the $B^{\pm} \to \phi K^{\pm}$ *CP* asymmetry, the well known value of $\mathcal{A}^{CP}(B^{\pm} \to J/\psi K^{\pm})$ [11, 80] is used to correct the raw value for the production and detection asymmetry effects.

7.1 Data samples and event selection

7.1.1 Real data

The analysis is performed using the data collected by LHCb in 2011 at $\sqrt{s} = 7$ TeV, corresponding to an integrated luminosity of approximately $1\,\text{fb}^{-1}$.

Data are processed using the `Reco12` version of the reconstruction configuration with BRUNEL v41r1 and are stripped with the `Stripping17b` configuration of the stripping selection using DAVINCI v30r0p1.

7.1.2 Monte Carlo simulation data

The Monte Carlo simulation is handled by the GAUSS software [64]. In this analysis MC11 Monte-Carlo simulation data based on GAUSS v41r2 are used in order to study signals and backgrounds. The fully-simulated MC samples consist of:

- 416×10^3 $B^\pm \to \phi\pi^\pm$ signal events (LHCb event type 12103071).

- 244×10^3 $B^\pm \to \phi K^\pm$ signal events (LHCb event type 12103061).

- 398×10^3 $B^0 \to \phi K^{*0}$ signal events (LHCb event type 11104020).

The `Stripping17b` selection is run on these events in a private production of the simulation chain.

7.1.3 Event selection

As already mentioned in Chapter 6, candidates are filtered offline by a dedicated stripping line, `BetaSQ2B3piSelectionLine`. The stripping selection criteria are listed in Table 7.1. The stripped events are reconstructed both as $B^\pm \to \phi\pi^\pm$ and $B^\pm \to \phi K^\pm$, with the ϕ meson reconstructed in the K^+K^- final state. Specific trigger conditions are required, as shown in Table 7.2, and a further offline selection is applied.

The selections of the $B^\pm \to \phi\pi^\pm$ and $B^\pm \to \phi K^\pm$ candidates are identical, except for the requirement on the bachelor hadron PID variable, $\mathrm{DLL}_{K\pi}$. The other requirements are chosen to minimize the relative statistical uncertainty on the $B^\pm \to \phi K^\pm$ signal yield. A full list of the cuts applied in the offline selection is given in Table 7.3.

7.1.4 Definition of the π-like and K-like samples

The variable chosen to distinguish between $B^\pm \to \phi\pi^\pm$ and $B^\pm \to \phi K^\pm$ candidates is the $\mathrm{DLL}_{K\pi}$ of the primary kaon or pion from the $B^\pm$ decay. The selected candidates with $\mathrm{DLL}_{K\pi} < -1$ are reconstructed under the $B^\pm \to \phi\pi^\pm$ mass hypothesis, and form a sample called "π-like sample". All the other candidates (with $\mathrm{DLL}_{K\pi} \geq -1$) form the so-called "$K$-like sample": they are considered as $B^\pm \to \phi K^\pm$ candidates, and their invariant mass is reconstructed under the $B^\pm \to \phi K^\pm$ mass hypothesis. The value of $\mathrm{DLL}_{K\pi} = -1$ is chosen in order to reduce the number of true $B^\pm \to \phi K^\pm$ decays in the π-like sample while keeping a good efficiency for the true $B^\pm \to \phi\pi^\pm$ decays in the same sample.

After all selection cuts are applied, the fraction of events with more than one candidate in a given sample is very small: 0.18% in the π-like sample and 0.22% in the K-like sample. In each sample, these multiple candidates are removed by keeping from each event only the candidate with the smallest $B^\pm$ vertex χ^2.

The final data samples after full selection contain 2169 $B^\pm \to \phi\pi^\pm$ and 6251 $B^\pm \to \phi K^\pm$ candidates in the mass regions $5000 < m_B < 5500\,\text{MeV}/c^2$ and $1000 < m_\phi < 1050\,\text{MeV}/c^2$.

Table 7.1 *Pre-selection cuts applied in the* `BetaSQ2B3piSelectionLine` *stripping line for the generic $B^\pm \to \rho^0\pi^\pm$ reconstruction. The variable m_{corr} is defined as $m_{\text{corr}} = \sqrt{m^2 + |p_{\text{T miss}}|^2} + |p_{\text{T miss}}|$ [82], where m is the reconstructed B mass, and $p_{\text{T miss}}$ is the missing transverse momentum relative to the direction of flight of the B candidate as determined from its production and decay vertices.*

Variable		Requirement
Pions		
transverse momentum	p_{T}	$> 0.25\,\text{GeV}/c$
primary vertex impact parameter	χ^2_{IP}	> 25
Bachelor $\pi^\pm$		
transverse momentum	p_{T}	$> 1\,\text{GeV}/c$
momentum	p	$> 1\,\text{GeV}/c$
Resonance (ρ^0)		
transverse momentum	p_{T}	$> 2\,\text{GeV}/c$
momentum	p	$> 10\,\text{GeV}/c$
mass	$m_{\pi\pi}$	$< 1\,\text{GeV}/c^2$
vertex quality	χ^2/ndf	< 9
B meson		
mass	$m_{\pi\pi\pi}$	$4.4 < m_{\pi\pi\pi} < 5.7\,\text{GeV}/c^2$
corrected mass	m_{corr}	$< 6\,\text{GeV}/c^2$
vertex quality	χ^2/ndf	< 9

Table 7.2 *Trigger lines required at the different trigger levels. Each line contains specific requirements that the event has to satisfy in order to be selected. TOS events are selected on signal, while TIS events are selected on the rest of the event.*

L0	HLT1	HLT2
Hadron (TOS)	TrackAllL0 (TOS)	Topo2BodyBBBDT (TOS)
Global (TIS)		Topo3BodyBBBDT (TOS)
		IncPhi (TOS)
		IncPhiSidebands (TOS)

7.1.5 Selection efficiencies

The selection efficiencies of the $B^\pm \to \phi\pi^\pm$ and $B^\pm \to \phi K^\pm$ decay modes are computed as explained in Sec. 6.2. It has to be noticed that $\varepsilon^{\text{PID|sel\&geom}} = 1$ for $B^\pm \to \phi K^\pm$ because its yield will be calculated as the sum of the yields measured in the π-like and K-like

Table 7.3 *Offline requirements common to the $B^\pm \to \phi K^\pm$ and $B^\pm \to \phi\pi^\pm$ selections.*

Variable		Requirement
Basic particles		
track fit quality	χ^2/ndf	< 4
PV impact parameter significance	χ^2_{IP}	> 25
transverse momentum	p_{T}	$> 0.25\,\mathrm{GeV}/c$
Bachelor kaon or pion		
momentum	p	$> 10\,\mathrm{GeV}/c$
transverse momentum	p_{T}	$> 2.5\,\mathrm{GeV}/c$
Kaons from ϕ		
PID	$\mathrm{DLL}_{K\pi}$	> 2
transverse momentum	p_{T}	$> 0.25\,\mathrm{GeV}/c$
ϕ candidate		
mass	m_{KK}	$1.00 < m_{KK} < 1.05\,\mathrm{GeV}/c^2$
momentum	p	$> 10\,\mathrm{GeV}/c$
transverse momentum	p_{T}	$> 2\,\mathrm{GeV}/c$
B meson candidate		
mass	m_{KKh}	$5.0 < m_{KKh} < 5.5\,\mathrm{GeV}/c^2$
transverse momentum	p_{T}	$> 2\,\mathrm{GeV}/c$
vertex quality	χ^2/ndf	< 9
direction angle	DIRA	> 0.9999

samples, and therefore none of the $\mathrm{DLL}_{K\pi}$ values are excluded. The efficiencies are summarised in Table 7.4 and the efficiency ratio is found to be

$$\frac{\varepsilon(B^\pm \to \phi\pi^\pm)}{\varepsilon(B^\pm \to \phi K^\pm)} = 0.762 \pm 0.031\,, \tag{7.1}$$

where the quoted error arises from the statistical uncertainty from the Monte Carlo samples.

Table 7.4 *Efficiencies for the $B^\pm \to \phi\pi^\pm$ and $B^\pm \to \phi K^\pm$ signals.*

	$B^\pm \to \phi\pi^\pm$	$B^\pm \to \phi K^\pm$
$\varepsilon^{\mathrm{geom}}$	$(18.0\pm0.4)\%$	$(18.3\pm0.5)\%$
$\varepsilon^{\mathrm{sel|geom}}$	$(6.22\pm0.04)\%$	$(6.33\pm0.05)\%$
$\varepsilon^{\mathrm{PID|sel\&geom}}$	$(84.6\pm1.1)\%$	
$\varepsilon^{\mathrm{trig|PID\&sel\&geom}}$	$(45.3\pm0.3)\%$	$(48.6\pm0.4)\%$
TOTAL	$(0.43 \pm 0.02)\%$	$(0.56 \pm 0.02)\%$

7.2 Fit model description

The $B^{\pm} \to \phi\pi^{\pm}$ and $B^{\pm} \to \phi K^{\pm}$ yields are determined from a simultaneous extended maximum likelihood fit of the π-like and K-like samples. An overview of the maximum likelihood method is given in Chapter 6. This section presents a detailed description of the full fit model, as well as its underlying assumptions. In the next section, Sec. 7.3, the studies and cross-checks performed to elaborate and validate this model, based on fully-simulated MC samples, data samples, and fast MC (toy) samples are presented.

The development of the fit model has been performed in an iterative process on simulated and real data. The model presented in this section therefore depends on the studies presented in Sec. 7.3.

7.2.1 Simultaneous $B^{\pm} \to \phi\pi^{\pm}$ and $B^{\pm} \to \phi K^{\pm}$ fit

The two fitted variables are the $K^+K^-\pi^{\pm}$ and K^+K^- invariant masses (denoted $m_{\phi\pi}$ and m_{KK}, respectively) for the π-like sample, and the $K^+K^-K^{\pm}$ and K^+K^- invariant masses (denoted $m_{\phi K}$ and m_{KK}, respectively) for the K-like sample. The generic notation m for both $m_{\phi\pi}$ and $m_{\phi K}$ will be adopted in the following description.

The $m_{\phi\pi}$ and $m_{\phi K}$ distributions are described by three contributions: a peaking component centered on the $B^{\pm}$ mass, a broad low-mass distribution with end-point near $5150 \,\text{MeV}/c^2$ due to partially-reconstructed B decays, and a linear component from random combinations. The m_{KK} distribution is described by two contributions: a peaking component centred on the ϕ mass, and a linear component from random combinations of two kaons. The three $m_{\phi\pi}$ or $m_{\phi K}$ contributions and the two m_{KK} contributions lead to six possible combinations for each sample. In addition, contributions from mis-identified $B^{\pm} \to \phi K^{\pm}$ and $B^{\pm} \to K^+K^-K^{\pm}$ in the π-like sample have been considered. The list of these 14 components included in the fit is given in Table 7.5, together with the type of probability density function (PDF) used for their description.

The following assumptions are made on the fit components:

(a) The two fitted variables m and m_{KK} are treated as independent, *i.e.* the joint probability density function (PDF) for each component is the product of two one-dimensional PDFs, one for m and one for m_{KK}. This assumption is checked on MC signal samples, where the correlation between these two variables is found to be less than 3%.

(b) The $B^{\pm} \to \phi\pi^{\pm}$ and $B^{\pm} \to \phi K^{\pm}$ signals, as well as the true non-resonant $B^{\pm} \to K^+K^-\pi^{\pm}$ and $B^{\pm} \to K^+K^-K^{\pm}$ components, are each described in the variable m with a double-sided Crystal Ball function, $\text{CB}(m; m_B, \sigma, \alpha_L, n_L, \alpha_R, n_R)$ (Eq. 6.11). The six parameters are common to all components. The tails parameters are fixed to the values obtained on signal MC samples, $\alpha_L = 1.97$, $\alpha_R = 1.97$, $n_L = 1.76$ and $n_R = 3.8$ (see Sec. 7.3.1).

(c) The misidentified background components of the π-like sample ($B^{\pm} \to \phi K^{\pm}$

Table 7.5   *Description of the components of the simultaneous two-dimensional fit of the π-like and K-like samples. The functions CB, CBM, ARG, LIN and BWG are given in Eqs. (6.11), (7.2), (6.13), (6.16) and (6.15), respectively.*

Component of the π-like sample	PDF($m_{\phi\pi}$)	PDF(m_{KK})
$B^\pm \to \phi\pi^\pm$ signal	CB	BWG
Non-resonant $B^\pm \to K^+K^-\pi^\pm$ background	CB	LIN
Misidentified $B^\pm \to \phi K^\pm$ background	CBM	BWG
Misidentified non-resonant $B^\pm \to K^+K^-K^\pm$ background	CBM	LIN
Partially reconstructed $b \to \phi X$ background	ARG	BWG
Partially reconstructed $b \to$ non-ϕX background	ARG	LIN
Combinatorial background with true ϕ meson	LIN	BWG
Combinatorial background without true ϕ meson	LIN	LIN

Component of the K-like sample	PDF($m_{\phi\pi}$)	PDF(m_{KK})
$B^\pm \to \phi K^\pm$ signal	CB	BWG
Non-resonant $B^\pm \to K^+K^-K^\pm$ background	CB	LIN
Partially reconstructed $b \to \phi X$ background	ARG	BWG
Partially reconstructed $b \to$ non-ϕX background	ARG	LIN
Combinatorial background with true ϕ meson	LIN	BWG
Combinatorial background without true ϕ meson	LIN	LIN

misidentified as $B^\pm \to \phi\pi^\pm$ and $B^\pm \to K^+K^-K^\pm$ misidentified as $B^\pm \to K^+K^-\pi^\pm$) are each described in m with an event-by-event Crystal Ball function, given by

$$\text{CBM}(m; \delta m, m_B, \sigma_B, \rho, \alpha_L, n_L, \alpha_R, n_R) = \text{CB}(m; m_B - \delta m, \rho\sigma_B, \alpha_L, n_L, \alpha_R, n_R),$$
(7.2)

where the variable

$$\delta m = m_{\phi K} - m_{\phi\pi} \tag{7.3}$$

is a conditional variable that takes a different value for each candidate. The fitting parameters m_B, σ_B, α_L, n_L, α_R and n_R are common and shared with the signal and non-resonant components. The parameter ρ is common to the two misidentified components and fixed to the value $\rho = 1.26$, obtained as the ratio of the $B^\pm \to \phi K^\pm$ mass resolutions in the π-like and K-like regions (see Sec. 7.3.2).

(d) Possible misidentified background components of the K-like sample are ignored, as the number of $B^\pm \to \phi\pi^\pm$ decays misidentified as $B^\pm \to \phi K^\pm$ is negligible in comparison to the other components.

(e) The partially-reconstructed background components, $B^\pm \to (KK)(K\pi^{\pm,0})$ in the K-like sample and $B^\pm \to (KK)(\pi\pi^{\pm,0})$ in the π-like sample with a non-reconstructed pion, are described in m with an ARGUS function convoluted with a Gaussian resolution function (Eq. 6.13). The shape is determined on data, performing a fit of the K-like sample alone, as explained in Sec. 7.3.2. Two partially-reconstructed

components are considered in each sample, with or without a true ϕ meson. The resolution parameter σ_B is common and shared with the signal, non-resonant and misidentified components. The end-point parameter is common to all partially-reconstructed background components and fixed to $m_0 = 5150\,\text{MeV}/c^2$ (as justified in Sec. 7.3.2). The power parameter p_h is fixed to $p_K = 0.5$ for the K-like components and $p_\pi = 1.0$ for the π-like components (see Sec. 7.3.2). The parameter c_h is common to the components within the same sample, but different for the π-like (c_π) and K-like (c_K) samples.

(f) The non-b combinatorial background components are each described in m with a linear function (Eq. 6.16).

(g) The components involving a true ϕ meson are each described in m_{KK} with a relativistic Breit-Wigner function convoluted with a Gaussian function (Eq. 6.15).

(h) The background components without a true ϕ meson are each described in m_{KK} with a linear function (Eq. 6.16). The non-resonant $B^\pm \to K^+K^-\pi^\pm$ and $B^\pm \to K^+K^-K^\pm$ components share the same slope parameter because of the low sensitivity, while all other components have their own slope parameter.

(i) The joint PDF describing the π-like sample depends on δm, which is an event-by-event variable. It is therefore a conditional PDF. To avoid fit biases (dubbed "Punzi effects" [83]) expected in case the various components have different δm distributions, the PDF for $m_{\phi\pi}$ of each component should in principle be multiplied by the PDF of δm for that component. Instead, it has been decided in this analysis to divide the π-like sample in four subsamples defined by $\delta m < 30\,\text{MeV}/c^2$, $30 < \delta m < 36\,\text{MeV}/c^2$, $36 < \delta m < 45\,\text{MeV}/c^2$, and $\delta m > 45\,\text{MeV}/c^2$. The same PDFs are used to describe the four subsamples, with common fitting parameters except for the yields of the various components, which can vary independently in the four sub-samples.

(j) In each π-like subsample, the ratio of the yield of the misidentified non-resonant $B^\pm \to K^+K^-K^\pm$ background to the yield of the misidentified $B^\pm \to \phi K^\pm$ background is constrained to the ratio of the corresponding correctly-identified components in the K-like sample.

The fit counts 52 free parameters in total:

- the $B^\pm$ and ϕ masses, m_B and m_ϕ;

- the $B^\pm$ and ϕ mass resolutions, σ_B and σ_ϕ;

- two ARGUS background parameters, c_π for the π-like sample and c_K for the K-like sample;

- nine linear background slopes, four in m and five in m_{KK};

- 37 yields, corresponding to eight components in each of the four π-like sub-samples (the total yield of the misidentified non-resonant background being constrained to be a function of other yields) and the six components of the K-like sample.

7.2.2 *CP* asymmetry fit

In order to measure the *CP* asymmetry in the $B^\pm \to \phi K^\pm$ decay, a fit of the K-like sample is performed. As mentioned in Chapter 6, the K-like sample has been split in two subsamples, one with events selected by the L0Hadron TOS trigger line and the other containing L0Global TIS (and not-TOS) events. A simultaneous two-dimensional fit of the $B^- \to \phi K^-$ and $B^+ \to \phi K^+$ candidates in both trigger subsamples is performed. The fit model is identical to the model for the K-like sample in the full fit described above. A list of the fit components can be found in the second part of Table 7.5. It is assumed that no difference is present in the models used for the four subsamples, therefore all the PDF shape parameters are shared. In total, there are 34 free parameters:

- the $B^\pm$ and ϕ masses, m_B and m_ϕ;
- the $B^\pm$ and ϕ mass resolutions, σ_B and σ_ϕ;
- one ARGUS background parameter, c_K for the K-like sample;
- five linear background slopes, two in m and three in m_{KK};
- six yields, corresponding to the six components of the K-like sample for the L0Hadron TOS subsample and six yields for the L0Global TIS subsample;
- six *CP* asymmetries, one for each of the six components of the K-like sample for the L0Hadron TOS subsample and six *CP* asymmetries for the L0Global TIS subsample.

The yield N_j and raw *CP* asymmetry $\mathcal{A}^{CP}_{\text{raw},j}$ for component j are the fitted parameters, and are related to the yields of the positive (N_j^+) and negative (N_j^-) charge yields via

$$N_j = N_j^- + N_j^+ \tag{7.4}$$

and

$$\mathcal{A}^{CP}_{\text{raw},j} = \frac{N_j^- - N_j^+}{N_j^- + N_j^+}. \tag{7.5}$$

7.3 Validation of the fit model

The fit model has been studied and validated on MC samples, real data and toy MC samples. In the next sections the main studies performed and their conclusions are documented.

7.3.1 Fully-simulated MC studies

The shapes of the signals and misidentified components have been studied on the large fully-simulated $B^\pm \to \phi\pi^\pm$ and $B^\pm \to \phi K^\pm$ samples listed in Sec. 7.1.2.

$B^\pm \to \phi\pi^\pm$ and $B^\pm \to \phi K^\pm$ signal

The signal model is validated by fitting the two-dimensional mass distribution of $B^\pm \to \phi\pi^\pm$ ($B^\pm \to \phi K^\pm$) candidates reconstructed and selected as π-like (K-like) in a MC sample of $B^\pm \to \phi\pi^\pm$ ($B^\pm \to \phi K^\pm$) events. The fitting function is a linear combination of a joint PDF for the signal,

$$f_{\text{sig}}(m, m_{KK}; m_B, \sigma_B, \alpha, n, m_\phi, \Gamma_\phi, \sigma_\phi) = \text{CB}(m; m_B, \sigma_B, \alpha, n) \times \text{BWG}(m_{KK}; m_\phi, \Gamma_\phi, \sigma_\phi),$$
(7.6)

and a joint PDF $f_{\text{bck}}(m, m_{KK}) = C$, where C is a (normalisation) constant, to describe a small flat background component that may be present because the MC candidates are not matched to the truth. The results are shown in Figs. 7.1 and 7.2, and in Table 7.6.

Table 7.6 *Results of the fit to signal MC data.*

Parameter	signal $B^\pm \to \phi\pi^\pm$	signal $B^\pm \to \phi K^\pm$	mis-reconstructed $B^\pm \to \phi K^\pm$
m_B [MeV/c^2]	5279.78 ± 0.17	5280.11 ± 0.19	5280.07 ± 1.00
σ_B [MeV/c^2]	15.87 ± 0.18	15.95 ± 0.19	17.93 ± 0.84
α_L	1.95 ± 0.06	2.00 ± 0.08	1.97 fixed
n_L	1.65 ± 0.13	2.11 ± 0.23	1.76 fixed
α_R	1.88 ± 0.11	2.09 ± 1.23	1.97 fixed
n_R	5.8 ± 1.6	3.44 ± 0.74	3.8 fixed
m_ϕ [MeV/c^2]	1019.43 ± 0.03	1019.39 ± 0.04	1019.44 ± 0.15
σ_ϕ [MeV/c^2]	1.16 ± 0.06	1.07 ± 0.07	0.16 ± 5.29

With the exception of n_L and n_R, the fitted parameters in the two samples are compatible within statistical uncertainties. This holds in particular for the $B^\pm$ mass resolution, as expected because the kinematics of the two decays are similar and the PID requirements are very efficient (and hence do not bias significantly the momentum distribution of the primary pion or kaon). It is therefore assumed that the signal parameters for the two modes are common and the tails parameters are fixed to the central value of the weighted averages of the fitted MC values for $B^\pm \to \phi\pi^\pm$ and $B^\pm \to \phi K^\pm$: $\alpha_L = 1.97 \pm 0.04$, $n_L = 1.76 \pm 0.11$, $\alpha_R = 1.97 \pm 0.08$ and $n_R = 3.8 \pm 0.7$.

To evaluate the effect of the requirement $\text{DLL}_{K\pi} < -1$ on the resolution of the $B^\pm \to \phi K^\pm$ signal, the $K^+K^-K^\pm$ and K^+K^- mass distributions of π-like $B^\pm \to \phi K^\pm$ candidates selected in the MC sample of $B^\pm \to \phi K^\pm$ events are fitted. The results, shown in Fig. 7.3 and in Table 7.6, are fully compatible with the ones obtained for the K-like sample of
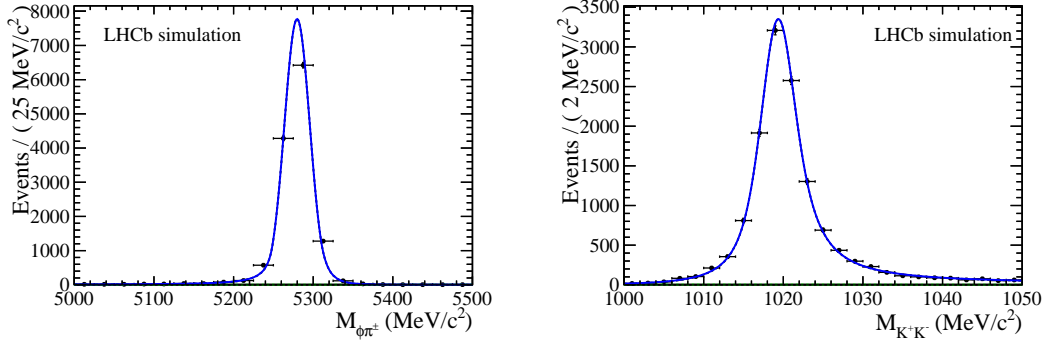
Figure 7.1 $K^+K^-\pi^{\pm}$ *(left) and K^+K^- (right) mass distributions of π-like $B^{\pm} \to \phi\pi^{\pm}$ candidates in $B^{\pm} \to \phi\pi^{\pm}$ MC events. The result of the two-dimensional fit described in the text is superimposed.*
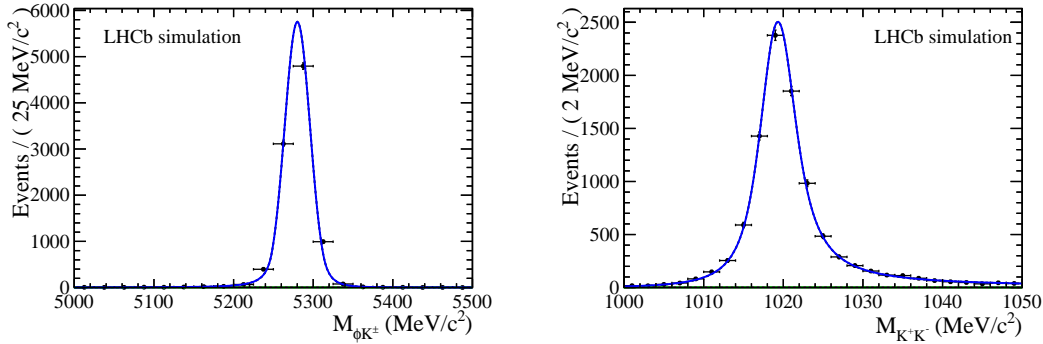
Figure 7.2 $K^+K^-K^{\pm}$ *(left) and K^+K^- (right) mass distributions of K-like $B^{\pm} \to \phi K^{\pm}$ candidates in $B^{\pm} \to \phi K^{\pm}$ MC events. The result of the two-dimensional fit described in the text is superimposed.*
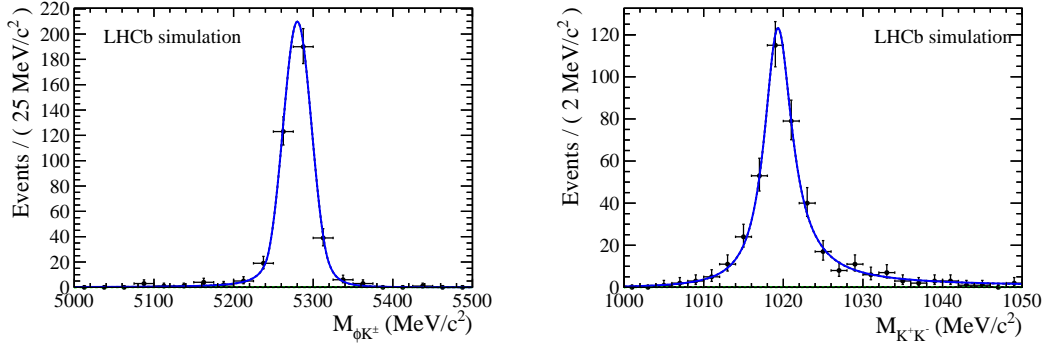
Figure 7.3 $K^+K^-K^{\pm}$ *(left) and K^+K^- (right) mass distributions of π-like $B^{\pm} \to \phi K^{\pm}$ candidates in $B^{\pm} \to \phi K^{\pm}$ MC events, i.e. candidates where the primary kaon is misidentified as a pion. The result of the two-dimensional fit described in the text is superimposed.*

$B^{\pm} \to \phi K^{\pm}$ events, with the exception of a larger value of the $B^{\pm}$ mass resolution. The ratio of the $B^{\pm} \to \phi K^{\pm}$ mass resolutions in the π-like and the K-like regions is

$$\rho_{\mathrm{MC}} = (17.93 \pm 0.84)/(15.95 \pm 0.19) = 1.12 \pm 0.05. \tag{7.7}$$

This can be explained by the harder momentum spectrum of the primary kaon misidentified as a pion, and consequently a worse resolution.

$B^{\pm} \rightarrow \phi K^{\pm}$ background misidentified as $B^{\pm} \rightarrow \phi \pi^{\pm}$

The π-like sample is expected to contain true $B^{\pm} \rightarrow \phi K^{\pm}$ decays where the primary kaon passes the $\text{DLL}_{K\pi} < -1$ requirement and hence is misidentified as a pion. Therefore, a background component peaking below the $B^{\pm}$ mass is expected in the $K^+ K^- \pi^{\pm}$ mass distribution. A MC sample of $B^{\pm} \rightarrow \phi K^{\pm}$ events reconstructed as $B^{\pm} \rightarrow \phi \pi^{\pm}$ has been analysed in order to determine the optimal PDF.

This background component is described with the same probability density function as for the signal but with the $B^{\pm}$ mass shifted by the event-by-event quantity δm:

$$f_{\text{misID}}(m_{\phi\pi}, m_{KK}; m_B, \sigma_B, \alpha, n, m_\phi, \Gamma_\phi, \sigma_\phi) = f_{\text{sig}}(m_{\phi\pi}, m_{KK}; m_B - \delta m, \sigma_B, \alpha, n, m_\phi, \Gamma_\phi, \sigma_\phi). \tag{7.8}$$

The results for m_B and σ_B (Table 7.7) are consistent with those obtained when fitting the correctly reconstructed π-like $B^{\pm} \rightarrow \phi K^{\pm}$ signal candidates (last column of Table 7.6), thus validating the use of Eq. (7.8) to describe the $B^{\pm} \rightarrow \phi K^{\pm}$ background mis-identifed as $B^{\pm} \rightarrow \phi \pi^{\pm}$. The fitted distributions are illustrated in Fig. 7.4.
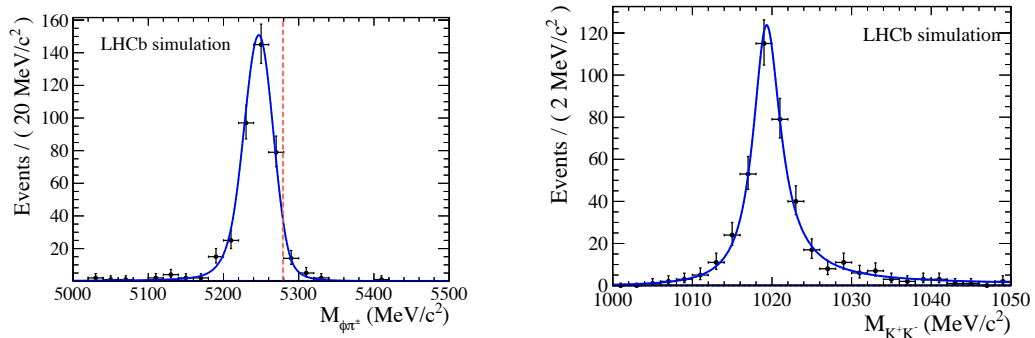
Figure 7.4 *$K^+ K^- \pi^{\pm}$ (left) and $K^+ K^-$ (right) mass distributions of mis-identified $B^{\pm} \rightarrow \phi K^{\pm}$ MC events in the π-like sample (background due to misidentification). The vertical dotted red line indicates the true $B^{\pm}$ mass. The results of the fit are superimposed, using the joint probability density function with a shift by the event-by-event quantity δm.*

Table 7.7 *Fit results of π-like $B^{\pm} \to \phi\pi^{\pm}$ candidates selected in the $B^{\pm} \to \phi K^{\pm}$ MC sample (background due to misidentification). The sample is fitted both with a per-event Crystal Ball (with the δm conditional variable).*

Parameter	Fit result with use of δm
m_B [MeV/c^2]	5280.33 ± 0.99
σ_B [MeV/c^2]	15.86 ± 0.74
α_L	1.97 fixed
n_L	1.76 fixed
α_R	1.97 fixed
n_R	3.8 fixed
m_ϕ [MeV/c^2]	1019.44 ± 0.15
σ_ϕ [MeV/c^2]	0.05 ± 2.88

7.3.2   Validation using real data samples

Two-dimensional fit of the K-like sample alone

The functional form of the partially-reconstructed and combinatorial backgrounds has been studied on the K-like sample. The two-dimensional fit described in Sec. 7.2.1 is applied, removing the π-like part. The tail parameters of the Crystal Ball function are fixed to their MC values and the ARGUS power parameter is fixed to $p = 0.5$. Because of the high correlation between the ARGUS parameters, the fitted ARGUS end-point is fixed to $m_0 = 5150\,\text{MeV}/c^2$, which is near the expectation if partially-reconstructed events due to B decays with a non-reconstructed pion are considered. In total there are 16 free parameters. The fit results are shown in Fig. 7.5 and in Table 7.8.

The $B^{\pm}$ mass resolution is not as good as in the MC simulation (which underestimates σ_B by approximately 20%).

Simultaneous two-dimensional fit of $B^{\pm} \to \phi K^{\pm}$ data candidates in the two different $\text{DLL}_{K\pi}$ regions

In order to determine the ratio of the $B^{\pm} \to \phi K^{\pm}$ mass resolutions in the π-like and K-like regions (parameter ρ), a two-dimensional fit is performed simultaneously on the K-like sample and on a sample of $B^{\pm} \to \phi K^{\pm}$ data candidates passing the requirement $-7 < \text{DLL}_{K\pi} < -1$.

The latter requirement is similar to the one imposed on the $B^{\pm} \to \phi\pi^{\pm}$ candidates of the π-like sample and is chosen in order to have a negligible contamination of $B^{\pm} \to \phi\pi^{\pm}$ and $B^{\pm} \to K^+K^-\pi^{\pm}$ events. The components considered are the ones of the K-like sample shown in Table 7.5 and are the same for both samples. All the signal parameters are shared between the two samples except the $B^{\pm}$ mass resolution.
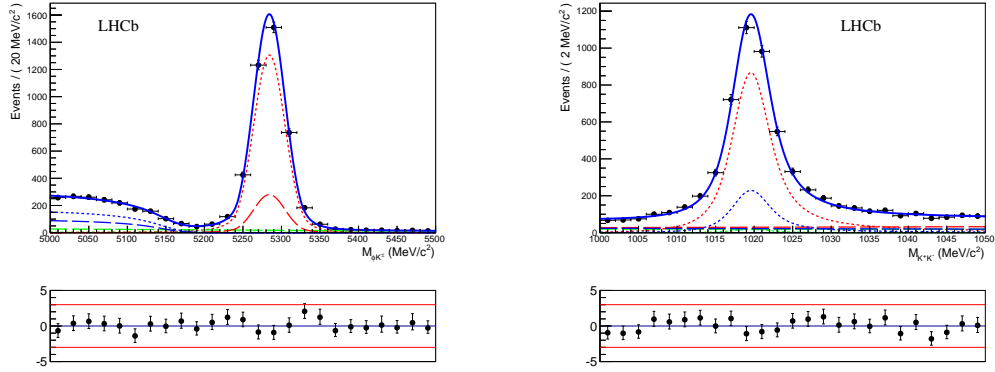
Figure 7.5 $K^+K^-K^\pm$ *(left) and* K^+K^- *(right) mass distributions of K-like* $B^\pm \to \phi K^\pm$ *data candidates. The curves represent the results of the two-dimensional fit described in the text, with the following components:* $B^\pm \to \phi K^\pm$ *signal (dotted red), non-resonant* $B^\pm \to K^+K^-K^\pm$ *background (dashed red), partially reconstructed b-hadron background with (dotted blue) or without (dashed blue) a true ϕ meson, and combinatorial background with (dotted green) or without (dashed green) true ϕ meson. The total fit function is shown as the solid blue curves. The fit pulls are displayed in the small plots at the bottom.*

Table 7.8 *Two-dimensional fit results of the K-like data sample (displayed in Fig. 7.5). The five linear background slopes are not indicated.*

Parameter			Value and error
$B^\pm$ mass	m_B	[MeV/c^2]	5284.29 $\pm$ 0.36
$B^\pm$ mass resolution	σ_B	[MeV/c^2]	20.3 $\pm$ 0.3
Crystal Ball tail parameter	α_L		1.97 fixed
Crystal Ball tail parameter	n_L		1.76 fixed
Crystal Ball tail parameter	α_R		1.97 fixed
Crystal Ball tail parameter	n_R		3.8 fixed
ϕ mass	m_ϕ	[MeV/c^2]	1019.63 $\pm$ 0.06
ϕ mass resolution	σ_ϕ	[MeV/c^2]	1.31 $\pm$ 0.10
ARGUS end-point	m_0	[MeV/c^2]	5150 fixed
ARGUS power	p_K		0.5 fixed
ARGUS c parameter	c_K		-9 $\pm$ 2
Yield of $B^\pm \to \phi K^\pm$ signal			3482 $\pm$ 76
Yield of non-resonant $B^\pm \to K^+K^-K^\pm$ background			741 $\pm$ 53
Yield of partially reconstructed $b \to \phi X$ background			883 $\pm$ 53
Yield of partially reconstructed $b \to$ non-ϕX background			510 $\pm$ 58
Yield of combinatorial background with true ϕ meson			124 $\pm$ 74
Yield of combinatorial background without true ϕ meson			511 $\pm$ 70

The ratio of the $B^\pm \to \phi K^\pm$ mass resolutions in the two samples is found to be

$$\rho = 1.26 \pm 0.10 \,, \tag{7.9}$$

in statistical agreement with the value determine from MC simulation (see Eq. 7.7). In the full final fit, the parameter ρ will be fixed to 1.26.

Simultaneous one-dimensional fit of the π-like and K-like samples

A further check of the fitting procedure is performed in order to test the fit behaviour when the conditional variable δm is used. The π-like, split in four δm bins, and K-like data samples are fitted simultaneously in a one-dimensional fit of the $B^{\pm}$ mass distributions alone. The number of components is reduced by a factor of two with respect to the list given in Table 7.5 since each pair of components with the same PDF in $m_{\phi\pi}$ (or in $m_{\phi K}$) is merged.

The bins in δm defining the four π-like subsamples ($\delta m < 30\,\text{MeV}/c^2$, $30 < \delta m < 36\,\text{MeV}/c^2$, $36 < \delta m < 45\,\text{MeV}/c^2$, and $\delta m > 45\,\text{MeV}/c^2$) are chosen to ensure a large enough number of events in each subsample. Because of the large correlations and uncertainties, constraints are applied to the parameters of the ARGUS functions. The end-point is fixed to $m_0 = 5150\,\text{MeV}/c^2$ in both the π-like and the K-like samples. This fit shows a large uncertainty on the parameter p_{π} and a large correlation with the parameter c_{π}. It is therefore decided to fix this parameter in the final fit to the value obtained in the one-dimensional fit, $p_{\pi} = 1.0$. The fit results are shown in Fig. 7.6 and Table 7.9.
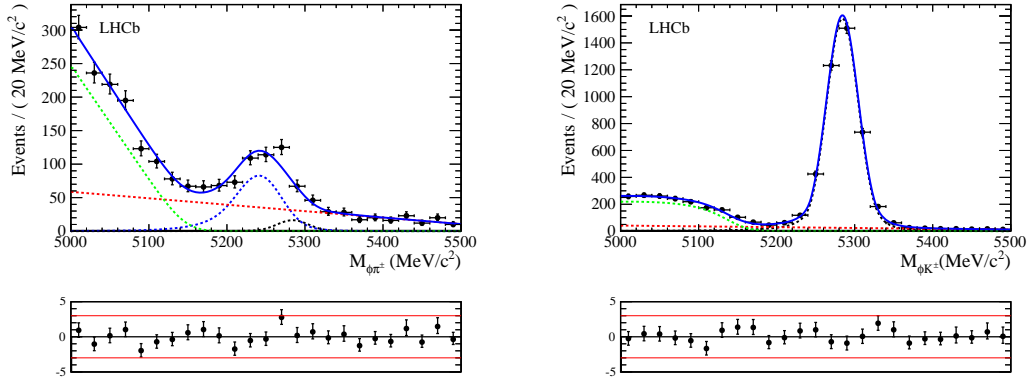
Figure 7.6   *$K^+ K^- \pi^{\pm}$ mass distribution of π-like $B^{\pm} \to \phi\pi^{\pm}$ data candidates (left) and $K^+ K^- K^{\pm}$ mass distribution of K-like $B^{\pm} \to \phi K^{\pm}$ data candidates (right). The curves represent the results of the simultaneous one-dimensional fit described in the text, with the following components: $B^{\pm} \to K^+ K^- \pi^{\pm}$ signal (dotted black on the left), $B^{\pm} \to K^+ K^- K^{\pm}$ signal (dotted black on the right), $B^{\pm} \to K^+ K^- K^{\pm}$ misidentified as $B^{\pm} \to K^+ K^- \pi^{\pm}$ (dotted blue on the left), partially reconstructed decays (dotted green), and combinatorial background (dotted red). The total fit function is shown as the solid blue curves. The fit pulls are displayed in the small plots at the bottom.*

7.3.3   Validation using toy Monte Carlo samples

Pure and embedded toy samples are used to test the fit model. All the fit components are taken into account and the number of events in each component is chosen to be in

Table 7.9 *Simultaneous one-dimensional fit results of the π-like and K-like samples (displayed in Fig. 7.6). The two linear background slopes are not shown.*

Parameter			Value and error
$B^\pm$ mass	m_B	[MeV/c^2]	5284.34 $\pm$ 0.37
$B^\pm$ mass resolution	σ_B	[MeV/c^2]	20.3 $\pm$ 0.3
Crystal Ball tail parameter	α_L		1.97 fixed
Crystal Ball tail parameter	n_L		1.76 fixed
Crystal Ball tail parameter	α_R		1.97 fixed
Crystal Ball tail parameter	n_R		3.8 fixed
ARGUS end-point	m_0	[MeV/c^2]	5150 fixed
ARGUS power (π-like)	p_π		1.02 $\pm$ 0.13
ARGUS c parameter (π-like)	c_π		1 $\pm$ 7
ARGUS power (K-like)	p_K		0.5 fixed
ARGUS c parameter (K-like)	c_K		-9 $\pm$ 2
Yield of π-like $B^\pm \to K^+K^-\pi^\pm$ signal			44 $\pm$ 21
Yield of π-like misidentified $B^\pm \to K^+K^-K^\pm$ background			340 $\pm$ 32
Yield of π-like partially reconstructed b background			921 $\pm$ 56
Yield of π-like combinatorial background			863 $\pm$ 73
Yield of K-like $B^\pm \to K^+K^-K^\pm$ signal			4220 $\pm$ 72
Yield of K-like partially reconstructed b background			1365 $\pm$ 64
Yield of K-like combinatorial background			666 $\pm$ 82

agreement with the results of the validation fits performed on the data (see Sec. 7.3.2). Because of the large uncertainty on the number of $B^\pm \to \phi\pi^\pm$ events predicted, samples with three different $B^\pm \to \phi\pi^\pm$ input yields, 0 or 15 or 30, are generated. Large uncertainties and instabilities in the fit, plus significant biases are observed if the fit is performed without the conditional variable δm. The introduction of δm improves the stability of the fit. However, despite the symmetric distribution of the fitted signal yields and a negligible fraction of fit failures, a significant bias is observed in the distribution of the $B^\pm \to \phi\pi^\pm$ signal yields. Small differences in the δm distributions of the various components are the source of this bias, illustrating the "Punzi effect" [83]. The obvious solution to remove the bias due to the use of the conditional variable δm is to fit this variable itself. However, the PDF of the δm variable would have to be determined from simulation. In order to develop the entire analysis with minimal dependence on the Monte Carlo simulation, this path is not followed. Instead the π-like sample is divided in δm bins, where the δm distributions for the various components are very similar by construction. The introduction of four δm bins results in a strong reduction of the fit bias. Three tests with different numbers of generated $B^\pm \to \phi\pi^\pm$ signal events, and different δm distributions for the background components, are performed. The results are shown in Table 7.10. For the case of 15 generated $B^\pm \to \phi\pi^\pm$ signal events, the distributions of the fitted signal yield, its estimated error and the corresponding pull are presented in Fig. 7.7.

Table 7.10 *Signal results obtained from fits to embedded toy samples using the δm variable and with δm bins. The number of generated events ("In"), the mean value of the distribution of the fitted yield ("Out"), the mean value of the distribution of the error on the fitted yield ("Err") and the mean bias on the fitted yield ("Bias", computed as "Out"–"In") are shown for the $B^\pm \to \phi\pi^\pm$ and $B^\pm \to \phi K^\pm$ components.*

Component	In	Out	Err	Bias
$B^\pm \to \phi\pi^\pm$	0	1.4	15.2	1.4 ± 0.7
$B^\pm \to \phi K^\pm$ (π-like)	274	272.4	21.1	-1.6 ± 0.7
$B^\pm \to \phi K^\pm$ (K-like)	3407	3378	72.0	$-29 \;\;\pm 2$
$B^\pm \to \phi\pi^\pm$	15	15.2	16.1	0.2 ± 0.7
$B^\pm \to \phi K^\pm$ (π-like)	274	272.6	21.2	-1.4 ± 0.7
$B^\pm \to \phi K^\pm$ (K-like)	3407	3379	72.0	$-28 \;\;\pm 2$
$B^\pm \to \phi\pi^\pm$	30	29.9	17.0	-0.1 ± 0.7
$B^\pm \to \phi K^\pm$ (π-like)	274	272.8	21.4	-1.2 ± 0.7
$B^\pm \to \phi K^\pm$ (K-like)	3407	3379	72.0	$-28 \;\;\pm 2$
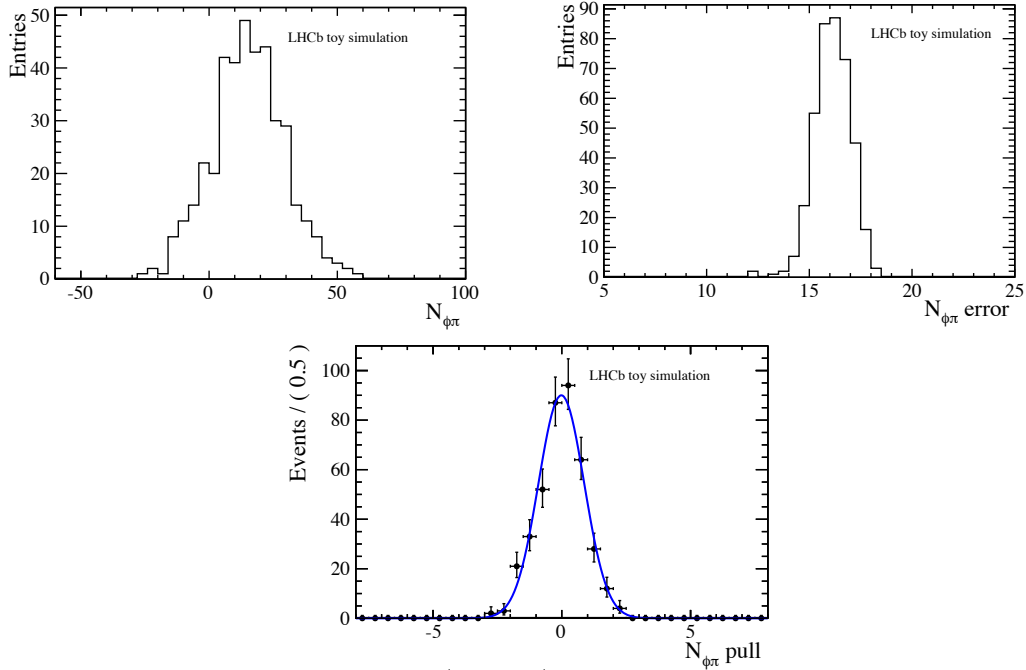
Figure 7.7 *Distributions of the fitted $B^\pm \to \phi\pi^\pm$ signal yield (top left), its estimated error (top right) and the corresponding pull (bottom), obtained from 400 embedded toy samples generated with 15 signal events each. The conditional variable δm is used in the fits and the π-like sample is divided in four δm bins. The mean value and the RMS of the signal yield distribution are 15.2 ± 0.7 and 14.2 ± 0.5, respectively. The mean value and width obtained from a Gaussian fit to the pull distribution are -0.02 ± 0.04 and 0.89 ± 0.03, respectively. The width is smaller than 1 because the number of events in each sample is fixed in the generation.*

Tests with more than four bins are also performed, leading to less stable fits. Given the stability, and the small bias obtained with the fit described above, it is decided to use only four bins.

The bias in the $B^\pm \to \phi K^\pm$ yield is due to the presence of both MC-truth-matched and non MC-truth-matched $B^\pm \to \phi K^\pm$ events in the embedded toy samples. Some of these events will contribute to the background components and, as a consequence, produce a negative bias. It is checked that about 1% of the fully-simulated $B^\pm \to \phi K^\pm$ events contribute to the combinatorial background. If this fraction is taken in account the remaining bias is compatible with zero.

7.4 Search for $B^\pm \to \phi\pi^\pm$ decays

7.4.1 Fit results

After the validation of the analysis strategy, the simultaneous two-dimensional fit of the real data is performed. The extracted $B^\pm \to \phi\pi^\pm$ signal yield is $N_{\phi\pi^\pm} = 19.1 \pm 19.2$, with a statistical significance equal to 1.0. The results of the fit are shown in Table 7.11 and Fig. 7.8.

In order to measure the ratio between the $B^\pm \to \phi\pi^\pm$ and $B^\pm \to \phi K^\pm$ branching fractions, a second fit is performed introducing the ratio between $N_{\phi\pi}$ and $N_{\phi K}$ as parameter in the fit. The extracted value is $(5.1^{+5.3}_{-5.0}) \times 10^{-3}$, is used to compute the limit on $\mathcal{B}(B^\pm \to \phi\pi^\pm)$. The likelihood scan as a function of the yield ratio $N_{\phi\pi}/N_{\phi K}$ is shown in Fig. 7.9.

The limit is calculated according to the method explained in Chapter 6. The final upper limit, including the systematic uncertainties is

$$\mathcal{B}(B^\pm \to \phi\pi^\pm) < 1.55(1.80) \times 10^{-7} \text{ at } 90\%(95\%) \text{ CL.} \tag{7.10}$$

Table 7.12 presents a compilation of the values entering the calculation of the final results, including the systematics described in the next section.

Table 7.11 *Results of the simultaneous two-dimensional fit of the $B^{\pm} \to \phi\pi^{\pm}$ and $B^{\pm} \to \phi K^{\pm}$ data samples (displayed in Fig. 7.8). Only the total yield of each component in the π-like sample is shown. The nine slopes are omitted.*

Parameter			Value and error
$B^{\pm}$ mass	m_B	[MeV/c^2]	5284.25 $\pm$ 0.36
$B^{\pm}$ mass resolution	σ_B	[MeV/c^2]	20.3 $\pm$ 0.3
Crystal Ball tail parameter	α_L		1.97 fixed
Crystal Ball tail parameter	n_L		1.76 fixed
Crystal Ball tail parameter	α_R		1.97 fixed
Crystal Ball tail parameter	n_R		3.8 fixed
ϕ mass	m_{ϕ}	[MeV/c^2]	1019.56 $\pm$ 0.05
ϕ mass resolution	σ_{ϕ}	[MeV/c^2]	1.28 $\pm$ 0.10
ARGUS end-point	m_0	[MeV/c^2]	5150 fixed
ARGUS power (π-like)	p_{π}		1.0 fixed
ARGUS c parameter (π-like)	c_{π}		7 $\pm$ 4
ARGUS power (K-like)	p_K		0.5 fixed
ARGUS c parameter (K-like)	c_K		-9 $\pm$ 2
Yield of π-like $B^{\pm} \to \phi\pi^{\pm}$ signal			19 $\pm$ 19
Yield of π-like non-resonant $B^{\pm} \to K^+K^-\pi^{\pm}$ background			17 $\pm$ 19
Yield of π-like misidentified $B^{\pm} \to \phi K^{\pm}$ background			280 $\pm$ 25
Yield of π-like misidentified $B^{\pm} \to K^+K^-K^{\pm}$ background			fixed
Yield of π-like partially reconstructed $b \to \phi X$ background			558 $\pm$ 39
Yield of π-like partially reconstructed $b \to$ non-ϕX background			318 $\pm$ 46
Yield of π-like combinatorial background with true ϕ meson			213 $\pm$ 42
Yield of π-like combinatorial background without true ϕ meson			705 $\pm$ 60
Yield of K-like $B^{\pm} \to \phi K^{\pm}$ signal			3486 $\pm$ 76
Yield of K-like non-resonant $B^{\pm} \to K^+K^-K^{\pm}$ background			731 $\pm$ 52
Yield of K-like partially reconstructed $b \to \phi X$ background			872 $\pm$ 65
Yield of K-like partially reconstructed $b \to$ non-ϕX background			502 $\pm$ 58
Yield of K-like combinatorial background with true ϕ meson			138 $\pm$ 80
Yield of K-like combinatorial background without true ϕ meson			522 $\pm$ 71
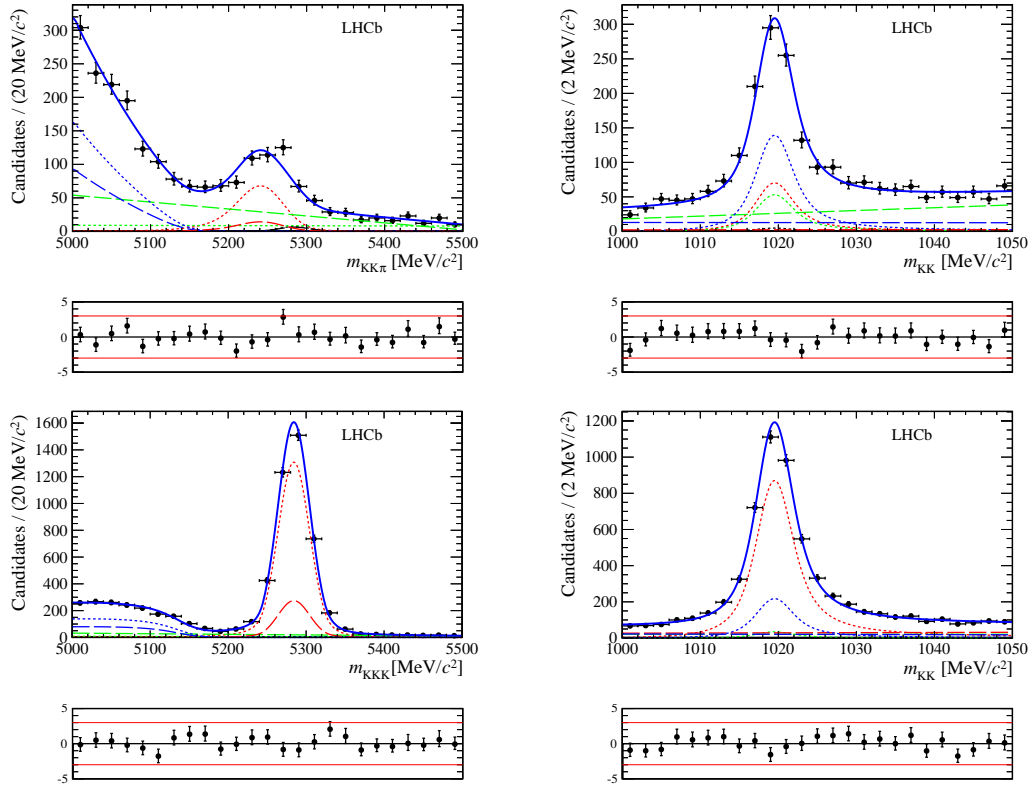
Figure 7.8 $\phi\pi^{\pm}$ *(top left) and* $K^{+}K^{-}$ *(top right) mass distributions of the events in the π-like sample, and* $\phi K^{\pm}$ *(bottom left) and* $K^{+}K^{-}$ *(bottom right) mass distributions of the events in the K-like sample. The blue solid curves represent the results of the simultaneous two-dimensional fit described in the text, with the following components:* $B^{\pm} \to \phi\pi^{\pm}$ *signal (dotted black), non-resonant* $B^{\pm} \to K^{+}K^{-}\pi^{\pm}$ *background (dashed black),* $B^{\pm} \to \phi K^{\pm}$ *signal (dotted red), non-resonant* $B^{\pm} \to K^{+}K^{-}K^{\pm}$ *background (dashed red), partially reconstructed b-hadron background with (dotted blue) or without (dashed blue) a true ϕ meson, and combinatorial background with (dotted green) or without (dashed green) true ϕ meson. The fit pulls are displayed in the small plots at the bottom.*
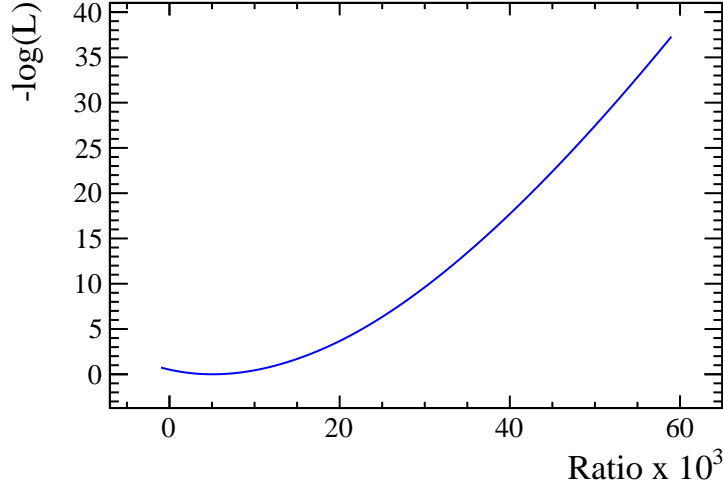
Figure 7.9   *Log-likelihood scan as a function of the yield ratio $N_{\phi\pi}/N_{\phi K}$.*

Table 7.12   *Quantities entering the calculation of the final results of the $B^\pm \to \phi\pi^\pm$ search. $N_{\phi K}$ is defined as $N_{\phi K(K-\text{like})} + N_{\phi K(\pi-\text{like})}$.*

Quantity	Value
$N_{\phi\pi}$	19.1 ± 19.2
$N_{\phi K(K-\text{like})}$	3486 ± 76
$N_{\phi K(\pi-\text{like})}$	280 ± 25
$N_{\phi\pi}/N_{\phi K}$	$(5.1^{+5.3}_{-5.0}(\text{stat}) \pm 2.1(\text{syst})) \times 10^{-3}$
significance (stat. only)	1.0
$\epsilon(B^\pm \to \phi\pi^\pm)/\epsilon(B^\pm \to \phi K^\pm)$	$0.76 \pm 0.03 \pm 0.04$
$\mathcal{B}(B^\pm \to \phi\pi^\pm)/\mathcal{B}(B^\pm \to \phi K^\pm)$	$(6.6 \pm^{+6.9}_{-6.6}(\text{stat}) \pm 2.8(\text{syst})) \times 10^{-3}$ < 0.018 at 90% CL < 0.020 at 95% CL
$\mathcal{B}(B^\pm \to \phi K^\pm)$ [11]	$(8.8^{+0.7}_{-0.6}) \times 10^{-6}$
$\mathcal{B}(B^\pm \to \phi\pi^\pm)$	$(5.8^{+6.1}_{-5.8} \pm 2.5) \times 10^{-8}$ $< 1.55 \times 10^{-7}$ at 90% CL $< 1.80 \times 10^{-7}$ at 95% CL

7.4.2 Systematic uncertainties

Since the branching fraction of the $B^{\pm} \to \phi \pi^{\pm}$ decay is measured with respect to that of the $B^{\pm} \to \phi K^{\pm}$ decay, and the selection for the two channels is almost identical, only few sources of systematics are expected for this measurement. The contributions to the systematic error are listed in Table 7.13 and discussed below. The total systematic uncertainty, obtained as the quadratic sum of all contributions, is 0.036 on the efficiency ratio and 2.14×10^{-3} on the yield ratio.

Event selection systematics

To evaluate a possible systematic uncertainty due to the event selection, and therefore associated with the total selection efficiency ratio, a 10% variation of the kinematic cut values applied on the momentum and transverse momentum of the bachelor kaon or pion, and on the transverse momentum of the reconstructed B meson is considered. The values of the ratio of the $B^{\pm} \to \phi \pi^{\pm}$ and $B^{\pm} \to \phi K^{\pm}$ total selection efficiencies for various kinematic cuts are all compatible with the value found with the nominal selection. The maximum variation, equal to 0.03, is taken as a systematic uncertainty, corresponding to a relative uncertainty of 3.9% on the efficiency ratio.

The systematic error associated with the PID selection is computed with the `PidCalib` package as the difference of the PID efficiency using the standard binning scheme or one bin for each kinematic variable on the calibration sample [76]. For the cut $\text{DLL}_{K\pi} < -1$, it is equal to 0.0038. In order to take into account the fluctuation due to the method, the value of this systematic uncertainty as a function of $\text{DLL}_{K\pi}$ is linearly interpolated and the maximum positive and negative deviations from the linear shape dependence are added in quadrature to 0.0038, leading to an uncertainty of 0.0074. Since parallel studies on the `PidCalib` package affirmed that the tools underestimate the PID efficiency systematic uncertainty, it has been choosen to take the current best estimate of 0.02 as systematic uncertainty, corresponding to a 2.4% relative uncertainty on the efficiency ratio. The effect of an increase of the systematic has been checked and it is concluded that even a large increase does not modify the upper limit, since the systematic error is dominated by the fit model uncertainty (see Sec. 7.4.2) and the statistical error is much larger than the systematic.

Trigger systematics

The main source of systematic uncertainty in the trigger selection efficiency is expected to be due to the track p_{T} cut applied by the L0Hadron TOS trigger line. The different p_{T} distributions of the bachelor kaon and pion in the K-like and π-like sample, respectively, can lead to a different efficiency. To evaluate the systematic uncertainty due to the trigger requirements, the effect of the kinematic cut applied by the L0Hadron TOS trigger line ($p_{\mathrm{T}} > 4144 \, \text{MeV}/c$) on the efficiency ratio is studied on both $B^{\pm} \to \phi K^{\pm}$ and $B^{\pm} \to \phi \pi^{\pm}$ signal MC. A 10% variation of the value of this cut produces an efficiency ratio variation

Table 7.13 *Relative systematic uncertainties on the efficiency ratio and on the yield ratio.*

	Source	Systematic uncertainty
	Kinematic selection	3.9%
Efficiency ratio	PID selection	2.4%
	Trigger	1%
	Fit model	41%
Yield ratio	Fit bias	3.4%
	S-wave	8.4%

of 1%, which is assigned as systematic uncertainty.

Fit model systematics

Possible systematics uncertainties are introduced because of the model used to fit data. The following sources are considered:

- the fixed parameters α_L, α_R, n_L and n_R of the Crystal Ball function for the $B^{\pm}$ mass;

- the fixed parameters of the ARGUS function used to describe the partially reconstructed background;

- the ratio between the resolutions of the $B^{\pm} \to \phi K^{\pm}$ components in the π-like and K-like samples;

- the modeling of the combinatorial background with a linear function in the $B^{\pm}$ mass distribution.

The corresponding systematic errors on the yield ratio, $N(B^{\pm} \to \phi\pi^{\pm})/N(B^{\pm} \to \phi K^{\pm})$, are evaluated by changing the fixed parameters within their uncertainties, and replacing the linear background function with an exponential function, finding a final relative systematic uncertainty of 41%. The uncertainty on the resolution ratio is the dominant source of systematic uncertainty, because of the overlap between the signal and the mis-reconstructed $B^{\pm} \to \phi K^{\pm}$ events.

Fit bias systematics

Embedded and pure toys studies are repeated using the yields and PDF parameters from the fit to the data, and the $B^{\pm} \to \phi\pi^{\pm}$ signal yield and the yield ratio $N_{\phi\pi}/N_{\phi K}$ are extracted. The results obtained with toys studies are compatible with the value obtained from the nominal fit, therefore no corrections need to be applied to the fit result. The uncertainty on the mean value of the ratio distribution in the embedded toys, equal to 3.4%, is taken as a systematic uncertainty.
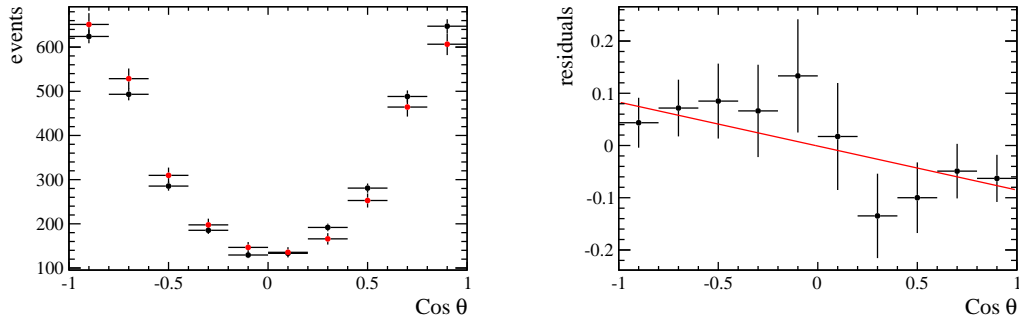
Figure 7.10   *Left: distribution of the cosine of the ϕ decay angle for $B^{\pm} \to \phi K^{\pm}$ signal from Monte Carlo (black) and data (red). Right: relative difference between data and Monte Carlo (normalised to the Monte Carlo), fitted with a linear function.*

S-wave contribution uncertainty

A possible contribution to the systematic error can be due to the interference between the S-wave component (such as $B^{\pm} \to K^{+}K^{-}K^{\pm}$) and the P-wave component (signal). Since this contribution is expected to be negligible, and because of the very low statistics in the π-like sample, an angular analysis is not performed. However it is decided to estimate a systematic uncertainty analysing the angular distribution of the $B^{\pm} \to \phi K^{\pm}$ decay in the K-like sample. We consider the ϕ decay angle, defined as the angle θ between the momenta of the K^{+} from the ϕ decay and the $B^{\pm}$ in the ϕ rest frame. The distribution of $\cos\theta$ is extracted for the data signal using the *sPlot* technique [84] and compared with that of MC. The left plot of Fig. 7.10 shows the distribution of $\cos\theta$ for $B^{\pm} \to \phi K^{\pm}$ signal from Monte Carlo (black) and data (red). The plot on the right shows the relative difference between data and Monte Carlo (normalised to the Monte Carlo) as a function of $\cos\theta$. This difference is fitted with a linear function, with a slope of -0.084 ± 0.028. From this fit a systematic uncertainty of 8.4% is assigned.

7.5   Measurement of $\mathcal{A}^{CP}(B^{\pm} \to \phi K^{\pm})$

7.5.1   Raw asymmetry

From the simultaneous fit of the $B^{+} \to \phi K^{+}$ and $B^{-} \to \phi K^{-}$ candidates in the two trigger subsamples of the K-like region (described in Sec. 7.2.2) the following values for the raw $B^{\pm} \to \phi K^{\pm}$ CP asymmetries (Eq. 7.5) are found:

$$A_{\text{raw,TOS}}^{CP}(B^{\pm} \to \phi K^{\pm}) \;\; = \;\; +0.027 \pm 0.026\,, \tag{7.11}$$

$$A_{\text{raw,TIS}}^{CP}(B^{\pm} \to \phi K^{\pm}) \;\; = \;\; -0.053 \pm 0.035\,. \tag{7.12}$$

The $B^{\pm} \to \phi K^{\pm}$ fit results are presented in Figs. 7.11 and 7.12, for the TOS and TIS samples, respectively, and Table 7.14.
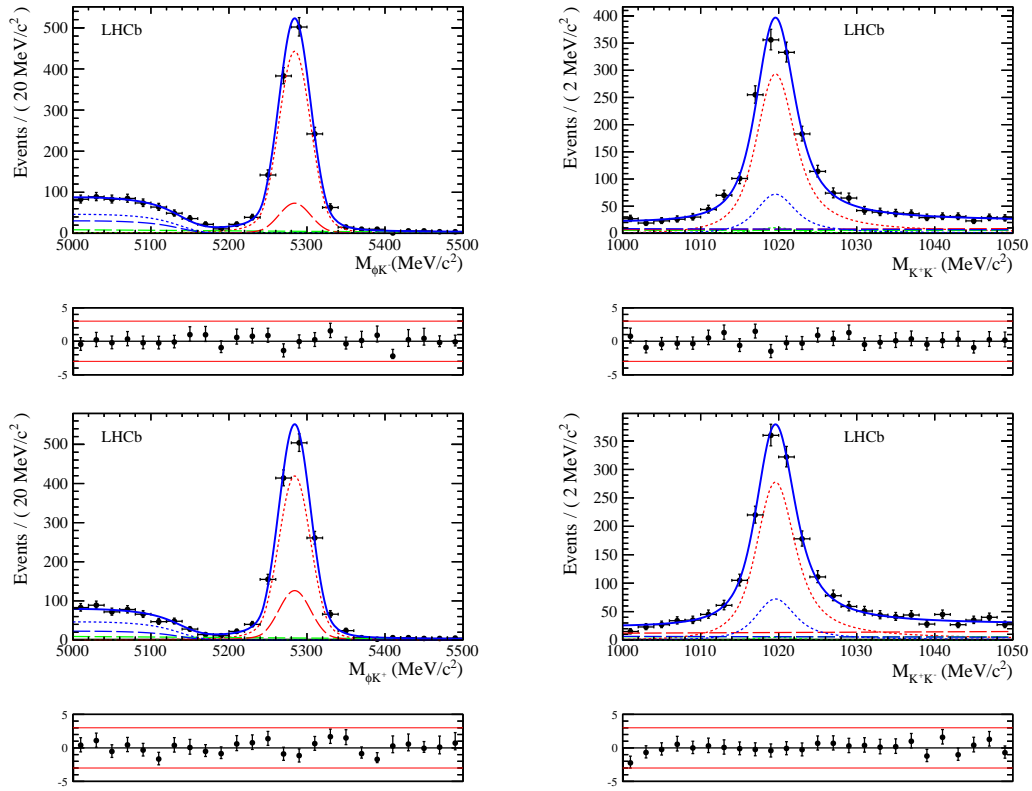
Figure 7.11 *$K^{+}K^{-}K^{\pm}$ (left) and $K^{+}K^{-}$ (right) mass distributions of K-like $B^{-} \to \phi K^{-}$ (top) and $B^{+} \to \phi K^{+}$ (bottom) data candidates in the subsample selected by the L0Hadron TOS trigger line. The curves represent the results of the simultaneous two-dimensional fit described in the text. The following components are present: $B^{\pm} \to \phi K^{\pm}$ signal (dotted red), non-resonant $B^{\pm} \to K^{+}K^{-}K^{\pm}$ background (dashed red), partially reconstructed b-hadron background with (dotted blue) or without (dashed blue) a true ϕ meson, and combinatorial background with (dotted green) or without (dashed green) true ϕ meson. The total fit function is shown as the solid blue curves. The fit pulls are displayed in the small plots at the bottom.*

Figure 7.12 $K^+K^-K^{\pm}$ *(left) and* K^+K^- *(right) mass distributions of K-like* $B^- \to \phi K^-$ *(top) and* $B^+ \to \phi K^+$ *(bottom) data candidates in the subsample selected by the L0Global TIS (and not TOS) trigger line. The curves represent the results of the simultaneous two-dimensional fit described in the text. The following components are present:* $B^{\pm} \to \phi K^{\pm}$ *signal (dotted red), non-resonant* $B^{\pm} \to K^+K^-K^{\pm}$ *background (dashed red), partially reconstructed b-hadron background with (dotted blue) or without (dashed blue) a true* ϕ *meson, and combinatorial background with (dotted green) or without (dashed green) true* ϕ *meson. The total fit function is shown as the solid blue curves. The fit pulls are displayed in the small plots at the bottom.*

Table 7.14   *Results of the simultaneous two-dimensional $\mathcal{A}^{CP}$ fit of the $B^- \to \phi K^-$ and $B^+ \to \phi K^+$ candidates in the two trigger subsamples of the K-like region (displayed in Figs. 7.11 and 7.12) to measure the CP asymmetry of the $B^\pm \to \phi K^\pm$ decay. The 5 linear background slopes are not indicated.*

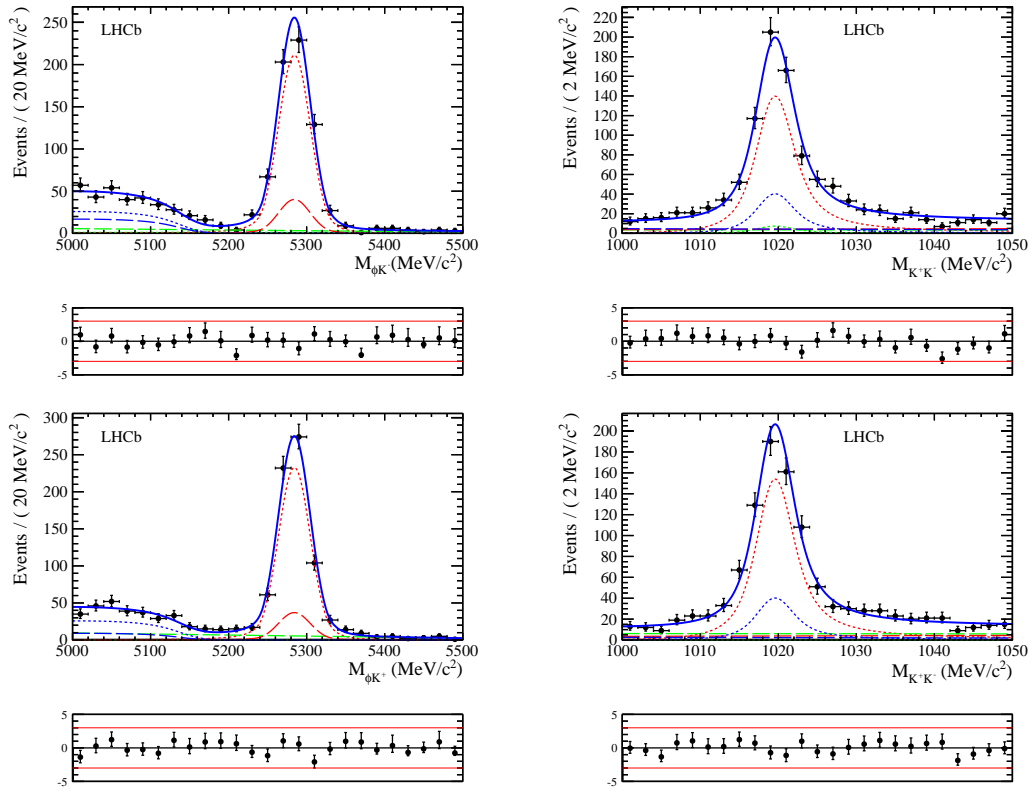| Parameter			Value and error		
$B^\pm$ mass	m_B	[MeV/c^2]	5284.27	$\pm$	0.36
$B^\pm$ mass resolution	σ_B	[MeV/c^2]	20.38	$\pm$	0.33
Crystal Ball tail parameter	α_L		1.97		fixed
Crystal Ball tail parameter	n_L		1.76		fixed
Crystal Ball tail parameter	α_R		1.97		fixed
Crystal Ball tail parameter	n_R		3.8		fixed
ϕ mass	m_ϕ	[MeV/c^2]	1019.63	$\pm$	0.06
ϕ mass resolution	σ_ϕ	[MeV/c^2]	1.32	$\pm$	0.10
ARGUS end-point	m_0	[MeV/c^2]	5150		fixed
ARGUS power	p_K		0.5		fixed
ARGUS c parameter	c_K		-9	$\pm$	2
$\mathcal{A}_{\text{raw}}^{CP}(B^\pm \to \phi K^\pm)$ (TOS)			0.027	$\pm$	0.026
Yield of $B^\pm \to \phi K^\pm$ signal (TOS)			2306	$\pm$	59
Yield of non-resonant $B^\pm \to K^+K^-K^\pm$ background (TOS)			535	$\pm$	43
Yield of partially reconstructed $b \to \phi X$ background (TOS)			583	$\pm$	35
Yield of partially reconstructed $b \to$ non-ϕX background (TOS)			334	$\pm$	40
Yield of combinatorial background with true ϕ meson (TOS)			60	$\pm$	26
Yield of combinatorial background without true ϕ meson (TOS)			283	$\pm$	46
$\mathcal{A}_{\text{raw}}^{CP}(B^\pm \to \phi K^\pm)$ (TIS)			-0.053	$\pm$	0.035
Yield of $B^\pm \to \phi K^\pm$ signal (TIS)			1192	$\pm$	43
Yield of non-resonant $B^\pm \to K^+K^-K^\pm$ background (TIS)			204	$\pm$	29
Yield of partially reconstructed $b \to \phi X$ background (TIS)			330	$\pm$	27
Yield of partially reconstructed $b \to$ non-ϕX background (TIS)			159	$\pm$	32
Yield of combinatorial background with true ϕ meson (TIS)			17	$\pm$	29
Yield of combinatorial background without true ϕ meson (TIS)			250	$\pm$	41

7.5.2   *CP* asymmetry

As already mentioned in Chapter 6, the $B^\pm \to J/\psi K^\pm$ mode is used as reference channel to correct the raw $B^\pm \to \phi K^\pm$ asymmetry for the detection and production asymmetries. The results of the raw $B^\pm \to J/\psi K^\pm$ asymmetry are taken from the $B^\pm \to K^+K^-K^\pm$ analysis [85] performed by the LHCb collaboration with the 2011 data.

The difference between the $B^\pm \to \phi K^\pm$ and $B^\pm \to J/\psi K^\pm$ physics asymmetries, computed separately for TIS and TOS, are combined as follow:

$$\Delta\mathcal{A}^{CP} = f\Delta A_{\text{TOS}}^{CP} + (1-f)\Delta A_{\text{TIS}}^{CP} \tag{7.13}$$

Table 7.15 *Raw charge asymmetries for the $B^{\pm} \to \phi K^{\pm}$ and $B^{\pm} \to J/\psi K^{\pm}$ decays, their difference $\Delta \mathcal{A}^{CP}$, and the fraction (f) of $B^{\pm} \to \phi K^{\pm}$ signal events in each trigger subsample. All uncertainties are statistical only.*

	TOS sub-sample	TIS (not TOS) sub-sample
$\mathcal{A}_{\text{raw}}^{CP}(B^{\pm} \to \phi K^{\pm})$	0.0274 ± 0.0256	-0.0530 ± 0.0350
$\mathcal{A}_{\text{raw}}^{CP}(B^{\pm} \to J/\psi K^{\pm})$	-0.0243 ± 0.0075	-0.0080 ± 0.0049
$\Delta \mathcal{A}^{CP}$	0.0518 ± 0.0266	-0.0450 ± 0.0354
f	65.9%	34.1%
weighted $\Delta \mathcal{A}^{CP}$ average	0.0188 ± 0.0213	

where f is the fraction of $B^{\pm} \to \phi K^{\pm}$ events selected by the L0Hadron TOS trigger line. A value of $\Delta \mathcal{A}^{CP} = (1.9 \pm 2.1) \times 10^{-2}$ is found. All the values are summarised in Table 7.15.

Using the world average measurement $\mathcal{A}^{CP}(B^{\pm} \to J/\psi K^{\pm}) = 0.003 \pm 0.006$ [11], the CP asymmetry of the $B^{\pm} \to \phi K^{\pm}$ decay is found to be

$$\mathcal{A}^{CP}(B^{\pm} \to \phi K^{\pm}) = (2.2 \pm 2.1(\text{stat}) \pm 0.7(\text{syst}) \pm 0.6(J/\psi K^{\pm})) \times 10^{-2}, \qquad (7.14)$$

which includes the systematic uncertainties described in the following section.

7.5.3 Systematics uncertainties

The different systematic contributions to the $\mathcal{A}^{CP}$ measurement are summarized in Table 7.16. The total systematic uncertainty, obtained as the quadratic sum of all contributions, is 0.70×10^{-2}.

Table 7.16 *Absolute systematic uncertainties on $\mathcal{A}^{CP}(B^{\pm} \to \phi K^{\pm})$.*

Source	Absolute systematic uncertainty $\times 10^2$
Fit model	0.27
Trigger asymmetry	0.35
S-wave	0.17
$B^{\pm} \to J/\psi K^{\pm}$ kinematics	0.48
Fiducial cut	0.19
Total	0.70

Fit model

A first possible contribution to the systematic uncertainties can be due to the model chosen for the fit. The following sources of systematics are considered:

- the fixed parameters α_L, α_R, n_L and n_R of the Crystal Ball function for the $B^\pm$ mass;

- the fixed parameter of the ARGUS function used to describe the partially reconstructed background;

- the modeling of the combinatorial background with a linear function in the $B^\pm$ mass distribution.

The corresponding systematic errors on the $\mathcal{A}^{CP}_{\text{raw}}$ is evaluated by changing the fixed parameters within their uncertainties, and replacing the linear background function with an exponential function. The differences with respect to the nominal value are summed in quadrature and the final value, equal to 0.27×10^{-2}, is taken as systematic uncertainty.

Trigger asymmetry

The trigger asymmetry for kaons, present in the events selected by the L0Hadron TOS line is not completely cancelled in the difference between the signal and the control channel asymmetries [85]. This is due to the different number of kaons in the final state of the two channels. To evaluate the associated systematic uncertainty, the difference between the raw $B^\pm \to J/\psi K^\pm$ asymmetry computed with and without the kaon TOS trigger correction [85], equal to 0.005, is multiplied by the fraction of events selected by the TOS trigger line (65.9%), leading to a systematic uncertainty of 0.33×10^{-2}. For the events selected by the L0Global TIS a similar effect is not present, since they are not triggered on the signal kaons.

To take into account the effect of the events selected both by the L0Global TIS and the L0Hadron TOS trigger lines, we compute the asymmetry with the raw $B^\pm \to J/\psi K^\pm$ asymmetry extracted from the full TIS sample ($B^\pm \to J/\psi K^\pm = 0.0092$ [85]), reweighed by the fractions of events in each trigger category in the $B^\pm \to \phi K^\pm$ sample. The difference between this and the nominal asymmetry, equal to 0.12×10^{-2}, is applied as systematic uncertainty. Summing in quadrature the two contributions a total trigger uncertainty of 0.35×10^{-2} is obtained.

S-wave contribution

From the angular distribution the S-wave contribution is estimated to be less than 8.4% (Sec. 7.4.2). Assuming the S-wave components has no CP asymmetry we evaluate the corrected CP asymmetry, A, to be related to the measured raw asymmetry by the following equation:

$$A^{CP}_{\text{raw}} = A \times (1 - 0.084) + 0 \times 0.084 \,. \tag{7.15}$$

It follows that the difference is

$$\delta A = A - A^{CP}_{\text{raw}} = 9.2\% A^{CP}_{\text{raw}} \,. \tag{7.16}$$

This difference, equal to 0.17×10^{-2}, is applied as systematic uncertainty.

$B^{\pm} \to J/\psi K^{\pm}$ kinematic selection

The different kinematic selection of the control channel and the $B^{\pm} \to \phi K^{\pm}$ decay needs to be taken in account. The same kinematic selection of the bachelor kaon in the $B^{\pm} \to \phi K^{\pm}$ sample ($p(K) > 10000$ and $p_T(K) > 2500$) is applied to the bachelor kaon of the control sample. The fit to the $B^{\pm} \to J/\psi K^{\pm}$ data is reproduced with the new kinematic selections and the difference with respect to the result obtained with the nominal selection is applied as systematic. The systematic uncertainty is computed independently for the TIS and TOS subsamples, and then averaged in quadrature weighting them with the fraction of signal events passing each trigger selection, leading to a systematic uncertainty of 0.42×10^{-2}. To check the effect of the differences in the momentum distribution of the $B^{\pm} \to \phi K^{\pm}$ and $B^{\pm} \to J/\psi K^{\pm}$ channels the asymmetry is measured in bins of p and we combined them after weighting by the fraction of events in each bin in both samples. The difference, equal to 0.24×10^{-2} is added in quadrature to 0.42×10^{-2}, obtaining a final systematic of 0.48×10^{-2}.

Fiducial cut

Because of the magnetic field, a charge-dependent acceptance that breaks the left-right symmetry of the detector needs to be taken in account. The same fiducial cut as in Ref. [85] is applied,

$$|P_x| \leqslant 0.317 \times (P_z - 2400 \,\text{MeV}/c), \tag{7.17}$$

where P_x and P_z are respectively the x and z component of the bachelor kaon. The sample is fitted and $\Delta\mathcal{A}^{CP}$ is computed. The difference with respect to the nominal $\Delta\mathcal{A}^{CP}(B^{\pm} \to \phi K^{\pm})$, equal to 0.19×10^{-2}, is taken as systematic uncertainty.

7.5.4 Further checks

Magnet polarity

To check a possible difference due to the magnet polarity each of the four subsamples is further split in two according to the magnetic field polarity. Two independent fits are performed to the data selected with the magnet up-polarity and down-polarity respectively. The results of *CP* asymmetries extracted from the two fits are compatible both for the TIS and the TOS events. The results are displayed in Table 7.17.

Table 7.17   *Raw CP asymmetry for magnet up and magnet down.*

	L0Hadron TOS	L0Global TIS (not TOS)
Magnet up	-0.002 ± 0.040	0.010 ± 0.057
Magnet down	0.042 ± 0.036	-0.078 ± 0.050
Compatibility (σ)	0.8	-1.2

7.6   Update of $\mathcal{A}^{CP}(B^\pm \to \phi K^\pm)$ with 2012 data

An update of the measurement of the $B^\pm \to \phi K^\pm$ charge asymmetry is performed including the data collected in 2012. The procedure is the same as for the $\mathcal{A}^{CP}(B^\pm \to \phi K^\pm)$ measurement with the 2011 data, except for a few differences that will be pointed out, together with the results, in this section. Since this measurement is performed together with the measurement of $\mathcal{A}^{CP}(B^\pm \to \eta' K^\pm)$ and the search for the $B_s^0 \to \eta'\eta'$ decay, presented in Chapter 8, forward references will be given for the methods common with the other two measurements.

7.6.1   Data samples

The analysis exploits the data collected by LHCb in 2011 and 2012 at $\sqrt{s} = 7$ TeV and $\sqrt{s} = 8$ TeV, respectively, corresponding to a total integrated luminosity of approximately $3\,\text{fb}^{-1}$. After the compatibility has been verified, the two samples are merged to extract the CP asymmetry.

Two signal MC samples are used:

- $B^\pm \to \phi K^\pm$ (events type 12103061) at $\sqrt{s} = 8$ TeV: 1057999 signal events;

- $B^\pm \to \phi K^\pm$ (events type 12103061) at $\sqrt{s} = 7$ TeV: 523248 signal events.

Further information on data and MC production are given in Sec. 8.1.1.

7.6.2   Event selection

As for the analysis with 7 TeV data, the event selection proceeds in three steps, the stripping, the trigger and the offline selection. Since the $B^\pm \to \phi K^\pm$ channel is used as control channel for efficiency studies in the search for the $B_s^0 \to \eta'\eta'$ decay, the selection of the two channels is kept as similar as possible. The same stripping and trigger selection is applied (cuts are given in Tables 8.1 and 8.2).

The offline selection cuts on the ϕ resonance and on the kaons of the $B^\pm \to \phi K^\pm$ channel are optimised by minimising the relative statistical uncertainty on the signal yield, while the other cuts are taken from the optimization of the $B_s^0 \to \eta'\eta'$ selection (see Sec. 8.1.3). The full list of offline cuts can be found in Table 7.18.

Table 7.18 *Offline requirements on top of stripping selection for $B^{\pm} \to \phi K^{\pm}$ channel.*

Variable		Requirement
Bachelor kaon		
transverse momentum	p_T	$> 1.2\,\text{GeV}/c$
PID	Prob_K	> 0.3
Kaons from ϕ		
PID	Prob_K	> 0.2
transverse momentum	p_T	$> 0.25\,\text{GeV}/c$
ϕ candidate		
mass	m_{KK}	$1.00 < m_{KK} < 1.05\,\text{GeV}/c^2$
momentum	p	$> 4.0\,\text{GeV}/c$
transverse momentum	p_T	$> 0.5\,\text{GeV}/c$
vertex quality	χ^2/ndf	< 9
B meson candidate		
mass	m	$5.0 < m < 5.5\,\text{GeV}/c^2$
transverse momentum	p_T	$> 1.5\,\text{GeV}/c$
vertex quality	χ^2/ndf	< 6
direction angle	DIRA	> 0.99995
distance of closest approach	DOCA	< 0.04

After the offline selection, multiple candidates are removed by keeping from each event only the candidate with the smallest $B^{\pm}$ vertex χ^2. The final size of the data samples is:

- $B^{\pm} \to \phi K^{\pm}$ (2012): 12828 events;

- $B^{\pm} \to \phi K^{\pm}$ (2011): 5309 events.

7.6.3 Fit model and validation

The model used for the fit to the $B^{\pm} \to \phi K^{\pm}$ events is identical to that of the analysis with 7 TeV data only (see Sec. 7.2.2), except for the shape of the peaking $B^{\pm}$ components for which the sum of a double-sided Crystal Ball function (CB) and a Gaussian function is used (see Eq. 6.14). The tail parameters and the fraction of events describes by the CB with respect to the total number of signal events are fixed to the central values obtained from the signal MC sample and are reported in Table 7.19. Moreover, we allow for different slope parameters in the two trigger categories.

In total, the fit has 40 free parameters:

- the $B^{\pm}$ and ϕ masses, m_B and m_{ϕ};

- the $B^{\pm}$ and ϕ mass resolutions, σ_{B-CB}, σ_{B-G} and σ_{ϕ};

- one ARGUS background parameter, c;

- ten linear background slopes, two in m and three in m_{KK} for each trigger category;

- six yields for the L0Hadron TOS subsample and six yields for the L0 TIS (not TOS) subsample;

- six *CP* asymmetries, one for each of the six components of the L0Hadron TOS subsample and six *CP* asymmetries for the L0 TIS (not TOS) subsample.

The shapes of the fit components and the compatibility between 7 TeV and 8 TeV data, is validated with MC and real data.

Study of the $B^{\pm} \to \phi K^{\pm}$ signal Monte Carlo

A two-dimensional fit of the $m_{\phi K^{\pm}}$ and $m_{K^+K^-}$ variables is performed. The $m_{\phi K^{\pm}}$ signal is described with a sum of a Crystal Ball and a Gaussian function sharing the same mean value, while the $m_{K^+K^-}$ signal is described by a relativistic Breit-Wigner function. The product of the two signal pdfs is linearly combined with a small component linear in both variables, to take in account a small background due to events not matched to the truth. All the parameters are compatible within the statistical errors, with the exception of the $B^{\pm}$ mass. In order to determine the tail parameters, a simultaneous two-dimensional fit of the two samples is done, with all the parameters free except the width of the ϕ resonance. Two different $B^{\pm}$ masses are allowed for the 7 TeV and for the 8 TeV data samples, while all the other parameters are shared. The results are summarised in Fig. 7.13 and Table 7.19. A discrepancy of 2.2 σ is found for the $B^{\pm}$ mass variable. Further studies on real data (see Sec 7.6.3) will show that this discrepancy has a negligible impact on the measurement.

Table 7.19   *Results of the simultaneous two-dimensional fit to the 7 TeV and 8 TeV $B^{\pm} \to \phi K^{\pm}$ signal MC candidates (displayed in Fig. 7.13). The "Fraction" parameter indicates the fraction of signal events described by the Crystal Ball.*

Parameter			Value and error
$B^{\pm}$ mass (2012)	m_B	[MeV/c^2]	5280.89 ± 0.10
$B^{\pm}$ mass (2011)	m_B	[MeV/c^2]	5280.52 ± 0.13
$B^{\pm}$ mass resolution	σ_{B-CB}	[MeV/c^2]	16.31 ± 0.25
$B^{\pm}$ mass resolution	σ_{B-G}	[MeV/c^2]	12.4 ± 0.4
Fraction			0.65 ± 0.04
$B^{\pm}$ mass tail parameter	α_L		1.46 ± 0.11
$B^{\pm}$ mass tail parameter	n_L		2.09 ± 0.15
$B^{\pm}$ mass tail parameter	α_R		1.36 ± 0.12
$B^{\pm}$ mass tail parameter	n_R		4.4 ± 0.6
ϕ mass	m_ϕ	[MeV/c^2]	1019.46 ± 0.02
ϕ mass resolution	σ_ϕ	[MeV/c^2]	1.07 ± 0.03

Figure 7.13 $K^+ K^- K^{\pm}$ *(top) and* $K^+ K^-$ *(bottom) mass distributions of the* $B^{\pm} \to \phi K^{\pm}$ *candidates in 2012 (left) and 2011 (right)* $B^{\pm} \to \phi K^{\pm}$ *MC events.*

Study of the $B^{\pm} \to \phi K^{\pm}$ real data samples

A simultaneous fit to the 7 TeV and 8 TeV real data samples is performed to study the discrepancy in the $B^{\pm}$ mass parameter, to study the background components, and to validate the fit model. The fit is two-dimensional in the $m_{\phi K}$ and m_{KK} variables and is simultaneous for the two samples. Five background components are found to be significant. The fixed parameters are the tail parameters of the Crystal Ball function, the fraction of signal events described by the Crystal Ball function, the m_h and p_h parameters of the partially reconstructed background, and the width of the ϕ resonance. Two different $B^{\pm}$ masses are allowed for 2011 and 2012, while all the other shape parameters are common to the 7 TeV and 8 TeV samples. In total the fit has 12 free shape parameters plus 12 free yields. The results of the fit are summarised in Fig. 7.14 and Table 7.20. The discrepancy observed in the MC for the $B^{\pm}$ mass parameters is not seen in real data. It is therefore decided to merge the 7 TeV and 8 TeV data samples for the CP asymmetry fit.
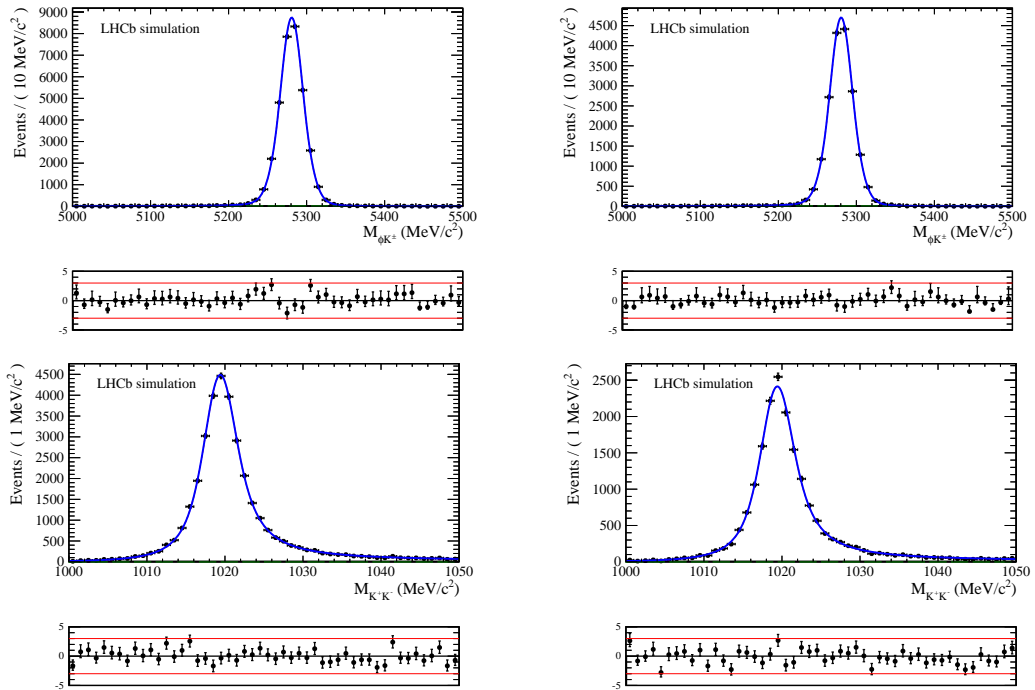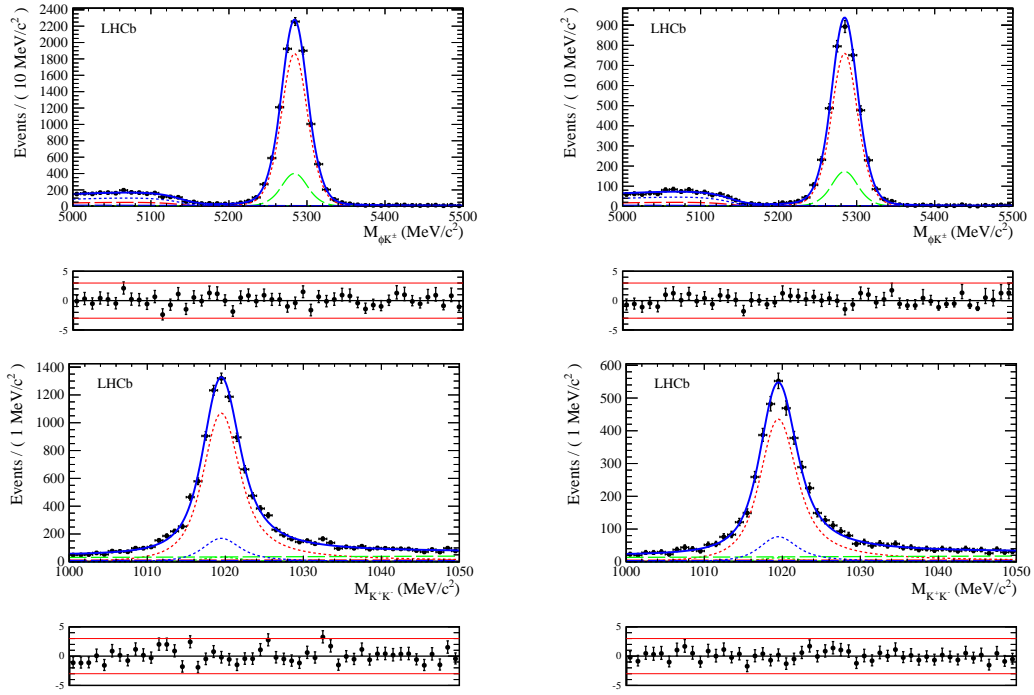
Figure 7.14   *$K^{+}K^{-}K^{\pm}$ (top) and $K^{+}K^{-}$ (bottom) mass distributions of the $B^{\pm} \to \phi K^{\pm}$ candidates in 2012 (left) and 2011 (right) $B^{\pm} \to \phi K^{\pm}$ real data events. The curves represent the results of the two-dimensional fit described in the text, with the following components: $B^{\pm} \to \phi K^{\pm}$ signal (dotted red), non-resonant $B^{\pm} \to K^{+}K^{-}K^{\pm}$ background (dashed red), partially reconstructed b-hadron background with (dotted blue) or without (dashed blue) a true ϕ meson, and combinatorial background with (dotted green) or without (dashed green) true ϕ meson. The total fit function is shown as the solid blue curves. The fit pulls are displayed in the small plots at the bottom.*

Table 7.20 *Results of the two-dimensional fit to the 7 TeV and 8 TeV $B^{\pm} \to \phi K^{\pm}$ data sample (displayed in Fig. 7.14).*

Parameter			Value and error
$B^{\pm}$ mass (2012)	m_B	[MeV/c^2]	5284.03 ± 0.19
$B^{\pm}$ mass (2011)	m_B	[MeV/c^2]	5284.53 ± 0.36
$B^{\pm}$ mass resolution	σ_{B-CB}	[MeV/c^2]	18.8 ± 0.4
$B^{\pm}$ mass resolution	σ_{B-G}	[MeV/c^2]	14.1 ± 0.8
ϕ mass	m_{ϕ}	[MeV/c^2]	1019.54 ± 0.03
ϕ mass resolution	σ_{ϕ}	[MeV/c^2]	1.19 ± 0.06
c Argus parameter	c		16.9 ± 1.4
p_1 - Poly 1 - comb bkg with true ϕ meson ($m_{\phi K^+}$)			-0.06 ± 0.36
p_1 - Poly 1 - comb bkg without true ϕ meson ($m_{\phi K^+}$)			-0.50 ± 0.13
p_1 - Poly 1 - comb bkg without true ϕ meson ($m_{K^+K^-}$)			0.06 ± 0.14
p_1 - Poly 1 - non-resonant $B^{\pm} \to K^+K^-K^{\pm}$ bkg ($m_{K^+K^-}$)			0.13 ± 0.05
p_1 - Poly 1 - partially reco $b \to$ non-ϕ X bkg ($m_{K^+K^-}$)			0.06 ± 0.09
Yield of $B^{\pm} \to \phi K^{\pm}$ signal (2012)			8366 ± 114
Yield of non-resonant $B^{\pm} \to K^+K^-K^{\pm}$ background (2012)			1798 ± 77
Yield of partially reconstructed $b \to \phi$ X background (2012)			627 ± 57
Yield of partially reconstructed $b \to$ non-ϕ X background (2012)			1320 ± 67
Yield of combinatorial background with true ϕ meson (2012)			267 ± 81
Yield of combinatorial background without true ϕ meson (2012)			449 ± 67
Yield of $B^{\pm} \to \phi K^{\pm}$ signal (2011)			3409 ± 71
Yield of non-resonant $B^{\pm} \to K^+K^-K^{\pm}$ background (2011)			777 ± 49
Yield of partially reconstructed $b \to \phi$ X background (2011)			260 ± 34
Yield of partially reconstructed $b \to$ non-ϕ X background (2011)			599 ± 36
Yield of combinatorial background with true ϕ meson (2011)			95 ± 34
Yield of combinatorial background without true ϕ meson (2011)			169 ± 35

7.6.4 Raw asymmetry

From the simultaneous fit to the $B^{+} \to \phi K^{+}$ and $B^{-} \to \phi K^{-}$ candidates in the two trigger subsamples the following values for the raw $B^{\pm} \to \phi K^{\pm}$ CP asymmetries are found:

$$A^{CP}_{\mathrm{raw,TOS}}(B^{\pm} \to \phi K^{\pm}) = (0.3 \pm 1.4) \times 10^{-2}, \tag{7.18}$$

$$A^{CP}_{\mathrm{raw,TIS}}(B^{\pm} \to \phi K^{\pm}) = (-1.1 \pm 1.8) \times 10^{-2}. \tag{7.19}$$

The fit results are summarised in Table 7.21, and shown in Figs. 7.15 and 7.16. The raw asymmetry of the $B^{\pm} \to J/\psi K^{\pm}$ control channel is extracted from the fit described in Sec. 8.2.2.
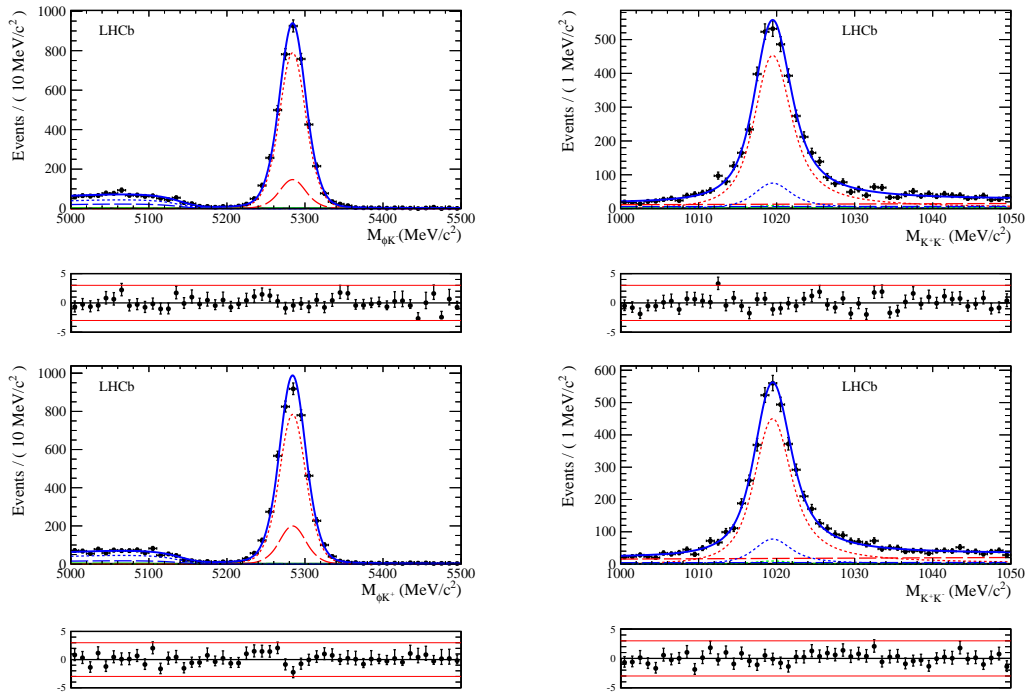

Figure 7.15 *$K^{+}K^{-}K^{\pm}$ (left) and $K^{+}K^{-}$ (right) mass distributions of $B^{-} \to \phi K^{-}$ (top) and $B^{+} \to \phi K^{+}$ (bottom) data candidates in the subsample selected by the L0Hadron TOS trigger line. The curves represent the results of the simultaneous two-dimensional fit described in the text. The following components are present: $B^{\pm} \to \phi K^{\pm}$ signal (dotted red), non-resonant $B^{\pm} \to K^{+}K^{-}K^{\pm}$ background (dashed red), partially reconstructed b-hadron background with (dotted blue) or without (dashed blue) a true ϕ meson, and combinatorial background with (dotted green) or without (dashed green) true ϕ meson. The total fit function is shown as the solid blue curves. The fit pulls are displayed in the small plots at the bottom.*

7.6.5 CP asymmetry

The raw asymmetry of the $B^{\pm} \to \phi K^{\pm}$ channel is corrected by the production and detection asymmetry by subtracting the raw asymmetry of the control channel, separately for
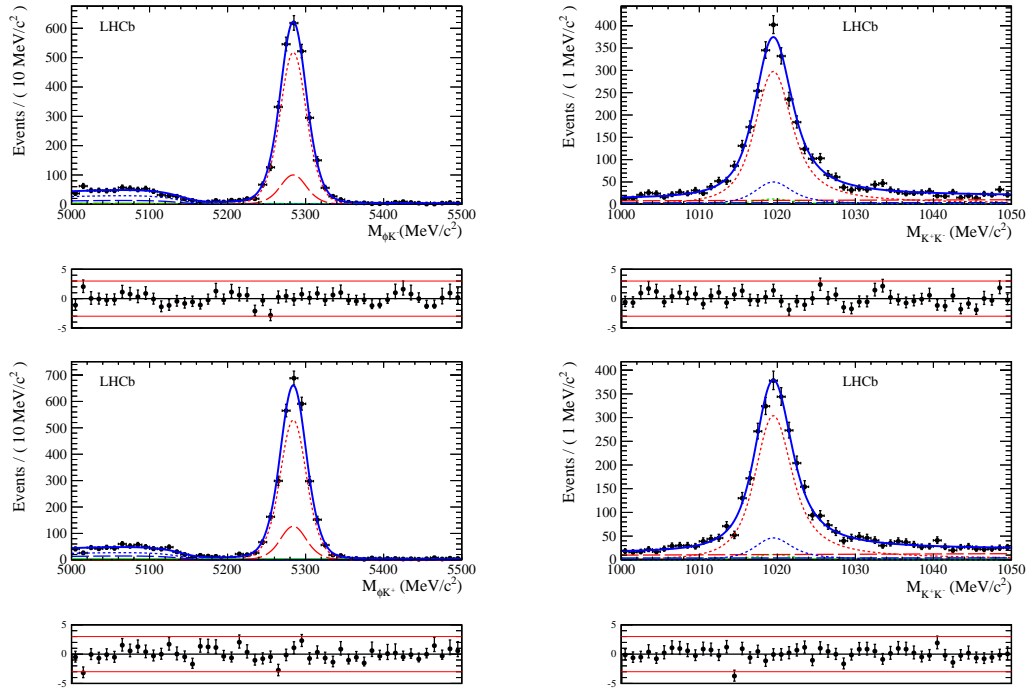
Figure 7.16 $K^+ K^- K^{\pm}$ *(left) and $K^+ K^-$ (right) mass distributions of $B^- \to \phi K^-$ (top) and $B^+ \to \phi K^+$ (bottom) data candidates in the subsample selected by the L0 TIS (not TOS) trigger lines. The curves represent the results of the simultaneous two-dimensional fit described in the text. The following components are present: $B^{\pm} \to \phi K^{\pm}$ signal (dotted red), non-resonant $B^{\pm} \to K^+ K^- K^{\pm}$ background (dashed red), partially reconstructed b-hadron background with (dotted blue) or without (dashed blue) a true ϕ meson, and combinatorial background with (dotted green) or without (dashed green) true ϕ meson. The total fit function is shown as the solid blue curves. The fit pulls are displayed in the small plots at the bottom.*

the TIS and the TOS trigger subsamples. The resulting asymmetries in the two trigger categories are then combined according to

$$\Delta \mathcal{A}^{CP} = f \Delta A_{\text{TOS}}^{CP} + (1 - f) \Delta A_{\text{TIS}}^{CP}, \tag{7.20}$$

where f is the fraction of events selected by the L0Hadron TOS trigger line. We find:

$$\Delta \mathcal{A}^{CP}(B^{\pm} \to \phi K^{\pm}) = 0.014 \pm 0.011, \tag{7.21}$$

that, combined with the $B^{\pm} \to J/\psi K^{\pm}$ physics asymmetry $\mathcal{A}^{CP}(B^{\pm} \to J/\psi K^{\pm}) = 0.003 \pm 0.006$ [11], gives:

$$\mathcal{A}^{CP}(B^{\pm} \to \phi K^{\pm}) = (1.7 \pm 1.1 \pm 0.2 \pm 0.6) \times 10^{-2}. \tag{7.22}$$

This result includes the systematic uncertainty computed in the next section. All the values are summarised in Table 7.22.

Table 7.21   *Results of the simultaneous two-dimensional $\mathcal{A}^{CP}$ fit of the $B^- \to \phi K^-$ and $B^+ \to \phi K^+$ candidates in the two trigger subsamples (displayed in Figs. 7.15 and 7.16) to measure the CP asymmetry of the $B^{\pm} \to \phi K^{\pm}$ decay.*

Parameter			Value and error
$B^{\pm}$ mass	m_B	[MeV/c^2]	5284.17 ± 0.16
$B^{\pm}$ mass resolution	σ_{B-CB}	[MeV/c^2]	18.83 ± 0.37
$B^{\pm}$ mass resolution	σ_{B-G}	[MeV/c^2]	14.2 ± 0.8
ϕ mass	m_ϕ	[MeV/c^2]	1019.54 ± 0.03
ϕ mass resolution	σ_ϕ	[MeV/c^2]	1.19 ± 0.06
c Argus parameter	c		15.4 ± 1.4
p_1 - Poly 1 - comb bkg with true ϕ meson ($m_{\phi K^+}$ TOS)			0.4 ± 1.1
p_1 - Poly 1 - comb bkg without true ϕ meson ($m_{\phi K^+}$ TOS)			-0.58 ± 0.18
p_1 - Poly 1 - comb bkg without true ϕ meson ($m_{K^+K^-}$ TOS)			0.18 ± 0.20
p_1 - Poly 1 - non-resonant $B^{\pm} \to K^+K^-K^{\pm}$ bkg ($m_{K^+K^-}$ TOS)			0.16 ± 0.06
p_1 - Poly 1 - partially reco $b \to$ non-ϕ X bkg ($m_{K^+K^-}$ TOS)			0.10 ± 0.11
p_1 - Poly 1 - comb bkg with true ϕ meson ($m_{\phi K^+}$ TIS)			-0.1 ± 0.4
p_1 - Poly 1 - comb bkg without true ϕ meson ($m_{\phi K^+}$ TIS)			-0.39 ± 0.19
p_1 - Poly 1 - comb bkg without true ϕ meson ($m_{K^+K^-}$ TIS)			-0.27 ± 0.18
p_1 - Poly 1 - non-resonant $B^{\pm} \to K^+K^-K^{\pm}$ bkg ($m_{K^+K^-}$ TIS)			0.09 ± 0.07
p_1 - Poly 1 - partially reco $b \to$ non-ϕ X bkg ($m_{K^+K^-}$ TIS)			-0.02 ± 0.13
$\mathcal{A}_{\text{raw}}^{CP}(B^{\pm} \to \phi K^{\pm})$ (TOS)			0.003 ± 0.014
Yield of $B^{\pm} \to \phi K^{\pm}$ signal (TOS)			7078 ± 106
Yield of non-resonant $B^{\pm} \to K^+K^-K^{\pm}$ background (TOS)			1549 ± 71
Yield of partially reconstructed $b \to \phi$ X background (TOS)			1215 ± 70
Yield of partially reconstructed $b \to$ non-ϕ X background (TOS)			512 ± 54
Yield of combinatorial background with true ϕ meson (TOS)			120 ± 61
Yield of combinatorial background without true ϕ meson (TOS)			304 ± 63
$\mathcal{A}_{\text{raw}}^{CP}(B^{\pm} \to \phi K^{\pm})$ (TIS)			-0.011 ± 0.018
Yield of $B^{\pm} \to \phi K^{\pm}$ signal (TIS)			4704 ± 85
Yield of non-resonant $B^{\pm} \to K^+K^-K^{\pm}$ background (TIS)			1029 ± 58
Yield of partially reconstructed $b \to \phi$ X background (TIS)			741 ± 51
Yield of partially reconstructed $b \to$ non-ϕ X background (TIS)			384 ± 45
Yield of combinatorial background with true ϕ meson (TIS)			193 ± 61
Yield of combinatorial background without true ϕ meson (TIS)			300 ± 53

Table 7.22 *Raw charge asymmetries for the $B^{\pm} \to \phi K^{\pm}$ and $B^{\pm} \to J/\psi K^{\pm}$ decays, their difference $\Delta \mathcal{A}^{CP}$, and the fraction of $B^{\pm} \to \phi K^{\pm}$ signal events in each trigger sub-sample. All uncertainties are statistical only.*

	TOS sub-sample	TIS (not TOS) sub-sample
$\mathcal{A}^{CP}_{\mathrm{raw},k}(B^{\pm} \to \phi K^{\pm})$	0.003 ± 0.014	-0.011 ± 0.018
$\mathcal{A}^{CP}_{\mathrm{raw},k}(B^{\pm} \to J/\psi K^{\pm})$	-0.0203 ± 0.0035	-0.0107 ± 0.0026
$\Delta \mathcal{A}^{CP}(B^{\pm} \to \phi K^{\pm})$	0.024 ± 0.015	0.0002 ± 0.0178
$N_k/(N_{\mathrm{TOS}} + N_{\mathrm{TIS}})(B^{\pm} \to \phi K^{\pm})$	60.1%	39.9%
weighted $\Delta \mathcal{A}^{CP}$ average $(B^{\pm} \to \phi K^{\pm})$	0.014 ± 0.011	
weighted $\Delta \mathcal{A}^{CP}$ average $(B^{\pm} \to \eta' K^{\pm})$	-0.005 ± 0.012	

Systematic uncertainties

The systematic contributions to the $\mathcal{A}^{CP}$ measurement, summarized in Table 7.23, lead to a total systematic uncertainty of 0.22×10^{-2}. The strategy adopted to compute the systematic uncertainties is the same of that used for the measurement of the $B^{\pm} \to \eta' K^{\pm}$ *CP* asymmetry (see 8.5.1). The source of uncertainties are described below.

Table 7.23   Absolute systematic uncertainties on $\mathcal{A}^{CP}(B^{\pm} \to \phi K^{\pm})$.

Source	Absolute systematic uncertainty $\times 10^2$
Fit model	0.20×10^{-2}
$B^{\pm} \to J/\psi K^{\pm}$ kinematics	0.08×10^{-2}
Fiducial cut	0.05×10^{-2}
Total	0.22×10^{-2}

- The fit model systematic uncertainty is due to two different contributions. The first takes into account the uncertainty due to the fixed parameters in the fit. To estimate it, the real data sample is fitted 5000 times varying the fixed parameters according to a Gaussian distribution centred on the value used in the nominal fit and with a width equal to the MC uncertainty. The RMS of the *CP* asymmetry distributions of the two trigger subsamples are combined in quadrature with weights equal to the fraction of events in each subsample, and the result, equal to 0.018×10^{-2}, is applied as a systematic uncertainty. In addition we consider five sources on uncertainty in the fit model: we replace the linear components in $m_{\phi K^{\pm}}$ with exponential components, we replace the linear components in $m_{K^+K^-}$ with a quadratic shape, we fix the end point of the Argus function to (5150 ± 2) MeV/c^2 and we fix the p parameter of the Argus function to 1.0 ± 0.1. The variation of the Argus end point and of the p parameter is chosen equal to the their uncertainty, which is obtained when the fit shown in Fig. 7.14 is performed leaving these two parameters separately floating. The differences between the nominal $\Delta\mathcal{A}^{CP}$ and that obtained from the new fits are summed in quadrature, leading to a systematic uncertainty of 0.20×10^{-2}. Together, the two contributions gives a total systematic uncertainty of 0.20×10^{-2}.

- A systematic uncertainty is introduced to take in account the effect of the different kinematic distribution of the bachelor kaon in the signal channels and in the reference channel (shown in Fig. 8.16). The asymmetry is computed in bins of p_{T} and then combined taking into account the fraction of events in each bin. The difference with respect to the nominal $\Delta\mathcal{A}^{CP}$ value, equal to 0.08×10^{-2}, is applied as a systematic uncertainty.

- To take into account the left-right asymmetry of the detector, the fiducial cut of

Ref. [85] is applied,

$$|P_x| \leqslant \alpha(P_z - P_0), \alpha = 0.317, P_0 = 2400\,\text{MeV}/c\,, \tag{7.23}$$

where P_x and P_z are respectively the x and z components of the bachelor kaon momentum. The difference with respect to the nominal $\Delta\mathcal{A}^{CP}$ value, equal to 0.05×10^{-2}, is applied as a systematic uncertainty.

7.6.6 Further checks

Magnet polarity

To investigate the effect of the magnet polarity on the $B^\pm \to \phi K^\pm$ asymmetry, the *CP* measurement is repeated separately for the two magnetic field polarities. The results, shown in Table 7.24, are fully compatible.

Table 7.24   *Comparison between magnet-up and magnet-down raw CP asymmetries in $B^\pm \to \phi K^\pm$ decays.*

	L0Hadron TOS	L0 TIS (not TOS)
Magnet up	$(-1.3 \pm 2.1)\%$	$(0.4 \pm 2.7)\%$
Magnet down	$(1.6 \pm 1.9)\%$	$(-2.1 \pm 2.4)\%$
Compatibility (σ)	1.0	0.7

S-wave contribution

The two-dimensional fit of the $B^\pm \to \phi K^\pm$ sample allows to distinguish between the P-wave signal and the S-wave $B^\pm \to K^+K^-K^\pm$ component. Contribution from others S-wave components, such as f_0 or a_0, are negligible because of the tight cuts on the mass variables and because the m_ϕ distribution is fitted. However a contribution due to the interference between the P-wave and the S-wave components, which is not flat in the signal region, could be present. We do not perform an angular analysis, however, we compare the signal *sPlot* angular distribution with the MC angular distribution to check if a systematic uncertainty needs to be added. We consider the decay angle defined as the angle between the momentum of the K^+ from the ϕ decay and the $B^\pm$ in the ϕ rest frame. The plot on the left of Fig. 7.17 shows the cosine of this angle for signal *sPlot* (black) and MC (red), while the plot on the right shows the ratio between the two. A fit of this ratio gives a slope of -0.008 ± 0.032, compatible with zero. No systematic uncertainty is therefore applied.
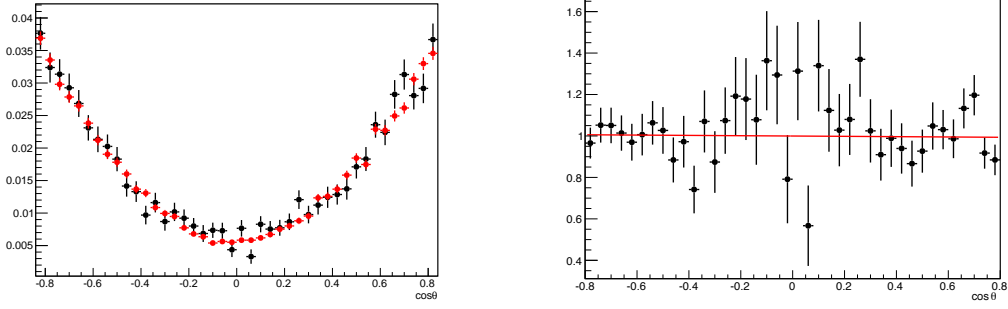
Figure 7.17   *Left: normalised distributions of the cosine of the decay angle for $B^{\pm} \to \phi K^{\pm}$ signal from Monte Carlo (red) and data (black). Right: ratio between data and Monte Carlo, fitted with a linear function. The decay angle is defined as the angle between the momentum of the K^{+} from the ϕ decay and the $B^{\pm}$ in the ϕ rest frame.*

7.7   Summary

The goal of this analysis was to search for the $B^{\pm} \to \phi\pi^{\pm}$ decay and measure $\mathcal{A}^{CP}(B^{\pm} \to \phi K^{\pm})$ with the $1\,\text{fb}^{-1}$ of data collected at $\sqrt{s} = 7\,\text{TeV}$. We find 19.1 ± 19.2 $B^{\pm} \to \phi\pi^{\pm}$ events with a statistical significance of 1.0. The yield ratio $N_{\phi\pi}/N_{\phi K}$ is equal to $(5.1^{+5.3}_{-5.0}(\text{stat}) \pm 2.1(\text{syst})) \times 10^{-3}$. The ratio between the $\mathcal{B}(B^{\pm} \to \phi\pi^{\pm})$ and the $\mathcal{B}(B^{\pm} \to \phi K^{\pm})$ is calculated as

$$\frac{\mathcal{B}(B^{\pm} \to \phi\pi^{\pm})}{\mathcal{B}(B^{\pm} \to \phi K^{\pm})} = \frac{N_{\phi\pi}\,\varepsilon(B^{\pm} \to \phi K^{\pm})}{N_{\phi K}\,\varepsilon(B^{\pm} \to \phi\pi^{\pm})} = (6.6 \pm^{+6.9}_{-6.6}(\text{stat}) \pm 2.8(\text{syst})) \times 10^{-3}, \quad (7.24)$$

where $\varepsilon(B^{\pm} \to \phi\pi^{\pm})/\varepsilon(B^{\pm} \to \phi K^{\pm}) = 0.76 \pm 0.03(\text{stat}) \pm 0.04(\text{syst})$.

The $B^{\pm} \to \phi\pi^{\pm}$ branching fraction is calculated, and we compute the 90% confidence level upper limit from the integral of the likelihood in the positive region, using the $B^{\pm} \to \phi K^{\pm}$ decay as reference channel ($\mathcal{B}(B^{\pm} \to \phi K^{\pm}) = (8.8^{+0.7}_{-0.6}) \times 10^{-6}$). The uncertainty on the $\mathcal{B}(B^{\pm} \to \phi K^{\pm})$ is found to be negligible in the computation of the upper limit. The upper limits obtained including the statistical and systematic uncertainties are

$$\mathcal{B}(B^{\pm} \to \phi\pi^{\pm}) < 1.55 \times 10^{-7} \text{ at } 90\% \text{ CL}, \quad (7.25)$$
$$\mathcal{B}(B^{\pm} \to \phi\pi^{\pm}) < 1.80 \times 10^{-7} \text{ at } 95\% \text{ CL}.$$

The $B^{\pm} \to \phi K^{\pm}$ CP asymmetry is also measured:

$$\Delta\mathcal{A}^{CP}(B^{\pm} \to \phi K^{\pm}) = (1.9 \pm 2.1(\text{stat}) \pm 0.7(\text{syst})) \times 10^{-2}. \quad (7.26)$$

Using the current world average $\mathcal{A}^{CP}(B^{\pm} \to J/\psi K^{\pm}) = 0.003 \pm 0.006$ [11], one obtains

$$\mathcal{A}^{CP}(B^{\pm} \to \phi K^{\pm}) = (2.2 \pm 2.1(\text{stat}) \pm 0.7(\text{syst}) \pm 0.6(J/\psi K^{\pm})) \times 10^{-2}. \quad (7.27)$$

In conclusion, using the LHCb 2011 dataset, no evidence for the decay $B^{\pm} \to \phi\pi^{\pm}$ is

found. However an upper limit $\mathcal{B}(B^{\pm} \to \phi\pi^{\pm}) < 1.55 \times 10^{-7}$ at 90% CL is obtained, which improves on the previous best upper limit set by the BaBar collaboration [37], $\mathcal{B}(B^{\pm} \to \phi\pi^{\pm}) < 2.4 \times 10^{-7}$ at 90% CL.

The measurement of the *CP* charge asymmetry of the $B^{\pm} \to \phi K^{\pm}$ decay is also improved. We obtain $\mathcal{A}^{CP}(B^{\pm} \to \phi K^{\pm}) = 0.022 \pm 0.023$, which is compatible with no asymmetry, but has a smaller uncertainty than the current world average $\mathcal{A}^{CP}(B^{\pm} \to \phi K^{\pm}) = 0.10 \pm 0.04$.

An update of the $B^{\pm} \to \phi K^{\pm}$ *CP* asymmetry measurement is performed including the $2\,\text{fb}^{-1}$ of data collected at $\sqrt{s} = 8\,\text{TeV}$, and leads to:

$$\mathcal{A}^{CP}(B^{\pm} \to \phi K^{\pm}) = (1.7 \pm 1.1 \pm 0.2 \pm 0.6) \times 10^{-2}. \tag{7.28}$$

The statistical error reduces as expect from the increase in statistics. A clear improvement of the systematic uncertainty can be also observed. This is explained in part by the increase in data statistics, which better constrains the fit model.

Search for $B_s^0 \to \eta'\eta'$ decays and measurement of the charge asymmetry in $B^\pm \to \eta'K^\pm$ decays

The goals of the study presented in this chapter are the search for the $B_s^0 \to \eta'\eta'$ decay and the measurement of the $B^\pm \to \eta'K^\pm$ CP asymmetry, using the $3\,\text{fb}^{-1}$ of data collected at $\sqrt{s} = 7\,\text{TeV}$ and $\sqrt{s} = 8\,\text{TeV}$ during the LHC Run 1. Hereafter we will refer to the samples with different centre-of-mass energies as the 7 TeV and 8 TeV samples.

The approach used is very similar to that of the $B^\pm \to \phi h^\pm$ analysis described in Chapter 7. The $B_s^0 \to \eta'\eta'$ branching fraction is measured with respect to that of the $B^\pm \to \eta'K^\pm$ decay. The selection, optimised for the search of the $B_s^0 \to \eta'\eta'$ mode, is as similar as possible for the signal and the reference channel in order to reduce most of the systematic effects. Two data samples, one with events reconstructed as $B_s^0 \to \eta'\eta'$ and the other with events reconstructed as $B^\pm \to \eta'K^\pm$, are fitted simultaneously in order to extract the $B_s^0 \to \eta'\eta'$ and the $B^\pm \to \eta'K^\pm$ signal yields: the fit is multi-dimensional in the masses of the decaying particles of the two decay chains, and the 7 TeV and 8 TeV samples are merged. A simultaneous fit to the 7 TeV and 8 TeV samples is instead performed to directly measure the ratio of the branching fractions.

The measurement of the $B^\pm \to \eta'K^\pm$ CP asymmetry is performed fitting the positively and negatively charged candidates of the $B^\pm \to \eta'K^\pm$ sample, simultaneously in two trigger categories. The raw value of the asymmetry is corrected for production and detection asymmetries using the $B^\pm \to J/\psi K^\pm$ control channel.

8.1 Data samples and event selection

8.1.1 Real data

The analysis is performed using the data collected by LHCb in 2011 and 2012 at $\sqrt{s} = 7$ TeV and $\sqrt{s} = 8$ TeV, respectively, corresponding to a total integrated luminosity of approximately $3\,\text{fb}^{-1}$. The samples are taken from the `Reco14-Stripping20r0(1)p2`

`BhadronCompleteEvent` stream and are processed with BRUNEL v43r2p3 and DAVINCI v32r2p12.

8.1.2 Monte Carlo simulation data

The following Monte Carlo simulation samples, based on GAUSS v45r3 and GAUSS v45r7, and generated with PYTHIA 8, are used:

- $B_s^0 \to \eta'\eta'$ (event type 13104241) at $\sqrt{s} = 8\,\text{TeV}$: 1758107 signal events;

- $B_s^0 \to \eta'\eta'$ (event type 13104241) at $\sqrt{s} = 7\,\text{TeV}$: 900127 signal events;

- $B^\pm \to \eta'K^\pm$ (event type 12103211) at $\sqrt{s} = 8\,\text{TeV}$: 1028498 signal events;

- $B^\pm \to \eta'K^\pm$ (event type 12103211) at $\sqrt{s} = 7\,\text{TeV}$: 539745 signal events.

The η' resonance is forced to decay in the $\pi^+\pi^-\gamma$ final state.

8.1.3 Event selection

As explained in Chapter 6, the event selection proceeds through the trigger, the stripping and the offline selection. The selection criteria used in the version `Reco14-Stripping20r0(1)p2` of the stripping lines `BetaSQ2B3piSelectionLine` and `BetaSQ2B4piSelectionLine` are listed in Table 8.1.

The events selected by the above stripping lines are reconstructed as $B_s^0 \to \eta'\eta'$ and $B^\pm \to \eta'K^\pm$, respectively. In all cases, the η' mesons are reconstructed in the $\pi^+\pi^-\gamma$ final state. In order to better understand the trigger efficiency, reconstructed events are required to pass the specific triggers listed in Table 8.2.

Finally, an offline selection is applied to further reduce the background. The cuts are optimised on the $B_s^0 \to \eta'\eta'$ mode, using the figure of merit in Eq. 6.1 for the values $a = 2, 3, 4$, and 5. The same set of optimised cuts is obtained in all four cases. A second method of optimisation, based on Monte Carlo pseudo-experiments (see Sec. 6.1), is applied as a cross-check. The set of cuts obtained is identical to that obtained with the first method.

The same offline selection is applied to the events reconstructed as $B^\pm \to \eta'K^\pm$. On top of this selection, cuts on the bachelor kaon are separately optimised. All the cuts are listed in Table 8.3.

After the offline selection, multiple candidates are removed by keeping from each event only the candidate with the smallest $B^\pm$ or B_s^0 vertex χ^2. The final size of the data samples is:

- $B^\pm \to \eta'K^\pm$ (8 TeV): 10939 events;

- $B^\pm \to \eta' K^\pm$ (7 TeV): 4275 events;

- $B_s^0 \to \eta' \eta'$ (8 TeV): 266 events;

- $B_s^0 \to \eta' \eta'$ (7 TeV): 85 events.

Table 8.1 *Pre-selection cuts applied by the* `BetaSQ2B3piSelectionLine` *(3π) and* `BetaSQ2B4piSelectionLine` *(4π) stripping lines. The variable m_{corr} is defined in Table 7.1.*

Variable		Requirement	
		3π line	4π line
Pions			
PV impact parameter χ^2	χ^2_{IP}	> 25	> 25
Track ghost probability		< 0.5	< 0.5
Bachelor $\pi^\pm$			
transverse momentum	p_{T}	$> 1.0\,\mathrm{GeV}/c$	
Resonance (ρ^0)			
transverse momentum	p_{T}	$> 1.0\,\mathrm{GeV}/c$	$> 0.6\,\mathrm{GeV}/c$
mass	$m_{\pi\pi}$	$< 1.1\,\mathrm{GeV}/c^2$	$< 1.1\,\mathrm{GeV}/c^2$
vertex quality	χ^2/ndf	< 9	< 9
B meson			
mass	m	$4.2 < m < 6.7\,\mathrm{GeV}/c^2$	$3.5 < m < 5.7\,\mathrm{GeV}/c^2$
corrected mass	m_{corr}	$< 7.0\,\mathrm{GeV}/c^2$	$< 6.0\,\mathrm{GeV}/c^2$
vertex quality	χ^2/ndf	< 9	< 9
transverse momentum	p_{T}	$> 2.5\,\mathrm{GeV}/c$	$> 2.5\,\mathrm{GeV}/c$
trigger		`Hlt1Track*Decision (TOS)`	

Table 8.2 *Trigger lines required at different levels. In order to be selected, an event must satisfy, at each trigger level, the specific requirements of at least one of the listed lines. TOS events are selected on the signal final state, while TIS events are selected on the rest of the event.*

L0	HLT1	HLT2
`Hadron (TOS)`	`TrackAllL0 (TOS)`	`Topo2BodyBBBDT (TOS)`
`Hadron (TIS)`		`Topo3BodyBBBDT (TOS)`
`Photon (TIS)`		`Topo4BodyBBBDT (TOS)`
`Muon (TIS)`		
`Electron (TIS)`		

8.1.4 Selection efficiencies

The efficiencies of the $B_s^0 \to \eta' \eta'$ and $B^\pm \to \eta' K^\pm$ selections are computed according to Eq. 6.4, and are summarised in Table 8.4. These are based on MC samples where the

Table 8.3   *Offline requirements applied on top of the stripping to select $B_s^0 \to \eta'\eta'$ and $B^\pm \to \eta'K^\pm$ candidates.*

Variable		Requirement
Bachelor kaon		
transverse momentum	p_T	$> 1.2\,\mathrm{GeV}/c$
PID	ProbNNk	> 0.3
Pions from η'		
PID	ProbNNπ	> 0.1
transverse momentum	p_T	$> 0.25\,\mathrm{GeV}/c$
Photon from η'		
confidence level	CL_γ	> 0.1
transverse momentum	p_T	$> 0.50\,\mathrm{GeV}/c$
η' meson		
mass	$m_{\pi\pi\gamma}$	$0.88 < m_{\pi\pi\gamma} < 1.04\,\mathrm{GeV}/c^2$
momentum	p	$> 4.0\,\mathrm{GeV}/c$
transverse momentum	p_T	$> 1.5\,\mathrm{GeV}/c$
$\pi\pi$ invariant mass	$m_{\pi\pi}$	$> 0.56\,\mathrm{GeV}/c^2$
vertex quality	χ^2/ndf	< 9
B_s^0 ($B^\pm$) meson candidate		
mass	m	$5.0 < m < 5.6(5.5)\,\mathrm{GeV}/c^2$
transverse momentum	p_T	$> 1.5\,\mathrm{GeV}/c$
vertex quality	χ^2/ndf	< 6
direction angle	DIRA	> 0.99995
distance of closest approach	DOCA	$< 0.04\,\mathrm{mm}$

true $B_s^0 \to \eta'\eta'$ lifetime was set to 1.517 ps. However, in absence of *CP* violation, only the light mass eigenstate of the $B_s^0 - \bar{B}_s^0$ system contributes to this decay. To account for this, we reweigh the MC events to a lifetime of 1.406 ps [86], and determine a correction of 2.9% to apply to the efficiency ratio.

The efficiency ratios used for the measurement of $\mathcal{B}(B_s^0 \to \eta'\eta')$ are:

$$\frac{\varepsilon(B^\pm \to \eta'K^\pm)}{\varepsilon(B_s^0 \to \eta'\eta')} = 7.85 \pm 0.26 \; (2012), \qquad \frac{\varepsilon(B^\pm \to \eta'K^\pm)}{\varepsilon(B_s^0 \to \eta'\eta')} = 8.46 \pm 0.35 \; (2011), \quad (8.1)$$

which include the lifetime correction.

SPD multiplicity

The SPD multiplicity is not well reproduced in the simulation. As a consequence, the cut applied by the L0 trigger lines on the SPD multiplicity (< 600) rejects a smaller fraction of events in the Monte Carlo than in real data. Figure 8.1 shows the SPD multiplicity distribution in real data and Monte Carlo data.

Table 8.4   *Efficiencies for the 7 TeV and 8 TeV $B^{\pm} \to \eta' K^{\pm}$ and $B^0_s \to \eta' \eta'$ signals.*

	$B^{\pm} \to \eta' K^{\pm}$	$B^0_s \to \eta' \eta'$
	8 TeV (2012)	
$\varepsilon^{\text{geom}}$	$(17.80 \pm 0.05)\%$	$(16.55 \pm 0.023)\%$
$\varepsilon^{\text{sel|geom}}$	$(1.420 \pm 0.012)\%$	$(0.193 \pm 0.004)\%$
$\varepsilon^{\text{PID|sel\&geom}}$	$(87.928 \pm 0.002)\%$	$(97.226 \pm 0.002)\%$
$\varepsilon^{\text{trig|PID\&sel\&geom}}$	$(42.95 \pm 0.36)\%$	$(40.35 \pm 0.77)\%$
TOTAL	$(0.0954 \pm 0.0012)\%$	$(0.0125 \pm 0.0004)\%$
	7 TeV (2011)	
$\varepsilon^{\text{geom}}$	$(17.55 \pm 0.03)\%$	$(16.029 \pm 0.024)\%$
$\varepsilon^{\text{sel|geom}}$	$(1.589 \pm 0.018)\%$	$(0.202 \pm 0.005)\%$
$\varepsilon^{\text{PID|sel\&geom}}$	$(87.120 \pm 0.002)\%$	$(96.812 \pm 0.003)\%$
$\varepsilon^{\text{trig|PID\&sel\&geom}}$	$(44.01 \pm 0.55)\%$	$(41.55 \pm 1.05)\%$
TOTAL	$(0.1069 \pm 0.0018)\%$	$(0.0130 \pm 0.0005)\%$
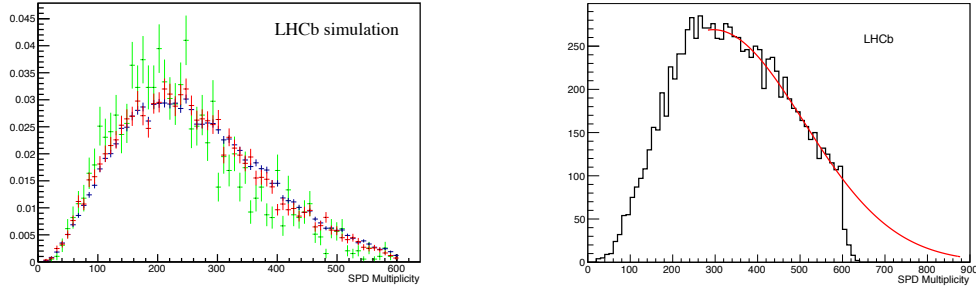
Figure 8.1   *Left: normalised SPD multiplicity distributions of $B^0_s \to \eta' \eta'$ (green), $B^{\pm} \to \eta' K^{\pm}$ (red) and $B^{\pm} \to \phi K^{\pm}$ (blue) Monte Carlo events. Right: SPD multiplicity distribution of real $B^{\pm} \to \phi K^{\pm}$ data candidates.*

To estimate the fraction of rejected events, the $B^{\pm} \to \phi K^{\pm}$ data sample used for the update of the *CP* asymmetry with $3\,\text{fb}^{-1}$ is taken as reference, since a similar selection is applied and the statistics are higher. The SPD multiplicity distribution of the real $B^{\pm} \to \phi K^{\pm}$ data is fitted in the region below 600 with an ad-hoc function in order to estimate the fraction of rejected events above 600. The value of the SPD multiplicity cut in $B^{\pm} \to \phi K^{\pm}$ MC events that gives the same fraction of rejected events as in real data is found to be 430. This cut at 430 is then applied to the $B^{\pm} \to \eta' K^{\pm}$ and $B^0_s \to \eta' \eta'$ MC samples to determine the efficiency for these two channels. We obtain:

- $(94.6 \pm 0.9)\%$ for the $B^0_s \to \eta' \eta'$ mode (2012)

- $(98.5 \pm 0.5)\%$ for the $B^0_s \to \eta' \eta'$ mode (2011)

- $(92.4 \pm 0.7)\%$ for the $B^{\pm} \to \eta' K^{\pm}$ mode (2012)

- $(96.4 \pm 0.5)\%$ for the $B^\pm \to \eta'K^\pm$ mode (2011)

The error is the sum in quadrature of three different contributions. The first is the Poissonian error on the expected number of events with SPD multiplicity larger than 600 in real data. The second uncertainty is due to the fit to the SPD multiplicity distribution, which is computed from $B^\pm \to \phi K^\pm$ Monte Carlo in the following way: two fits are performed to extrapolate the shape of the SPD multiplicity distribution, one in the region below 430 and the second in the full range. The difference between the two integrated functions is applied as error to the predicted number of Monte Carlo events. The last uncertainty is the binomial uncertainty on the efficiency.

Photon efficiency correction

A correction to the photon efficiency is estimated from the tables in Ref. [87], where the efficiency corrections are given in bins of the photon p_T. A weighted average, based on the photon p_T distribution in $B_s^0 \to \eta'\eta'$ signal MC events, gives a correction of $(98.78 \pm 3.4)\%$. The photon p_T distributions in the $B_s^0 \to \eta'\eta'$ and $B^\pm \to \eta'K^\pm$ Monte Carlo samples are compatible. Moreover no discrepancy between 2011 and 2012 data is observed. Therefore the same correction is applied to all the photons.

8.2   Fit model description

In order to measure the $B_s^0 \to \eta'\eta'$ and $B^\pm \to \eta'K^\pm$ yields, a simultaneous extended maximum likelihood fit to the $B_s^0 \to \eta'\eta'$ and $B^\pm \to \eta'K^\pm$ candidates is performed. As a consequence of the studies on Monte Carlo and real data presented in Sec. 8.3 the model for 7 TeV and 8 TeV data samples is the same, and the fit is performed with these two data sets merged. We will refer to this fit as the "yields fit".

A second fit is performed in order to directly extract the ratio of branching fractions. Fitting the ratio, the uncertainties due to $\sigma(pp \to b\bar{b})$ and $\mathcal{L}$ cancel (Sec. 6.6.2). Because of the different efficiencies for 7 TeV and 8 TeV data, a simultaneous fit is performed in four categories defined by the beam energy and the decay channel. We will refer to this fit as the "ratio fit".

An independent fit of the events reconstructed as $B^\pm \to \eta'K^\pm$ is also done to measure $\mathcal{A}^{CP}(B^\pm \to \eta'K^\pm)$, merging the 7 TeV and 8 TeV data samples.

A detailed description of the fit models is presented in this section.

8.2.1   Simultaneous $B_s^0 \to \eta'\eta'$ and $B^\pm \to \eta'K^\pm$ fit

The fit to the $B_s^0 \to \eta'\eta'$ and $B^\pm \to \eta'K^\pm$ candidates is multi-dimensional. The fitted variables are the $\pi^+\pi^-\gamma\pi^+\pi^-\gamma$ invariant mass ($m_{\eta'\eta'}$) and the two $\pi^+\pi^-\gamma$ invariant masses ($m_{(\pi\pi\gamma)_1}$ and $m_{(\pi\pi\gamma)_2}$, sometimes generically referred to as $m_{\pi\pi\gamma}$) for the $B_s^0 \to$

Table 8.5 *Description of the components of the simultaneous multi-dimensional fits to the $B_s^0 \to$ $\eta'\eta'$ and $B^\pm \to \eta'K^\pm$ samples. The functions CB, ARG, LIN and QUADR are given in Eqs. 6.11, 6.13, 6.16 and 6.18, respectively. The components present only in the "yields fit" are in parentheses.*

Component of the $B_s^0 \to \eta'\eta'$ sample	PDF $m_{\eta'\eta'}$	PDF $m_{(\pi\pi\gamma)_1}$	PDF $m_{(\pi\pi\gamma)_2}$
$B_s^0 \to \eta'\eta'$ signal	CB	CB	CB
(Partially reco bkg with one real η')	ARG	CB	QUADR
(Partially reco bkg with one real η')	ARG	QUADR	CB
Partially reco bkg without real η'	ARG	QUADR	QUADR
(Combinatorial bkg with one true η')	LIN	CB	QUADR
(Combinatorial bkg with one true η')	LIN	QUADR	CB
Combinatorial bkg without true η'	LIN	QUADR	QUADR

Component of the $B^\pm \to \eta'K^\pm$ sample	PDF $m_{\eta'K^\pm}$	PDF $m_{\pi\pi\gamma}$
$B^\pm \to \eta'K^\pm$ signal	CB	CB
Combinatorial bkg with true η'	LIN	CB
Combinatorial bkg without true η'	LIN	QUADR

$\eta'\eta'$ candidates, and the $\pi^+\pi^-\gamma K^\pm$ and $\pi^+\pi^-\gamma$ invariant masses ($m_{\eta'K}$ and $m_{\pi\pi\gamma}$, respectively) for the $B^\pm \to \eta'K^\pm$ candidates.

To ensure that the mass variables are independent from each other, the η' candidates are mass constrained when building B candidates. In order not to make any distinction between the two η', and therefore to use the same probability density function (PDF) for their description, the η' candidates in $B_s^0 \to \eta'\eta'$ mode are randomly assigned to $m_{(\pi\pi\gamma)_1}$ or $m_{(\pi\pi\gamma)_2}$.

The $m_{\eta'\eta'}$ distribution is described with a peaking component centred on the B_s^0 mass, a linear component to parametrise the random combinations and a low mass component to describe the partially reconstructed $B_{(s)}$ decays. No significant contributions due to partially reconstructed B decays are found in the $\eta'K$ mass spectrum. Therefore, the two contributions describing the $m_{\eta'K}$ observable are a peaking component centred on the $B^\pm$ mass, and a linear component to describe the random combinations. The $m_{\pi\pi\gamma}$ variable is described in both samples with two components: a peaking one, centred on the η' mass, and a quadratic shape that describes the random $\pi^+\pi^-\gamma$ combinations.

Six non-negligible components are found, three in the $B^\pm \to \eta'K^\pm$ and three in the $B_s^0 \to \eta'\eta'$ data samples. Four more components are included in the "yields fit" in the $B^\pm \to \eta'\eta'$ sample, and are found to be compatible with zero. The studies leading to the choice of the components to include in the fit model are presented in Sec. 7.3. Because fast MC studies show that the "ratio fit" is not completely stable if all 10 components are present, the four components which are compatible with zero are removed from this fit. The components included in the fit and the PDFs used for their description are summarised in Table 8.5.

The chosen PDFs are validated with studies based on fully-simulated MC samples, fast MC (toy) samples and data samples. The assumptions resulting from these studies are the following:

(a) The $B_s^0 \to \eta'\eta'$ and $B^\pm \to \eta'K^\pm$ signals are described with double-sided Crystal Ball functions in the $m_{\eta'\eta'}$ and $m_{\eta'K^\pm}$ variables, $CB(m; m_B, \sigma, \alpha_L, n_L, \alpha_R, n_R)$ (Eq. 6.11).

Constraints to the mass and resolution parameters are applied, fixing the mass difference to the PDG value, $m_{B_s^0} - m_{B^\pm} = 87.35 \pm 0.23\,\text{MeV}/c^2$, and the resolution ratio to the MC value, $\sigma_{B_s^0}/\sigma_{B^\pm} = 1.26 \pm 0.06$. The tail parameters of the B_s^0 peaking component in the $B_s^0 \to \eta'\eta'$ sample are fixed to the values obtained from signal MC samples, $\alpha_L = 1.65 \pm 0.15$, $n_L = 2.4 \pm 0.6$, $\alpha_R = 1.64 \pm 0.17$, $n_R = 1.9 \pm 0.5$, while the tail parameters of the $B^\pm$ peaking component are free in the fit because of inconsistencies observed between data and MC.

(b) All the peaking components in the $m_{\pi\pi\gamma}$ distributions are also fitted with a common double-sided CB function in both the $B^\pm \to \eta'K^\pm$ and $B^\pm \to \eta'\eta'$ samples. The mass, $m_{\eta'}$, and the resolution, $\sigma_{\eta'}$, are free in the fit, while the tail parameters are fixed to the MC values, $\alpha_L = 1.41 \pm 0.11$, $n_L = 42 \pm 70$, $\alpha_R = 1.03 \pm 0.07$, $n_R = 12 \pm 6$.

(c) The partially-reconstructed background components in the $B_s^0 \to \eta'\eta'$ sample are described in $m_{\eta'\eta'}$ with a common ARGUS function f_{ARG} convoluted with the same Gaussian resolution function G as for the signal (Eq. 6.13). Three partially-reconstructed components are considered in the fit, two of them with one peaking η' and one without peaking η' resonance. The parameter c_h is free in the fit and is common to the three components, while the other parameters are fixed, $p = 1.5$ and $m_0 = 5226\,\text{MeV}/c^2$, because of the high correlation.

(d) The combinatorial components are described in the $m_{\eta'\eta'}$ and $m_{\eta'K^\pm}$ with a linear function (Eq. 6.16). Two different slope parameters are used to describe the combinatorial background with and without a true η' resonance in the $B^\pm \to \eta'K^\pm$ sample, while only one parameter is used for the three combinatorial components in the $B_s^0 \to \eta'\eta'$ sample because of the lower sensitivity.

(e) The background components without a true η' meson are described in the $m_{\pi\pi\gamma}$ variable with a quadratic function (Eq. 6.18). The parameters a, b are free in the fit and are shared by all the components in both the $B_s^0 \to \eta'\eta'$ and $B^\pm \to \eta'K^\pm$ samples.

In total, the "yields fit" has 24 free parameters:

- the $B^\pm$ and η' masses, $m_{B^\pm}$ and $m_{\eta'}'$;
- the $B^\pm$ and η' mass resolutions, $\sigma_{B^\pm}$ and $\sigma_{\eta'}'$;
- the $B^\pm$ tail parameters α_L, α_R, n_L and n_R;

- one ARGUS background parameter, c, in the $B_s^0 \to \eta'\eta'$ sample;

- three linear background slopes, one in $m_{\eta'\eta'}$ and two in $m_{\eta'K}$;

- two parameters of the quadratic background in $m_{\pi\pi\gamma}$;

- 10 yields, corresponding to the seven components of the $B_s^0 \to \eta'\eta'$ sample and to the three components in the $B^+ \to \eta'K^+$ sample.

For the "ratio fit", we assume no difference in the models used for data collected at 7 and 8 TeV, therefore all the PDF shape parameters are shared. All assumptions made for the "yields fit" listed above are applied, except for the four components compatible with zero which are neglected: the two partially reconstructed components with a real η' and the two combinatorial components with a real η'. Independent yields are allowed for the control sample and for the $B_s^0 \to \eta'\eta'$ background components in the 7 TeV and 8 TeV data samples. The fit observable $N_i(B_s^0 \to \eta'\eta')/N_i(B^\pm \to \eta'K^\pm)$ (where the index i corresponds to the beam energy category) is parametrized taking into account the efficiency ratio and the fixed parameters, in order to extract directly the ratio of branching fractions that is a common parameter between the 7 and 8 TeV data.

8.2.2 *CP* asymmetry fit

The procedure adopted for the measurement of $\mathcal{A}^{CP}(B^\pm \to \eta'K^\pm)$ is the same used to measure $\mathcal{A}^{CP}(B^\pm \to \phi K^\pm)$:

- The $B^\pm \to J/\psi K^\pm$ mode is taken as reference channel for the correction of the asymmetry measurement. The $B^\pm \to J/\psi K^\pm$ events are obtained from the dimuon trigger lines and the `BetaSBu2JpsiKDetachedLine` stripping line.

- In order to take in account the different detector response when different trigger criteria are applied, we split the $B^\pm \to \eta'K^\pm$ and the $B^\pm \to J/\psi K^\pm$ samples in two subsamples each, one with events selected by the L0Hadron TOS trigger line and the other containing L0 TIS (not-TOS) events.

- Each trigger subsample is further split in two according to the charge of the bachelor kaon.

- A two-dimensional fit to the $m_{\eta'K}$ and $m_{\pi^+\pi^-\gamma}$ variables, simultaneous in the four subsamples, is performed to extract the asymmetries.

- We assume no difference in the models used for the four subsamples, but we allow for different parameters of the combinatorial background components in the two trigger categories.

- The final $\mathcal{A}^{CP}$ measurement is taken as the luminosity-weighted average between the two asymmetries obtained with the TOS and TIS (not-TOS) samples.

$B^\pm \to \eta'K^\pm$ fit model

The fit model used to extract the *CP* asymmetry in $B^\pm \to \eta'K^\pm$ decays is identical to the model used to describe events reconstructed as $B^\pm \to \eta'K^\pm$ in the simultaneous fit described in Table 8.5.

In total, the fit has 28 free parameters:

- the $B^\pm$ and η' masses, m_B and m'_η;
- the $B^\pm$ and η' mass resolutions, σ_B and $\sigma_{\eta'}$;
- four $B^\pm$ tail parameters, α_L, α_R, n_L and n_R;
- four linear background slopes in $m_{\eta'K}$, two for each trigger category;
- four parameters of the quadratic combinatorial background in $m_{\pi^+\pi^-\gamma}$, two for each trigger category;
- three yields for the L0Hadron TOS subsample and three yields for the L0 TIS subsample;
- three *CP* asymmetries, one for each of the three components of the L0Hadron TOS subsample, and three *CP* asymmetries for the L0 TIS subsample.

$B^\pm \to J/\psi K^\pm$ fit model

The model used to fit the control channel $B^\pm \to J/\psi K^\pm$ is studied on real data. A simultaneous fit to the B^+ and the B^- candidates is performed, separately for the L0Hadron TOS and the L0 TIS subsamples, because differences in the momentum spectra in the two subsamples lead to non-negligible differences in the $B^\pm$ mass resolutions and in the tail parameters. The PDFs used to describe the B^+ and B^- candidates share the same parameters, while different parameters are allowed for the two trigger categories. Each of the two fits has two significant components:

- a signal component, described by the sum of a double-sided Crystal Ball function and a Gaussian function (Eq. 6.14);
- a combinatorial background component, described by a linear function.

For each trigger category there are 12 free parameters in the fit:

- the $B^\pm$ mass, m_B;
- the $B^\pm$ mass resolutions, σ_B and σ_{1B};
- four $B^\pm$ tail parameters, α_L, α_R, n_L and n_R;
- a linear background slope,
- two yields;
- two *CP* asymmetries.

8.3 Validation of the fit model

8.3.1 Validation using fully-simulated MC studies

Studies on $B_s^0 \to \eta'\eta'$ and $B^\pm \to \eta'K^\pm$ MC samples are performed, separately for 7 TeV and 8 TeV data, in order to determine the signal PDFs and the compatibility between the two. For the $B_s^0 \to \eta'\eta'$ samples a three-dimensional fit to the B_s^0 and of the two η' masses is performed, while for the $B^\pm \to \eta'K^\pm$ samples a two-dimensional fit to the $B^\pm$ and the η' masses is done. The fitting function is a linear combination of the product of the signal PDFs and a linear component to describe the small background present because the MC signal candidates are not matched to the truth. The following conclusion are drawn:

- The tail parameters of the B_s^0 signal component are compatible between the 7 TeV and 8 TeV MC samples. The same conclusion can be drawn for the $B^\pm$ and η' signal components.

- The same parameters are shared among the η' signal components in the $B^\pm \to \eta'K^\pm$ and the $B_s^0 \to \eta'\eta'$ data samples. This assumption is based on the fact that no differences in the momentum distribution of the η' daughter particles are observed.

- The $B^\pm$ mass and resolution and the B_s^0 mass are compatible between the 7 TeV and 8 TeV data sample.

- Discrepancies between 7 TeV and 8 TeV data are observed in the B_s^0 resolution and in the η' mass. Further studies and considerations on the compatibility will be discussed in Secs. 8.3.2 and 8.3.3 and will show that these discrepancies are negligible in real data.

Since the chosen strategy consists in merging the 7 TeV and 8 TeV data samples, a simultaneous fit to the $B_s^0 \to \eta'\eta'$ and $B^\pm \to \eta'K^\pm$ MC events in the two beam energy categories, with all the parameters shared between the 7 TeV and 8 TeV samples, is performed in order to determine the tail parameters. The results of the fit are summarised in Table 8.6 and shown in Figs. 8.2 and 8.3.
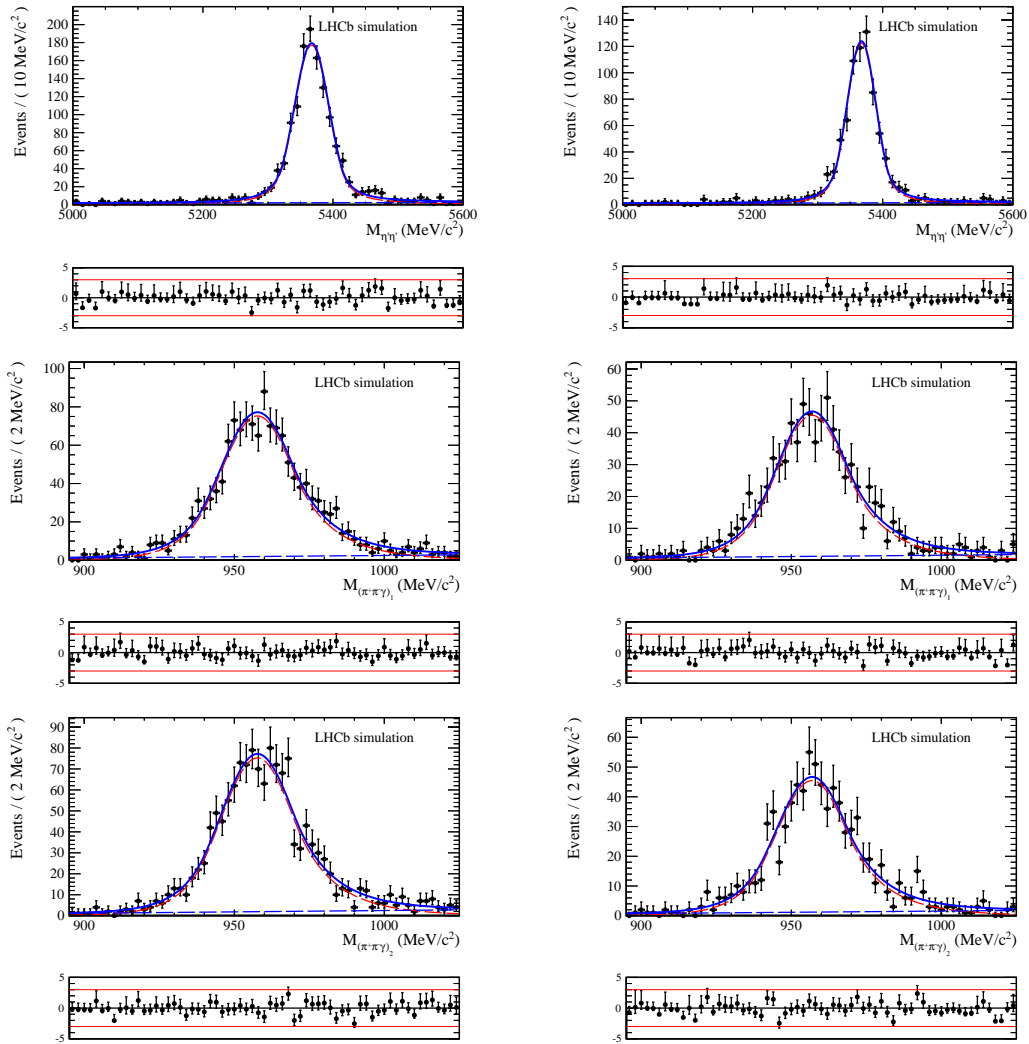
Figure 8.2   *$\eta'\eta'$ (top) and $\pi^+\pi^-\gamma$ (middle, bottom) mass distributions of the $B_s^0 \to \eta'\eta'$ candidates in 8 TeV (left) and 7 TeV (right) signal MC samples. The fit pulls are displayed in the small plots at the bottom.*

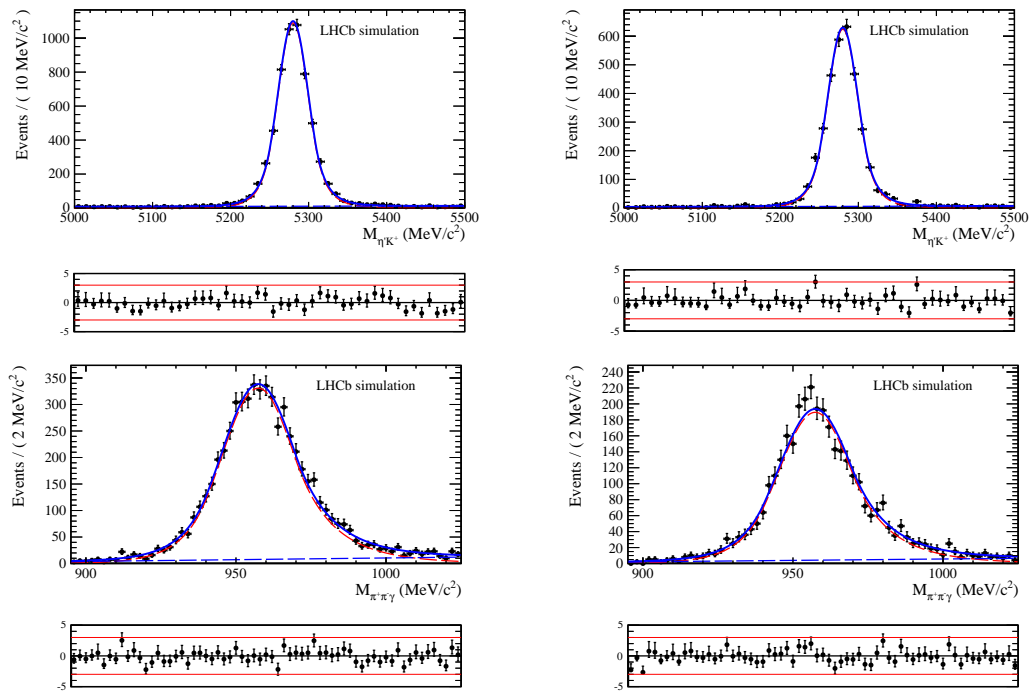**Figure 8.3** $\eta' K^{\pm}$ (top) and $\pi^+ \pi^- \gamma$ (bottom) mass distributions of the $B^{\pm} \to \eta' K^{\pm}$ candidates in 8 TeV (left) and 7 TeV (right) signal MC samples. The fit pulls are displayed in the small plots at the bottom.

Table 8.6 *Results of the simultaneous fit to the $B^\pm \to \eta'K^\pm$ and $B_s^0 \to \eta'\eta'$ candidates in 7 TeV and 8 TeV signal MC samples, displayed in Figs. 8.2 and 8.3. The combinatorial backgrounds are due to the non-matching of the MC candidate with the truth.*

Parameter			Value and error
B_s^0 mass	m_{B_s}	[MeV/c^2]	5367.0 $\pm$ 0.7
Resolution ratio	σ_{B_s}/σ_B	[MeV/c^2]	1.26 $\pm$ 0.06
B_s^0 mass tail parameter	α_L		1.65 $\pm$ 0.15
B_s^0 mass tail parameter	n_L		2.4 $\pm$ 0.6
B_s^0 mass tail parameter	α_R		1.64 $\pm$ 0.17
B_s^0 mass tail parameter	n_R		1.9 $\pm$ 0.5
$B^\pm$ mass	m_B	[MeV/c^2]	5280.1 $\pm$ 0.3
$B^\pm$ mass resolution	σ_B	[MeV/c^2]	19.5 $\pm$ 0.5
$B^\pm$ mass tail parameter	α_L		1.49 $\pm$ 0.21
$B^\pm$ mass tail parameter	n_L		12 $\pm$ 11
$B^\pm$ mass tail parameter	α_R		1.46 $\pm$ 0.12
$B^\pm$ mass tail parameter	n_R		9 $\pm$ 4
η' mass	$m_{\eta'}$	[MeV/c^2]	957.42 $\pm$ 0.20
η' mass resolution	$\sigma_{\eta'}$	[MeV/c^2]	12.23 $\pm$ 0.28
η' mass tail parameter	α_L		1.41 $\pm$ 0.11
η' mass tail parameter	n_L		42 $\pm$ 70
η' mass tail parameter	α_R		1.03 $\pm$ 0.07
η' mass tail parameter	n_R		12 $\pm$ 6
Yield of $B_s^0 \to \eta'\eta'$ signal (2012)			1294 $\pm$ 38
Yield of $B_s^0 \to \eta'\eta'$ signal (2011)			773 $\pm$ 29
Yield of $B^\pm \to \eta'K^\pm$ signal (2012)			5674 $\pm$ 78
Yield of $B^\pm \to \eta'K^\pm$ signal (2011)			3250 $\pm$ 59
Yield of $B_s^0 \to \eta'\eta'$ combinatorial background (2012)			137 $\pm$ 17
Yield of $B_s^0 \to \eta'\eta'$ combinatorial background (2011)			73 $\pm$ 12
Yield of $B_s^0 \to \eta'K^\pm$ combinatorial background (2012)			515 $\pm$ 31
Yield of $B_s^0 \to \eta'K^\pm$ combinatorial background (2011)			279 $\pm$ 22

8.3.2   Validation using real data samples

Study of the $B^\pm \to \eta' K^\pm$ real data signal

The 7 TeV and 8 TeV data samples of $B^\pm \to \eta' K^\pm$ candidates are fitted in order to determine the relevant background components, the functional form of the combinatorial background and the compatibility between the η' mass parameters. The fit is two-dimensional in the $B^\pm$ and η' variables and is simultaneous for the two samples. Only three components are found to be significant: a signal component and two combinatorial components, with and without a true η' resonance. The components and the shapes used are described in Sec. 8.2. The contribution due to the non-resonant $B_s^0 \to \pi^+ \pi^- \gamma$ background is found to be negligible. The tail parameters of the Crystal Ball functions are fixed to the MC values. The mass and the resolution of the $B^\pm$ peaking component are free in the fit but constrained to common values in the 7 TeV and 8 TeV samples, while different η' mass and resolution parameters are allowed in order to investigate the discrepancy observed in the MC study. The slope of the combinatorial background with no real η' in the $B^\pm$ spectrum is free and is different for the two samples, while all the other background parameters are free but constrained to common values because of the low sensitivity. No assumption is made about the yields. In total the fit has 18 free parameters: 12 shape parameters plus 6 yields.

The results of the fit are summarised in Table 8.7 and displayed in Fig. 8.4. The discrepancy observed in the MC between the η' mass parameters is not confirmed in the real data. It is therefore decided to use the same parameters for the η' resonance in the 7 TeV and 8 TeV samples.

Table 8.7   *Results of the simultaneous two-dimensional fit to the 7 TeV and 8 TeV $B^\pm \to \eta' K^\pm$ data candidates (displayed in Fig. 8.4). The linear background slopes are omitted.*

Parameter			Value and error
$B^\pm$ mass	m_B	[MeV/c^2]	5282.61 $\pm$ 0.28
$B^\pm$ mass resolution	σ_B	[MeV/c^2]	21.02 $\pm$ 0.25
η' mass (2012)	$m_{\eta'}$	[MeV/c^2]	959.25 $\pm$ 0.23
η' mass resolution (2012)	$\sigma_{\eta'}$	[MeV/c^2]	13.35 $\pm$ 0.21
η' mass (2011)	$m_{\eta'}$	[MeV/c^2]	958.9 $\pm$ 0.4
η' mass resolution (2011)	$\sigma_{\eta'}$	[MeV/c^2]	13.4 $\pm$ 0.3
Yield of $B^\pm \to \eta' K^\pm$ signal (2012)			6277 $\pm$ 88
Yield of combinatorial background with true η' meson (2012)			166 $\pm$ 78
Yield of combinatorial background without true η' meson (2012)			4496 $\pm$107
Yield of $B^\pm \to \eta' K^\pm$ signal (2011)			2502 $\pm$ 55
Yield of combinatorial background with true η' meson (2011)			144 $\pm$ 45
Yield of combinatorial background without true η' meson (2011)			1628 $\pm$ 61

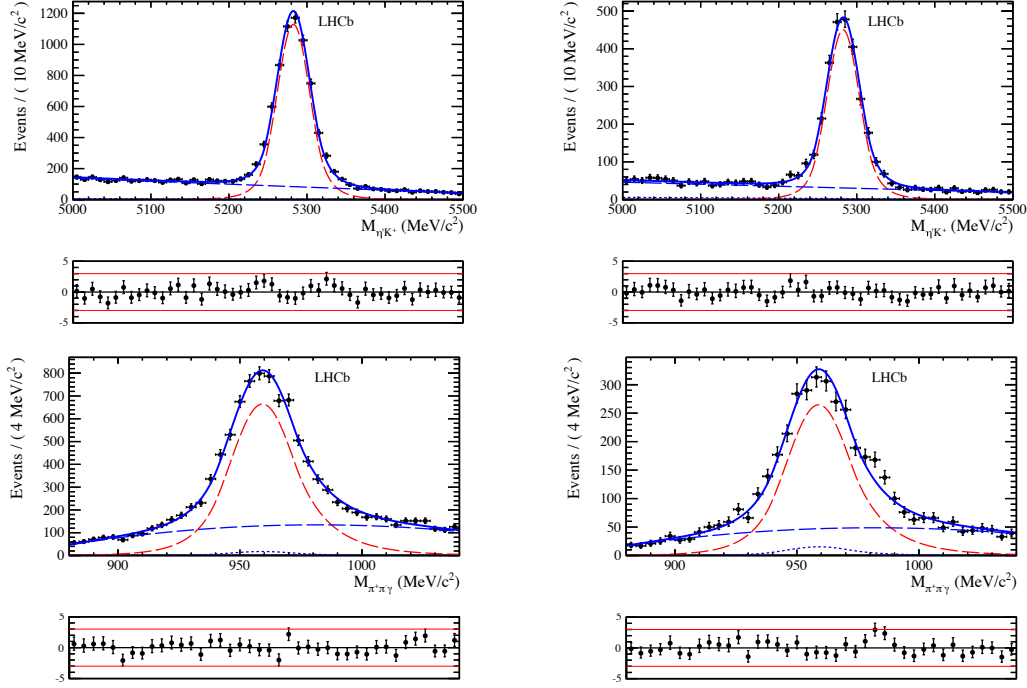**Figure 8.4**   *$\eta'K^\pm$ (top) and $\pi^+\pi^-\gamma$ (bottom) mass distributions of the $B^\pm \to \eta'K^\pm$ candidates in the 8 TeV (left) and 7 TeV (right) data samples. The solid blue curves represent the results of the simultaneous two-dimensional fit described in the text, with the following components: $B^\pm \to \eta'K^\pm$ signal (dashed red), combinatorial background with (dashed black) or without (dashed blue) a true η' meson. The fit pulls are displayed in the small plots at the bottom.*

Study of the $B_s^0 \to \eta'\eta'$ real data background

To identify the relevant background components in the fit of the $B_s^0 \to \eta'\eta'$ data samples, the mass sidebands of the 8 TeV data sample are studied. Two different fits are performed.

The first fit is a one-dimensional fit of the $m_{\eta'\eta'}$ variable for the events in the sidebands of at least one of the two η' ($\left| m_{\pi^+\pi^-\gamma} - 957.8 \right| > 40$ MeV/c^2). The selected sample contains 143 events. The shape parameters, except the combinatorial slope, are fixed because of the very low statistics to the values found in MC and $B^\pm \to \eta'K^\pm$ real data. The fit results are summarised in Fig. 8.5 and Table 8.8. No indication of a peaking B_s^0 component is found, however both a partially reconstructed component and a combinatorial component are significant.

The second fit is a two-dimensional fit of the two $m_{\pi^+\pi^-\gamma}$ variables for the data candidates outside of the B_s^0 signal region ($m_{\eta'\eta'} < 5282$ MeV/c^2 or $m_{\eta'\eta'} > 5456$ MeV/c^2). The sample contains 195 events. Because of the large uncertainty on the parameters, we fix all the shape parameters and we constrain the yields to positive values. The fit results are illustrated in Fig. 8.6, while the yields are summarised in Table 8.9. No indication of peaking η' components is present.
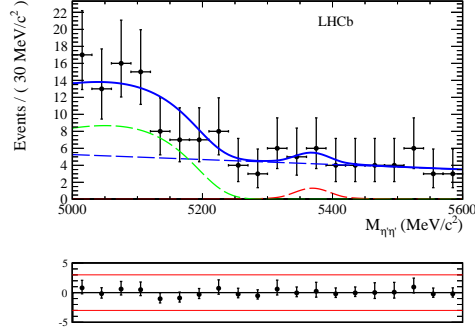
Figure 8.5 $\eta'\eta'$ mass distribution of the $B_s^0 \to \eta'\eta'$ candidates in the 8 TeV data sample with at least one of the two $\pi\pi\gamma$ invariant masses outside of the η' mass window. The solid blue curve represents the results of the fit, with the following components: peaking B_s^0 component (dashed red), partially reconstructed b-hadron background (dashed green), and combinatorial background (dashed blue). The fit pulls are displayed in the small plots at the bottom.

Table 8.8 Results of the fit to the $m_{\eta'\eta'}$ variable for the $B_s^0 \to \eta'\eta'$ candidates in the 8 TeV data sample with at least one of the two $\pi\pi\gamma$ masses outside of the η' mass window (displayed in Fig. 8.5).

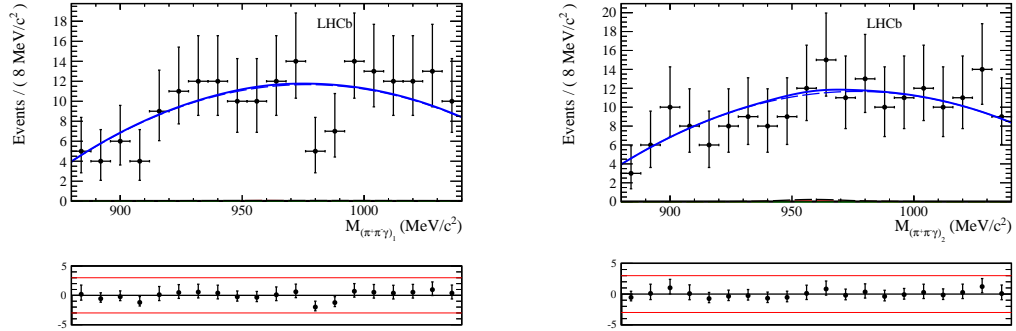| Parameter	Value and error
Yield of peaking B_s^0 background	3 $\pm$ 6
Yield of partially reconstructed background	52 $\pm$ 19
Yield of combinatorial background	88 $\pm$ 23

Figure 8.6 Distribution of the two $m_{\pi\pi\gamma}$ variables of the $B_s^0 \to \eta'\eta'$ data candidates falling outside of the B_s^0 mass window. The curves represent the result of the simultaneous fit described in the text, with the following components: double peaking η' backgrounds (dashed red, hardly visible), combinatorial background with a peaking η' component (dashed green and dashed black), combinatorial background without peaking η' components (dashed blue). The fit pulls are displayed in the small plots at the bottom.

From these sideband fits all the contributions peaking in the B_s^0 or in the η' masses are found to be negligible. In order to double-check this result a large number of inclusive

Table 8.9   *Results of the simultaneous fit to the two $m_{\pi\pi\gamma}$ variables of the $B_s^0 \to \eta'\eta'$ data candidates falling outside of the B_s^0 mass window (displayed in Fig. 8.6).*

Parameter	Value and error
Yield of double peaking background	0 ± 7
Yield of single peaking background (first η')	0 ± 8
Yield of single peaking background (second η')	1 ± 9
Yield of combinatorial background	193 ± 18

b-hadron MC events ($>$20 millions) are produced at the generator level and skimmed with the same selection applied to data. The following conclusions are drawn from the analysis of the selected events:

- No background events peaking in the B_s^0 mass pass the selection;

- No background events peaking in both η' masses are selected;

- Although many events passing the selection can contribute to the partially reconstructed background, no specific b-hadron decay modes produce dominant contributions;

- A few events with a real η' and not peaking in the B_s^0 mass pass the selection.

The first three considerations are in agreement with the sidebands fit results. It is therefore decided to not include a background component peaking in the B_s^0 mass and to not consider a background component peaking in both η' masses. We decide instead to take into account in the fit the four background components with a peaking η' (combinatorial or partially-reconstructed in B_s^0) since signs of such backgrounds are found in the inclusive b-hadron MC study.

8.3.3   Validation using toy Monte Carlo samples

In order to check the fit stability and to study the effect of a possible difference in the B_s^0 resolution between the 7 TeV and 8 TeV data, Monte Carlo pseudo-experiments (toy samples) are done. For each study 500 samples are generated and fitted using the fit models described in Sec. 8.2. All the fit components are taken into account and the number of events in each component reflects the results of the validation fits performed on data. Because of the large uncertainty on the number of predicted $B_s^0 \to \eta'\eta'$ events, samples with three different $B_s^0 \to \eta'\eta'$ input yields, 5 or 20 or 40, are generated. All the studies prove the stability of the fit and the absence of biases. In order to study the effect of a possible different resolution in real data, a test is performed generating 40 $B_s^0 \to \eta'\eta'$ signal events with two different PDFs for the B_s^0 particle. The two PDFs differ in the B_s^0 resolution, according to the MC results: 25% of the events are generated considering the smaller resolution, while the rest of the events use the wider crystal ball PDF. The

two samples are merged and fitted neglecting the presence of the narrower PDF. The effect is negligible and no significant bias is measured. As a consequence we decide to not distinguish between 7 TeV and 8 TeV events.

Pure and embedded toy samples are also generated to validate the $B^\pm \to \eta'K^\pm$ fit. The fit is stable and no biases are found.

8.4 Measurement of $\mathcal{B}(B_s^0 \to \eta'\eta')/\mathcal{B}(B^\pm \to \eta'K^\pm)$

8.4.1 Fit results

The $B_s^0 \to \eta'\eta'$ signal yield extracted from the "yields fit" described in Sec. 8.2 is found to be:

$$N(B_s^0 \to \eta'\eta') = 36.4 \pm 7.8, \tag{8.2}$$

with a statistical significance equal to:

$$s_{\text{stat}} = \sqrt{2(\ln \mathcal{L}_{\max} - \ln \mathcal{L}_0)} = 6.5, \tag{8.3}$$

where $\mathcal{L}_{\max}$ is the likelihood value resulting from the fit when all the parameters are free, and $\mathcal{L}_0$ is the likelihood value obtained from the fit when the number of signal events is fixed to 0. The results of the fit are shown in Figs. 8.7 and 8.8, and in Table 8.10, while the profile likelihood in function of $N(B_s^0 \to \eta'\eta')$, obtained by minimising the likelihood at each value of $N(B_s^0 \to \eta'\eta')$, is shown in Fig. 8.9. The results and significance including the systematic uncertainties are presented in Sec. 8.4.4.

The ratio of the branching fractions is directly obtained from the "ratio fit" according to:

$$
\begin{aligned}
\frac{\mathcal{B}(B_s^0 \to \eta'\eta')}{\mathcal{B}(B^\pm \to \eta'K^\pm)} &= \frac{f_d}{f_s} \times \frac{N_i(B_s^0 \to \eta'\eta')}{N_i(B^\pm \to \eta'K^\pm)} \times \frac{1}{\mathcal{B}(\eta' \to \pi^+\pi^-\gamma)} \times \frac{1}{c_{\varepsilon_\gamma}} \times \\
&\quad \times \frac{c_{SPD_i}(B^\pm \to \eta'K^\pm)}{c_{SPD_i}(B_s^0 \to \eta'\eta')} \times \frac{\varepsilon_i(B^\pm \to \eta'K^\pm)}{\varepsilon_i(B_s^0 \to \eta'\eta')}
\end{aligned}
\tag{8.4}
$$

where the index i corresponds to the 7 TeV or 8 TeV data set. The value $f_s/f_d = 0.259 \pm 0.015$ [88] measured by LHCb is used. The ratio of the branching fractions is found to be:

$$\frac{\mathcal{B}(B_s^0 \to \eta'\eta')}{\mathcal{B}(B^\pm \to \eta'K^\pm)} = 0.47 \pm 0.09. \tag{8.5}$$

The fit results are shown in Figs. 8.10 and 8.11, and in Table 8.11.

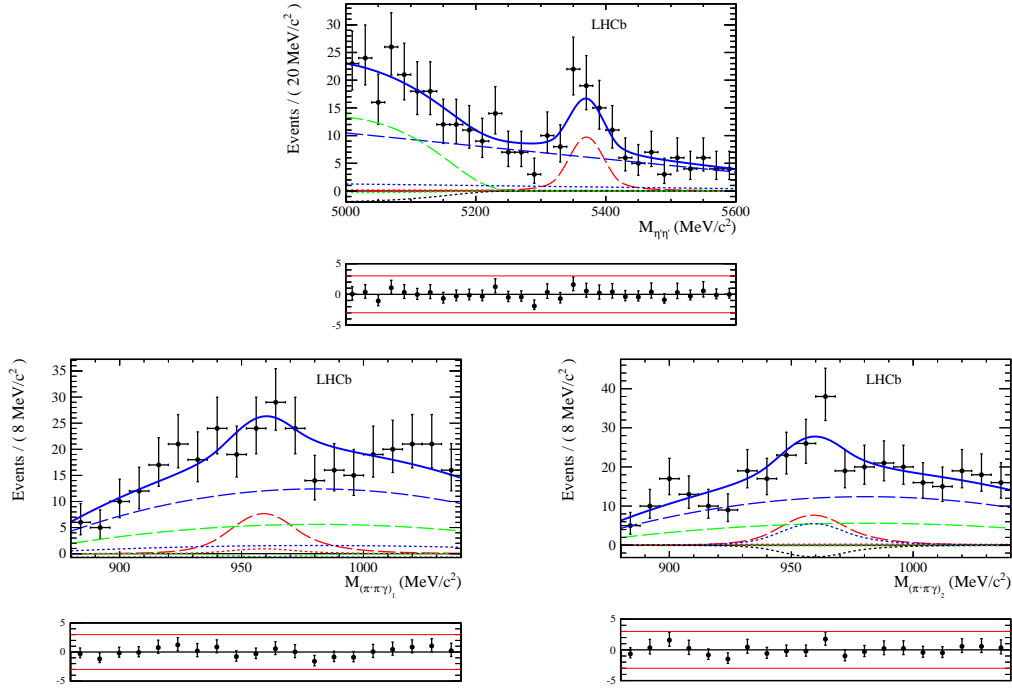**Figure 8.7**   *$\eta'\eta'$ (top) and of two $\pi^+\pi^-\gamma$ (bottom) mass distribution of the $B_s^0 \to \eta'\eta'$ data candidates. The solid blue curves represent the results of the simultaneous fit described in the text, with the following components: $B_s^0 \to \eta'\eta'$ signal (dashed red), partially reconstructed backgrounds with a real η' (dotted green and dotted black), partially reconstructed background without real η' (dashed green), combinatorial backgrounds with a real η' (dotted red and dotted blue) and combinatorial background without real η' (dashed blued). The fit pulls are displayed in the small plots at the bottom.*
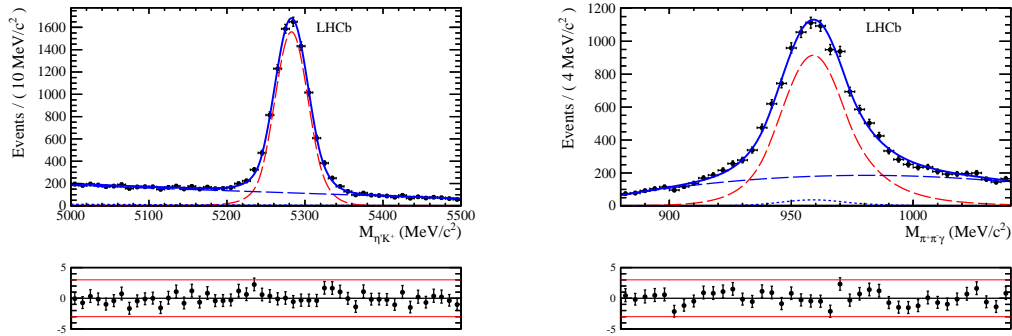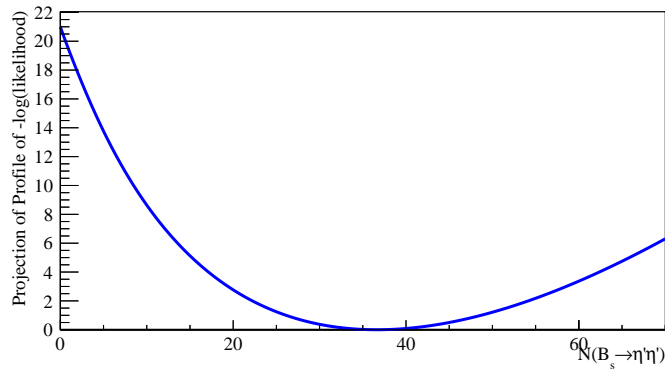

Figure 8.8   *$\eta'K^\pm$ (left) and $\pi^+\pi^-\gamma$ (right) mass distributions of the $B^\pm \to \eta'K^\pm$ data candidates. The solid blue curves represent the results of the simultaneous two-dimensional fit described in the text, with the following components: $B^\pm \to \eta'K^\pm$ signal (dashed red), combinatorial background with a real η' (dotted blue) and combinatorial background without real η' (dashed blued). The fit pulls are displayed in the small plots at the bottom.*

Table 8.10 *Results of the "yields fit" displayed in Figs. 8.7 and 8.8.*

Parameter			Value and error
$B^\pm$ mass	m_B	[MeV/c^2]	5282.8 ± 0.3
$B^\pm$ mass resolution	σ_B	[MeV/c^2]	21.4 ± 0.3
$B^\pm$ mass tail parameter	α_L		1.81 ± 0.14
$B^\pm$ mass tail parameter	n_L		5 ± 3
$B^\pm$ mass tail parameter	α_R		1.60 ± 0.10
$B^\pm$ mass tail parameter	n_R		99 ± 98
η' mass	$m_{\eta'}$	[MeV/c^2]	959.04 ± 0.19
η' mass resolution	$\sigma_{\eta'}$	[MeV/c^2]	13.51 ± 0.17
c ARGUS parameter	c		-15 ± 10
p_1 - Poly 1 - comb bkg with true η' meson ($m_{\eta'K^\pm}$)			-0.48 ± 0.02
p_1 - Poly 1 - comb bkg without true η' meson ($m_{\eta'K^\pm}$)			-1.00 ± 0.06
p_1 - Poly 2 - comb bkg without true η' meson ($m_{\pi^+\pi^-\gamma}$)			0.28 ± 0.02
p_2 - Poly 2 - comb bkg without true η' meson ($m_{\pi\pi\gamma}$)			-0.27 ± 0.03
p_1 - Poly 1 - comb bkg ($m_{\eta'\eta'}$)			-0.51 ± 0.15
Yield of $B_s^0 \rightarrow \eta'\eta'$ signal			36.4 ± 7.8
Yield of $B_s^0 \rightarrow \eta'\eta'$ partially reconstructed bkg with true η'_1			-3 ± 13
Yield of $B_s^0 \rightarrow \eta'\eta'$ partially reconstructed bkg with true η'_2			-13 ± 13
Yield of $B_s^0 \rightarrow \eta'\eta'$ partially reconstructed bkg without true η'			94 ± 28
Yield of $B_s^0 \rightarrow \eta'\eta'$ combinatorial bkg with true η'_1			4 ± 16
Yield of $B_s^0 \rightarrow \eta'\eta'$ combinatorial bkg with true η'_2			26 ± 40
Yield of $B_s^0 \rightarrow \eta'\eta'$ combinatorial bkg without true η'			207 ± 32
Yield of $B^\pm \rightarrow \eta'K^\pm$ signal			8672 ± 114
Yield of $B^\pm \rightarrow \eta'K^\pm$ combinatorial bkg with true η' meson			348 ± 104
Yield of $B^\pm \rightarrow \eta'K^\pm$ combinatorial bkg without true η' meson			6194 ± 128

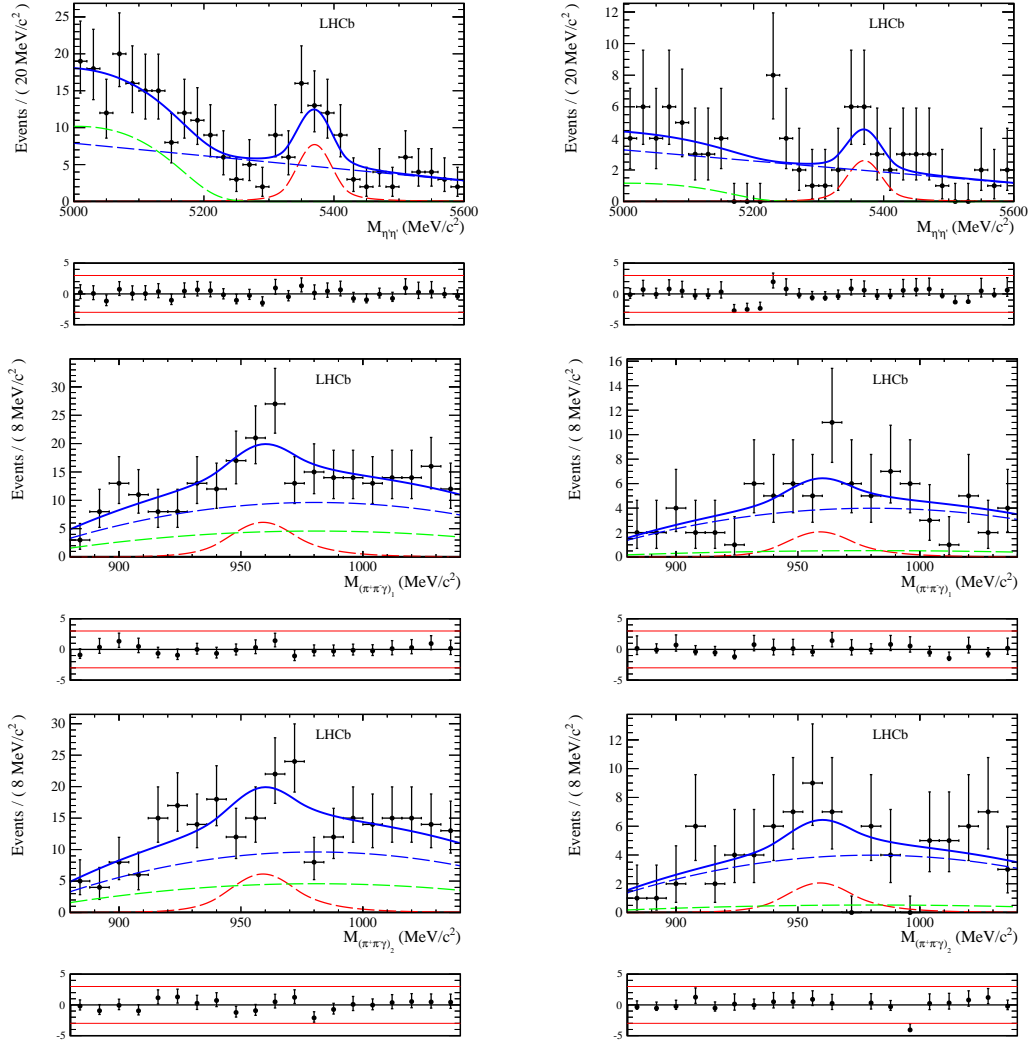***Figure 8.9*** *Likelihood profile as a function of the $B_s^0 \rightarrow \eta'\eta'$ signal yield.*

Figure 8.10   *$\eta'\eta'$ (top) and of two $\pi^+\pi^-\gamma$ (bottom) mass distribution of the 7 TeV (right) and 8 TeV (left) $B_s^0 \to \eta'\eta'$ data candidates. The solid blue curves represent the results of the simultaneous fit described in the text, with the following components: $B_s^0 \to \eta'\eta'$ signal (dashed red), partially reconstructed backgrounds with a real η' (dotted green and dotted black), partially reconstructed background without real η' (dashed green), combinatorial backgrounds with a real η' (dotted red and dotted blue) and combinatorial background without real η' (dashed blued). The fit pulls are displayed in the small plots at the bottom.*
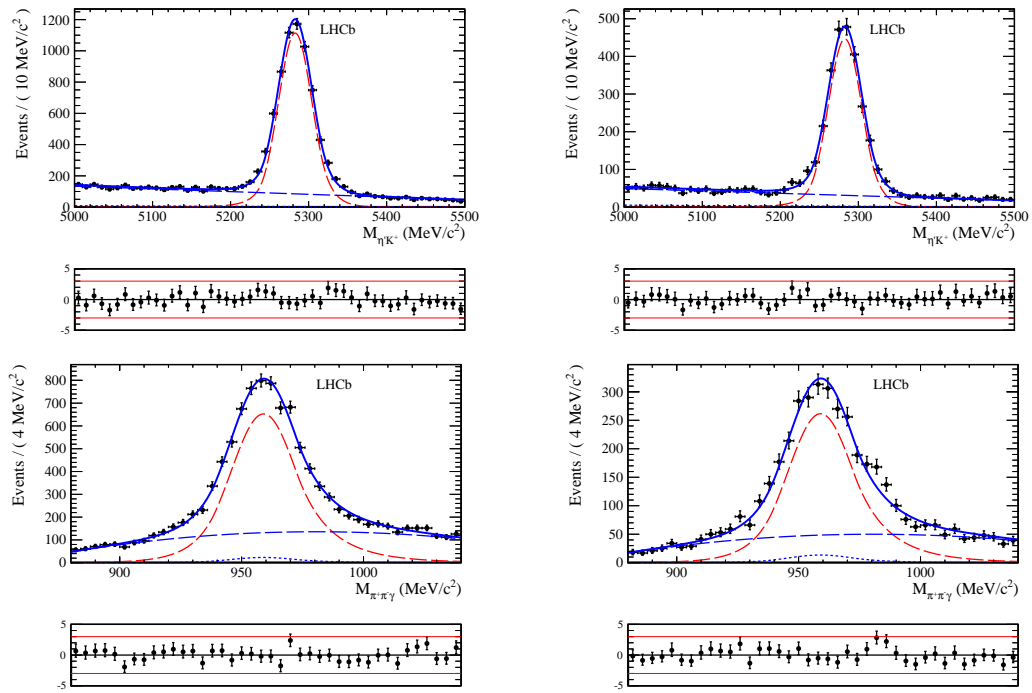
Figure 8.11   *$\eta'K^\pm$ (left) and $\pi^+\pi^-\gamma$ (right) mass distributions of the 7 TeV (right) and 8 TeV (left) $B^\pm \rightarrow \eta'K^\pm$ data candidates. The solid blue curves represent the results of the simultaneous two-dimensional fit described in the text, with the following components: $B^\pm \rightarrow \eta'K^\pm$ signal (dashed red), combinatorial background with a real η' (dotted blue) and combinatorial background without real η' (dashed blued). The fit pulls are displayed in the small plots at the bottom.*

Table 8.11 *Results of the "ratio fit" (displayed in Figs. 8.10 and 8.11)*

Parameter			Value and error
$B^\pm$ mass	m_B	[MeV/c^2]	5282.8 $\pm$ 0.3
$B^\pm$ mass resolution	σ_B	[MeV/c^2]	21.4 $\pm$ 0.3
$B^\pm$ mass tail parameter	α_L		1.8 $\pm$ 0.2
$B^\pm$ mass tail parameter	n_L		5 $\pm$ 5
$B^\pm$ mass tail parameter	α_R		1.60 $\pm$ 0.10
$B^\pm$ mass tail parameter	n_R		150 $\pm$141
η' mass	$m_{\eta'}$	[MeV/c^2]	959.04 $\pm$ 0.19
η' mass resolution	$\sigma_{\eta'}$	[MeV/c^2]	13.51 $\pm$ 0.17
c ARGUS parameter	c		-18 $\pm$ 9
p_1 - Poly 1 - comb bkg with true η' meson ($m_{\eta'K^\pm}$)			$-0.48 \pm$ 0.02
p_1 - Poly 1 - comb bkg without true η' meson ($m_{\eta'K^\pm}$)			$-1.00 \pm$ 0.06
p_1 - Poly 2 - comb bkg without true η' meson ($m_{\pi^+\pi^-\gamma}$)			0.28 $\pm$ 0.02
p_2 - Poly 2 - comb bkg without true η' meson ($m_{\pi\pi\gamma}$)			$-0.27 \pm$ 0.03
p_1 - Poly 1 - comb bkg ($m_{\eta'\eta'}$)			$-0.48 \pm$ 0.16
$\mathcal{B}(B_s^0 \to \eta'\eta')/\mathcal{B}(B^\pm \to \eta'K^\pm)$			0.47 $\pm$ 0.09
Yield of $B_s^0 \to \eta'\eta'$ partially reconstructed bkg without true η' (8 TeV)			76 $\pm$ 19
Yield of $B_s^0 \to \eta'\eta'$ combinatorial bkg without true η' (8 TeV)			160 $\pm$ 22
Yield of $B^\pm \to \eta'K^\pm$ signal (8 TeV)			6191 $\pm$103
Yield of $B^\pm \to \eta'K^\pm$ combinatorial bkg with true η' (8 TeV)			218 $\pm$ 92
Yield of $B^\pm \to \eta'K^\pm$ combinatorial bkg without true η' (8 TeV)			4531 $\pm$104
Yield of $B_s^0 \to \eta'\eta'$ partially reconstructed bkg without true η' (7 TeV)			9 $\pm$ 8
Yield of $B_s^0 \to \eta'\eta'$ combinatorial bkg without true η' (7 TeV)			67 $\pm$ 12
Yield of $B^\pm \to \eta'K^\pm$ signal (7 TeV)			2479 $\pm$ 58
Yield of $B^\pm \to \eta'K^\pm$ combinatorial bkg with true η' (7 TeV)			128 $\pm$ 47
Yield of $B^\pm \to \eta'K^\pm$ combinatorial bkg without true η' (7 TeV)			1667 $\pm$ 59

8.4.2   Systematic uncertainties on the $B^0_s \to \eta'\eta'$ yield

In this section, the systematic uncertainties on the "yields fit" are analysed. The different contributions are summarised in Table 8.12.

Systematic uncertainties can be introduced because of the fit model chosen to describe the data. Two different sources of uncertainties are taken in account:

- Uncertainty due to fixed parameters. In order to determine the systematic uncertainty the real data sample is fitted 5000 times. In each fit the fixed parameters (B^0_s and η' tail parameters, $\sigma_{B^0_s}/\sigma_B$ ratio and $m_{B^0_s} - m_B$) are taken randomly from a Gaussian distribution centred on the value used in the nominal fit and with width equal to the MC uncertainty. The width of the signal yield distribution (see Fig. 8.12 left), equal to 0.7 event, is assigned as systematic uncertainty on the yield.

- Uncertainty due to the PDF functional form. Several studies are performed on real data and MC in order to find shapes which describe properly signal and backgrounds, and many options have been excluded. For the systematic uncertainty we studied the following variations of the fit model:

  - we replaced the linear components in the $m_{\eta'\eta'}$ and $m_{\eta'K^\pm}$ distributions with exponential components;
  - we replaced the quadratic shape for the $m_{\pi^+\pi^-\gamma}$ combinatorial background with a 3rd order polynomial;
  - the ARGUS parameter p is fixed at 1.5 ± 0.8. The variation has been chosen according to the uncertainty obtained leaving this parameter free in the fit to the B^0_s mass in the η' tails (see Fig. 8.6);
  - the ARGUS parameter m is fixed at the nominal value $5226 \pm 10\,\text{MeV}/c$;
  - two different slope parameters are allowed to describe the $m_{\eta'\eta'}$ combinatorial components, one for the combinatorial component without real η' mesons and one for the two combinatorial components with a real η' meson;
  - the tail parameters of the $B^\pm$ peaking component are fixed to the MC value;
  - the tail parameters of the B^0_s peaking component are constrained to the tail parameters of the $B^\pm$ peaking component.

  For each test, the difference of the central value of the signal yield with respect to the nominal fit is computed. All the contributions (which are of similar magnitude) are summed in quadrature, leading to a systematic uncertainty of 1.4 event.

Finally, embedded toy studies are performed using the yields and PDF parameters extracted from the fit to the data. The distribution of the $B^0_s \to \eta'\eta'$ yield shows no bias. We decide to assign the uncertainty on the mean value of the distributions as systematic uncertainty. The estimated error is 0.4 event.

The total systematic uncertainty on the $B^0_s \to \eta'\eta'$ yield, computed as the sum in quadrature of the different contributions, is equal to 1.6 event.

Table 8.12   *Systematic uncertainties on the $B_s^0 \to \eta'\eta'$ signal yield.*

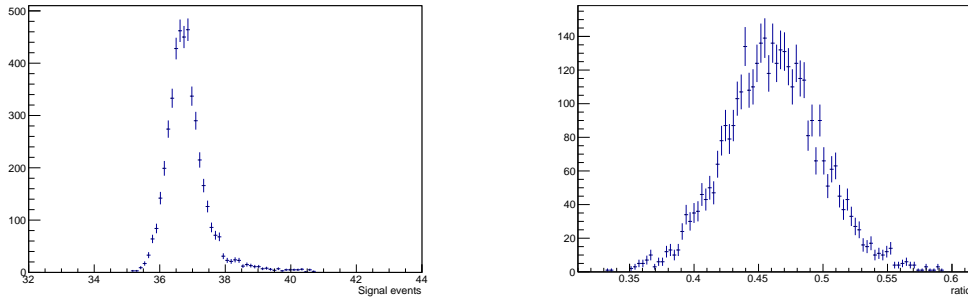| Source	Systematic uncertainty (event)
Fit model (fixed parameters)	0.7
Fit model (shapes)	1.4
Fit bias	0.4
Quadratic sum	1.6

Figure 8.12   *Distribution of the signal yield (left) and of the ratio of branching fractions (right). In each fit the fixed parameters are sampled randomly from a Gaussian distribution centred on the value used in the nominal fit and with resolution equal to the MC uncertainty. The distribution of the signal yield takes into account the shape parameters fixed in the fit, while the distribution of the ratio of branching fractions also takes into account the fixed parameters of Eq. 8.4.*

8.4.3   Systematic uncertainties on the $\mathcal{B}(B_s^0 \to \eta'\eta')/\mathcal{B}(B^\pm \to \eta'K^\pm)$

Most of the systematic uncertainties cancel in the ratio of the efficiencies and of the branching fractions. The systematic errors on the efficiencies are used as input to compute the systematic uncertainty on the ratio of branching fraction. The total systematic uncertainty on the efficiency ratio is 0.40 and 0.31 for the 7 TeV and 8 TeV data samples, respectively. The systematic uncertainty on the ratio of branching fractions is equal to 0.041, and includes the systematic uncertainty on the fit model, on the fixed parameters of Eq. 8.4 and uses as input the systematic uncertainty on the efficiency ratio.

The contributions to the systematic error on the efficiency ratio and on the ratio of branching fractions are listed in Table 8.13 and discussed below.

The following uncertainties contribute to the systematic error on the efficiency ratio:

- Uncertainty on the PID efficiency: it is due to different contributions like the size and the different kinematic properties of the calibration and reference samples. The size of the calibration sample leads to the uncertainties given in Table 7.4 while the other contributions above mentioned are propagated as systematic uncertainty using the dedicated tools [76], and lead to a systematic uncertainty of 0.013 and 0.010 on the 7 TeV and 8 TeV efficiency ratio, respectively.

Table 8.13 *Systematic uncertainties on the efficiency ratio and on the ratio of branching fractions.*

Fit model systematics		
	7 TeV data	8 TeV data
PID selection	0.013	0.010
Kinematic selection	0.19	0.17
Trigger	0.024	0.08
MC statistics (Eq. 8.1)	0.35	0.26
Quadratic sum	0.40	0.32
Ratio of branching fraction systematics (including error on efficiency)		
Fit model (fixed parameters)	0.038	
Fit model (shapes)	0.007	
Components fixed to 0	0.014	
Fit bias	0.005	
Quadratic sum	0.041	

- Uncertainty due to the kinematic selection: it is computed studying the effect of a variation of the cuts applied offline. The $B^\pm \to \eta'K^\pm$ channel is used as reference. For each variable used in the offline selection, the fraction of $B^\pm \to \eta'K^\pm$ events selected in real data, relative to the stripping candidates, is computed. The cut on MC data giving the same efficiency as obtained in real data is then determined, and used as reference. The ratio between the $B_s^0 \to \eta'\eta'$ and the $B^\pm \to \eta'K^\pm$ MC efficiencies is then computed with the new set of cuts and the difference with respect to the nominal efficiency is applied as systematic uncertainty. A relative systematic uncertainty on the efficiency ratio of 2.3% is found. Because of the large uncertainty due to the size of the 2011 sample, the same relative systematic uncertainty is applied to both the 7 TeV and 8 TeV efficiencies, corresponding to an absolute uncertainty of 0.19 for 7 TeV and 0.17 for 8 TeV.

- Uncertainty due to the trigger requirements: we studied the effect of the kinematic cut applied by the L0Hadron TOS trigger line (real $E_T > 3620\,\mathrm{MeV}/c$ in 2012 and real $E_T > 3500\,\mathrm{MeV}/c$ in 2011) on the efficiency ratio. A 10% variation of the value of this cut produces a variation of the efficiency ratio of 0.08 for 8 TeV and 0.024 for 7 TeV, applied as systematic uncertainty.

Following the same procedure adopted for the "yields fit" model systematics, the "ratio fit" is repeated 5000 times, varying all the fixed parameters of the model and of Eq. 8.4 according to a Gaussian distribution centred in the nominal value with a width equal to the uncertainty. This includes the following parameters:

- The parameters fixed from MC: $\alpha_L(B_s^0)$, $n_L(B_s^0)$, $\alpha_R(B_s^0)$ and $n_R(B_s^0)$ for the B_s^0 peaking components, $\alpha_L(\eta')$, $n_L(\eta')$, $\alpha_R(\eta')$ and $n_R(\eta')$ for the η' resonance, the difference $m_B - m_{B_s^0}$ and the ratio of resolutions $\sigma_{B_s^0}/\sigma_B$.

- The 2011 and 2012 efficiency ratios.

- The parameters of Eq. 8.4: f_d/f_s, $c_{SPD_i}(B^\pm \to \eta'K^\pm)$, $c_{SPD_i}(B_s^0 \to \eta'\eta')$, $\mathcal{B}(\eta' \to \pi^+\pi^-\gamma)$ and c_{ε_γ}.

The RMS of the distribution of the branching fraction ratio (see Fig. 8.12 right), equal to 0.038, is taken as systematic uncertainty.

The effect due to variations of the fit model is also taken in account:

- the linear components in the $m_{\eta'\eta'}$ and $m_{\eta'K^\pm}$ distributions are replaced by exponential components;

- the quadratic shape for the $m_{\pi^+\pi^-\gamma}$ combinatorial background are replaced by a 3rd order polynomial;

- different slopes are allowed in $m_{\eta'\eta'}$ and $m_{\eta'K^\pm}$ for 2011 and 2012;

- the ARGUS parameter p is fixed at 1.5 ± 0.8. The variation has been chosen according to the uncertainty obtained leaving this parameter free in the fit to the B_s^0 mass distribution in the η' tails;

- the ARGUS parameter m is fixed at the nominal value $5226 \pm 10\,\mathrm{MeV}/c$;

- different slopes are allowed for the $m_{\eta'\eta'}$ combinatorial backgrounds, one for the combinatorial component without real η' mesons and one for the two combinatorial components with a real η' meson;

- the tail parameters of the $B^\pm$ peaking component are fixed to the MC value;

- the tail parameters of the B_s^0 peaking component are constrained to the tail parameters of the $B^\pm$ peaking component.

The differences between the ratio obtained in these fits and the nominal result are summed in quadrature, leading to a systematic uncertainty of 0.007.

The two partially reconstructed components with a real η' and the two combinatorial components with a real η', which are compatible with zero in the "yields fit", are fixed to zero in the simultaneous fit used to extract the ratio of branching fractions. The fit is repeated leaving these components free, and the difference with respect to the nominal fit, equal to 0.014, is applied as systematic uncertainty.

Finallly, embedded toys studies are performed using the yields and PDF parameters extracted from the fit to the data. The distribution of the $\mathcal{B}(B_s^0 \to \eta'\eta')/\mathcal{B}(B^\pm \to \eta'K^\pm)$ shows a negligible bias. We decide to assign the uncertainty on the mean value of this distribution as systematic uncertainty. The estimated error is 0.005.

8.4.4 $B_s^0 \to \eta'\eta'$ final results

We find

$$N(B_s^0 \to \eta'\eta') = 36.4 \pm 7.8(\mathrm{stat}) \pm 1.6(\mathrm{syst})\,, \tag{8.6}$$

where the systematic error is significantly smaller than the statistical uncertainty. The significance including the systematic uncertainty, computed from

$$s = \frac{s_{\text{stat}}}{\sqrt{1 + (\sigma_{\text{syst}}/\sigma_{\text{stat}})^2}}, \tag{8.7}$$

is equal to $s = 6.4$.

The ratio of branching fractions $\mathcal{B}(B_s^0 \to \eta'\eta')/\mathcal{B}(B^\pm \to \eta' K^\pm)$ is equal to:

$$\frac{\mathcal{B}(B_s^0 \to \eta'\eta')}{\mathcal{B}(B^\pm \to \eta' K^\pm)} = 0.47 \pm 0.09\,(\text{stat}) \pm 0.04\,(\text{syst})\,. \tag{8.8}$$

Using the PDG value $\mathcal{B}(B^\pm \to \eta' K^\pm) = (7.06 \pm 0.25) \times 10^{-5}$ [11], the $B_s^0 \to \eta'\eta'$ branching fraction is computed to be

$$\mathcal{B}(B_s^0 \to \eta'\eta') = (3.31 \pm 0.64(\text{stat}) \pm 0.28(\text{syst}) \pm 0.12(B^\pm \to \eta' K^\pm)) \times 10^{-5}\,. \tag{8.9}$$

8.5 Measurement of $\mathcal{A}^{CP}(B^\pm \to \eta' K^\pm)$

The raw $B^\pm \to \eta' K^\pm$ asymmetries, extracted from a simultaneous fit to the positive and negative $B^\pm \to \eta' K^\pm$ candidates in the TOS and TIS (not TOS) trigger subsamples, are:

$$A_{\text{raw,TOS}}^{CP}(B^\pm \to \eta' K^\pm) = (-1.9 \pm 1.4) \times 10^{-2}, \tag{8.10}$$
$$A_{\text{raw,TIS}}^{CP}(B^\pm \to \eta' K^\pm) = (-2.7 \pm 2.0) \times 10^{-2}. \tag{8.11}$$

The fit results are shown in Figs. 8.13 and 8.14, and summarised in Table 8.14.

The fits to the positive and negative $B^\pm \to J/\psi K^\pm$ candidates, in the TOS and in the TIS (not TOS) trigger categories, give the following raw asymmetries:

$$A_{\text{raw,TOS}}^{CP}(B^\pm \to J/\psi K^\pm) = (-2.03 \pm 0.35) \times 10^{-2}, \tag{8.12}$$
$$A_{\text{raw,TIS}}^{CP}(B^\pm \to J/\psi K^\pm) = (-1.07 \pm 0.26) \times 10^{-2}. \tag{8.13}$$

The fit results are summarised in Tables 8.15 and 8.16, and shown in Fig. 8.15.

Following the strategy presented in Sec. 6.7, the difference between the physics asymmetry of the decay mode under study and the physics asymmetry of the control channel, computed separately for TIS and TOS and then combined according to Eq. 6.31, is:

$$\Delta\mathcal{A}^{CP}(B^\pm \to \eta' K^\pm) = -0.005 \pm 0.012. \tag{8.14}$$

All the values are summarised in Table 8.17. Including the systematic uncertainty computed in Sec. 8.5.1 and correcting by the $B^\pm \to J/\psi K^\pm$ physics asymmetry,

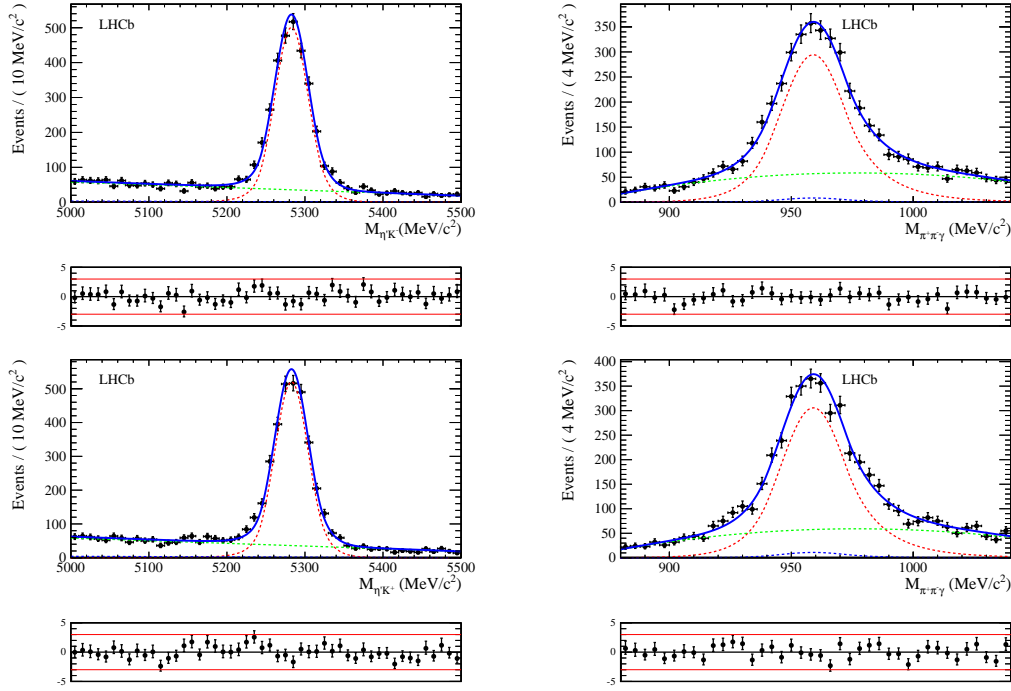**Figure 8.13**   *$\eta'K^\pm$ (left) and $\pi^+\pi^-\gamma$ (right) mass distributions of $B^- \to \eta'K^-$ (top) and $B^+ \to \eta'K^+$ (bottom) data candidates in the subsample selected by the L0 TOS trigger line. The solid blue curves represent the results of the simultaneous two-dimensional fit described in the text, with the following components: $B^\pm \to \eta'K^\pm$ signal (dotted red), non-resonant $B^\pm \to K^+K^-K^\pm$ background (dashed red), and combinatorial background with (dashed blue) or without (dashed green) true η' meson. The fit pulls are displayed in the small plots at the bottom.*

$\mathcal{A}^{CP}(B^\pm \to J/\psi K^\pm) = 0.003 \pm 0.006$ [11], we finally obtain:

$$\mathcal{A}^{CP}(B^\pm \to \eta'K^\pm) = (-0.2 \pm 1.2 \pm 0.1 \pm 0.6) \times 10^{-2}. \tag{8.15}$$

8.5.1   Systematic uncertainties

The systematic contributions to the $\mathcal{A}^{CP}$ measurement are discussed below and summarized in Table 8.18. Their sum in quadrature leads to a total systematic uncertainty of 0.13×10^{-2}.

Two different sources are taken in account for the fit model systematic uncertainty, which quadratic sum is 0.021×10^{-2}:

- Uncertainty due to fixed parameters. The same method adopted for the measurement of the $B_s^0 \to \eta'\eta'$ branching fraction is used. The real data sample is fitted 5000 times. In each fit the fixed parameters (tail parameters) are extracted randomly from a Gaussian distribution centred on the value used in the nominal
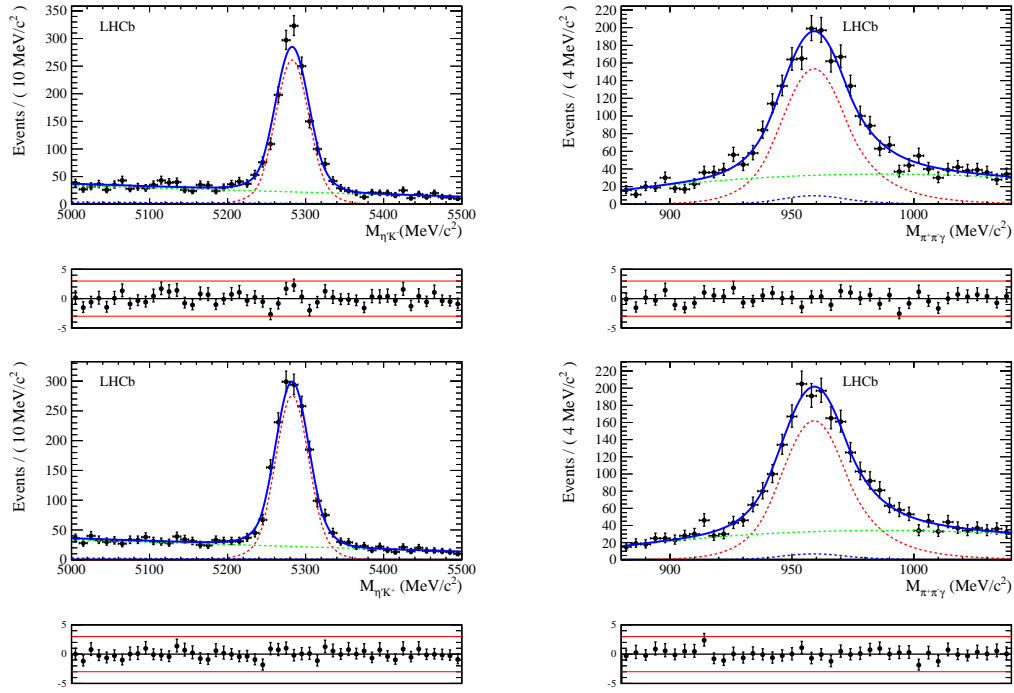
Figure 8.14 $\eta'K^\pm$ (left) and $\pi^+\pi^-\gamma$ (right) mass distributions of $B^- \to \eta'K^-$ (top) and $B^+ \to \eta'K^+$ (bottom) data candidates in the subsample selected by the L0 TIS (not TOS) trigger lines. The solid blue curves represent the results of the simultaneous two-dimensional fit described in the text, with the following components: $B^\pm \to \eta'K^\pm$ signal (dotted red), non-resonant $B^\pm \to K^+K^-K^\pm$ background (dashed red), and combinatorial background with (dashed blue) or without (dashed green) true η' meson. The fit pulls are displayed in the small plots at the bottom.

fit and with resolution equal to the MC uncertainty. The RMS of the *CP* asymmetry distributions of the two trigger subsamples are summed in quadrature weighting them by the fraction of events in each subsample, and the result is applied as systematic uncertainty. An absolute systematic uncertainty of 0.013×10^{-2} is found.

- Uncertainty due to the PDF functional form. Several studies are performed on real data and MC in order to find shapes which describe properly signal and backgrounds, and many options are excluded. We considered two sources of uncertainty: the first is due to the choice of the PDF used to describe the combinatorial component in the $m_{\eta'K^\pm}$ spectrum. For the systematic studies we replaced the linear components with exponential components. The second is due to the shape of the combinatorial component in $m_{\pi\pi\gamma}$ for which we use a 3rd order polynomial instead of a quadratic shape. The differences between the nominal $\Delta\mathcal{A}^{CP}$ and that obtained using the results of the new fits are summed in quadrature, leading to a total systematic of 0.017×10^{-2}, which is applied as systematic uncertainty.

The effect of the different kinematic distributions of the bachelor kaons in the signal and

Table 8.14 *Results of the simultaneous two-dimensional $\mathcal{A}^{CP}$ fit to the $B^- \to \eta' K^-$ and $B^+ \to \eta' K^+$ candidates in the two trigger subsamples (displayed in Figs. 8.13 and 8.14) to measure the CP asymmetry.*

| Parameter			Value and error
$B^\pm$ mass	m_B	[MeV/c^2]	5282.8 ± 0.3
$B^\pm$ mass resolution	σ_B	[MeV/c^2]	21.5 ± 0.3
η' mass	$m_{\eta'}$	[MeV/c^2]	959.05 ± 0.19
η' mass resolution	$\sigma_{\eta'}$	[MeV/c^2]	13.50 ± 0.17
$\mathcal{A}_{\mathrm{raw}}^{CP}(B^\pm \to \eta' K^\pm)$ (TOS)			-0.019 ± 0.014
Yield of $B^\pm \to \eta' K^\pm$ signal (TOS)			5684 ± 90
Yield of combinatorial background with true η' meson (TOS)			263 ± 78
Yield of combinatorial background without true η' meson (TOS)			3762 ± 96
$\mathcal{A}_{\mathrm{raw}}^{CP}(B^\pm \to \eta' K^\pm)$ (TIS)			-0.027 ± 0.020
Yield of $B^\pm \to \eta' K^\pm$ signal (TIS)			2987 ± 631
Yield of combinatorial background with true η' meson (TIS)			79 ± 53
Yield of combinatorial background without true η' meson (TIS)			2440 ± 72
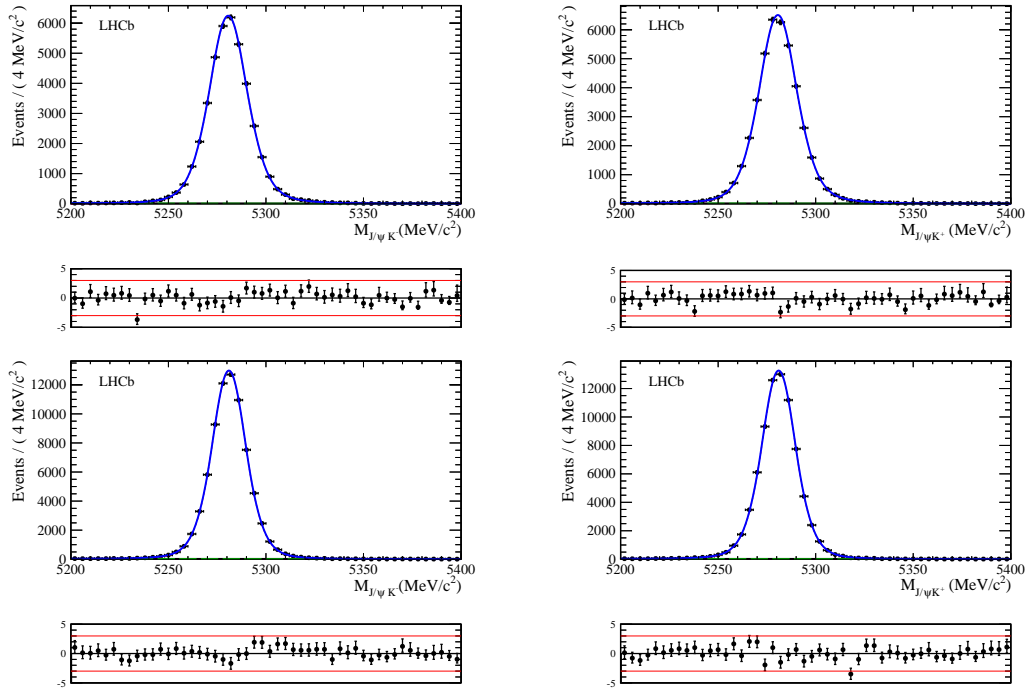
Figure 8.15 *$J/\psi K^\pm$ mass distributions of $B^- \to J/\psi K^-$ (right) and $B^+ \to J/\psi K^+$ (left) data candidates in the subsample selected by the L0 TOS (top) and L0 TIS (bottom) trigger lines. The curves solid blue represent the results of the simultaneous two-dimensional fit described in the text, with the following components: $B^\pm \to J/\psi K^\pm$ signal (dotted blue), combinatorial background (dotted green). The fit pulls are displayed in the small plots at the bottom.*

Table 8.15   *Results of the $\mathcal{A}^{CP}$ fit to the $B^- \to J/\psi K^-$ and $B^+ \to J/\psi K^+$ candidates in the TOS trigger subsample (displayed in Fig. 8.15 top).*

Parameter			Value and error	
$B^\pm$ mass	m_B	[MeV/c^2]	5280.64 $\pm$	0.05
$B^\pm$ mass resolution	σ_{B-CB}	[MeV/c^2]	10.05 $\pm$	0.09
$B^\pm$ mass resolution	σ_{B-G}	[MeV/c^2]	8.91 $\pm$	0.30
fraction	$N(\sigma_{B-CB})/N(\sigma_{B-G})$		0.69 $\pm$	0.03
$\mathcal{A}^{CP}_{\text{raw}}(B^\pm \to J/\psi K^\pm)$			-0.0203 ± 0.0035	
Yield of $B^\pm \to J/\psi K^\pm$ signal			83137	± 298
Yield of combinatorial background			934	$\pm$ 85

Table 8.16   *Results of the $\mathcal{A}^{CP}$ fit to the $B^- \to J/\psi K^-$ and $B^+ \to J/\psi K^+$ candidates in the TIS trigger subsample (displayed in Fig. 8.15 bottom).*

Parameter			Value and error	
$B^\pm$ mass	m_B	[MeV/c^2]	5282.8 $\pm$	0.3
$B^\pm$ mass resolution	σ_{B-CB}	[MeV/c^2]	9.17 $\pm$	0.11
$B^\pm$ mass resolution	σ_{B-G}	[MeV/c^2]	8.07 $\pm$	0.17
fraction	$N(\sigma_{B-CB})/N(\sigma_{B-G})$		0.51 $\pm$	0.03
$\mathcal{A}^{CP}_{\text{raw}}(B^\pm \to J/\psi K^\pm)$			-0.0107 ± 0.0026	
Yield of $B^\pm \to J/\psi K^\pm$ signal			151806	± 407
Yield of combinatorial background			1934	± 127

reference channel must also be taken into account in the systematic errors. Figure 8.16 shows the momentum and the transverse momentum distributions for the three channels. Because of the differences observed in the p_T distributions, we decide to measure the asymmetry in three p_T bins. The difference between the signal and the reference asymmetries is computed for each bin and the total $\Delta\mathcal{A}^{CP}$ is calculated as the weighted sum over the three bins. The bins defined in each trigger sample are: $p_T < 3500\,\text{MeV}/c$, $3500 < p_T < 7500\,\text{MeV}/c$, $p_T > 7500\,\text{MeV}/c$ in the L0Hadron TOS sample, and $p_T < 2200\,\text{MeV}/c$, $2200 < p_T < 3500\,\text{MeV}/c$, $p_T > 3500\,\text{MeV}/c$ for the L0 TIS sample. The difference with respect to the nominal $\Delta\mathcal{A}^{CP}$, equal to 0.018×10^{-2}, is applied as absolute systematic uncertainty on the *CP* measurement.

The last systematic uncertainty takes in account the left-right asymmetry. Indeed, the magnetic field is responsible of a charge-dependent acceptance, by bending the positive and negative particles in opposite direction. The same fiducial cut as in Ref. [85] is applied,

$$|P_x| \leqslant \alpha(P_z - P_0),\ \alpha = 0.317,\ P_0 = 2400\,\text{MeV}/c^2\,, \tag{8.16}$$

where P_x and P_z are respectively the *x* and *z* components of the bachelor kaon momentum. $\Delta\mathcal{A}^{CP}$ is computed by applying the fiducial cut to both the signal channels and

Table 8.17   *Raw charge asymmetries for the $B^\pm \to \eta'K^\pm$ and $B^\pm \to J/\psi K^\pm$ decay modes, their difference $\Delta\mathcal{A}^{CP}$, and the fraction of $B^\pm \to \eta'K^\pm$ signal events in each trigger sub-sample. All uncertainties are statistical only.*

	TOS sub-sample	TIS (not TOS) sub-sample
$\mathcal{A}_{\mathrm{raw},k}^{CP}(B^\pm \to \eta'K^\pm)$	-0.019 ± 0.014	-0.027 ± 0.020
$\mathcal{A}_{\mathrm{raw},k}^{CP}(B^\pm \to J/\psi K^\pm)$	-0.0203 ± 0.0035	-0.0107 ± 0.0026
$\Delta\mathcal{A}^{CP}(B^\pm \to \eta'K^\pm)$	0.001 ± 0.015	-0.017 ± 0.020
$N_k/(N_{\mathrm{TOS}} + N_{\mathrm{TIS}})(B^\pm \to \eta'K^\pm)$	63.8%	36.2%
weighted $\Delta\mathcal{A}^{CP}$ average ($B^\pm \to \eta'K^\pm$)	-0.005 ± 0.012	

Table 8.18   *Absolute systematic uncertainties on $\mathcal{A}^{CP}(B^\pm \to \eta'K^\pm)$.*

Source	Uncertainty
Fit model	0.021×10^{-2}
Kinematics	0.018×10^{-2}
Fiducial cut	0.13×10^{-2}
Total	0.15×10^{-2}
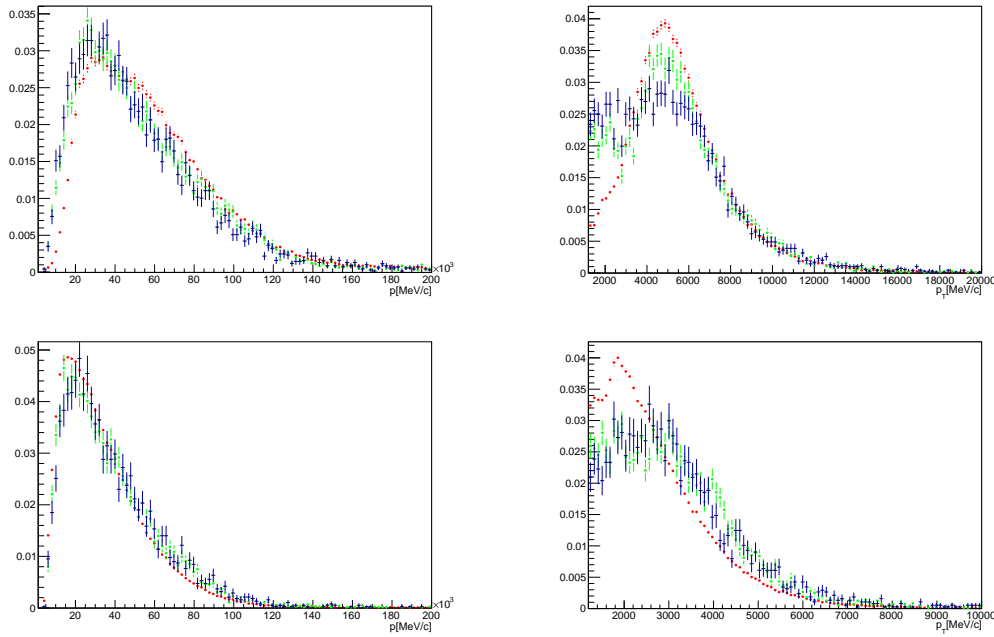
Figure 8.16   *Distribution of the momentum (top) and transverse momentum (bottom) of the bachelor kaon of the $B^\pm \to \eta'K^\pm$ (blue), $B^\pm \to \phi K^\pm$ (green) and $B^\pm \to J/\psi K^\pm$ (red) data candidates in L0 TOS (left) or L0 TIS (right) events.*

to the reference channel. The difference with respect to the nominal $\Delta\mathcal{A}^{CP}$, equal to 0.13×10^{-2}, is applied as absolute systematic uncertainty.

8.5.2 Further checks

Magnet polarity

In order to investigate the effect of the magnet polarity on the raw *CP* asymmetry the $B^{\pm} \to \eta' K^{\pm}$ subsamples are further split according to the magnetic field polarity. Independent fits to the data selected with the magnet up-polarity and down-polarity are performed. The results, shown in Table 8.19, are compatible with each other.

Table 8.19 *Raw CP asymmetry measured for $B^{\pm} \to \eta' K^{\pm}$ candidates in four different subsamples split according to trigger condition and magnet polarity.*

	L0Hadron TOS	L0 TIS (not TOS)
Magnet up	$(-0.1 \pm 2.1)\%$	$(-5.0 \pm 2.9)\%$
Magnet down	$(-3.4 \pm 1.9)\%$	$(-0.7 \pm 2.7)\%$
Compatibility (σ)	1.2	1.1

8.6 Summary

The goal of this analysis is the search for the $B_s^0 \to \eta'\eta'$ decay and the measurement of the *CP* asymmetry in $B^{\pm} \to \eta' K^{\pm}$ decays.

We find $(36.4 \pm 7.8 \pm 1.6)$ $B_s^0 \to \eta'\eta'$ signal events with a significance of 6.4 standard deviations, which includes both the statistical and the systematic uncertainty.

The ratio of branching fraction $\mathcal{B}(B_s^0 \to \eta'\eta')/\mathcal{B}(B^{\pm} \to \eta' K^{\pm})$ is extracted from the fit and is equal to:

$$\frac{\mathcal{B}(B_s^0 \to \eta'\eta')}{\mathcal{B}(B^{\pm} \to \eta' K^{\pm})} = 0.47 \pm 0.09 \, \text{stat} \pm 0.04 \, \text{syst.} \tag{8.17}$$

Using the PDG value $\mathcal{B}(B^{\pm} \to \eta' K^{\pm}) = (7.06 \pm 0.25) \times 10^{-5}$, the $B_s^0 \to \eta'\eta'$ is computed,

$$\mathcal{B}(B_s^0 \to \eta'\eta') = (3.31 \pm 0.64 \, (\text{stat}) \pm 0.28 \, (\text{syst}) \pm 0.12(B^{\pm} \to \eta' K^{\pm})) \times 10^{-5}. \tag{8.18}$$

The measurement of the $B^{\pm} \to \eta' K^{\pm}$ charge asymmetry is also performed, using the $B^{\pm} \to J/\psi K^{\pm}$ control channel to determine the production and detection asymmetries. Using the current world average, $\mathcal{A}^{CP}(B^{\pm} \to J/\psi K^{\pm}) = 0.003 \pm 0.006$ [11], we obtain

$$\mathcal{A}^{CP}(B^{\pm} \to \eta' K^{\pm}) = (-0.2 \pm 1.2(\text{stat}) \pm 0.1(\text{syst}) \pm 0.6(B^{\pm} \to J/\psi K^{\pm})) \times 10^{-2}. \tag{8.19}$$

9

Conclusions

The studies presented in this thesis, focused on specific aspects of both the hardware and the physics of the LHCb experiment, summarise my contribution to the LHCb collaboration.

The physics programme of the LHCb experiment requires an optimal knowledge of the momentum of the particles, which is a key element for the precision measurements of masses and lifetimes. In February 2011 a magnetic field campaign has been commissioned in order to solve inconsistencies observed in the software alignment and in mass measurement studies. After defining the data selection and evaluating the accuracy of the field measurements, a fit of the previous magnetic field map to the new measurements has been performed in order to determine possible rotations and translations. As a result of this work a new more reliable mapping of the field has been provided, and is used in the LHCb reconstruction since June 2011. With the new magnetic field map an improved mass resolution and a better agreement between the software alignment and the survey measurements of the tracking station positions is obtained. In view of Run 2 of the LHC, new measurements of the magnetic field have been taken in August 2014 and a new study is being performed in order to determine if a new map is needed for the incoming data.

On the physics analysis side this thesis is focused on charmless B decays. Charmless B decays constitute a very promising sector of B physics for new physics searches. The high suppression of $b \to u$ transitions make all charmless decays described by both a tree and a loop amplitudes potential candidates for new physics discovery. Moreover, the B_s^0 charmless decays constitute an almost unexplored sector. Precise measurements of these decays are fundamental to constrain the large theoretical uncertainties that still affect the predictions of the branching fractions, providing an important experimental feedback to the theoretical community.

Four charmless B decay modes have been investigated using either the $1\,\mathrm{fb}^{-1}$ of data collected at $\sqrt{s} = 7\,\mathrm{TeV}$ in 2011 or the full Run1 data sample which includes also the $2\,\mathrm{fb}^{-1}$ of data collected at $\sqrt{s} = 8\,\mathrm{TeV}$ in 2012. The first analysis, performed with the 2011 data, is dedicated to the search for the suppressed penguin $B^\pm \to \phi\pi^\pm$ decay and

to the measurement of the *CP* asymmetry in the $B^{\pm} \to \phi K^{\pm}$ mode, which is also used as reference channel for the search. The *CP*-violating charge asymmetry in the $B^{\pm} \to \phi K^{\pm}$ mode is predicted to be of the order of 1–2% in the SM. A larger asymmetry would indicate signal interference with an amplitude not described in the SM. The $B^{\pm} \to \phi \pi^{\pm}$ decay is instead highly suppressed. Even a small non-SM amplitude might dominate over the SM amplitude, enhancing the branching fraction. Moreover a measurement of its decay rate could be essential in the understanding of the $\omega - \phi$ mixing phenomenon. Finally, local *CP* asymmetries recently unveiled by the LHCb collaboration in the $B^{\pm} \to K^+K^-K^{\pm}$ and $B^{\pm} \to K^+K^-\pi^{\pm}$ modes further motivate the study of these channels. The $B^{\pm} \to \phi \pi^{\pm}$ signal yield is obtained from a simultaneous two-dimensional fit of the $B^{\pm}$ and ϕ masses, for events reconstructed as $B^{\pm} \to \phi \pi^{\pm}$ and $B^{\pm} \to \phi K^{\pm}$. As a result, the best upper limit of the $B^{\pm} \to \phi \pi^{\pm}$ branching ratio is obtained:

$$\mathcal{B}(B^{\pm} \to \phi \pi^{\pm}) < 1.55(1.80) \times 10^{-7} \text{ at } 90\% \ (95\%) \text{ CL} . \tag{9.1}$$

The *CP* asymmetry of the $B^{\pm} \to \phi K^{\pm}$ decay is instead determined from a simultaneous fit of the positively and negatively charged $B^{\pm} \to \phi K^{\pm}$ candidates in two trigger categories, and using the $B^{\pm} \to J/\psi K^{\pm}$ mode as reference channel to determine the production and detection asymmetries. The best measurement currently available of the *CP* asymmetry is obtained:

$$\mathcal{A}^{CP}(B^{\pm} \to \phi K^{\pm}) = (2.2 \pm 2.1(\text{stat}) \pm 0.7(\text{syst}) \pm 0.6(J/\psi K^{\pm})) \times 10^{-2} . \tag{9.2}$$

The results of this analysis are published by the LHCb collaboration in the journal Physics Letters B [89].

An update of $\mathcal{A}^{CP} (B^{\pm} \to \phi K^{\pm})$ is performed using the full 2011 and 2012 statistics, leading to an even better precision:

$$\mathcal{A}^{CP}(B^{\pm} \to \phi K^{\pm}) = (1.7 \pm 1.1(\text{stat}) \pm 0.2(\text{syst}) \pm 0.6(J/\psi K^{\pm})) \times 10^{-2} . \tag{9.3}$$

The second analysis described in this thesis has as main objective the first observation of the $B_s^0 \to \eta'\eta'$ mode, and exploits the full 2011 and 2012 statistics. Among all the B_s^0 decays into charmless final state, the $B_s^0 \to \eta'\eta'$ mode seems the most promising. Despite the large uncertainties on the predicted yield, its branching fraction might be enhanced compared to other B_s decays because of the high decay rate of the $B^{\pm} \to \eta' K^{\pm}$ and $B^0 \to \eta' K^0$ modes, to which $B_s^0 \to \eta'\eta'$ is related by U-spin and SU(3) symmetries. In order to cancel most of the systematic effects in the measurement, the $B^{\pm} \to \eta' K^{\pm}$ is used as reference channel for the branching fraction measurement. The $B_s^0 \to \eta'\eta'$ and $B^{\pm} \to \eta' K^{\pm}$ samples are fitted simultaneously. The fit is three-dimensional in the B_s^0 mass and in the two η' masses for the events reconstructed as $B_s^0 \to \eta'\eta'$, and two-dimensional in the $B^{\pm}$ and η' masses for events reconstructed as $B^{\pm} \to \eta' K^{\pm}$. The results show the first observation of the $B_s^0 \to \eta'\eta'$ mode, with a significance of 6.4 standard deviations. The $B_s^0 \to \eta'\eta'$ branching ratio is measured to be:

$$\mathcal{B}(B_s^0 \to \eta'\eta') = (3.31 \pm 0.64(\text{stat}) \pm 0.28(\text{syst}) \pm 0.12(B^{\pm} \to \eta' K^{\pm})) \times 10^{-5} . \tag{9.4}$$

Using the same procedure adopted for the measurement of the $B^{\pm} \to \phi K^{\pm}$ CP asymmetry, $\mathcal{A}^{CP}(B^{\pm} \to \eta' K^{\pm})$ is extracted, obtaining:

$$\mathcal{A}^{CP}(B^{\pm} \to \eta' K^{\pm}) = (-0.2 \pm 1.2(\text{stat}) \pm 0.1(\text{syst}) \pm 0.6(J/\psi K^{\pm})) \times 10^{-2} \qquad (9.5)$$

All the measurements presented in this thesis are compatible with the SM theoretical predictions, and they all represent improvements over previous measurements.

The next LHC run, with the foreseen steady increase in integrated luminosity and energy, will provide one of the largest datasets available for heavy flavour physics studies offering the opportunity to probe the presence of new physics to a higher degree of precision. Many charmless modes with light resonances in the intermediate state, still unobserved, will become within experimental reach, such as $B_s^0 \to \eta' \phi$ and $B_s^0 \to \eta \eta'$. Important constraints to phenomenological models can be set from branching fraction measurements, making possible the comparison of the predictive power of different effective theories. Moreover, higher statistics will give the possibility to measure charge and time-dependent asymmetries. In particular a time-dependent analysis of the $B_s^0 \to \eta' \eta'$ decay can provide a measurement complementary to the CP asymmetry measured in $B_s^0 \to \phi\phi$ without need for angular analysis.

This thesis demonstrates the LHCb potential for the discovery of new B_s^0 decays into charmless final states involving light neutral resonances, opening a new era in this only partially explained domain.

Bibliography

[1] ATLAS collaboration, "The ATLAS experiment at the CERN Large Hadron Collider", *JINST* **3** (2008) S08003. `doi:10.1088/1748-0221/3/08/S08003`. 1, 5, 19

[2] CMS collaboration, "The CMS experiment at the CERN LHC", *JINST* **3** (2008) S08004. `doi:10.1088/1748-0221/3/08/S08004`. 1, 5, 19

[3] M. Kobayashi and T. Maskawa, "CP-violation in the renormalizable theory of weak interaction", *Progress of Theoretical Physics* **49** (1973) 652–657. `doi:10.1143/PTP.49.652`. 1, 5

[4] N. Cabibbo, "Unitary symmetry and leptonic decays", *Phys. Rev. Lett.* **10** (Jun, 1963) 531–533. `doi:10.1103/PhysRevLett.10.531`. 1, 5

[5] Belle collaboration, "Observation of large CP violation in the neutral B meson system", *Phys. Rev. Lett.* **87** (2001) 091802, `arXiv:hep-ex/0107061`. `doi:10.1103/PhysRevLett.87.091802`. 1

[6] BaBar collaboration, "Measurement of the $B^0 - \overline{B}^0$ oscillation frequency with inclusive dilepton events", *Phys. Rev. Lett.* **88** (2002) 221803, `arXiv:hep-ex/0112045`. `doi:10.1103/PhysRevLett.88.221803`. 1

[7] S. Glashow, "Partial symmetries of weak interactions", *Nucl. Phys.* **22** (1961) 579–588. `doi:10.1016/0029-5582(61)90469-2`. 3

[8] S. Weinberg, "The quantum theory of fields. Vol. 2: Modern applications", *Cambridge University Press* (1996). 3

[9] A. Salam, "Weak and electromagnetic interactions", *Conf. Proc.* **C680519** (1968) 367–377. 3

[10] M. Han and Y. Nambu, "Three triplet model with double SU(3) symmetry", *Phys. Rev.* **139** (1965) B1006–B1010. `doi:10.1103/PhysRev.139.B1006`. 3

[11] Particle Data Group, "Review of particle physics", *Phys. Rev. D* **86** (2012) 010001, and 2013 partial update for the 2014 edition. `doi:10.1103/PhysRevD.86.010001`. 4, 6, 7, 14, 15, 71, 73, 75, 77, 96, 103, 113, 118, 149, 150, 155

[12] L. R. Evans and P. Bryant, "LHC Machine", *JINST* **3** (2008) S08001. 164 p. This report is an abridged version of the LHC Design Report (CERN-2004-003). 5, 17

[13] ATLAS collaboration, "Observation of a new particle in the search for the Standard Model Higgs boson with the ATLAS detector at the LHC", *Phys. Lett. B* **716** (2012) 1–29, `arXiv:1207.7214`. `doi:10.1016/j.physletb.2012.08.020`. 5

[14] CMS collaboration, "Observation of a new boson at a mass of 125 GeV with the CMS experiment at the LHC", *Phys. Lett. B* **716** (2012) 30–61, `arXiv:1207.7235`. `doi:10.1016/j.physletb.2012.08.021`. 5

[15] MINOS collaboration, "Measurement of neutrino oscillations with the MINOS detectors in the NuMI Beam", *Phys. Rev. Lett.* **101** (2008) 131802, `arXiv:0806.2237`. `doi:10.1103/PhysRevLett.101.131802`. 5

[16] Super-Kamiokande collaboration, "Evidence for an oscillatory signature in atmospheric neutrino oscillation", *Phys. Rev. Lett.* **93** (2004) 101801, `arXiv:hep-ex/0404034`. `doi:10.1103/PhysRevLett.93.101801`. 5

[17] M. Shaposhnikov, "Possible appearance of the baryon asymmetry of the Universe in an electroweak theory", *JETP Lett.* **44** (1986) 465–468. 5, 6

[18] Y. Kawamura, "Gauge hierarchy problem, supersymmetry and fermionic symmetry", `arXiv:1311.2365`. 5

[19] S. L. Glashow, J. Iliopoulos, and L. Maiani, "Weak interactions with lepton-hadron symmetry", *Phys. Rev. D* **2** (Oct, 1970) 1285–1292. `doi:10.1103/PhysRevD.2.1285`. 6

[20] L. Wolfenstein, "Parametrization of the Kobayashi-Maskawa matrix", *Phys. Rev. Lett.* **51** (1983) 1945–1947. `doi:10.1103/PhysRevLett.51.1945`. 6

[21] C. group, "*CP* violation and the CKM matrix: Assessing the impact of the asymmetric *B* factories", *Eur. Phys. J. C* **41** (2005) 1–131, `arXiv:hep-ph/0406184`. Updated results and plots available at . `doi:10.1140/epjc/s2005-02169-1`. 7, 8

[22] G. Buchalla, A. J. Buras, and M. E. Lautenbacher, "Weak decays beyond leading logarithms", *Rev. Mod. Phys.* **68** (1996) 1125–1244. `doi:10.1103/RevModPhys.68.1125`. 10, 12

[23] F. Su, Y.-L. Wu, Y.-B. Yang et al., "Charmless $B \to PP, PV, VV$ decays based on the six-quark effective hamiltonian with strong phase effects I", *J. Phys. G* **38** (2011) 015006, `arXiv:1006.1100`. `doi:10.1088/0954-3899/38/1/015006`. 10

[24] M. Beneke, G. Buchalla, M. Neubert et al., "QCD factorization for exclusive, nonleptonic *B* meson decays: General arguments and the case of heavy light final states", *Nucl. Phys. B* **591** (2000) 313–418, `arXiv:hep-ph/0006124`. `doi:10.1016/S0550-3213(00)00559-9`. 11

[25] Y.-Y. Keum, H.-n. Li, and A. I. Sanda, "Penguin enhancement and $B \to K\pi$ decays in perturbative QCD", *Phys. Rev. D* **63** (2001) 054008. `doi:10.1103/PhysRevD.63.054008`. 11

[26] C. W. Bauer, D. Pirjol, I. Z. Rothstein et al., "B→M(1)M(2): Factorization, charming penguins, strong phases, and polarization", *Phys. Rev. D* **70** (2004) 054015, `arXiv:hep-ph/0401188`. `doi:10.1103/PhysRevD.70.054015`. 11

[27] M. Gronau, O. F. Hernandez, D. London et al., "Electroweak penguins and two-body B decays", *Phys. Rev. D* **52** (1995) 6374–6382, `arXiv:hep-ph/9504327`. `doi:10.1103/PhysRevD.52.6374`. 11

[28] S. Okubo, "ϕ-meson and unitary symmetry model", *Phys. Lett.* **5** (1963) 165–168. `doi:10.1016/S0375-9601(63)92548-9`. 12

[29] G. Zweig, "An SU$_3$ model for strong interaction symmetry and its breaking", *CERN-TH-401 and CERN-TH-412* (1964). 12

[30] J. Iizuka, "A systematics and phenomenology of meson family", *Prog. Theor. Phys. Suppl.* **37-38** (1966) 21–34. `doi:10.1143/PTPS.37.21`. 12

[31] Y. Li, C. D. Lu and W. Wang, "Revisiting $B \to \phi\pi$ decays in the Standard Model", *Phys. Rev. D* **80** (2009) 014024, `arXiv:0901.0648`. `doi:10.1103/PhysRevD.80.014024`. 12, 13, 73

[32] M. Benayoun, P. David, L. DelBuono et al., "The dipion mass spectrum in e^+e^- annihilation and τ decay: a dynamical (ρ, ω, ϕ) mixing approach", *Eur. Phys. J. C* **55** (2008) 199–236, `arXiv:0711.4482`. `doi:10.1140/epjc/s10052-008-0586-6`. 13

[33] M. Benayoun, P. David, L. DelBuono et al., "A global treatment of VMD physics up to the ϕ: I. e^+e^- annihilations, anomalies and vector meson partial widths", *Eur. Phys. J. C* **65** (2010) 211–245, `arXiv:0907.4047`. `doi:10.1140/epjc/s10052-009-1197-6`. 13

[34] M. Beneke and M. Neubert, "QCD factorization for $B \to PP$ and $B \to PV$ decays", *Nucl. Phys. B* **675** (2003) 333–415, `arXiv:hep-ph/0308039`. `doi:10.1016/j.nuclphysb.2003.09.026`. 13, 14, 73

[35] M. Gronau and J. L. Rosner, "*B* decays dominated by $\omega - \phi$ mixing", *Phys. Lett. B* **666** (2008) 185–188, `arXiv:0806.3584`. `doi:10.1016/j.physletb.2008.07.016`. 13, 73

[36] LHCb collaboration, "First observation of $B^0 \to J/\psi K^+ K^-$ and search for $B^0 \to J/\psi \phi$ decays", *Phys. Rev. D* **88** (2013), no. 7, 072005, `arXiv:1308.5916`. `doi:10.1103/PhysRevD.88.072005`. 13

[37] BaBar collaboration, "Search for $B^+ \to \phi\pi^+$ and $B^0 \to \phi\pi^0$ decays", *Phys. Rev. D* **74** (2006) 011102, `arXiv:hep-ex/0605037`. `doi:10.1103/PhysRevD.74.011102`. 13, 119

[38] H.-Y. Cheng and C.-K. Chua, "QCD factorization for charmless hadronic B_s^0 decays revisited", *Phys. Rev. D* **80** (2009) 114026, `arXiv:0910.5237`. `doi:10.1103/PhysRevD.80.114026`. 13, 14, 73

[39] J.-f. Sun, G.-h. Zhu, and D.-s. Du, "Phenomenological analysis of charmless decays $B_{(s)} \to PP, PV$, with QCD factorization", *Phys. Rev. D* **68** (2003) 054003, `arXiv:hep-ph/0211154`. `doi:10.1103/PhysRevD.68.054003`. 13

[40] A. Ali, G. Kramer, Y. Li et al., "Charmless non-leptonic B_s^0 decays to PP, PV and VV final states in the pQCD approach", *Phys. Rev. D* **76** (2007) 074018, `arXiv:hep-ph/0703162`. `doi:10.1103/PhysRevD.76.074018`. 13

[41] A. R. Williamson and J. Zupan, "Two body B decays with isosinglet final states in SCET", *Phys. Rev. D* **74** (2006) 014003, `arXiv:hep-ph/0601214`. `doi:10.1103/PhysRevD.74.014003`. 13

[42] C.-W. Chiang and Y.-F. Zhou, "Flavor SU(3) analysis of charmless B meson decays to two pseudoscalar mesons", *JHEP* **0612** (2006) 027, `arXiv:hep-ph/0609128`. `doi:10.1088/1126-6708/2006/12/027`. 13

[43] H.-n. Li and S. Mishima, "Penguin-dominated $B \to PV$ decays in NLO perturbative QCD", *Phys. Rev. D* **74** (2006) 094020, `arXiv:hep-ph/0608277`. `doi:10.1103/PhysRevD.74.094020`. 14

[44] LHCb collaboration, "Measurement of CP violation in the phase space of $B^\pm \to K^\pm \pi^+ \pi^-$ and $B^\pm \to K^\pm K^+ K^-$ decays", *Phys. Rev. Lett.* **111** (2013) 101801, `arXiv:1306.1246`. `doi:10.1103/PhysRevLett.111.101801`. 14

[45] T. Feldmann, P. Kroll and B. Stech, "Mixing and decay constants of pseudoscalar mesons", *Phys. Rev. D* **58** (1998) 114006, `arXiv:hep-ph/9802409`. `doi:10.1103/PhysRevD.58.114006`. 15

[46] H.-Y. Cheng and J. G. Smith, "Charmless hadronic B-meson decays", *Ann. Rev. Nucl. Part. Sci.* **59** (2009) 215–243, `arXiv:0901.4396`. `doi:10.1146/annurev.nucl.010909.083136`. 15

[47] M. Bander, D. Silverman and A. Soni, "CP non-invariance in the decays of heavy charged quark systems", *Phys. Rev. Lett.* **43** (1979) 242–245. `doi:10.1103/PhysRevLett.43.242`. 15

[48] S. Barshay and G. Kreyerhoff, "The possibility of a sizable, direct *CP* violating asymmetry in $B^{\pm} \to K^{\pm}\eta$", *Phys. Lett. B* **578** (2004) 330–334, arXiv:hep-ph/0309245. doi:10.1016/j.physletb.2003.10.066. 15

[49] ALICE collaboration, "The ALICE experiment at the CERN LHC", *JINST* **3** (2008) S08002. doi:10.1088/1748-0221/3/08/S08002. 19

[50] LHCf collaboration, "The LHCf detector at the CERN Large Hadron Collider", *JINST* **3** (2008) S08006. doi:10.1088/1748-0221/3/08/S08006. 19

[51] TOTEM collaboration, "The TOTEM experiment at the CERN Large Hadron Collider", *JINST* **3** (2008) S08007. doi:10.1088/1748-0221/3/08/S08007. 19

[52] J. L. Pinfold, "The MoEDAL experiment at the LHC", *EPJ Web Conf.* **71** (2014) 00111. doi:10.1051/epjconf/20147100111. 19

[53] LHCb collaboration, "The LHCb Detector at the LHC", *JINST* **3** (2008) S08005. doi:10.1088/1748-0221/3/08/S08005. 20, 21

[54] G. Wilkinson and N. Zaitsev, "Choice of running luminosity for LHCb, and performance of pile-up tag", *LHCb note* (1997) LHCb–97–014, CERN–LHCb–97–014. 21

[55] LHCb collaboration, "LHCb magnet: Technical Design Report", technical report, CERN, Geneva, (2000). 23

[56] LHCb collaboration, "LHCb VELO (VErtex LOcator): Technical Design Report". Technical Design Report LHCb. CERN, Geneva, 2001. 23

[57] LHCb collaboration, "LHCb reoptimized detector design and performance", Technical Report CERN/LHCC/2003-030, CERN, (2003). 23

[58] LHCb collaboration, "LHCb inner tracker: Technical Design Report", Technical Report CERN-LHCC-2002-029, CERN, (2002). 23

[59] LHCb collaboration, "LHCb outer tracker: Technical Design Report". Technical Design Report LHCb. CERN, Geneva, 2001. 23

[60] LHCb collaboration, "LHCb RICH: Technical Design Report". Technical Design Report LHCb. CERN, Geneva, 2000. 23

[61] LHCb collaboration, "LHCb calorimeters: Technical Design Report". Technical Design Report LHCb. CERN, Geneva, 2000. 23

[62] LHCb collaboration, "LHCb muon system: Technical Design Report". Technical Design Report LHCb. CERN, Geneva, 2001. 23

[63] R. Fruhwirth, "Application of Kalman filtering to track and vertex fitting", *Nucl. Instrum. Meth.* **A262** (1987) 444–450. doi:10.1016/0168-9002(87)90887-4. 29

[64] LHCb collaboration, "The GAUSS project".
http://lhcb-release-area.web.cern.ch/LHCb-release-area/DOC/gauss/. 37, 78

[65] I. Belyaev, P. Charpentier, S. Easo et al., "Simulation application for the LHCb experiment", *eConf* **C0303241** (2003) TUMT003, arXiv:physics/0306035. 37

[66] T. Sjöstrand, S. Mrenna and P. Z. Skands, "PYTHIA 6.4 physics and manual", *JHEP* **0605** (2006) 026, arXiv:hep-ph/0603175.
doi:10.1088/1126-6708/2006/05/026. 37

[67] D. Lange, "The EvtGen particle decay simulation package", *Nucl. Instrum. Meth. A* **462** (2001) 152–155. doi:10.1016/S0168-9002(01)00089-4. 37

[68] E. Barberio, B. van Eijk, and Z. Was, "Photos a universal Monte Carlo for QED radiative corrections in decays", *Comp. Phy. Commun.* **66** (1991) 115 – 128.
doi:http://dx.doi.org/10.1016/0010-4655(91)90012-A. 37

[69] G. collaboration, "GEANT4: A simulation toolkit", *Nucl. Instrum. Meth. A* **506** (2003) 250–303. doi:10.1016/S0168-9002(03)01368-8. 37

[70] LHCb collaboration, "The BOOLE project".
http://lhcb-release-area.web.cern.ch/LHCb-release-area/DOC/boole/. 37

[71] LHCb collaboration, "The MOORE project".
http://lhcb-release-area.web.cern.ch/LHCb-release-area/DOC/moore/. 37

[72] LHCb collaboration, "The BRUNEL project".
http://lhcb-release-area.web.cern.ch/LHCb-release-area/DOC/brunel/. 37

[73] LHCb collaboration, "The DAVINCI project".
http://lhcb-release-area.web.cern.ch/LHCb-release-area/DOC/davinci/. 38

[74] "TMinuit". root.cern.ch/root/html/TMinuit.html. 54

[75] G. Punzi, "Sensitivity of searches for new signals and its optimization", *eConf* **C030908** (2003) MODT002, arXiv:physics/0308063. 66

[76] "PIDCalib Packages". PID Calibration web page. 68, 97, 146

[77] "L0 Hadron Trigger Efficiency". L0Hadron Trigger Efficiency web page. 68

[78] LHCb collaboration, "Measurement of $\sigma(pp \to b\bar{b}X)$ at $\sqrt{s}$=7 TeV in the forward region", *Phys. Lett. B* **694** (2010) 209–216, arXiv:1009.2731.
doi:10.1016/j.physletb.2010.10.010. 73

[79] LHCb collaboration, "Production of J/ψ and Y mesons in pp collisions at $\sqrt{s} = 8$ TeV", *JHEP* **1306** (2013) 064, arXiv:1304.6977.
doi:10.1007/JHEP06(2013)064. 73

[80] D0 collaboration, "Measurement of direct *CP* violation parameters in $B^\pm \to J/\psi\,K^\pm$ and $B^\pm \to J/\psi\,\pi^\pm$ decays with $10.4\,\mathrm{fb}^{-1}$ of Tevatron data", *Phys. Rev. Lett.* **110** (2013) 241801, `arXiv:1304.1655`. `doi:10.1103/PhysRevLett.110.241801`. 75, 77

[81] D0 collaboration, "Study of direct *CP* violation in $B^\pm \to J/\psi K^\pm(\pi^\pm)$ decays", *Phys. Rev. Lett.* **100** (2008) 211802, `arXiv:0802.3299`. `doi:10.1103/PhysRevLett.100.211802`. 75

[82] V. V. Gligorov, C. Thomas and M. Williams, "The HLT inclusive *B* triggers", Technical Report LHCb-PUB-2011-016. CERN-LHCb-PUB-2011-016. LHCb-INT-2011-030, CERN, Geneva, (Sep, 2011). LHCb-INT-2011-030. 79

[83] G. Punzi, "Comments on likelihood fits with variable resolution", *eConf* **C030908** (2003) WELT002, `arXiv:physics/0401045`. 83, 91

[84] M. Pivk and F. R. Le Diberder, "SPlot: A statistical tool to unfold data distributions", *Nucl. Instrum. Meth. A* **555** (2005) 356–369, `arXiv:physics/0402083`. `doi:10.1016/j.nima.2005.08.106`. 99

[85] I. Bediaga, A. Gomes, J. Helder et al., "*CP* violation measurement in $B^\pm \to K^\pm\pi^+\pi^-$ and $B^\pm \to K^\pm K^+ K^-$ decays in 2011 data". LHCb-ANA-2013-029_v4, 2013. 102, 104, 105, 117, 153

[86] "Simulation settings". Simulation settings web page. 124

[87] V. Belyaev, V. Egorychev, and D. Golubkov, "Study of π^0/γ reconstruction efficiency with 2011 data", Technical Report LHCb-INT-2012-001. CERN-LHCb-INT-2012-001, CERN, Geneva, (Jan, 2012). 126

[88] LHCb collaboration, "Updated average f_s/f_d *b*-hadron production fraction ratio for 7 TeV *pp* collisions", *conference note* (2013) LHCb–CONF–2013–011. 139

[89] LHCb collaboration, "Measurement of the charge asymmetry in $B^\pm \to \phi K^\pm$ and search for $B^\pm \to \phi\pi^\pm$ decays", *Phys. Lett. B* **728** (2014) 85–94, `arXiv:1309.3742`. `doi:10.1016/j.physletb.2013.11.036`. 158

JESSICA PRISCIANDARO

SUMMARY

I performed original research in high energy physics at the Large Hadron Collider (LHC), contributing to precision measurements in the b-physics sector and to hardware characterization. I used an object-oriented framework and distributed computing to analyze large multivariate datasets and exploited its internal correlation to infer statistically significant deviations from the known behaviors. I led two analyses from the conception to the final product (publication) overcoming with creativity the various different problems related to each step. I collaborated, taking leading roles when demanded, in a large and international team of physicists and engineers working towards a common objective.

PERSONAL INFO

Home address: Rue de Geneve 24, 01210 Ferney-Voltaire, FRANCE
Phone: +41227672518 (office), +41787762429 (mobile)
email: jessica.prisciandaro@epfl.ch, jessica.prisciandaro@cern.ch
Nationality: Italian, Swiss permit G
Date Of Birth: 22/12/1986

EDUCATION

ECOLE POLITECNIQUE FEDERAL DE LAUSANNE (SWITZERLAND)
Ph.D in particle physics   *Nov. 2014*
Thesis topic: Studies of charmless B$_{(s)}$ meson decays involving   *(Official endorsement Jan. 2015)*
η' and φ intermediate states at the LHCb experiment

UNIVERSITY OF TURIN (ITALY)
Master in physics   *2010*
grade: 110/110 cum laude
Thesis topic: Studies of Drell-Yan processes at Compass Experiment

UNIVERSITY OF TURIN (ITALY)
Bachelor in physics   *2008*
grade: 110/110 cum laude
Thesis topic: Muon radiography for high Z materials identification

WORKING EXPERIENCE

ECOLE POLITECNIQUE FEDERAL DE LAUSANNE / LHC COLLABORATION
Graduate student   *2010 - Present*
-I led and developed four measurements in high-energy b-physics at the LHCb experiment. I was responsible of each step of the analyses from the data skimming to statistical interpretation and publication. A first paper is published in 2013 by a major journal. A second paper is currently in review process within the LHCb collaboration.
- Editor of all documentation for my analyses (internal notes and papers).
- Collaborated to the commissioning of the LHCb magnetic field map (currently in use). I participated to a dedicated magnetic field data-taking campaign and I was responsible of the data analysis.
- Teaching and assistant duties: laboratory assistant (2 semesters), professor assistant for particle physics lectures (3 semesters), supervisor in particle physics project for a master student (1 semester).

UNIVERSITY OF TURIN (ITALY)
Assistant   *2007-2008*
I was professor assistant, organizing the material and the documentation for a university course.

SKILLS

Physics: deep knowledge of physics, especially targeted towards radiation and its interaction with matter
Statistics: During my graduate studies I learned statistical principles and I applied them on daily basis to achieve publication-worth results.
Computer skills:
  - **OS:** I have good knowledge of Linux, Windows and OSX operating system.
  - **Programming languages:** I have good experience with C++ and I am competent with python and shell programming.
  - **Scientific software:** I have a deep knowledge of ROOT scientific software, and its statistical library RooFit.
  - **Development tools:** I am a proficient user of version control softwares like SVN.
  - **Office suites:** I am a proficient user of office suites such as MS Office, Open Office, Apple iWork, Tex/LaTex word processing.

JESSICA PRISCIANDARO

LANGUAGES

Italian: mother tongue
English: fluent (C1)
French: basic (A2), currently improving to B1

CONFERENCES

SPS 2014, Fribourg (Switzerland), 30 June - 2 July 2014
Talk presented: "Charmless B decays at LHCb"

PHENO 2014, Pittsburgh (Pennsylvania-USA), 5-7 May 2014
Talk presented: "Studies of charmless B decays at LHCb"

PASCOS 2013, Taipei (Taiwan), 20-26 Nov 2013
Talk presented: "Studies of charmless B decays at LHCb"

LHCC 2013, CERN (Switzerland), 13 March 2013
Poster: "Charmless B→3 body decay at LHCb"

SLAC Summer School 2012, SLAC (California-USA), July 23-Aug 3, 2012
Poster: "Study of charmless $B^+ \to \phi h^+$ decays with the LHCb experiment"

SCIENTIFIC SCHOOLS

CHIPP PhD winter school 2012, Engelberg, Switzerland

SLAC Summer Institute 2012, SLAC National Accelerator Laboratory, U.S.A.

SELECTED PUBLICATIONS

I am coauthor of 225 LHCb publications (update to 8th December 2014)
https://cds.cern.ch/collection/LHCb%20Papers

I'm the main author of the published article:
LHCb collaboration "Measurement of the charge asymmetry in $B^\pm \to \phi K^\pm$ and search for $B^\pm \to \phi \pi^\pm$ decays" Phys. Lett. B 728 (2014) 85-94

INTERESTS

- Graduated in sol-fa, I played piano for 13 years.
- I worked in a voluntary association for children with disabilities.